FINAL REPORT
to the
AUSTRIAN ACADEMY OF SCIENCES (OeAW)
within the
EARTH SYSTEM SCIENCES
research program

SeisRockHT

Seismic Rockfall Monitoring in the Hohe Tauern region
by means of
Open - Design Products

December, 2020

Authors:

Binder Daniel, Mertl Stefan, Hartmeyer Ingo, Keuschnig Markus and Lenhardt Wolfgang

DOI: 10.1553/ESS-SeisRockHT

ISBN-online: 978-3-7001-8-8857-5

Citation:

Binder, D., Mertl, S., Hartmeyer, I., Keuschnig, M., & Lenhardt, W. (2020). SeisRockHT - Seismic Rockfall Monitoring in the Hohe Tauern region by means of Open-Design Products. *Austrian Academy of Sciences (OeAW), ESS - Final Report.* doi:10.1553/ESS-SeisRockHT, isbn-online: 978-3-7001-8-8857-5

Project team:

Zentralanstalt für Meteorologie und Geodynamik

Dr. Wolfgang Lenhardt (PI)

Daniel Binder, Mag. (Co-PI)

Mertl Research GmbH

Dr. Stefan Mertl

Georesearch Forschungsgesellschaft mbH

Dr. Ingo Hartmeyer

Dr. Markus Keuschnig

Project budget:

Requested amount:	€ 349,880.-
Approved amount:	**€ 169,759.-**

Project duration:

Spring 2015 - Autumn 2020

Contents

1 Summary **1**

2 Introduction **3**

2.1 Objectives 6

3 SeisRockHT - an Open-Design Project **7**

3.1 Ruwai - a FOSH Seismic Data Recorder 7

3.2 Seismic Sensors 21

3.3 The Sonnblick Seismological Network 23

3.3.1 Mains Powered Stations 25

3.3.2 Stand-Alone Stations 31

3.4 The Kitzsteinhorn Seismological Network 40

4 Data Availability and Quality **43**

4.1 Terrain Data 43

4.2 Seismic Data 46

4.3 Complementary Data 56

5 Analysis Tools and Methods **58**

5.1 Terrain Modeling 58

5.2 Seismic Processing 59

5.2.1 pSysmon - a FOSS Project 59

5.2.2 Analysis Methods 59

6 Results and Discussion **61**

6.1 TLS Terrain Monitoring 61

6.2 Visually Validated Rockfalls 67

6.3 Field Campaign 2017 70

6.3.1 Ambient Seismicity 71

6.3.2 Detected Events 76

6.3.3 Temporal Event Distribution and Correlation with Complementary Data 80

6.4 Extreme Weather Event 2018 83

6.4.1 Ambient Seismicity 88

6.4.2 Detected Events . . . 90
6.4.3 Temporal Event Distribution and Correlation with Complementary Data . . . 94
6.5 Miscellaneous Seismic Events . . . 97
6.6 Discussion . . . 106

7 Conclusions **108**

8 Future Perspectives **110**

9 Acknowledgements **112**

10 Author Contributions **113**

11 Dissemination and Outreach **114**

Bibliography **119**
References . . . 119
List of Figures . . . 125
List of Tables . . . 133

Appendix **135**
Appendix A: Seismic Data Availability . . . 135
Appendix B: Weekly Spectrograms . . . 143
Appendix C: Seismic Event Catalogs . . . 151
Appendix D: Ruwai Technical Reports . . . 166
Appendix E: Miscellaneous . . . 220
Appendix F: Dissemination and Outreach . . . 252

1. Summary

There is growing evidence that rockfall activity in permafrost-affected mountain areas increases in frequency and magnitude due to climate warming. To date, only a few robust time series with sufficient spatial and temporal resolution exist to investigate rockfall processes in high-alpine environments. However, many aspects of the long-term destabilization of rock slopes in a changing climate remain elusive.

Regular terrain surveys can accurately detect volume changes between two acquisition dates, but cannot distinguish whether the detected volume change is the result of one single rockfall event, or of a series of smaller adjacent and/or subsequent events. Thus, continuous monitoring strategies are needed to assess rockfall frequency and magnitude. Additionally, continuous complementary data provide valuable insights into the development and triggers of rockfall. This approach enables an advanced process-based understanding of the destabilization of rock slopes and thus emerging rockfall hazards in permafrost-affected mountain areas in a changing climate.

SeisRockHT installed seismological networks at two prominent alpine north-faces in the 'Hohe Tauern' region to continuously monitor rockfall activity with a long-term perspective. The Sonnblick, as well as the Kitzsteinhorn investigation site hosts renowned environmental monitoring programs which provided a suite of complementary data. Additional regular terrain surveys by terrestrial laser scanning (TLS) determined rockfall release zones and total rockfall volumes.

Due to a major reduction of the project budget, *SeisRockHT* followed a low-cost and open-design approach to establish the seismological networks. The *Ruwai* data recorder was deployed for the first time in the field, and delivered high quality seismic data for the Sonnblick site. At Kitzsteinhorn, persistent electromagnetic interferences made the acquired data unusable. The recorded Sonnblick data exhibited several data gaps throughout the five-year monitoring period, which were mainly caused by power shortages during winter. Over the course of the project the annual seismic data yield was more than doubled.

TLS results for both north-faces revealed disparity in altitude with higher rockfall activity at lower elevations. At Kitzsteinhorn, a higher susceptibility for climate change induced processes at lower elevations is a likely explanation. For Sonnblick, however, an artificial bias due to incomplete data coverage cannot be ruled out as cause for the observed disparity in altitude.

Seismic data from the Sonnblick network for two distinct periods were analysed. The first was a two-month period during autumn, 2017, and the second period covered an extreme weather event in October, 2018. Ambient seismicity recorded at the Kolm Saigurn valley floor suggested a correlation with discharge of local creeks for both periods. Furthermore, ongoing construction work for the new Sonnblick observatory cable car in 2017 was reflected in ambient seismicity. Detected seismic events of the two investigation periods were manually divided into seven categories, from which *Rockfall Candidate Short* and *Rockfall Candidate Long* were related to rockfalls. The number of detected *Rockfall Candidates Short* events showed a strong correlation with positive air temperatures. However, further analysis is indispensable in order to conclude any connection to global warming induced permafrost degradation. The *Rockfall Candidate Long* events were correlated to episodes of rainfall.

In conclusion, the Sonnblick seismological network yielded ambient seismicity and abundant seismic events for distinct periods which could be linked to environmental and anthropogenic sources. The deduced seismic sources were supported by abundant complementary data. However, continuous data availability, as well as automation of rockfall event detection, must be further pursued in order to ensure a continuous rockfall

monitoring on a long-term basis. Eventually, this effort builds a solid future base for comprehensive natural hazards research in alpine environments.

2. Introduction

High-alpine mass wasting and in particular the erosion of steep rock walls is largely controlled by rockfall (e.g. Hartmeyer et al. (2020b); Matasci et al. (2015)). In densely populated mountain regions such as the Alps, rockfall also poses a serious geohazard for man and infrastructure (e.g. Stähli et al. (2015); Volkwein et al. (2011)). The impact on rockfall activity of the current climate change with the accompanying deglaciation and permafrost degradation is, however, still not fully understood (Krautblatter and Leith (2015); Ravanel and Deline (2015); S. Allen and Huggel (2013); Krautblatter et al. (2013); Gruber and Haeberli (2007)).

Sass and Oberlechner (2012) analysed an existing rockfall inventory of Austria with 252 events from ∼1900 to 2010. Their analysis showed a weak temperature correlation and no increase of rockfall frequency during warmer periods. The peak of rockfall activity was distinguished to be in spring, while a second maximum was found in summer for more recent decades. Nevertheless, their final conclusion was that an increase in rockfall hazard due to rising temperature is not supported by their data. However, the analysed rockfall inventory was based on mainly non-permafrost areas, hence no sound conclusions could be drawn for the impact of permafrost degradation on rockfall activity. In a similar study for Switzerland, Gruner (2008) concluded that cold climate periods and single cold winters represent the main triggers of small and medium events, while warmer climate periods and warmer summers generally decrease rockfall activity. The by Gruner (2008) applied data was, however, lacking permafrost-prone settings. Ravanel and Deline (2011) analyzed the climate impact on rockfalls since the end of the Little Ice Age for the high-alpine Aiguilles de Chamonix north-face (Mont Blanc massif, France). They suggested that a climatically driven permafrost degradation has triggered many of the recent rockfalls in high-alpine steep rockwalls, especially during warmer summers. Eventually, the generally limited data availability of historical rockfall activity in permafrost-prone alpine settings hinders rigorous conclusions of long-term rockfall trends in a changing climate (Glade et al. (2020); Paranunzio et al. (2016); Ravanel and Deline (2015)).

Several studies stress the likely relation of steep rock slope failure and permafrost degradation (Magnin et al. (2019); Haeberli et al. (2017); Krautblatter and Leith (2015); S. Allen and Huggel (2013); Gruber and Haeberli (2007)). Gruber et al. (2004) reported on the impact of the hot summer of 2003 on permafrost thaw in the Swiss Alps. They concluded that this led to destabilization of rock walls and resulted in increased rockfall activity at high elevations, especially for north-facing slopes. Fischer et al. (2006) documented for the Monte Rosa east-face, Italian Alps, an enhanced mass movement activity and development of new detachment zones since about 1990. Additional to geological transition zones, new detachment zones were documented at the lower permafrost boundary altitude and sectors where surface ice recently disappeared. Hartmeyer et al. (2020b) showed an exceptionally high retreat rate due to enhanced rockfall activity for a recently deglaciated cirque headwall in the Austrian Alps. Although, steep bedrock destabilization by permafrost degradation is still discussed (Hasler et al. (2012); Gruber and Haeberli (2007)), three types of field evidences are indicated in literature: *(1)* the exposure of ice at rockfall backscarps subsequent to failure (Haeberli et al. (2004); Dramis et al. (1995)), and *(2)* the spatial and *(3)* temporal coincidence of rock slope failure and thermal disturbances in permafrost walls (Noetzli et al. (2006); Gruber et al. (2004)). Furthermore, Krautblatter et al. (2013) quantitatively demonstrated by a laboratory-based model the influence of permafrost degradation on steep rock slope failure of varying magnitudes.

Regular terrain surveys can accurately detect rockfall release zones and cumulated rockfall volumes between two survey dates (e.g. Hartmeyer et al. (2020a)). It cannot be distinguished, however, if the detected rockfall volume originated from a series of adjacent and/or subsequent rockfall events, or from a single rockfall event. Continuous long-term monitoring strategies with high temporal resolution are thus required to further examine the current knowledge of rock slope failure due to permafrost degradation. Continuous seismic monitoring is a well established strategy to capture occasional events like rockfalls. Rockfall events were detected by seismic networks designed to actually monitor e.g. earthquakes (Deparis et al. (2008)), volcanic activity (Hibert et al. (2011)), land- and rockslides (Brückl and Mertl (2013); Occhiena et al. (2012); Walter, Arnhardt, and Joswig (2012); Walter, Schwaderer, and Joswig (2012); Helmstetter and Garambois (2010); Amitrano et al. (2010); Spillmann (2007)), and cliff-topplings (Lévy et al. (2011); Got et al. (2010)). Parameters of rockslides and rockfalls with volumes larger than 100 m^3 could be related to seismic signal characteristics recorded by regional monitoring networks, whereas the characteristics were defined over the entire seismic signal (Fuchs et al. (2018); Manconi et al. (2016); Dammeier et al. (2011); Deparis et al. (2008)). Deparis et al. (2008) found that signal duration was roughly correlated with the potential energy and the run out distance. Dammeier et al. (2011) found a good correlation of seismic signal duration, peak envelope velocity, and envelope area, with rockfall volume and potential energy. Finally, Manconi et al. (2016) and Fuchs et al. (2018) proposed relationships of rockfall and rockslide volumes with signal duration and local magnitude, respectively. Regional seismic networks feature distances of the order of tens of kilometers between the discharged rock and the network stations. The recorded seismic signal is thus modified by media inhomogeneities on the signal's raypath from the actual event to the recording stations and make the different rockslide and rockfall dynamic phases indistinguishable.

Local seismic monitoring is able to delineate distinct rockfall dynamic phases like detachment, free fall, first and intermittent impacts, fragmentation, arrival at the talus slope and subsequent slope activity (Le Roy et al. (2019); Dietze et al. (2017a)). However, relating seismic signal properties to rockfall parameters at this spatial scale is challenging due to the dominance of other, process-inherent factors, such as free fall height, degree of fragmentation, and subsequent talus slope activity. Hibert et al. (2017) conducted controlled single-block releases in a marl gulley and could demonstrate that the recorded maximum seismic amplitude generated by the impact of a single particle is proportional to its kinetic energy. Dietze et al. (2017a), as well as Le Roy et al. (2019) could not find a relationship between the rockfall volume and the total released seismic energy or peak amplitude. Le Roy et al. (2019) additionally segregated rockfalls experiencing a free fall from those with sliding or bouncing transport modes, and focused on the seismic signal of rockfall detachment and impact. This way they found a relation between the potential energy of a rockfall and the seismic energy generated during the impact. Thus, both the potential energy of a block and its free-fall height could be estimated from the seismic signals which led to an accurate estimate of the rockfall volume.

Environmental seismology studies near-surface processes originating, or affected by external triggers, outside the solid earth. This includes for instance the coupling between the solid earth and the atmosphere, cryosphere, and/or the hydrosphere (Larose et al. (2015)). Complementary environmental data is indispensable to properly investigate these coupled processes and infer potential environmental trigger mechanisms of e.g. rockfalls. The geological setting of a site is a key parameter to rockfall activity, but exhibits a rather stable behaviour in time and space. In comparison, parameters like rainfall or temperature exhibit large variations. Dietze et al. (2017b) detected 37 potential rockfalls in a 37-days monitoring period in the autumn for a near-vertical cliff section of the Lauterbrunnen Valley in the Swiss Alps. Following the environmental seismology approach, they concluded that freeze–thaw transitions accounted only for a minor part ($\sim$10 %) of the detected rockfalls, whereas the majority ($\sim$40 %) was triggered by rainfall. Another major part ($\sim$35 %) was triggered by diurnal temperature changes and occurred during the coldest hours of the day and during the highest temperature change rates. Eventually, none of the seismic rockfall studies were conducted in a permafrost-prone setting. Therefore, a long-term local seismic monitoring strategy is needed to compile a solid data base for permafrost-related rockfall research.

High-resolution seismic networks are expensive to install, and need resource-intense maintenance: one high-resolution seismic station costs in the order of tens of thousands of €uros to build and equip for field operation. Despite a loss of signal resolution, low-cost solutions are becoming increasingly attractive for seismic monitoring applications (Cochran (2018)), especially for remote investigation sites in harsh environments requiring enhanced logistics and costs. Manconi et al. (2018) applied the low-cost seismic sensor *Raspberry Shake* to monitor rockfalls on a slope adjacent to the Great Aletsch Glacier in the Swiss Alps and could clearly discriminate rockfalls from other events. However, local seismic networks require small event-sensor distances and the *Raspberry Shake's* maximum signal sampling rates of 50-100 samples per second (sps) are a clear limitation for extended signal analysis.

SeisRockHT installed two local seismic networks of different spatial scales in two high-alpine, permafrost-affected settings. During the *SeisRockHT* project a long-term monitoring strategy with main focus on rockfall activity was pursued. Annual terrestrial laser scan surveys delivered rockfall release zones and annually accumulated rockfall volumes throughout the project. The environmental monitoring programs at both investigation sites made an abundant variety of complementary data accessible. With the end of the *SeisRockHT* project, both implemented seismological networks were embedded into the environmental long-term monitoring programs, hence, assuring the long-term perspective of the *SeisRockHT* research initiative. *SeisRockHT* employed free and open-source hardware (*FOSH*) and software (*FOSS*) to implement the long-term seismic monitoring networks. The *open-design* approach provided freedom of customization at low-costs. However, setbacks due to hard- and software shortcomings needed to be examined and overcome within the project which substantially prolonged the total project duration. Seismic data of two distinct periods were analysed and discussed with the available complementary data.

Based on the current state of knowledge and the *SeisRockHT* investigation site characteristics hypotheses hereafter emerged. Due to the fact that testing the hypotheses require a solid data base, this is a rather long-term task. *SeisRockHT* hypotheses are:

→ Rockfall activity is increasing with climate warming for permafrost-prone settings in the Alps.

→ Permafrost-related rockfall events will especially occur during hot summers.

→ Classic rockfall events will occur during periods of low and decreasing temperatures.

→ Particular weather situations trigger rockfall events.

→ Distinct rockfall dynamic phases can be delineated by *SeisRockHT* seismic data.

→ There is a relation between rockfall parameters and their seismic characteristics.

2.1 Objectives

The original *SeisRockHT* project objectives and work packages had to be reduced and rearranged due to the considerable cut of >50% of the originally requested project budget. Consequently, the project mainly concentrated on the establishment of the seismological networks to assure the long-term monitoring perspective and enable future research.

The main objective of the *SeisRockHT* project was the installation of two local seismological networks by means of *open-design* products to build a starting point of continuous long-term rockfall monitoring in two prominent permafrost-affected investigation sites. Consequently, a main *SeisRockHT* focus was optimization of the seismological networks towards a continuous operation. Besides, the *SeisRockHT* networks were embedded into the long-term monitoring programs *ASBO* (Sonnblick site, see section 3.3) and *OpAL* (Kitzsteinhorn site, see section 3.4) to assure the *SeisRockHT* long-term perspective. Additionally, *SeisRockHT* data were incorporated into the established operational data management by the *Seismological Service of Austria* based at the ZAMG. Beside these main objectives, *SeisRockHT* aimed to

... evaluate temporal and spatial ambient seismicity characteristics.

... optimize methods for characterization, detection and localization of seismic events.

... compile characteristic seismic events registered at the two sites.

... evaluate correlation between seismic and complementary data.

... evaluate correlation between seismic data and rockfall parameters.

3. SeisRockHT - an Open-Design Project

"The open-design movement involves the development of physical products, machines and systems through use of publicly shared design information. This includes the making of both free and open-source software (FOSS), as well as free and open-source hardware (FOSH). The process is generally facilitated by the Internet and often performed without monetary compensation. Open-design is a form of co-creation, where the final product is designed by the users, rather than an external stakeholder such as a private company." (Wikipedia (2020))

SeisRockHT followed an open-design approach to implement novel long-term monitoring initiatives at two investigation sites. In detail, *SeisRockHT* deployed the *FOSH Ruwai* seismic data recorder (section 3.1) on the one hand, and on the other, the *FOSS pSysmon* (section 5.2.1) for seismic data processing and *CloudCompare* (section 5.1) for terrain data processing. Miscellaneous soft- and hardware, as well as strategies developed within *SeisRockHT* are described in this report, and further elaborated in the following chapters and appendix of this report. Despite the fact that the low-cost open-design approach involves the risk of failure due to component shortcomings, it also provides a high degree of innovation potential through tailor-made solutions. Alternative low-cost data recorders like the *digos DataCube*[3], or the *raspberry shake* were considered. Eventually, proprietary licensing and technical restrictions of the two products on the one hand, as well as the perspective of a tailor-made and open *SeisRockHT* data recorder on the other, led to the decision to use the *FOSH Ruwai* data recorder.

3.1 Ruwai - a FOSH Seismic Data Recorder

The proof of concept and a first prototype of the *Ruwai* seismic data recorder was developed in the year 2014 by *SeisRockHT* project partner *Mert Research GmbH* within the *CEON* project funded by the *Netidee* program of the *Internet Privatstiftung Austria (IPA)*. Within the *SeisRockHT* project, the construction of a batch of units and the usability for a high-alpine deployment was tested for the first time.

Transparency and good documentation is crucial for *FOSH* projects to facilitate the co-creation process and reproducibility. All *Ruwai* hardware design files are published under the *Cern Open Hardware License* and the software source code under the *GNU GPL 3.0 license*. The hardware design- and software files are provided in the public git repository *http://www.repo.or.cz/ruwai.git*. An overview of the *Ruwai* project can be found online on *https://www.mertl-research.at/projects/ruwai/*. In the following, a short overview of the *Ruwai* seismic data recorder, the construction process and the specific *SeisRockHT* application is given.

The complete technical reports about the assembly (Mertl (2017a)) and the performance (Mertl (2017c)) of the *Ruwai* seismic data recorder can be found in Appendix D.

System Overview

The *Ruwai* seismic data recorder is based on the *Arduino Mega 2560* microcontroller board and the *BeagleBone Black* single board computer. Four custom printed circuit boards (PCBs) were designed for the *Arduino Mega 2560* using the free software *KiCad* (*https://kicad-pcb.org/*), these PCBs are called *shields*. The block diagram in Figure 3.1 shows all major hardware components and its interconnections. Basically, the system is split up into the *Arduino Stack* and the *BeagleBone Black*. The *Arduino Stack* (shown in Figure 3.2) consists of the the *Arduino Mega 2560* with four shields stacked on top of each other:

- the *GPS Timing Shield*
- the *Analog to Digital Converter (ADC) Main Shield*
- the *Analog Interface Programmable Gain Amplifier (PGA) Shield*
- the *Power Supply Shield*

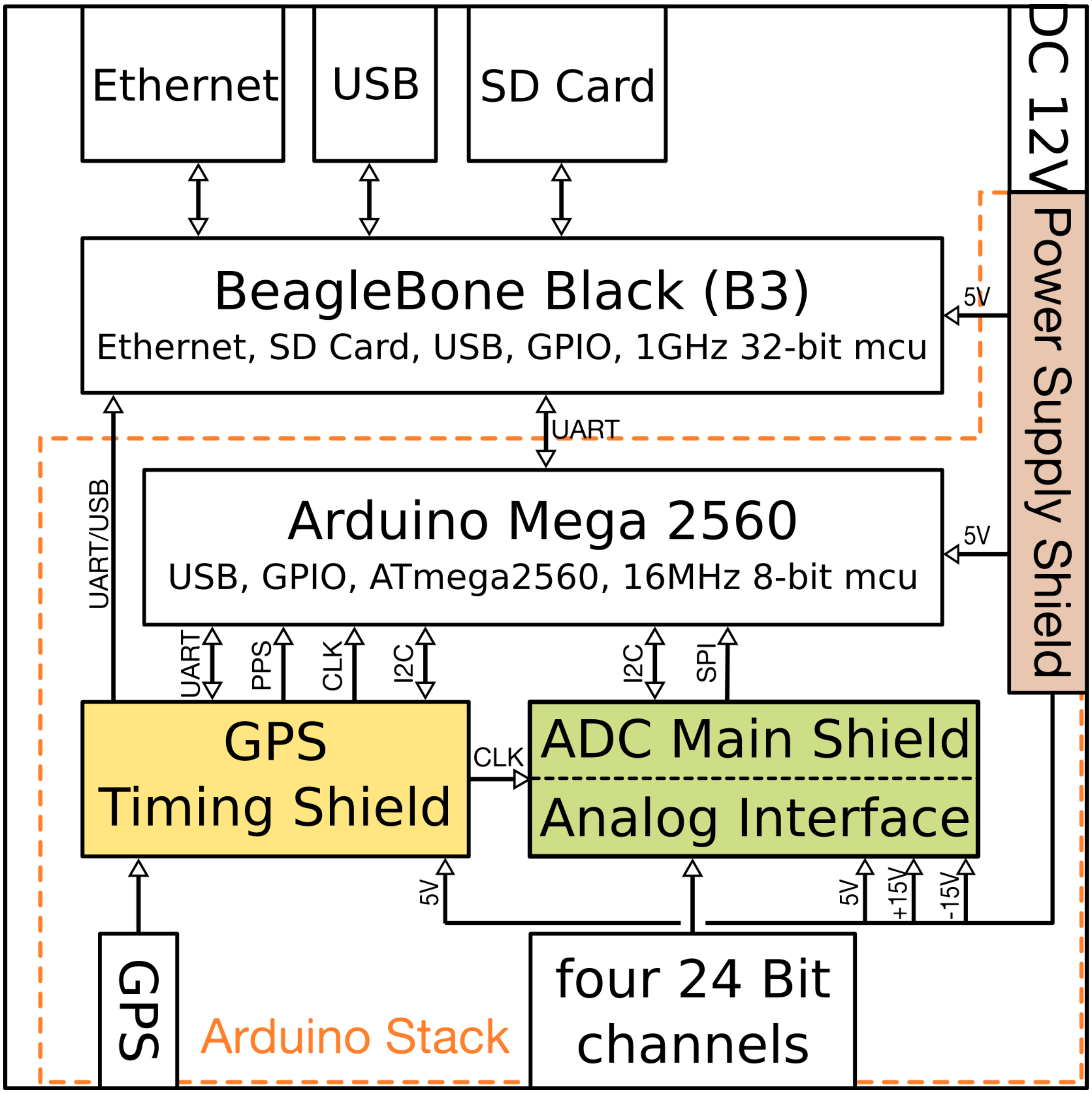

Figure 3.1: Block diagram of the major *Ruwai* hardware components.

The *Arduino Stack* handles processes that require real-time performance, e.g. collecting the digitized samples from the analog to digital converter and providing each sample with a timestamp. The *BeagleBone Black* is used for extensive computational tasks such as data storage, logging, function control and ethernet communication.

The *Arduino Stack* and the *BeagleBone Black* are mounted in a *Pelicase 1200* enclosure with an ingress protection rating of IP67 (see Figure 3.3). The *Arduino Stack* is shielded from electronic interference using an aluminum enclosure. The *Pelicase 1200* enclosure features connectors for the sensor, the power supply, an external GPS antenna and an ethernet connection. The used connectors are *Bulgin 400 Series Buccaneer* for the power supply and ethernet connection, *Bulgin 7000 Series Buccaneer* for the sensor and *Bulgin 400 Series SMB* for the GPS connector. All connectors are rated at IP68.

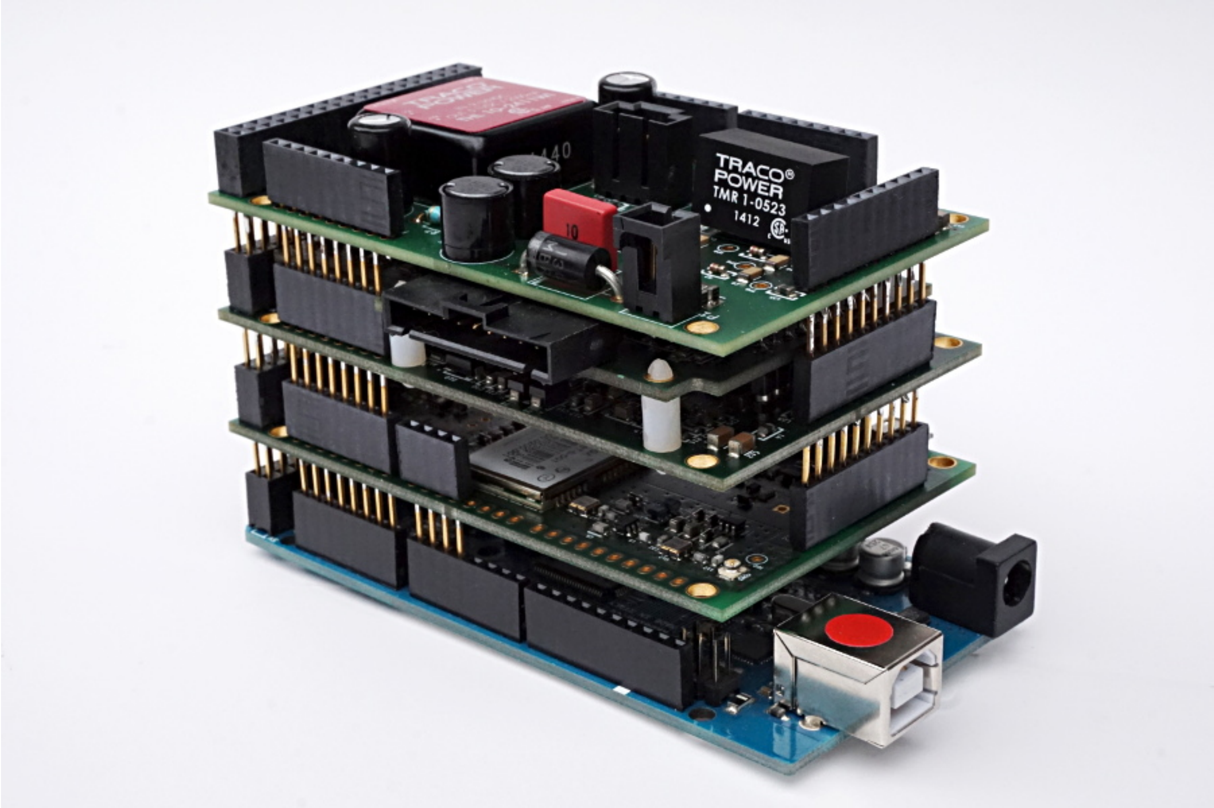

Figure 3.2: The *Arduino Stack* of the *Ruwai* seismic data recorder. The *Arduino Mega 2560* microcontroller builds the base, with the *GPS Timing Shield*, the *ADC Main shield* with the *Analog Interface PGA Shield*, and the *Power Supply Shield* stacked on top of each other.

The *Ruwai* data recorder provides four differential analog input channels with maximum input voltages of ± 2.5 V. Pre-amplification (gain) values between 0.125 and 176 can be chosen for the analog input. Sampling rates between 100 and 1000 samples per second are available for digitalization of the analog signal. Timestamping of the digitized samples is realized through a pulse-per-second (PPS) signal provided by the *uBlox LEA-6T* GPS module. The sample timestamp accuracy of the *Ruwai* data recorder was tested by running it parallel with a commercial data recorder and comparing the recorded waveforms. The timing of both recorded waveforms was equal at sample level and no time shift was observed. Finally, the digitized data is saved on a micro-SD card in miniSEED file format. The *Ruwai* data recorder is operated with a DC power supply from 9 - 36 V and has a power consumption of ∼3 Watts.

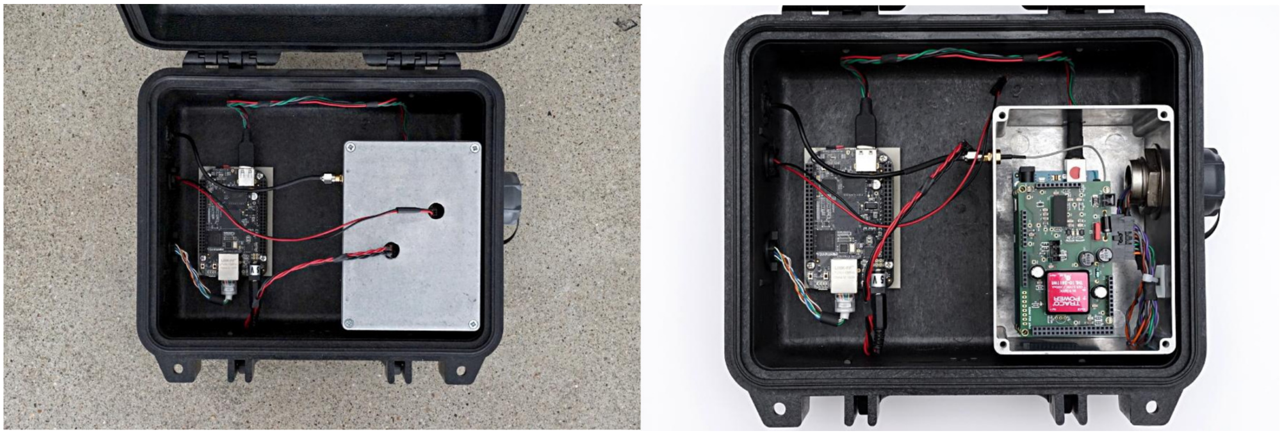

Figure 3.3: The *Arduino Stack* inside the *Pelicase* enclosure with closed and open shielding. The left element is the *BeagleBone Black* single-board computer.

Instrument Self-Noise

A common method to test the system inherent electronic noise of a data logger is recording the data logger's outputs with shorted inputs, which essentially means zero amplitude inputs. For an ideal data logger without any electronic self-noise the recorded outputs would be zero as well. However, in reality the system output contains the system's inherent electronic noise, and therefore, is a measure of the quality, or rather, sensitivity of the data recorder.

The minimum resolvable ground velocity, or minimum noise floor, is used to characterize the performance of the whole recording system (data recorder + seismic sensor). The minimum noise floor is the smallest possible ground motion that can be resolved by the data recorder with a specific sensor. The inverse transfer function of the seismic sensor, as well as the chosen pre-amplification value are used to compute the ground motion equivalent of the recorded shorted input signal, which represents the minimum noise floor of the specific recording system. Any ground motion amplitude below the recording system's minimum noise floor does not create voltage high enough to exceed the internal noise of the data recorder, hence cannot be resolved by the recording system.

The self-noise of the *Ruwai* data recorder was tested thoroughly. A detailed description can be found in the attached technical report *Performance of the seismic recorder Ruwai* (Mertl (2017c)). Figure 3.4a shows the power spectral density of the *Ruwai* recording system with shorted input channels. Figure 3.4b illustrates the minimum noise floors of the applied *SeisRockHT* recording system (*Ruwai* data recorder + 4.5 Hz GS-11D sensor) for various pre-amplification factors. The two grey lines represent the low and high global seismic background noise models by Peterson (1993), respectively. Figure 3.4b shows that the low background noise model cannot be resolved by the *SeisRockHT* recording system. However, a moderate seismic background noise level is assumed for the *SeisRockHT* investigation sites, and, furthermore, higher seismic amplitudes by rockfalls are expected. This makes the chosen seismic recording system suitable for rockfall monitoring at the *SeisRockHT* investigation sites.

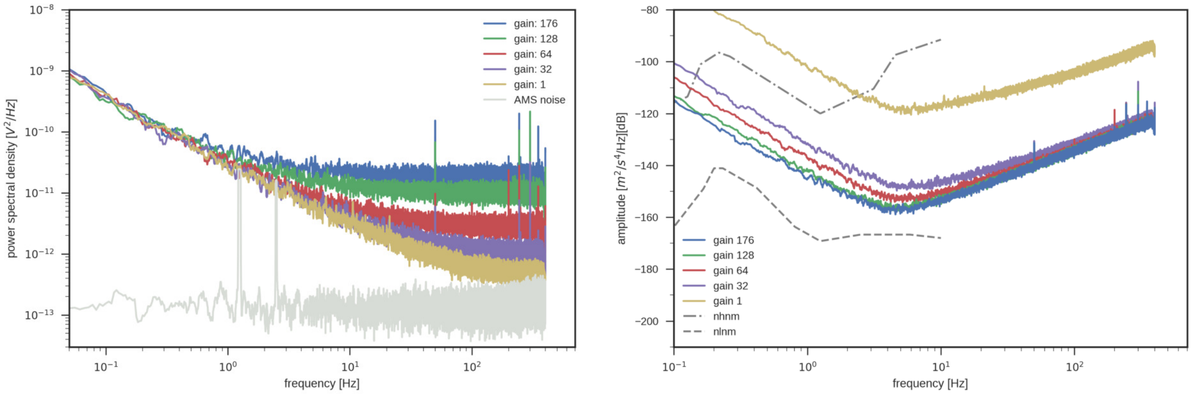

(a) (b)

Figure 3.4: (a) Power spectral density of the *Ruwai* recorder with shorted input channels at a sampling rate of 800 sps. The colored lines represent the average of all 4 channels for various pre-amplification factors. The light grey line represents the noise of channel 1 of the *ADC Main Shield* only. (b) Minimum noise floor of the *SeisRockHT* recording system (*Ruwai* data logger + 4.5 Hz GS-11D seismic sensor) with a sampling rate of 800 sps for various pre-amplification factors. All power spectral densities were smoothed using an 11 samples long moving average filter.

Software

The Arduino microcontroller software is written in C using the Arduino C libraries (*https://www.arduino.cc/reference/en/*) and custom built libraries to communicate with the GPS, the ADC and the PGA.

The *BeagleBone Black* runs a Linux operation system, and the *Ruwai* recording software *ruwaicom* is written in C++. *ruwaicom* handles the communication with the *Arduino Stack*, the storage of the digitized data in miniSEED file format, and the logging of the state-of-health. The *ruwaicom* and *Arduino Stack* configuration parameters are defined in an *INI* configuration file. A continuous operation of *ruwaicom* in case of unexpected program errors or power-downs is assured by using the Linux service system.

DIY Assembly

The *Ruwai* data recorder was designed to be built in a Do-It-Yourself (DIY) manner. All electronic and mechanical components are off-the-shelf and can be obtained from well known distributors. *Ruwai* assembly applies simple low-cost tools that are available in a hobby workshop. The production of the 8 *Ruwai* data recorders for *SeisRockHT* was the first assembly of a smaller batch and a good feasibility test of the intended construction strategies.

The construction includes the manual assembly of surface-mount technology (SMT) printed circuit boards (PCBs), reflow soldering using low-cost equipment, and the assembly of the rugged field enclosure. The actual PCB fabrication had to be outsourced to a professional service as to date, multi-layered PCBs cannot be manufactured without high-end equipment.

The PCB hardware design files as well as the bill-of-material of the electronic and electro-mechanical components are available in the Git repository of the *Ruwai* project (*http://www.repo.or.cz/ruwai.git*). A detailed step-by-step assembly instruction of a *Ruwai* data recorder built for the *SeisRockHT* project is described in the technical report *Assembly of the seismic data recorder Ruwai* (Mertl (2017a)). Python scripts were created to automatically compile order lists for electronic components, and to create graphical aids (pick-and-place maps) for a reliable manual assembly of the PCBs.

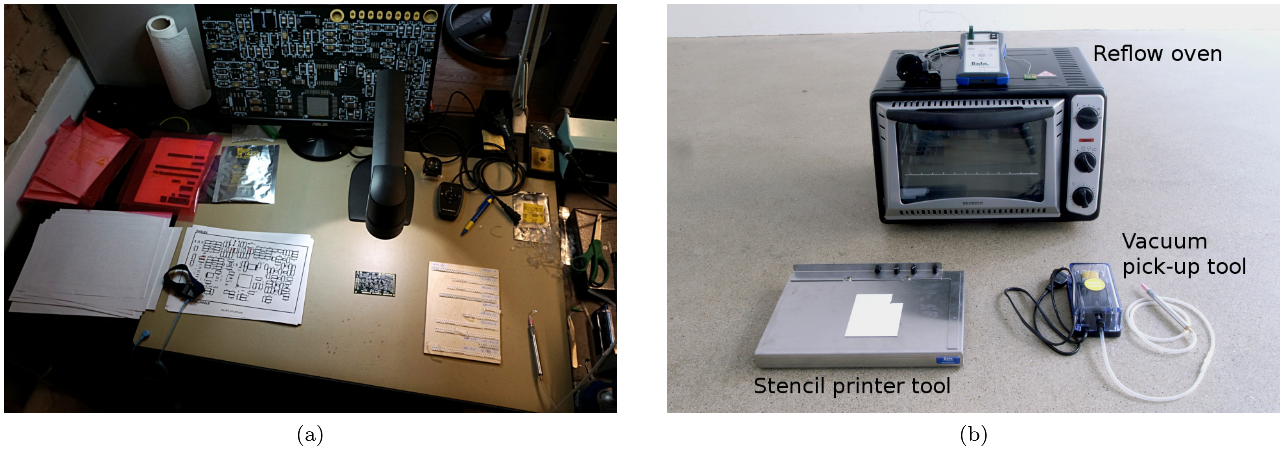

Figure 3.5: The workplace setup (a) and the tools (b) used for the manual assembly of the PCBs.

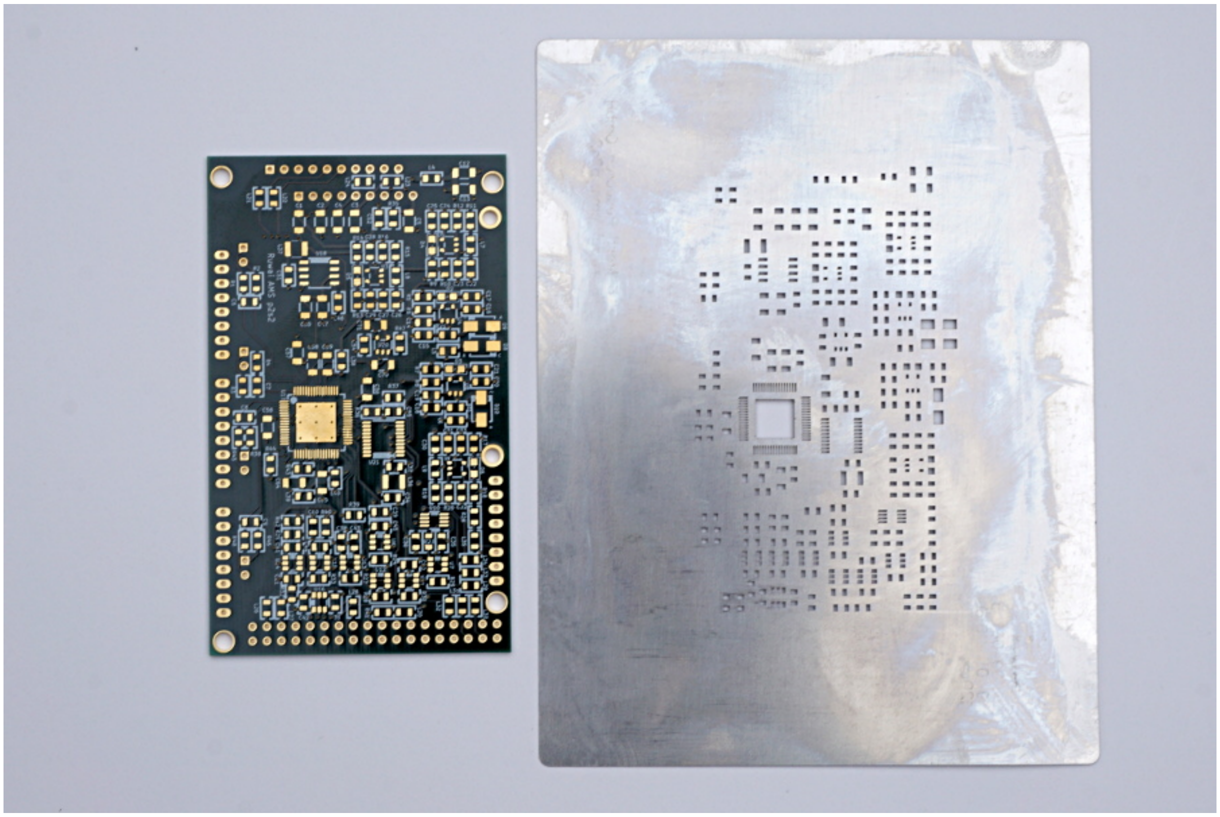

Figure 3.6: Clean printed circuit board (left) and the corresponding metal solder paste stencil (right).

Figure 3.5 shows the workplace setup as well as the tools used for the manual assembly and reflow soldering of the PCBs. The tools are a metal frame for stencil printing of the solder paste, a DIY vacuum pump for picking and placing the electronic components, and a standard desktop oven with a BETA Layout temperature controller for reflow soldering.

Besides the manual placement of the electronic components on the PCB, the main PCB construction step is the application of the solder paste onto the PCBs by stencil printing technique before placing the components (Figures 3.6 and 3.7). The metal stencil can be ordered from the PCB manufacturer together with the PCBs. A clean application of the solder paste is crucial for a proper reflow soldering to avoid shorted pins of electronic components and subsequently time consuming repair work. Hence, during the manual application of the solder paste, frequent cleaning of the stencil with a solvent cleaner is needed to obtain a good separation of narrow pads and avoid smearing of the solder paste. In Figure 3.7 an example of the applied solder paste is given. The standard desktop oven with the temperature controller as DIY reflow oven worked well and gave reproducible results. Figure 3.8 shows an example of a fine pitch electronic component before and after reflow soldering.

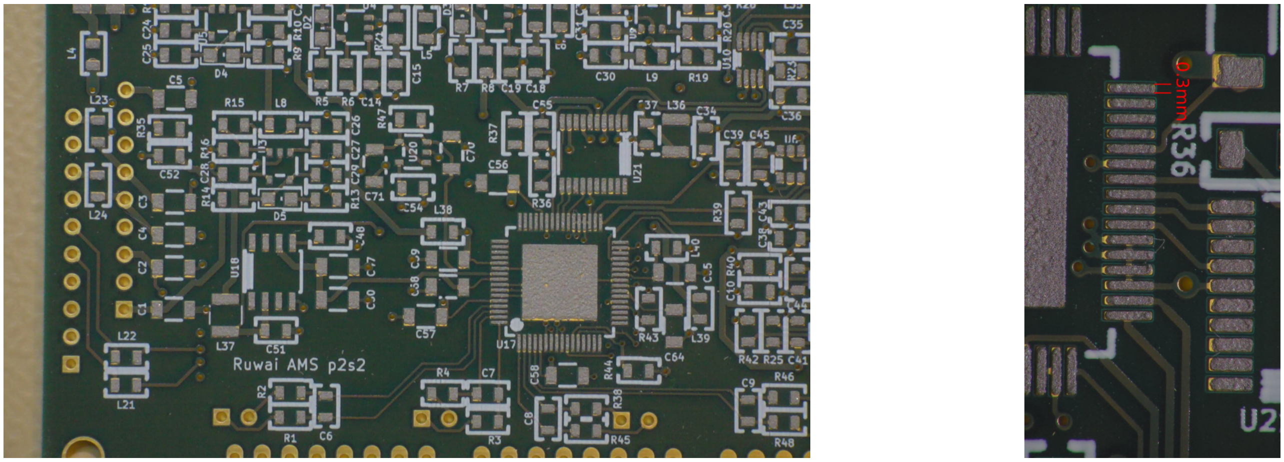

(a) (b)

Figure 3.7: The solder paste applied to the PCB (a) and a close-up (b).

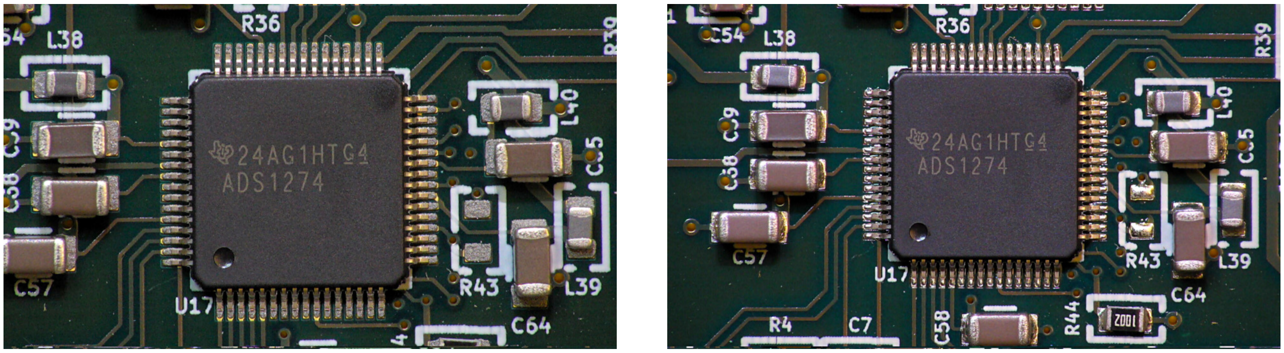

(a) (b)

Figure 3.8: Close-up view of the ADS1274 ADC on the PCB before (a) and after (b) reflow soldering.

Electromagnetic Interference

SeisRockHT was the first field application of the *Ruwai* data recorder and we could gain valuable information to further improve the system towards routine operation applications.

The laboratory tests of the unshielded *Arduino Stack* and the *BeagleBone Black* showed no major electromagnetic disturbances, despite a 50 Hz noise signal with related harmonics, whereas this noise signal could easily be removed by frequency filtering. Based on these tests it was decided to use a plastic field enclosure without a shielding against electromagnetic interference.

Figure 3.9:
The first *Ruwai* recorder version for the *SeisRockHT* project. The *BeagleBone Black* single board computer is mounted next to the unshielded *Arduino Stack*.

The *Ruwai* field version employs a rugged *Pelicase 1200* enclosure where all the electronics are mounted inside (Figure 3.9). After the installation of the first version in the field, first data showed unexpected major electromagnetic interference for mains powered stations, which made the data unusable. Large peak to peak amplitudes of about 30 mV and regular DC-offsets of the data were present (Figure 3.10). This was the starting point of the search for the entering points of the electromagnetic interference into the *Ruwai* system (including sensors and cables) to develop a proper shielding concept. All carried out experiments and the results are described in detail in the technical report *Electromagnetic Interference and the Ruwai recording system* (Mertl (2017b)). The complete technical report can also be found in Appendix D.

The outcome of the experiments was the shielding of the *Ruwai* data recorder (Figure 3.3) and the application of shielded sensor cables to improve the electromagnetic compatibility of the recording system. The shielding resulted in a major improvement of the data quality for stations located nearby mains power supply and powered by mains power (compare Figure 3.11 and Figure 3.10). The only remaining part of the electromagnetic interference is originating from a potential quasi-stationary magnetic field which cannot be shielded by a metal enclosure.

Although all the shielding and grounding measures reduced the noise of the mains powered stations of the Sonnblick network, the noise remained at the mains powered stations of the Kitzsteinhorn site. The grounding situation seems to be fundamentally different for the Kitzsteinhorn network. Several grounding strategies were tested throughout the project duration, but unfortunately the destructive electromagnetic interference remained and made all gathered data of the Kitzsteinhorn unusable for further analysis.

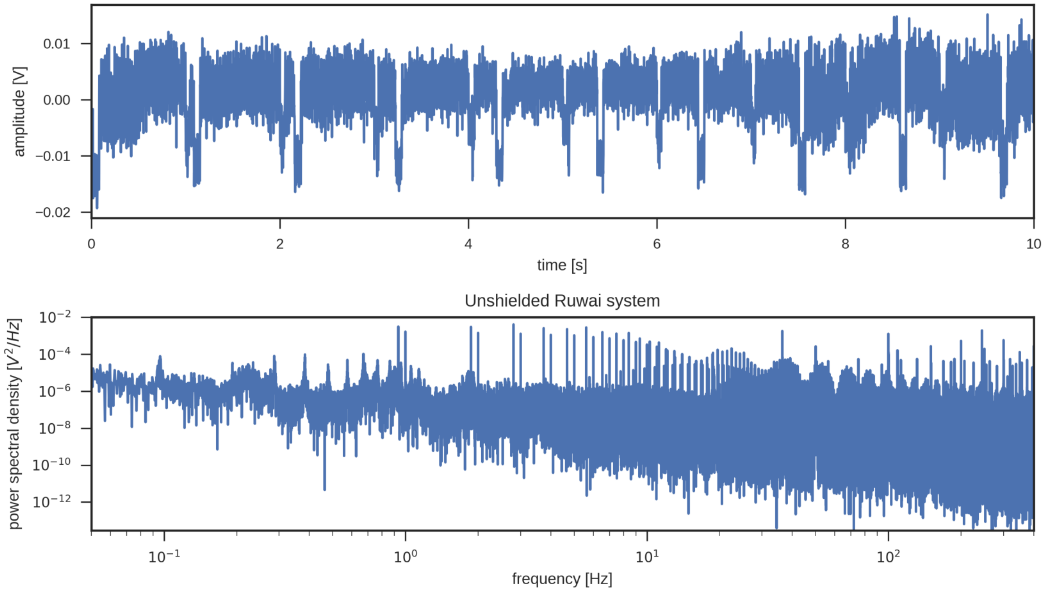

Figure 3.10: Field data recorded with an unshielded *Ruwai* recording system at station STO of the Sonnblick seismological network. 10 seconds of the waveform data (top) and the power spectral density of a 1 hour recording (bottom) are shown.

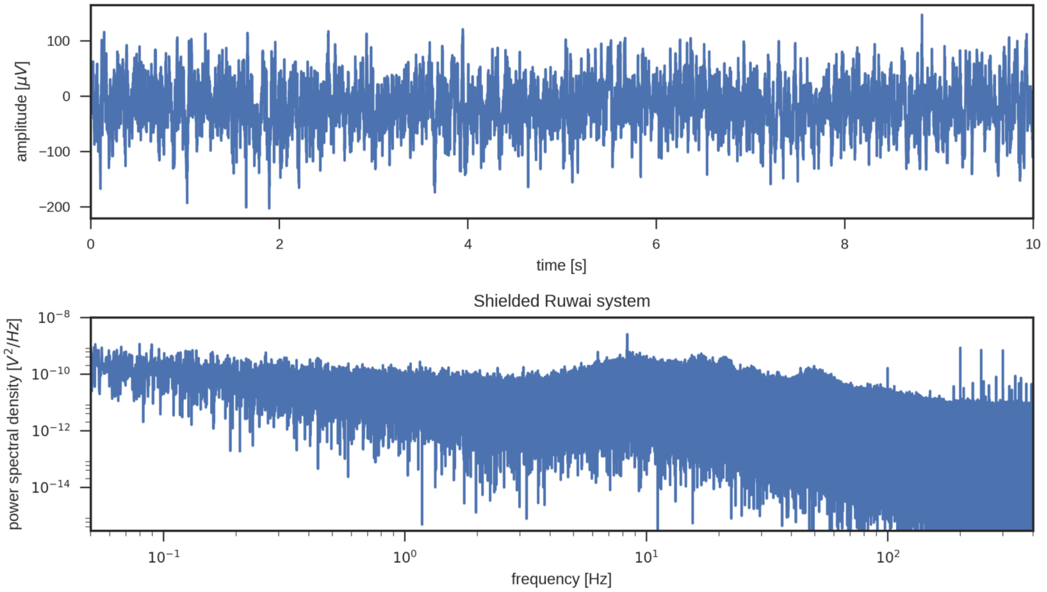

Figure 3.11: Field data recorded with the shielded *Ruwai* recording system at station STO of the Sonnblick seismological network. 10 seconds of the waveform data (top) and the power spectral density of a 1 hour recording (bottom) are shown. Note the different magnitude of waveform amplitude (μVolts) compared to Figure 3.10 (Volt).

Routine Operation and System Adaption

The deployment of the *Ruwai* recorders at Hoher Sonnblick and Kitzsteinhorn revealed hard- and software issues that became obvious only during long-time operation in a rugged environment. Several issues were identified and most of them could be solved by software adjustment. Hardware-related problems usually involve a costly change of the whole system, therefore, most of the hardware improvements were integrated in a further development of the *Ruwai* data recorder (see section *The next Ruwai generation - Ruwai se*). The following is an overview of the most crucial issues encountered and the measures taken.

Hang after Restart Occasionally, the *Ruwai* data logger did not restart after an unexpected power-down due to e.g. power shortage. This was a major issue, because it caused a complete outage of the recorder. The problem could be identified as an issue of the *BeagleBone Black* bootloader *u-boot*. The startup routine of the bootloader could be interrupted by sending a random key to a serial port. The *Arduino Stack* is connected to the USB Serial Port of the *BeagleBone Black* and serial data sent to this port during startup has caused the restart problems. The issue was fixed by an update of the Linux operating system which included a fix of the bootloader. It is now mandatory to enter a special key ('s') to stop the boot process.

Loss of Serial Communication Sometimes, the serial connection between the *BeagleBone Black* and the *Arduino Stack* was lost and no data was sent from the stack to the *BeagleBone Black*. The system itself was operating, but no data was recorded. This problem was fixed by a software update of the custom *Ruwai* recording software running on the *BeagleBone Black* and the *Arduino Stack*. A handshaking between the *BeagleBone Black* and the *Arduino Stack* was added to check for the presence of the stack and a correct configuration of it. Moreover, a watchdog was added to check for proper digitization of the data on the *Arduino Stack* and the reception of data at the *BeagleBone Black*. If no data is available for some time, the watchdog initiate a restart of the software.

Weatherproof Access In bad weather conditions it was difficult to check the state-of-health of the *Ruwai* units and to retrieve the data by exchanging microSD cards. The cause is the fact that for this tasks the *Ruwai* enclosure must be opened and the electronic components are then exposed to the weather. This issue has not been fixed for the currently operating units, but was taken care of in the next *Ruwai* generation.

Error-Prone Connectors Although the used Bulgin Buccaneer connectors are rated at IP68 and had a trustworthy look, they caused several problems due to loose connections and water entry. Their sealing O-rings are easily lost while connector handling which leads to loose connections and susceptibility to water entry. This issue has not been fixed for the currently operating units, but was taken care of in the next *Ruwai* generation.

The next Ruwai generation - Ruwai se

Throughout the project, the encountered issues and feature requests were collected and resulted in a redesign of the *Ruwai* data recorder. Figure 3.12 shows some views of the *Ruwai se* (Ruwai second edition). The major improvements of *Ruwai se* are:

Active Filter Noise The operations amplifiers used in the anti-aliasing filter were identified as low frequency noise source causing a high 1/f-noise. The components were replaced with Texas Instruments OPA2209 units, which show a better 1/f-noise characteristics (see Figure 3.13 and Figure 3.14).

Electric Shielding All electronics are contained in a metal enclosure using 0.1 mm thick aluminum foil and a metal top panel.

Connectors The connectors were changed to *Samtec Acclimate Bayonet* metal connectors and the GPS connector was changed to a standard type-N connector.

Weatherproof Service Access A metal top panel was added to protect the electronic parts from weather while unit servicing.

Data Access A SD-card slot mounted outside the top metal panel is used to hold the data storage card. Data storage cards can now be exchanged without exposing the electronic parts.

State of Health The metal top panel holds a LCD display which shows important status information of the recorder.

Power Supply Separation The Power Supply Shield was separated from the *Arduino Stack* because bad placement of the power supply wiring caused interference with the analog sensor input.

Serial Communication The serial communication between the *BeagleBone Black* and the *Arduino Stack* is realized by a universal asynchronous receiver-transmitter (UART) interface of the *BeagleBone Black*. This avoids the usage of the UBS serial interface and results in a more reliable control of the serial interface.

Four units of *Ruwai se* were financed and built by *Mertl Research GmbH* to evaluate the actual improvements in data quality and handling. However, none of the *SeisRockHT Ruwai* units have been updated due to lack of funds for hardware and labor costs.

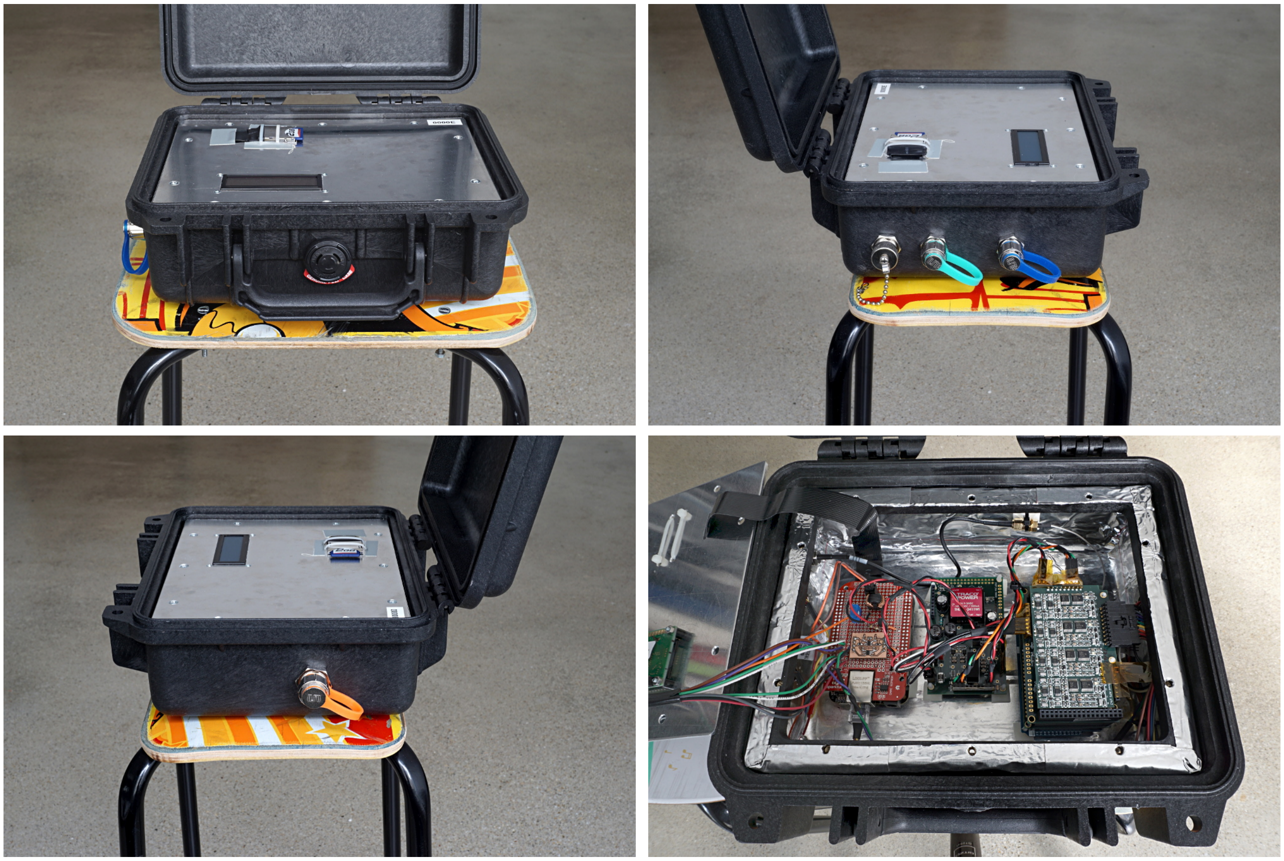

Figure 3.12: Throughout the *SeisRockHT* project the new *Ruwai se* prototype was developed including major software fixes and a better usability in the field.

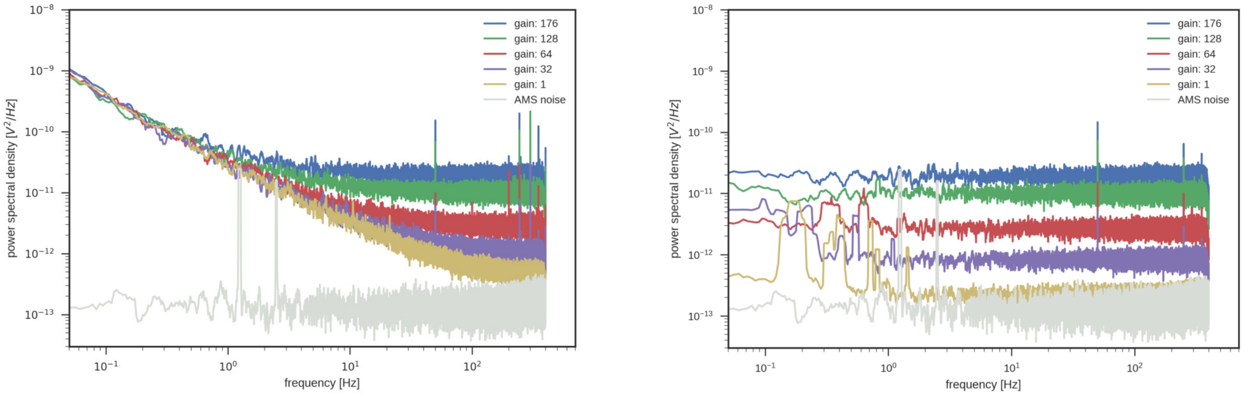

(a) (b)

Figure 3.13: Power spectral density averaged for all four channels with a sampling rate of 800 sps. The light grey line represents the noise of channel 1 of the *ADC Main Shield* only. All power spectral densities were smoothed using an 11 samples long moving average filter. The change of the operational amplifier of the anti aliasing filter significantly improved the 1/f-noise at low frequencies, as can bee seen in the comparison of the old system (a) with the *Ruwai se* (b).

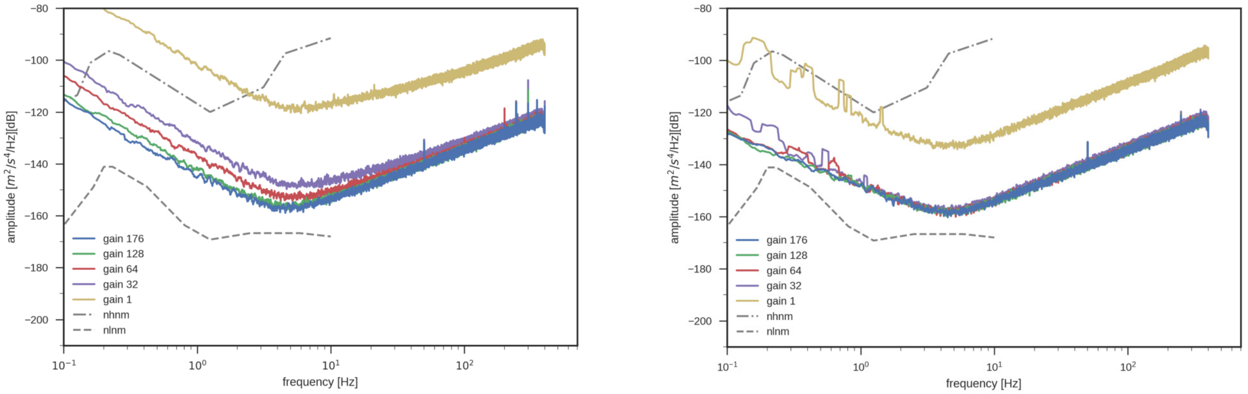

(a) (b)

Figure 3.14: Minimum noise floor of the old (a) and the new (b) *Ruwai* systems with a 4.5 Hz GS-11D sensor and a sampling rate of 800 sps. The *Ruwai se* does not show a lower noise floor for gain values larger than 32. This suggests, that the noise source is located before the signal amplifier.

Field Installation and On-Site Service

An aluminum mast mount was designed to hold the *Pelicase 1200* field enclosure of the *Ruwai* data recorder (Figure 3.15). The detailed measures of the aluminum mast mount can be found in Appendix E. The custom-built mast mount does not require any drilled mounting holes destroying the enclosure ingress protection. Besides the non-invasive character, the mast mount is small and lightweight (<0.5 kg). A tarpaulin cover provides another protection layer for the *Ruwai* data recorder.

A *SeisRockHT* data recorder service protocol and script were created for standardized station maintenance and documentation. The service protocol as well as the service script with an output example can be found in Appendix E.

Figure 3.15: The *Ruwai* mast mount strategy. The core is the custom-built *Pelicase 1200* aluminum mast mount. A tarpaulin cover provides additional protection.

3.2 Seismic Sensors

Generally, the *SeisRockHT* project employed robust, industrial geophones as seismic sensors. These passive and low-cost sensors are particularly suitable for the *SeisRockHT* approach. Precisely, *SeisRockHT* employed the geophone models *GS-11D* (the product name was changed to *GS-ONE LF* lately) and *OMNI-2400* from *Geospace* with corner frequencies of 4.5 and 15 Hz, respectively, and a damping of 70% to obtain a flat frequency response. The geophone sensitivities at 70% damping are 81 V/m/s (*GS-11D*) and 43 V/m/s (*OMNI-2400*). The *GS-11D* geophone needs to be installed levelled to avoid spurious data due to sensor tilt. The omni-directional geophone *OMNI-2400* is applied for sites where a levelled sensor installation cannot be accomplished. The *OMNI-2400* geophone has an operational tilt range from 0 to 180°. Surface geophones are installed in standard land cases. All borehole sensors are custom-built by *Geosono*. Three-component sensors installed in deep boreholes (depth >20 m), where sensor orientation cannot be assured, include a magnetic sensor to determine the final sensor orientation after installation. Generally, the three orthogonal sensor components are denoted with Z for the vertical, and X and Y for the two horizontal components (see Tables 3.1 and 3.2). Figures 3.16 and 3.17 show examples for seismic borehole sensors built by *Geosono* for the *SeisRockHT* project.

Figure 3.16: Three component (X Y Z) borehole sensor constructed by *Geosono* for the Sonnblick summit station (OBS). In the foreground of the right picture the thermistor string sinking weight is shown. The sinking weight was replaced by the seismometer.

Figure 3.17: *Geosono* single component (Z) borehole sensor for the Kitzsteinhorn BH1 station. The sensor is mounted at the bottom of a stiff rod along which the thermistor string is also fixed.

3.3 The Sonnblick Seismological Network

In 1886 the Sonnblick Observatory (SBO) was established on the summit of 'Hoher Sonnblick' (3,106 m a.s.l.) to monitor and study the atmosphere. Since then, the focus continuously broadened and can be described today as global ecosystem sciences with core disciplines of meteorological, climate and environmental monitoring and research. The SBO is part of several global networks among which are the *World Meteorological Organization (WMO)* programs *Global Atmosphere Watch (GAW)* and *Global Cryosphere Watch (GCW)*. The Sonnblick summit renovation in 2003/2004 initiated the SBO permafrost research with the establishment of three deep (∼20 m) boreholes to monitor vertical ground temperature profiles. Thereafter, the boreholes were supplemented with a summit-wide network of surface and near-surface temperature sensors (Figure 3.19, Schöner et al. (2012)). All in all, the SBO provides an established research infrastructure with an abundant selection of meteorological, climate and environmental data predestined for research projects.

The *ZAMG* program *Active Sonnblick Observatory (ASBO)* assures the continuation of the core SBO long-term monitoring and research activities. Since 2018, the seismological monitoring established by *SeisRockHT* is part of the *ASBO* program. In summer 2019, a permanent seismic station of the *Seismological Service of Austria* was installed on the Sonnblick summit (Figure 3.19). This new seismic station is an additional asset for the local seismological monitoring.

Figure 3.18 shows the installed *SeisRockHT* seismological network to monitor the Sonnblick north-face. The OBS and STO stations are mains powered with buffer batteries as backup in case of power outage. They feature three component sensors (*X Y Z*, Table 3.1), whereas the OBS sensor is installed in one of the deep summit boreholes (BH1, Figure 3.19). The STO station is situated at the end of a ∼50 m deep tunnel at the valley floor. The STO geophones are inside a standard three component surface land case (Table 3.1). The MIT, MOR and PIL stations are stand-alone stations. Generally, the locations of the stand-alone stations are a compromise of north-face coverage and proximity, as well as optimum solar irradiance for power production by solar panels. Furthermore, the monitoring stations have to be situated in locations which offer protection from high-alpine natural hazards to assure a long-term deployment. In summer 2015, the data quality of potential station locations was also assessed by a test survey (see 1. Status Report). Balancing all the limitations and the test survey outcome, led to the final locations of the MIT, MOR and PIL stations. All stand-alone stations are designed as mini arrays employing three vertical surface geophones (*Z Z Z*, Table 3.1).

	OBS	**MIT**	**MOR**	**PIL**	**STO**
Altitude [m a.s.l.]	3106	2050	2250	2260	1650
Deployment type	Borehole	Surface	Surface	Surface	Surface
	→Depth 21 m	→MA	→MA	→MA	→Tunnel
Sensor type	*GS-11D*	*GS-11D*	*GS-11D*	*GS-11D*	*GS-11D*
Sensor components	*X Y Z*	*Z Z Z*	*Z Z Z*	*Z Z Z*	*X Y Z*

Table 3.1: Station characteristics of the Sonnblick seismological network. OBS sensor is situated at the bottom of a 21 m deep borehole. MIT, MOR and PIL stations feature a mini array ('MA') deployment type. STO station is located at the face of a ∼50 m long tunnel close to the valley floor.

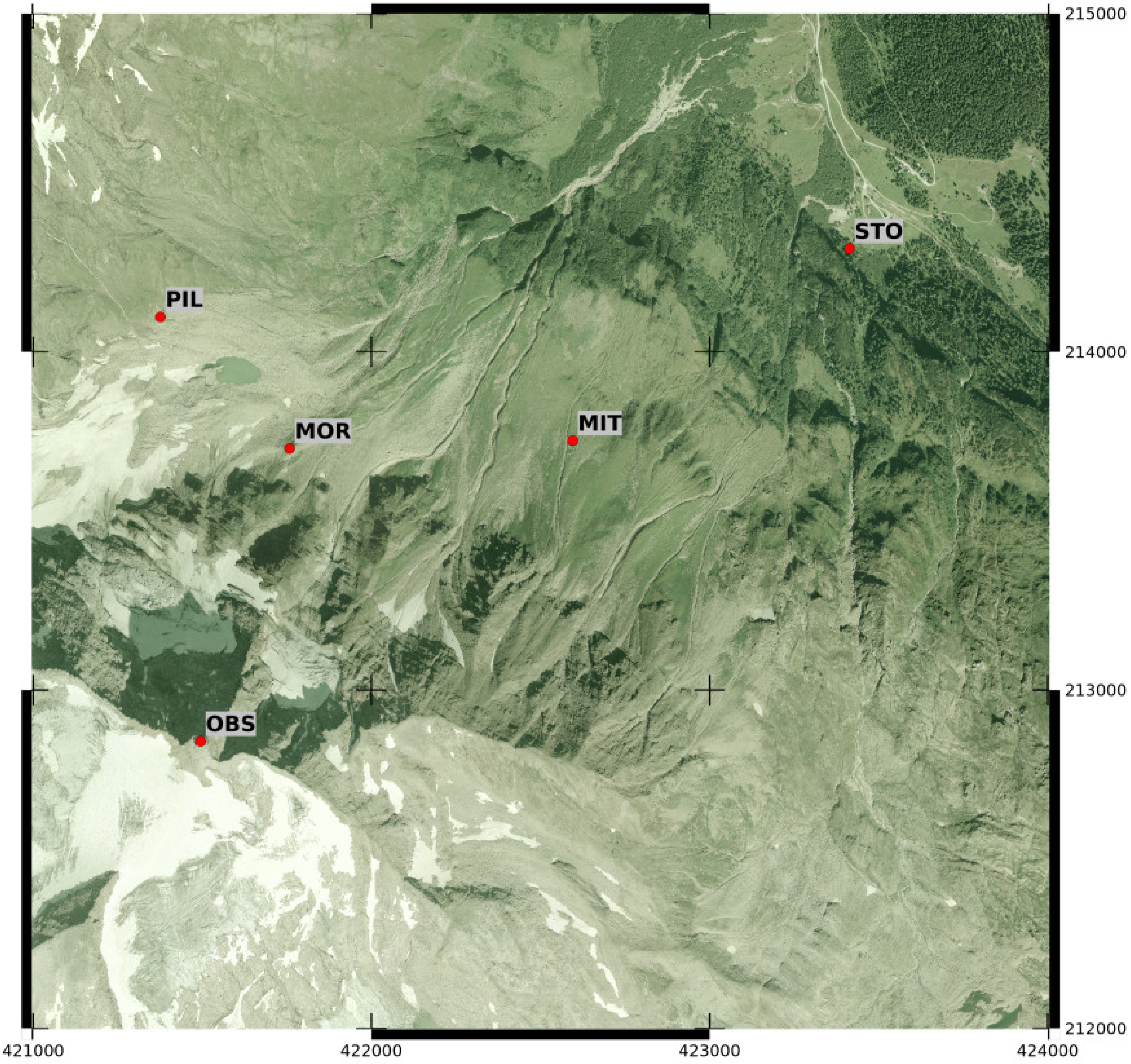

Figure 3.18: Overview of the *SeisRockHT* monitoring network. The OBS and STO stations are mains powered, whereas MIT, MOR and PIL are stand-alone stations. The stand-alone stations power supply is realized by a combination of solar panels, wind turbines and battery packs. The overview map covers an area of 3x3 km. (Coordinate System: MGI/Austria GK 31, EPSG:31258)

Seismic signals of each station are registered by *Ruwai* data recorders with a sampling rate of 800 samples per second. Synchronized time of the individual recorders is essential for multi-station processing (e.g. seismic event localization). The recorders time synchronization is realized through the PPS signal of the internal GPS modules, hence a good GPS signal reception must be assured. Whereas, GPS signal reception of the stand-alone stations was sufficient with minimum GPS equipment, more sophisticated GPS installations were necessary for the two mains powered stations.

A challenge for the stand-alone stations was the power supply. Originally, the power supply system of a station built up on a solar panel - battery system controlled by a solar regulator (*Phocos Eco 10*). The solar panel was rated with ∼100 W and the battery with a capacity of 900 Wh. The battery and the solar regulator were stored in a *Pelicase 1460*. However, the original power supply system turned out to be not sufficient enough and was extended with wind turbines (*LE-v50*) and rugged high-capacity (∼3,600 Wh) battery packs during the project. The high-capacity battery pack was designed to provide high ruggedness at low costs. A detailed battery pack construction guidance can be found in Appendix E.

Eventually, the installation, maintenance and necessary improvements to assure a long-term monitoring of the Sonnblick seismological network turned out to be the most resource intense *SeisRockHT* project objective. Every single station site of the north-face monitoring network exhibited distinct characteristics which demanded individual strategies. The next section gives an overview of the individual challenges and chosen strategies.

3.3.1 Mains Powered Stations

The OBS station

The OBS station is located on the summit of 'Hoher Sonnblick' (3,106 m a.s.l., Figure 3.18). It is equipped with a *Geosono* three component borehole seismometer (*X Y Z*, Table 3.1) featuring a magnetic sensor to determine sensor orientation after installation (see also section 3.2 and Figure 3.16). The borehole seismometer is situated at the lower end of the thermistor string in the 21 m deep summit borehole 1 (BH1, Figure 3.19 and 3.20).

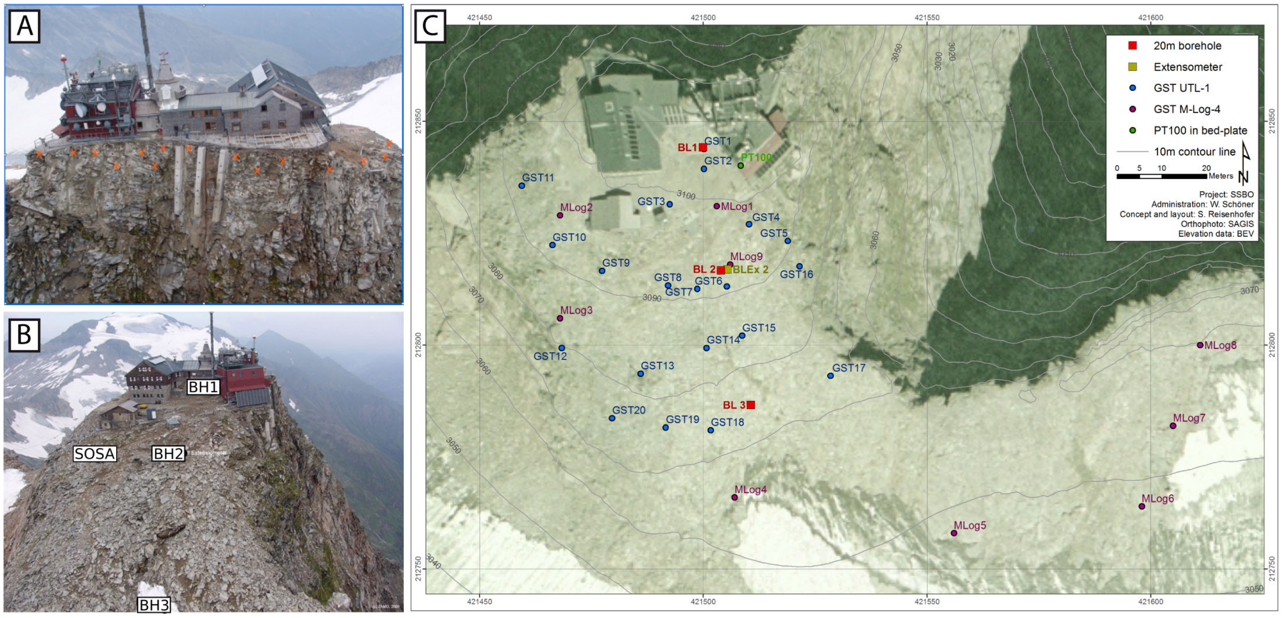

Figure 3.19: Overview of the 'Hoher Sonnblick' summit (3,106 m a.s.l.). (A) shows the steep summit north-face during the summit renovation in 2003/04. (B) shows the summit south-face with the three deep boreholes (BH1-3). The three component borehole seismometer of the *SeisRockHT* OBS station was installed in BH1. In August 2019, the *Seismological Service of Austria* installed a permanent surface seismometer (SOSA). (C) gives an overview of the summit-wide surface and subsurface temperature sensor network.

Figure 3.20: The OBS three component seismometer is sunk in the 21 m deep BH1. The sensor is situated at the lower end of a thermistor string.

Lightning is an omnipresent threat at the exposed Sonnblick summit. In summer 2016, electrical components of the OBS station were destroyed by an electrical surge caused by lightning. However, since the installation of a electrical surge protection no electrical component of the OBS station was destroyed anymore.

The GPS signal is fundamental for the time synchronization of the *Ruwai* data recorder. Initially, a standard GPS antenna was mounted on the close by wind tower foundation (Figure 3.21). Despite satisfying signal tests during and after the installation of the OBS station, it eventually turned out that the signal shadowing of the adjacent buildings was too high to provide the required GPS signal quality on a longer term. Consequently, an alternative GPS concept had to be developed. Figure 3.22 shows the acquired material for the developed GPS concept. Finally, the GPS antenna was installed at the rather distant SBO terrace (Figure 3.23). An optic fibre solution guiding the GPS signal from the terrace to the OBS data recorder was designed to minimize risks of lightning-induced electrical surges. The optic fibre solution was finally completed in October 2016 and is since then delivering the fundamental GPS signal in a constant good quality.

Unfortunately, the OBS station is not operational since 2019. Apparently, the borehole seismometer got stuck during a thermistor string exchange, and all the cable connections were destroyed. The repair of the OBS station was planned for summer 2020, but was delayed due to the COVID-19 pandemy. However, the new surface seismometer by the *Seismologocal Service of Austria* is currently used as OBS station replacement.

Figure 3.21:
GPS signal tests after the OBS station installation. The GPS antenna (red encircled) was initially mounted on the close by wind tower foundation.

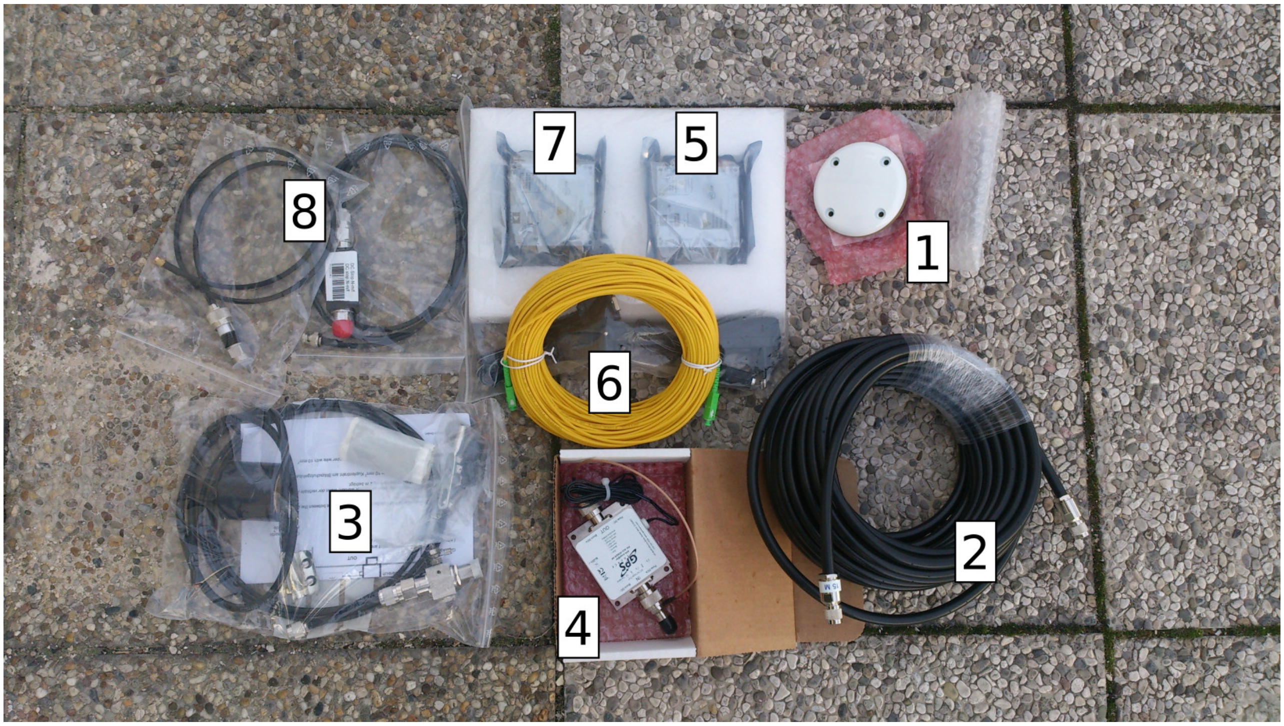

Figure 3.22: Material for the alternative GPS concept of the OBS station. Numbering follows the way of the incoming GPS signal until the data recorder: (1) GPS antenna, (2) GPS antenna cable, (3) lightning protection, (4) GPS signal amplifier, (5) A/D converter, (6) optic fibre, (7) D/A converter, (8) signal attenuator module.

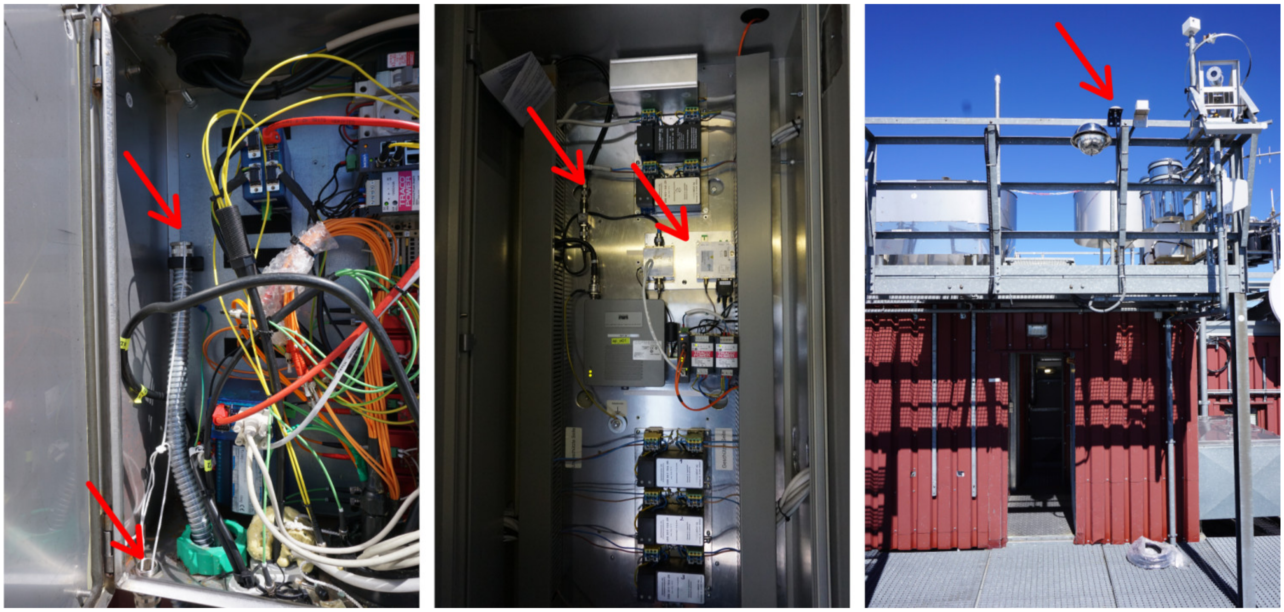

Figure 3.23: Snapshots of the installed alternative OBS station GPS concept. Due to the omnipresent lightning risk at the Sonnblick summit, the concept is based on an optic fibre connection. Left picture shows the outdoor switchbox with the installed metal protection conduits for the optic fibre. The optic fibre is guided inside an underground pipe from the borehole to the switchbox (upper arrow), and then continues towards the terrace (lower arrow). The middle picture shows the terrace's anteroom switchbox with the installed devices. Left arrow points at the lightning protection of the incoming antenna cable and the right arrow points at the mounted aluminum board with the GPS signal amplifier (left) and the A/D-converter. The right picture shows the installed GPS antenna on the terrace balustrade.

The STO station

The STO station was installed at the end of a ~50 m tunnel close to the valley floor of Kolm Saigurn (Figure 3.24). The STO station serves as a reference station to better distinguish actual rockfall events from non rockfall-related local seismicity. Furthermore, the sheltered location was well-suited for ambient seismicity analysis. The STO station applies a standard three component surface sensor (X Y Z, Table 3.1). The essential GPS signal is guided into the tunnel, where it is then amplified and retransmitted by a GPS signal repeater (Figure 3.26). Originally, the GPS antenna was installed too close to the portal rockwall which resulted in a poor GPS signal strength. In January 2017 a ~0.5 m beam was mounted to realize a higher sky view percentage for the GPS antenna (Figure 3.25). This measure significantly improved the GPS signal strength.

The mains power supply is provided by an underground cable guided up from the *Naturfreundehaus*. However, periods without mains power supply were experienced due to a broken underground cable, or unintentionally disconnection of the power plug by the *Naturfreundehaus* staff. In summer 2019, the buffer batteries were stocked up and provide now a total capacity of 1800 Wh, which secures a station power supply of about 25 days.

Figure 3.24: The tunnel portal and the ~50 m long tunnel. The GPS antenna is mounted on top of the tunnel portal.

Figure 3.25: Originally, the GPS antenna was mounted directly on the rockwall. In January 2017, a ∼0.5 m beam was mounted to raise the antenna's sky view percentage which substantially improved the GPS signal strength.

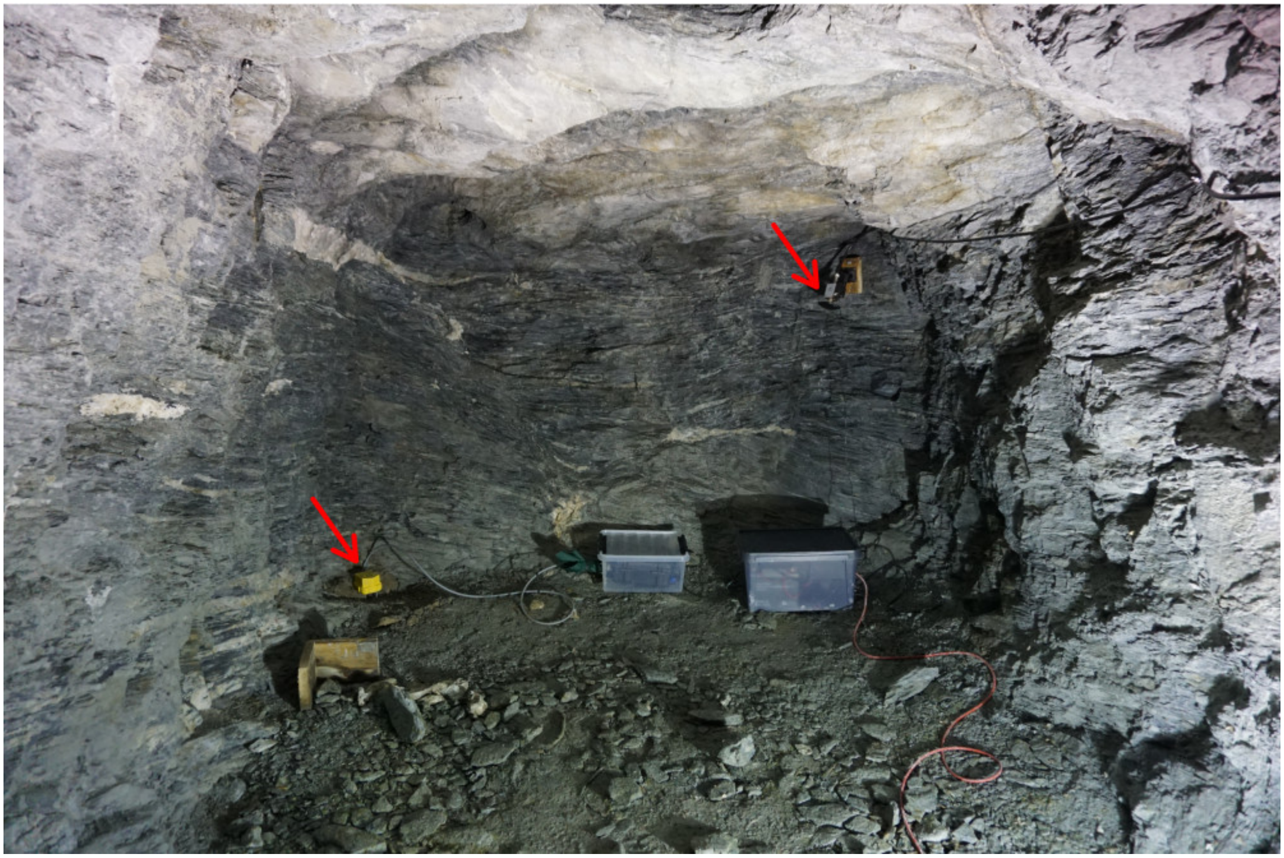

Figure 3.26: The STO station is located at the face of a 50 m deep tunnel. The left arrow points at the three component sensor, and the right one at the GPS signal repeater. The left box contains the *Ruwai* data recorder and the box to the right the power supply.

3.3.2 Stand-Alone Stations

In the first year after installation, data gaps from later autumn to spring were partly present due to power shortage. During the entire project, the power supply was constantly improved to achieve a continuous monitoring. Beside the power supply, the general logistics due to the rather remote locations of the stand-alone stations were demanding. The SBO cable car was used to deliver station material (Figure 3.27). Nevertheless, material for the MOR and PIL stations had to be distributed from the MIT station, and partly carried up from the valley (Figure 3.28).

All the stand-alone stations were designed as mini arrays. The three vertical geophones (Z Z Z, Table 3.1) were arranged in a star-like geometry with cable lengths between 20 and 60 m. Geophones and cables were dug into the ground about 0.5 and 0.1 m, respectively, to suppress surface noise and potential damages by rockfall or wildlife (Figure 3.29). Beside the general challenges of the high-alpine environment, coincidences like the construction of a new SBO cable car in the summer 2018 had direct consequences for the *SeisRockHT* network.

Figure 3.27: The Sonnblick Observatory cable car was used to deliver equipment.

Figure 3.28: Nice weather, but heavy load. The material for the PIL and MOR stations were partly carried up from the valley via backpack transport.

Figure 3.29: Geophones and cables were dug into the ground about 0.5 and 0.1 m, respectively, to suppress surface noise and potential damages by rockfall or wildlife.

The MIT station

Originally, the MIT station deployed the SBO cable car pillar 'Mittelstütze' as station mast (Figure 3.30). The rugged pillar represented an ideal station mast. Beside the fact that no new mast had to be set up, it was further dimensioned to withstand avalanches regularly discharged by the steep slopes above the MIT station. However, the 'Mittelstütze' pillar had to be removed within construction works for the new SBO cable car, and a new MIT station was set up in summer 2018.

Figure 3.30: The first MIT station. The *Ruwai* data recorder and the solar panel were mounted on the SBO cable car pillar 'Mittelstütze'. The battery box was placed in the left corner of the basement's downward side.

The only fairly avalanche-proof spot at this location is the top of the avalanche wall, originally built to protect the 'Mittelstütze' pillar. Consequently, a new station concept was designed and realized on the highest point of the avalanche wall (Figure 3.31). The new station mast concept applied *stage trussing elements*. Stage trussing elements turned out to be ideal due to their ruggedness and modularity, as well as numerous available accessories. This effort was also used to improve the station's power supply by installation of a wind turbine (Figure 3.32). Furthermore, a new battery enclosure was mounted in summer 2019. The new enclosure hosts larger batteries which increased the total capacity from 900 to 3240 Wh (Figure 3.31 and 3.33).

Figure 3.31: The avalanche wall above the old cable car pillar 'Mittelstütze'. The new MIT station was installed on top of the avalanche wall. The original battery box (wrapped in a green tarp) was situated in the lower right corner. The new battery enclosure was mounted right below the original battery box.

Figure 3.32: The new MIT station is equipped with a wind turbine. The *Ruwai* data recorder and the solar panel are mounted on a trussing element.

Figure 3.33: In autumn 2019, a new battery enclosure was mounted. The new enclosure hosts two batteries providing a total capacity of 3240 Wh.

The MOR station

The MOR station is located on top of the orographic right side moraine of the Pilatuskees (Figure 3.34). The Pilatuskees is a debris-covered glacier with a proglacial lake. It is situated in the elevated Pilatus side valley at the foot of the western Sonnblick north-face (Figure 3.18). The MOR station is the station closest to the north-face and thus receives the lowest solar irradiance of all stand-alone stations (Figure 3.35). Consequently, the MOR station initially showed the biggest data gaps due to power shortage. The MOR station consists of two ground-anchored masts, each stabilized with eight guy wires. One is carrying the solar panel and the *Ruwai* data recorder, the battery box is placed at the mast foot. The other mast carries a wind turbine which was installed in summer 2017 due to the present power shortage. Despite a potential interference with the seismic sensors, the MOR power supply situation left no alternative. The individual seismic sensors feature distances between 5 and 40 m from the wind turbine mast and to date no major interference was observed in the recorded seismic data. Furthermore, MOR data was not employed for ambient sesimicity analysis. In summer 2019, the original battery box was replaced with a high-capacity battery pack (see Appendix E) which ensured a further improvement of the power supply.

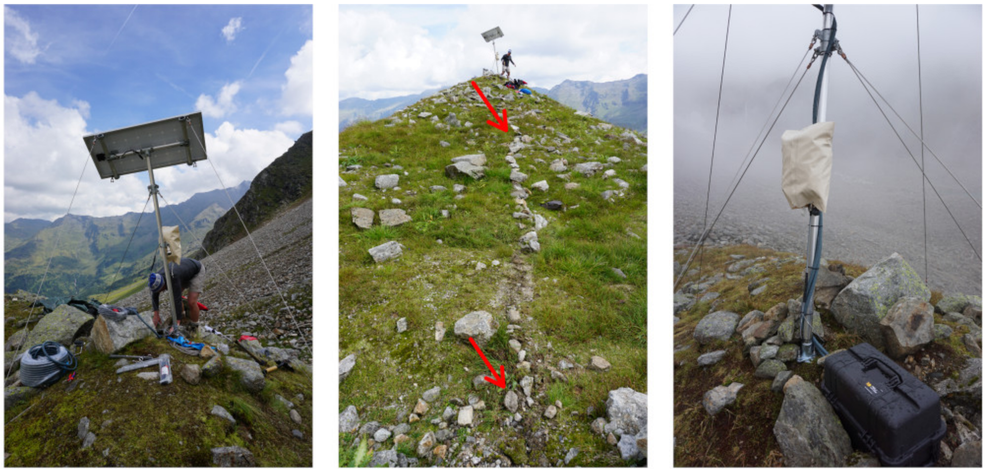

Figure 3.34: The solar panel and the *Ruwai* recorder were mounted on a ground-anchored mast. Red arrows are pointing at a buried geophone cable.

Figure 3.35: The mast and the solar panel were each stabilized by four guy wires. In summer 2017, a wind turbine was installed. The MOR station exhibits the lowest solar irradiance of all stand-alone stations.

The PIL station

The PIL station is located on the southeast-facing slope foot of the Pilatus side valley (Figure 3.18). The solar panel was mounted on a southeast-facing rockwall, originally at a height of about 3 m above ground. Figure 3.36 shows the original PIL station set up in 2016. The winter 2016/17 showed that the PIL location exhibits an extensive snow cover (∼5-10 m) caused presumably by major snow redistribution by wind. Figure 3.37 shows images of the *Ruwai* data recorder recovery in January 2017. During spring 2017, the settlement of the wet spring snow sheared off the rock anchoring bolts holding the solar panel frame and wrecked the solar panel itself. In May 2017, the wrecked solar panel was recovered and a new solar panel was mounted at a height of about 10 m above ground (Figure 3.38). The wiring of the new solar panel was done in summer 2017 (Figure 3.39). The *Ruwai* data recorder was put in a low-cost rugged aluminum case (Zarges A5, see Appendix E) which was placed next to the battery box. However, during the winter season 2017/18 the new set up was also destroyed. Most likely the power cable leading from the solar panel down to the battery box got caught either by the wet snow pack creeping steadily downwards, or by a wet snow slide(s) originating from the slope above the rockwall. However, a combination of these two processes could have been also the cause. Furthermore, the immense snow load also partly sheared off the lid of the original battery box (*Pelicase 1460*), which was located at the foot of the rockwall (Figure 3.40). In late summer 2018 a temporary station was installed to gather data for the remaining summer/autumn season (Figure 3.41). The temporary station was uninstalled before winter.

Figure 3.36: The first version of the PIL station. The solar panel was mounted on a southeast-facing rockwall in a height of about 3 m above ground. The *Ruwai* data recorder was mounted on a ∼1 m mast. The battery box is placed below the mast base.

Figure 3.37: Recovery of the PIL *Ruwai* data recorder in January 2017.

Figure 3.38: In May 2017 a new solar panel was mounted at about 10 m above ground. In the foreground of the right image the recovered wrecked solar panel can be seen. The background shows the new solar panel mounted on the upper rockwall. Furthermore, the image gives an impression of the snow masses accumulated over winter which had to be removed to actually recover the old solar panel.

Figure 3.39: Installation of the solar panel power cable in late summer 2017.

Figure 3.40: The left photo shows the solar panel remains after the winter season 2017/18. The remains of the solar panel frame are encircled in red, the arrow points at the crushed solar cells. The photo also illustrates PIL snow conditions on July 2, 2018. Furthermore, the huge snow load partly sheared off the lid of the battery box (right image).

Figure 3.41: The temporary PIL station in late summer 2018. The left arrow points at the semi-flexible solar panel (50 W) fixed with cord on the rock. The right arrow points at the with a green tarp covered battery and data recorder boxes.

All these past experiences led to the current solar panel mounting concept. The concept is based on a semi-flexible solar panel (∼100 W) and a custom-built frame. The frame features a ramp transition to the rockwall to offer downward sliding snow a minimum resistance. Solid aluminum tubes bolted directly into the rockwall connected with flexible conduits serve as cable guidance. Figure 3.42 shows the new PIL solar panel which was installed in late summer 2019. The new solar panel installation was also used to transfer the GPS antenna up to the solar panel frame. Originally, the GPS antenna was mounted on top of the data recorder box and the substantial snow pack was attenuating the GPS signal. Especially, the GPS signal attenuation owing to the wet spring snow pack had spurious data as a consequence. Due to substantial amounts of deposited snow at the PIL location, the snow cover usually lasts far into summer (Figure 3.40). The GPS antenna elevated to the solar panel frame potentially assures a continuously sufficient GPS reception throughout the year. Furthermore, the PIL station was equipped with a high-capacity battery pack. However, summer 2020 and the coming years will reveal if the new strategy was successful.

Figure 3.42: The new PIL solar panel installation. The GPS antenna is mounted at the lower left corner, next to the solar panel wiring.

3.4 The Kitzsteinhorn Seismological Network

Long-term monitoring at the Kitzsteinhorn was initiated in 2010 within the *MOREXPERT* project, funded by the *Austrian Research Promotion Agency (FFG)*. The multi-scale monitoring of the Kitzsteinhorn summit region focuses on high-alpine climate change impacts. The *Open-Air-Lab Kitzsteinhorn (OpAL)* monitoring network combines surface and subsurface measurements equipped with meteorological, geophysical and geotechnical sensors (Figure 3.43). Besides automated weather stations (AWSs), the *OpAL* monitoring includes thermistor strings in shallow to deep boreholes (1-30 m; Hartmeyer et al. (2012)), electrical resistivity tomography (ERT) profiles (Keuschnig et al. (2017), Supper et al. (2014)), rock anchor load cells (Pläsken et al. (2017)), and crackmeters (Ewald et al. (2019)). Consequently, *OpAL* builds a solid foundation for research initiatives like *SeisRockHT*. Furthermore, *SeisRockHT* could gain added value through synergies with the *GlacierRocks* project, funded as well by the *Austrian Academy of Sciences (OeAW)* within the *Earth System Sciences (ESS)* initiative.

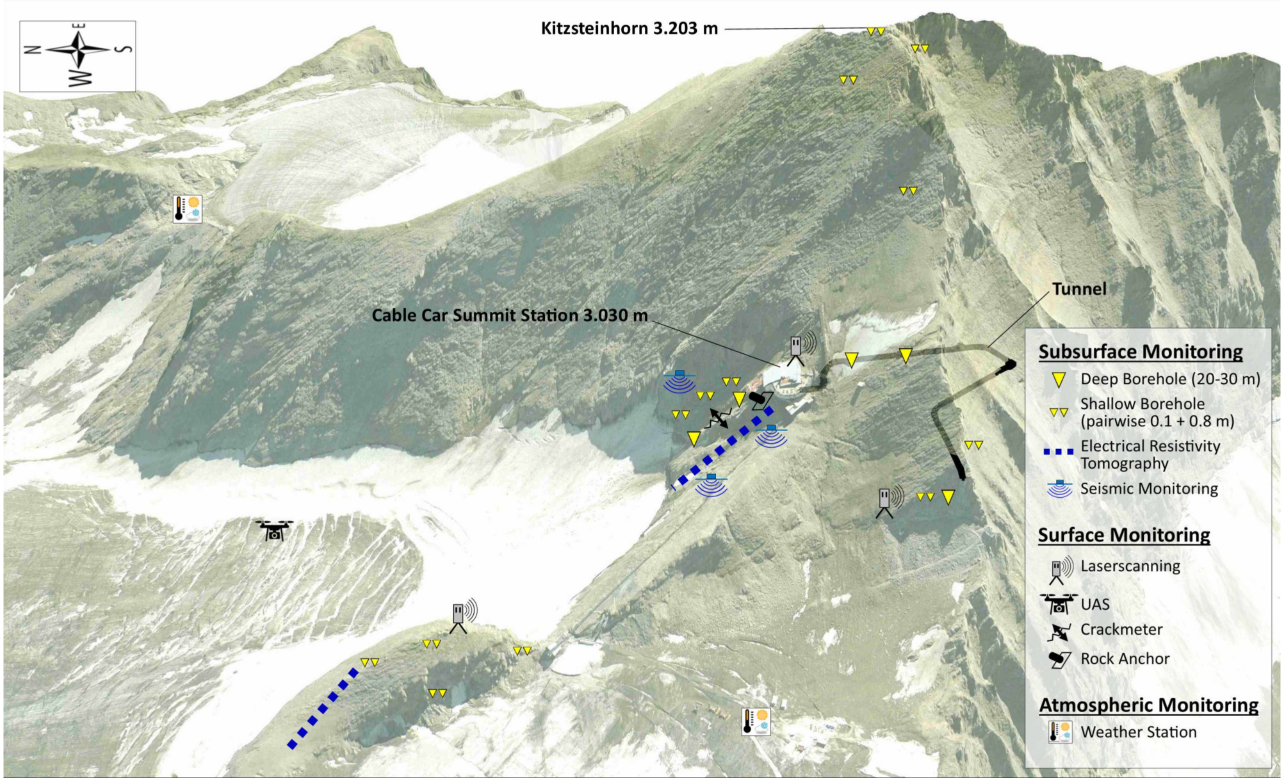

Figure 3.43: Schematic overview of the *Open-Air-Lab Kitzsteinhorn (OpAL)* monitoring network. Seismic monitoring stations were installed within the *SeisRockHT* project.

Figure 3.43 gives an overview of the entire *OpAL* monitoring network. The seismological network was installed within the *SeisRockHT* project. All seismic sensors are deployed in boreholes of varying depths in solid rock (Figures 3.44 and 3.45). The seismic signal of each sensor is registered by *Ruwai* data loggers with a sampling rate of 800 samples per second. Synchronized time of the individual recorders is essential for multi-station processing (e.g. locate seismic events within a network). The time synchronization is guaranteed by the GPS time signal, hence a good GPS signal reception must be assured. A three-component borehole sensor with GS-11D geophones was installed in the vertical borehole 3 (BH3). As borehole 1 (BH1) and borehole 2 (BH2) exhibit inclinations of 41° and 37°, respectively, omni-directional geophones OMNI-2400 were deployed. BH1 is equipped with a single-component sensor, whereas BH2 with a three-component sensor. Table 3.2 gives a summary of the borehole and sensor characteristics.

	BH1	**BH2**	**BH3**
Altitude [m a.s.l.]	3016	2985	3003
Depth [m]	21.5	30	6
Inclination [°]	41	37	0
Azimuth [°]	30	20	-
Sensor type	*OMNI-2400*	*OMNI-2400*	*GS-11D*
Sensor components	*Z*	*X Y Z*	*X Y Z*

Table 3.2: Borehole and sensor characteristics of the *OpAL* seismological network.

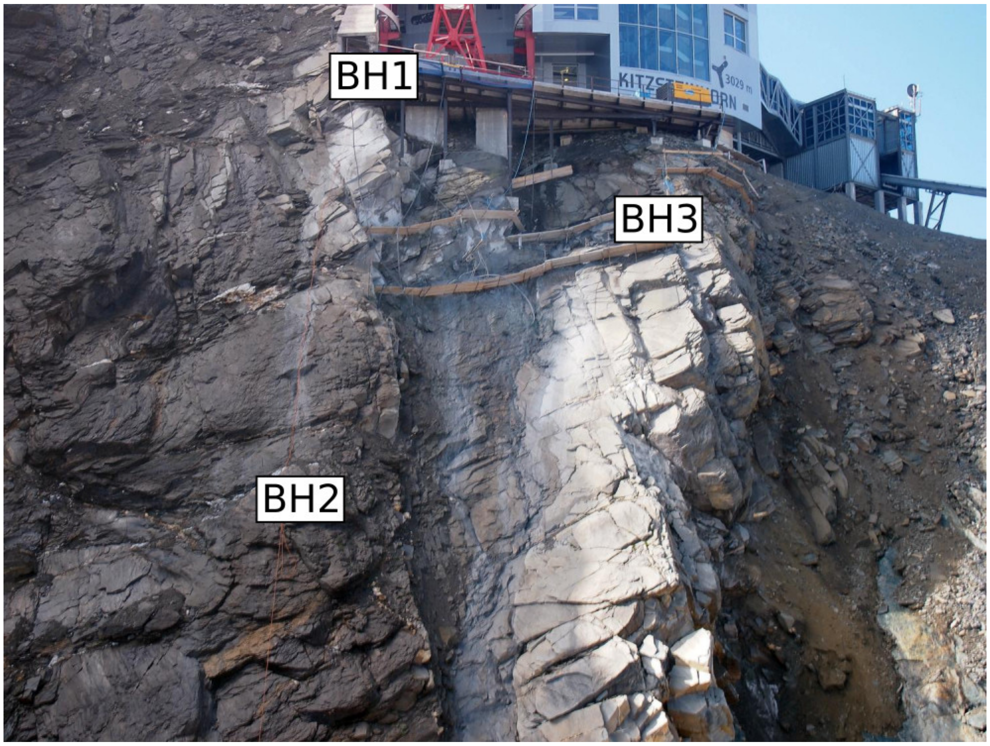

Figure 3.44: *SeisRockHT* investigation site at the north-face below the Kitzsteinhorn cable car top station. Deep boreholes 1 (BH1) and 2 (BH2) are normal to the local surface which results in a borehole inclination of about 40°. The 6 m deep borehole 3 (BH3) is vertical (borehole inclination 0°). All boreholes are drilled into solid rock.

The *OpAL* seismological network is powered by batteries regularly charged by mains power. Due to the prominent risk of electrial surges by lightning for this setting, power cables are physically disconnected for the non-charging periods. This power supply strategy was made possible by the *Gletscherbahnen Kaprun AG*. However, lightning strikes are an ongoing issue and burnt electrical elements were experienced throughout the whole *SeisRockHT* project.

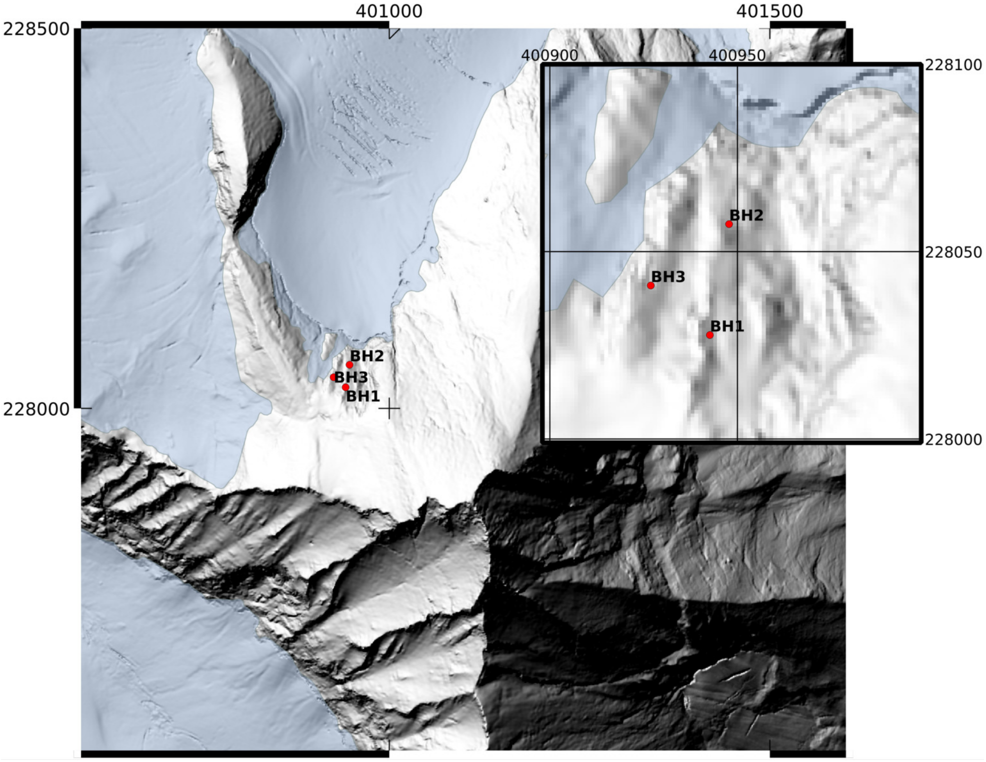

Figure 3.45: Overview map of the *OpAL* seismological station network (BH1-3). The blue shaded area indicates the Schmiedingerkees glacier. The overview map covers an area of 1x1 km, whereas the network blow-up covers an area of 100x100 m. (Coordinate System: MGI/Austria GK 31, EPSG:31258)

4. Data Availability and Quality

4.1 Terrain Data

Regular terrestrial laser scan (TLS) surveys were carried out at both *SeisRockHT* investigation sites. A Riegl LMS-Z620i long-range terrestrial laserscanner was deployed for the measurements. The laser scanner was mounted on a tripod for data acquisition, and scanning positions were recorded with a differential GPS (Trimble Pathfinder ProXRT 800B). Due to severe alpine hazards in the steep and unstable rockwalls, no reflectors were installed for the TLS surveys. Signal reflectivity of the bare rockwall was excellent, because of the near-infrared wavelength of the employed laserscanner. However, fresh snow and glacier ice signal reflectivity was poor. Annual TLS surveys were carried out during snow-free summer periods. Because of the significantly lower object distances at the Kitzsteinhorn site (∼300 m) compared to the Sonnblick site (∼1,000 m), a much higher spatial resolution was achieved for the Kitzsteinhorn site.

Sonnblick

Sonnblick TLS surveys were carried out from 2015 to 2018 (survey dates: 26/08/2015, 26/08/2016, 17/08/2017, 20/07/2018). The survey area covered the entire Sonnblick north-face with a vertical extent of around 700 meters (2400 - 3100 m a.s.l.), and a total surface area of around 470 km^2 (Figure 4.1). The acquired point clouds consisted of approximately five million data points, equalling a point density of around 10 points/m^2. Three different scan positions were necessary to improve the coverage of the heavily incised rockwall. However, significant occlusion effects within the main north-face couloirs remained (Figure 4.1). Since summer 2019, a new long-term monitoring initiative was initiated employing unmanned aircraft vehicles (UAVs; for details see chapter 8). This approach delivers a full coverage of the Sonnblick north-face.

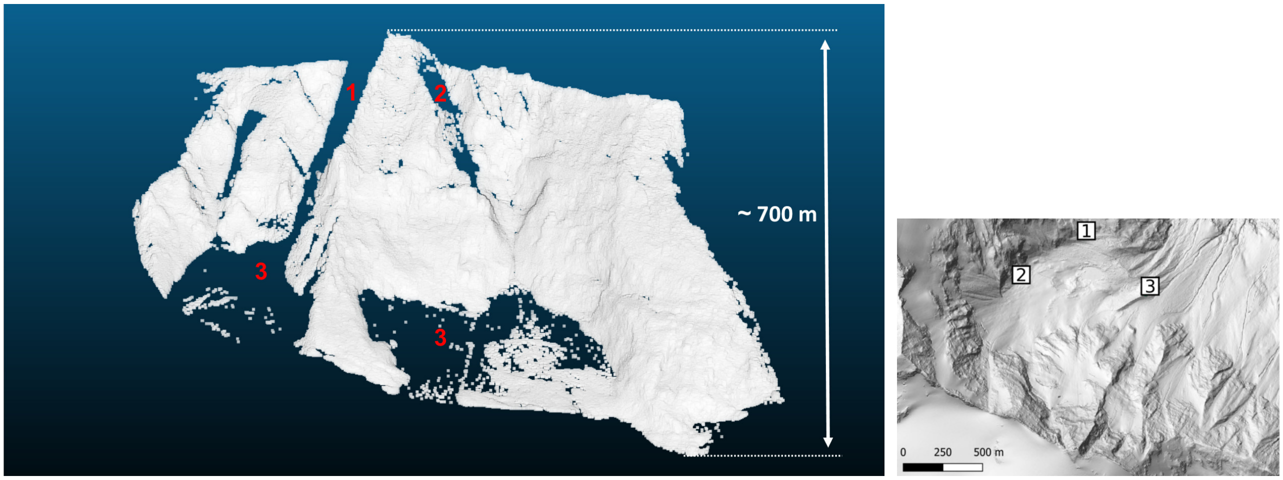

Figure 4.1: TLS surveys at the Sonnblick north-face covered the area between the glaciated slope foot (∼2400 m a.s.l.) and the summit (∼3106 m a.s.l.). Significant occlusion effects within the main north-face couloirs are evident (1, 2). Glaciated areas returned little to no TLS signal (3). The right image shows the three different scan positions (1, 2, 3) used to improve the coverage of the heavily incised Sonnblick north-face.

Kitzsteinhorn

TLS surveys at the Kitzsteinhorn were embedded into a major campaign focusing on the detection of rockwall changes related to recent deglaciation. Since 2011 TLS surveys were carried out at least once a year, financially and logistically supported by different institutions (*FFG*, *OeAW*, *Gletscherbahnen Kaprun AG*).

TLS monitoring focused on the side- and backwalls of the two main glacial cirques covering a total surface area of 235 km^2 (Figure 4.2). The *SeisRockHT* investigation site covered about 10% ($\sim$23.5 km^2) of the total area considered and a vertical extent of approximately 200 m (2900-3100 m a.s.l.). The low object distance during TLS surveys ($\sim$300 m) yielded a high spatial resolution for the *SeisRockHT* investigation site. Point clouds with a total of $\sim$five million points and point densities of $\sim$200 points/m^2 were acquired, which enabled the detection of volume differences below 0.1 m^3 (Hartmeyer et al. (2020b)).

Figure 4.2: Aerial view of the two main Kitzsteinhorn cirques that were monitored during the major TLS monitoring campaign. The Kitzsteinhorn north-face ('KN') was the *SeisRockHT* investigation site. Whereas, the extended TLS campaign also included the Kitzsteinhorn northwest-face ('KNW'), Magnetkoepfl east-face ('MKE'), Magnetkoepfl west-face ('MKW'), and Maurergrat east-face ('MGE'). The deployed scan positions were: SMK... Scan Position 'Magnetkoepfl', SCC... Scan Position 'Cable Car Top Station', SG1... Scan Position 'Glacier 1', SG2... Scan Position 'Glacier 2', SMG... Scan Position 'Maurergrat' (modified after Hartmeyer et al. (2020b))

4.2 Seismic Data

Due to the *SeisRockHT* high-alpine environment, station installation, optimization, as well as most maintenance tasks were limited to mid and late summer (compare sections 3.3 and 3.4).

All seismic stations were installed in summer 2015 and 2016. Throughout the project manifold causes of data loss became evident. Power shortages over the winter season was the main cause of data gaps of the stand-alone stations. As *SeisRockHT* focused on the snow free season, the initial power supply was not equipped for a year-round operation. However, *SeisRockHT* was aiming a year-round operation, thus, the power supply was gradually improved over the project duration. Lightning strike damage and mechanically broken cables caused data loss of the mains powered stations. Another fundamental cause of data loss was due to the fact, that currently recorded data is still stored locally and memory cards have to be replaced every 2-3 months. This was not always possible due to logistical and weather-related restrictions. Another reason for data loss were shortcomings of the *Ruwai* hardware and software that have emerged during the project. Finally, consequences of the harsh environment and man-made events, e.g. the construction of the new SBO cable car, caused periods without operating monitoring stations.

The aimed continuous seismological monitoring was, however, constantly pursued through several mitigation strategies. The main developed mitigation strategies were already discussed in chapter 3. Throughout the project, the percentage of the annual data yield was increased from 24% (2016) to 57% (2019) for the Sonnblick monitoring network (Table 4.1). Currently, the Sonnblick monitoring network's power supply is approaching a continuous operation, nevertheless, still present issues like the local data storage need to be addressed to assure a continuous long-term monitoring in the future. The Kitzsteinhorn network is facing a fundamental problem which was already discussed in section 3.1 and will be further described below.

Sonnblick

All plots of the seismological network's monthly data availability for the period 2016 - 2019 can be found in Appendix A. The data gathered within the test survey 2015 are not considered, neither in the monthly data availability plots, nor in the following discussion about emerged major data availability issues.

The continuous optimization of the technical requirements for year-round operation led to a steadily increasing annual data yield (Table 4.1), with late summer and autumn showing the highest intra-annual amount of gathered data. However, the individual stations did not necessarily show a steady increase in annual data yield over the entire project. The different reasons for each station are explained below.

Generally, during winter the basic memory card exchange was not possible for the stations OBS and PIL. In the period autumn 2017 to late summer 2018 a comprehensive *Ruwai* data recorder software and hardware update was carried out to improve field operation reliability. This caused data gaps for the periods in which the individual data loggers were removed from stations to carry out the crucial update. This necessary measure emerged during a *SeisRockHT* campaign in September 2017, where the MIT completely failed due to software shortcomings.

	OBS	**MIT**	**MOR**	**PIL**	**STO**	**mean**	**ME**
2016	20%	25%	19%	19%	39%	24%	3
2017	48%	23%	19%	14%	51%	31%	4
2018	23%	25%	25%	12%	74%	32%	4
2019*	42%	90%	91%	32%	31%	57%	7

Table 4.1: Percentages of the annual data yield for the single stations of the Sonnblick seismological network. The mean percentages ('mean') and monthly equivalents ('ME') describe annual data output of the entire network. 2019* takes into account SOSA data instead of the non-operational OBS station.

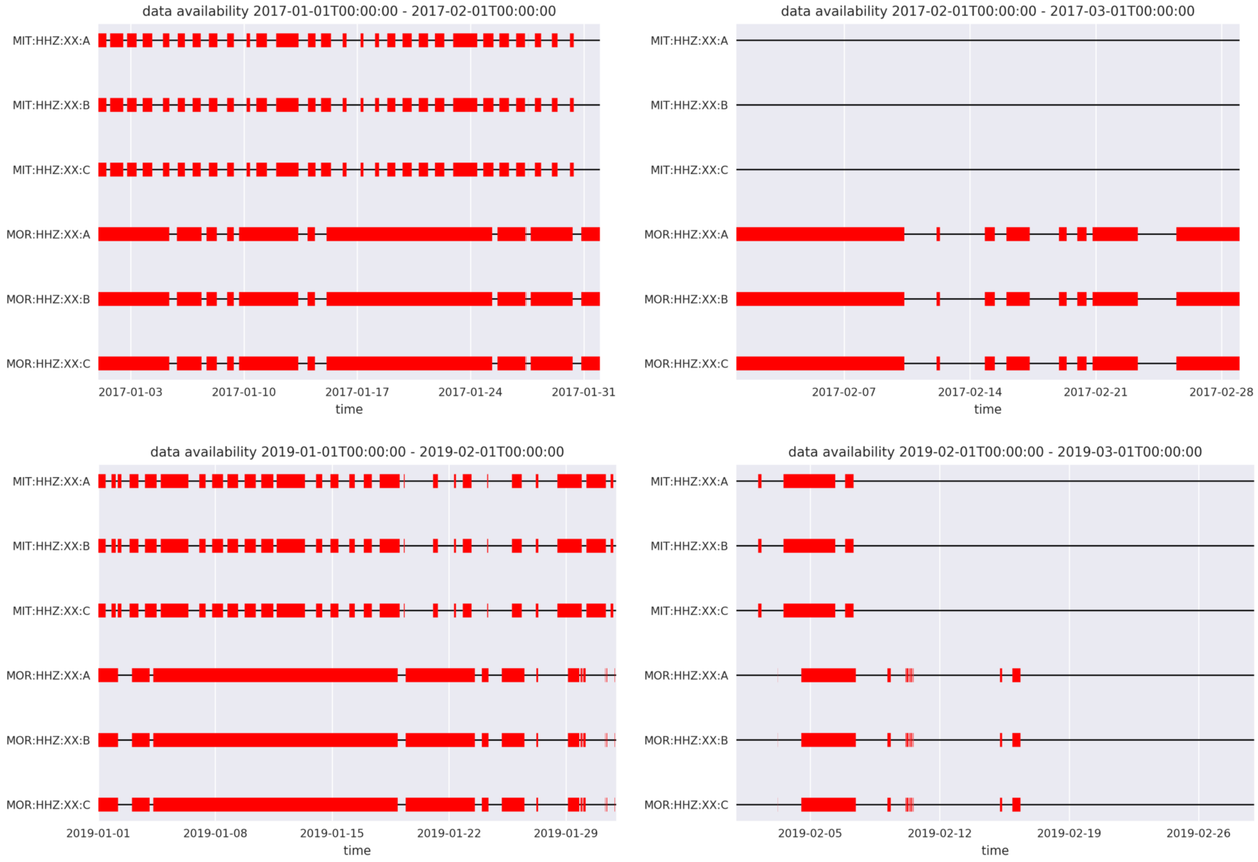

Figure 4.3: Comparison of the MIT and MOR data availability for January and February of the years 2017 (top row) and 2019. The difference in sola panel shading of the two stations is striking for the month of January (left column). Whereas, the MIT station exhibited a quasi diurnal cycle, the MOR station showed rather persistent periods without data due to the shading of the close-by north-face. Since summer 2018, both stations are equipped with a wind turbine which led to a general higher data yield for 2019.

The construction work of the new SBO cable car interrupted the MIT station operation from September 2017 to September 2018. The vast snow amount at the PIL location (Figure 3.38 and 3.40) caused power supply outages which led to data gaps. Furthermore, a PIL sensor cable broke and led to data loss from October 2018 to September 2019 for one of the three PIL channels. However, the current PIL station setup potentially assures a substantial higher data yield (compare section 3.3.2). Between December 2018 and September 2019, the STO station was not operational due to damage of the *Naturfreundehaus* underground power cable. In late summer 2018, the OBS borehole sensor got stuck during a thermistor string exchange attempt. This culminated in a totally broken OBS data cable during another exchange attempt in 2019 and a OBS data gap since end of November 2018. Nevertheless, since August 2019 the new SOSA seismic station (Figure 3.19) is delivering data and is used as OBS station replacement.

As already discussed in section 3.3.2, the MOR station initially showed larger data gaps due to power shortage because of low solar irradiance. Figure 4.3 shows MIT and MOR data availability for the months January and February in 2017 and 2019. The different shading situation of the two stations is striking for the month of January. Whereas, the MIT station exhibited a quasi diurnal cycle, the MOR station showed rather persistent periods without data due to the more dominant shading of the close-by north-face. Since summer 2018, both stations are equipped with a wind turbine which led to a general higher data yield for 2019. Figure 4.4 compares the month of December for the years 2016 and 2019. All applied power supply measures throughout the project eventually closed data gaps of the MIT and MOR station. PIL and STO data was not considered. However, the new PIL station set up (section 3.3.2) substantially reduced the data gap present in 2016. The OBS borehole sensor is not operational, but the data of the new SOSA station (Figure 3.19) is used instead. Principally, MIT station data is available, but since summer 2019 spurious data is recorded. In summer 2020, the ingress of water into the sensor plug was identified as cause of the spurious MIT data and was fixed.

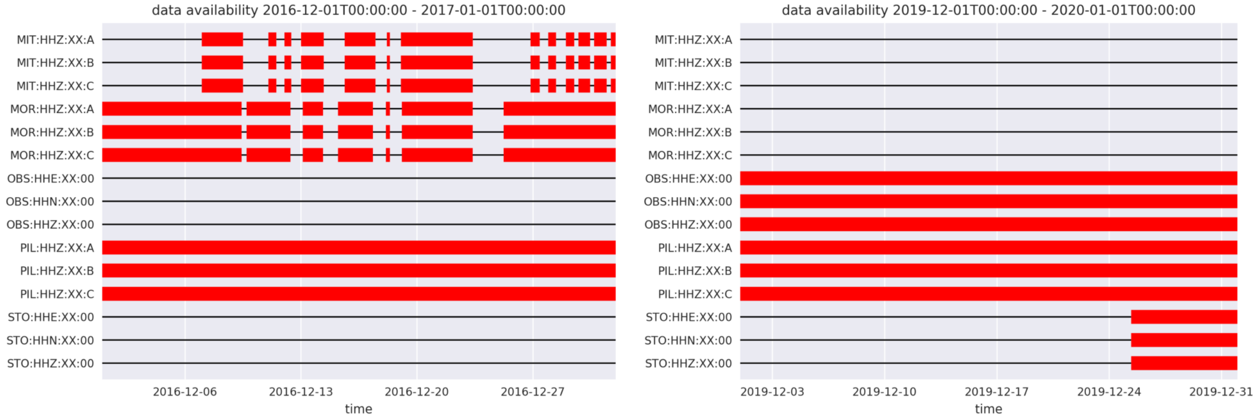

Figure 4.4: Sonnblick seismological network data availability for the month of December compared for the years 2016 (left) and 2019. In December 2019 MIT and MOR stations showed no data loss. The OBS borehole sensor is not operational, but the data of the new SOSA station was used instead.

Data Quality

Basically, a seismic event can be detected once the event amplitude exceeds the ambient noise amplitude of the seismic monitoring system. The frequency-dependent ambient noise level is determined by system internal and external drivers. In-system drivers are the electronic noise level of the data recording setup, as well as the sensitivity and the ground coupling of the sensor (compare section 3.1). System externally, the site-specific impulse response function of the ground, and the local environmental and anthropogenic noise contributes to the total ambient noise level. Consequently, the frequency dependent ambient noise level varies with space and time, and is characteristic for each station.

The probabilistic power spectral density (PPSD; McNamara and Buland (2004)) is a well established method to characterize the frequency-dependent ambient noise level of a seismic station, as well as to detect operational problems. Figures 4.5, 4.6 and 4.7 show calculated exemplary PPSDs of all stations for the available data of 2017. The two gray lines in the PPSD plots represent the minimum and maximum seismic background noise which can be expected worldwide (Peterson (1993)). A station-specific PPSD in between these two global ambient noise extremes qualifies the station for seismological monitoring.

Prinicipally, all stations of the Sonnblick network feature a PPSD in between the two global ambient noise extremes. The stations PPSD increase and eventually overshooting of the maximum global noise level towards lower frequencies is due to the applied sensor (GS-11D, compare section 3.2) with a corner frequency of 4.5 Hz. The PPSDs are calculated for selected sensor components/channels which are shown next to the station names in the individual PPSD titles. Sensor component notations are *HHZ* for vertical (Z), and *HHN* and *HHE* for the horizontal components ($X\ Y$).

The mains powered stations (OBS and STO, Figure 4.5) generally show less spread in their PPSD functions than the stand-alone stations (MIT, MOR and PIL; Figure 4.7). This is caused by the rather quiet OBS and STO station characteristics due to the sensor installations in a deeper borehole and in a tunnel, respectively (compare section 3.3.1). The STO station is the most quiet station, hence, ideally qualified as reference station of the Sonnblick network and for ambient seismicity analysis. The elevated PPSD amplitudes for the OBS and the MIT stations in the frequency range 30 to 40 Hz is likely to be caused by the SBO cable car. Due to the setting, the OBS horizontal components are more susceptible for the induced seismicity by the regular cable car operations. Consequently, the horizontal components of the OBS borehole sensor show a more distinct PPSD amplitude increase in the 30 to 40 Hz range than the OBS vertical component (Figure 4.6). The MIT station shows the highest PPSD amplitude variation of all stations potentially due to the near-by cable car pillar. Figure 4.8 shows the PPSD of a selected channel of the MIT station for October 2019 and clearly illustrates the recorded spurious data for this period. As already discussed above, the ingress of water into the sensor plug was identified as cause of the spurious MIT data and was fixed in autumn 2020. Despite distinct periods with spurious data owing to repairable causes, all stations generally feature PPSDs in between the two global ambient noise extremes, hence, can be utilized for seismological monitoring.

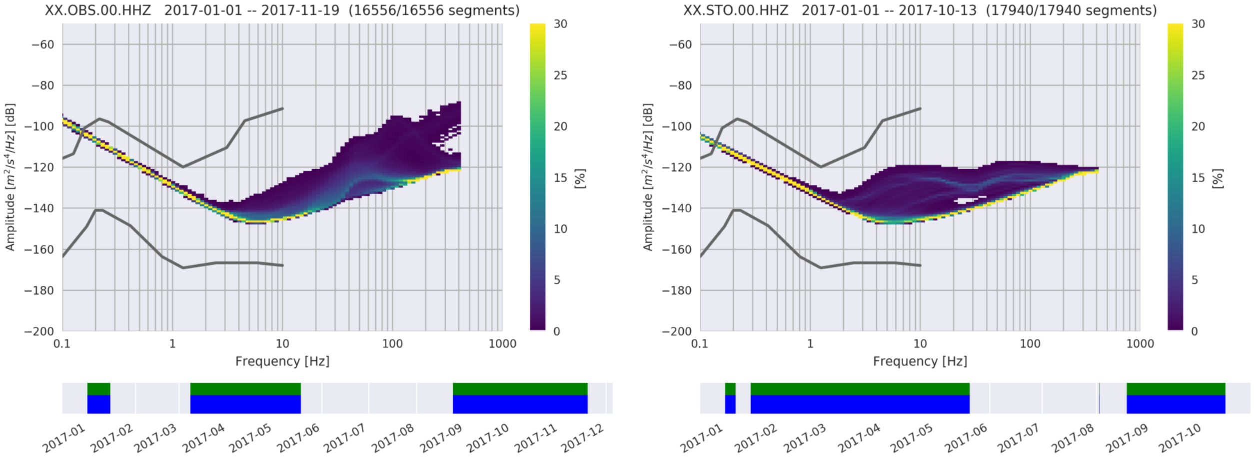

Figure 4.5: Calculated probabilistic power spectral density (PPSD) for the mains powered stations OBS (left) and STO for available 2017 data. Mains powered stations feature lower amplitude variations due to their sensor installations in a borehole and in a tunnel. Details about the PPSD calculation are given in each PPSD's title. Horizontal green and blue bar at the bottom indicate data availability.

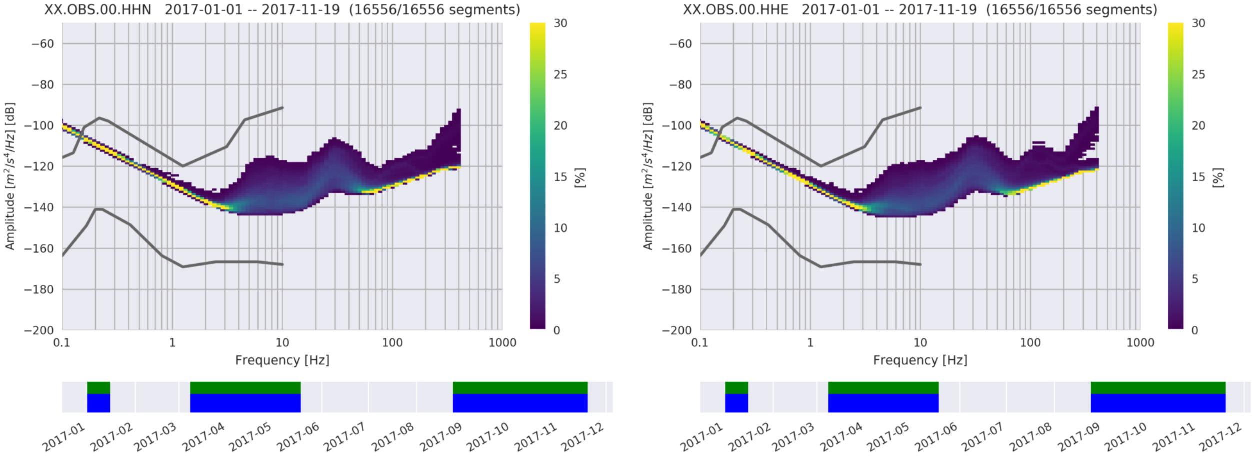

Figure 4.6: Probabilistic power spectral density (PPSD) for the two horizontal components of the OBS station for 2017. The distinctively elevated amplitudes for the frequency range 30-40 Hz is presumably caused by regular cable car operations. Details about the PPSD calculation are given in each PPSD's title. Horizontal green and blue bar at the bottom indicate data availability.

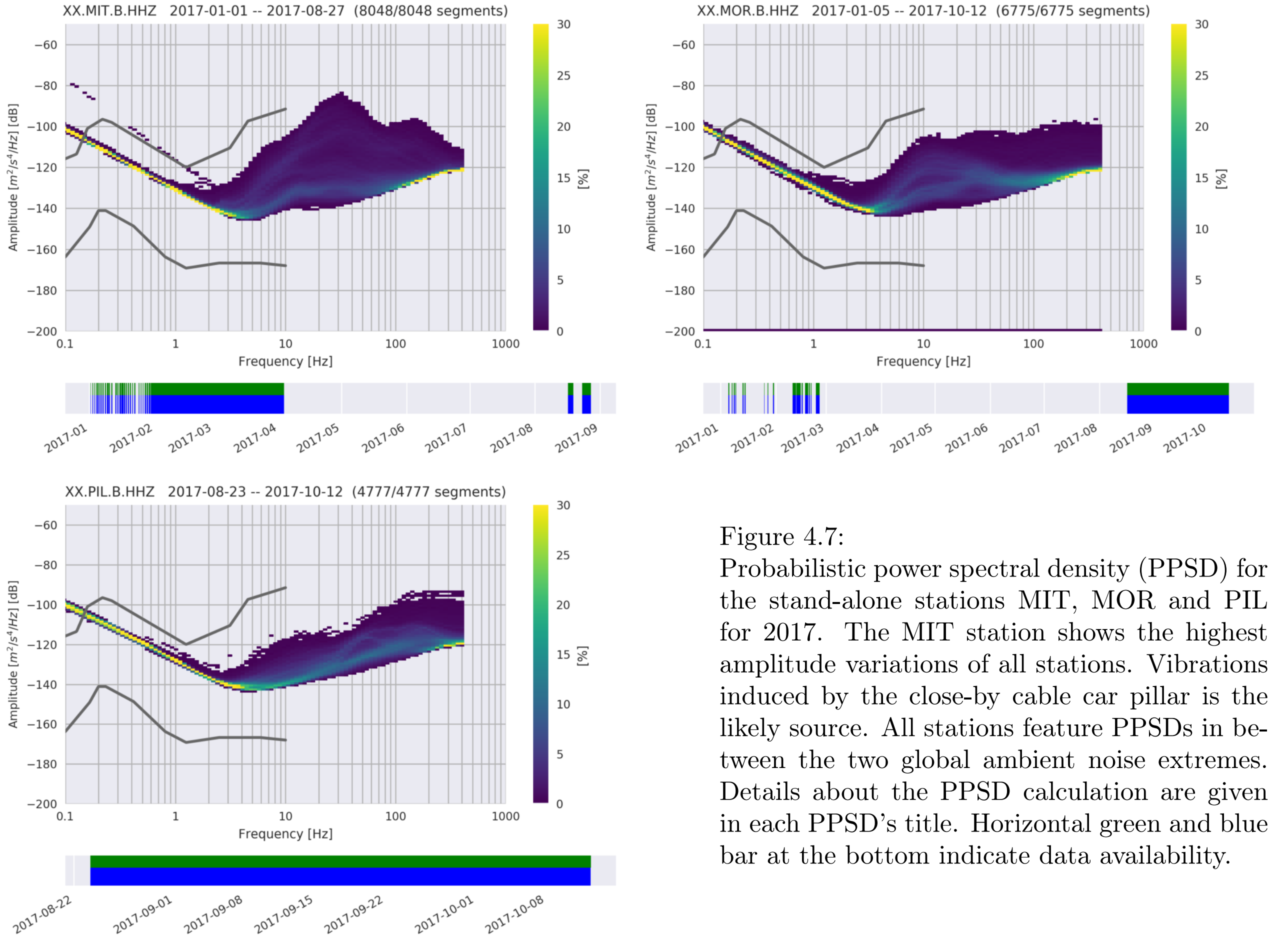

Figure 4.7:
Probabilistic power spectral density (PPSD) for the stand-alone stations MIT, MOR and PIL for 2017. The MIT station shows the highest amplitude variations of all stations. Vibrations induced by the close-by cable car pillar is the likely source. All stations feature PPSDs in between the two global ambient noise extremes. Details about the PPSD calculation are given in each PPSD's title. Horizontal green and blue bar at the bottom indicate data availability.

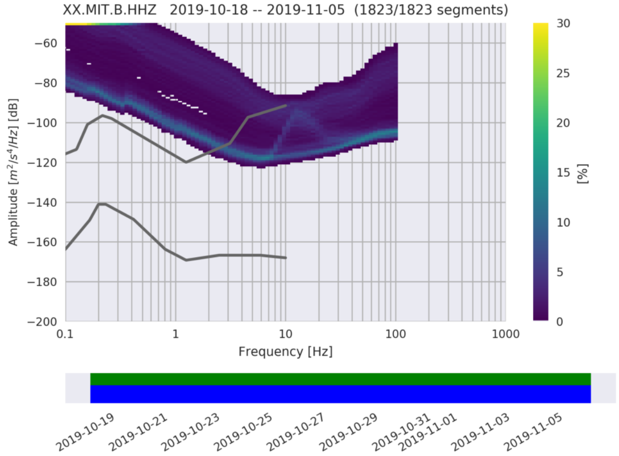

Figure 4.8:
Probabilistic power spectral density (PPSD) for the stand-alone station MIT for October 2019. The PPSD clearly shows that the MIT station was recording spurious data. Details about the PPSD calculation are given in the PPSD title. Horizontal green and blue bar at the bottom indicate data availability.

Central Italy Earthquake Event

In 2016, central Italy experienced an intense earthquake sequence with severe consequences. Among the numerous events, the earthquake on October 30, 06:40:18.3 UTC, with a magnitude of 6.5 was the strongest recorded in Italy since 1980 (find more in *Seismological Service of Austria summary October 2016*).

Nevertheless, the earthquake event represented an opportunity to check the impulse response and timing accuracy of the *SeisRockHT* seismological network at the Sonnblick. The earthquake was recorded by all stations of the Sonnblick seismological network. Figure 4.9 shows the comparison of representative PPSDs of the PIL station for the active week 43 (24. - 30. 10.) and the rather quiet week 45 (07. - 13. 11.). The active week 43 shows clearly the higher PPSD amplitudes for lower frequencies due to the central Italy earthquake sequence.

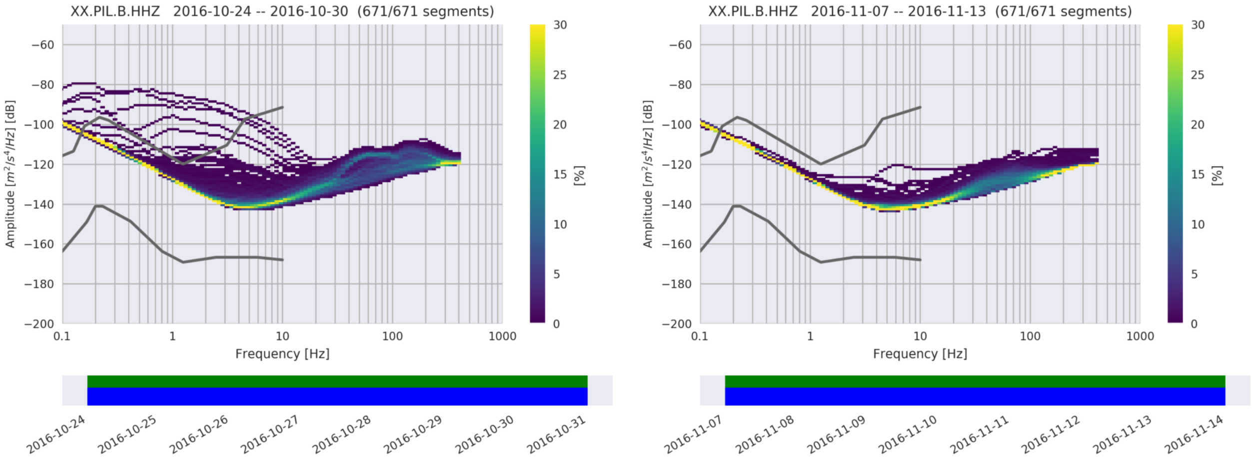

Figure 4.9: Comparison of representative PPSDs of the PIL station for the active week 43 (24. - 30. 10.) and the rather quiet week 45 (07. - 13. 11.) in 2016. The active week 43 clearly illustrates the higher PPSD amplitudes for lower frequencies due to the central Italy earthquake sequence.

Figure 4.10 shows recorded waveforms of the Sonnblick network and two selected stations of the Austrian earthquake network (MYKA and BIOA). Generally, all waveforms are displayed in the digital unit of counts. If not stated differently, the waveform scaling is individual for every seismogram. The map in figure 4.10 illustrates the entire earthquake network of Austria which employs high-resolution broadband and strong-motion seismometers. The SOSA station indicates the location of the *SeisRockHT* Sonnblick network. The SOSA station itself was operational with August 2019. Recorded waveforms of the *SeisRockHT* and the earthquake stations differ due to the deployed sensor types. MYKA and BIOA high-resolution broadband seismometers resolved the low frequency and high amplitude surface waves arriving after the faster body waves. The body waves are also clearly visible in the *SeisRockHT* data, whereas the featured *SeisRockHT* sensor types (compare section 3.2) are technically not able to resolve the surface waves due to their low frequency. The red vertical line in the plot of the individual seismograms marks the first arrival of the earthquake event's body waves at the southerly MYKA station. Delayed body wave first arrivals in northerly direction confirm the correct timing of the *SeisRockHT* stations.

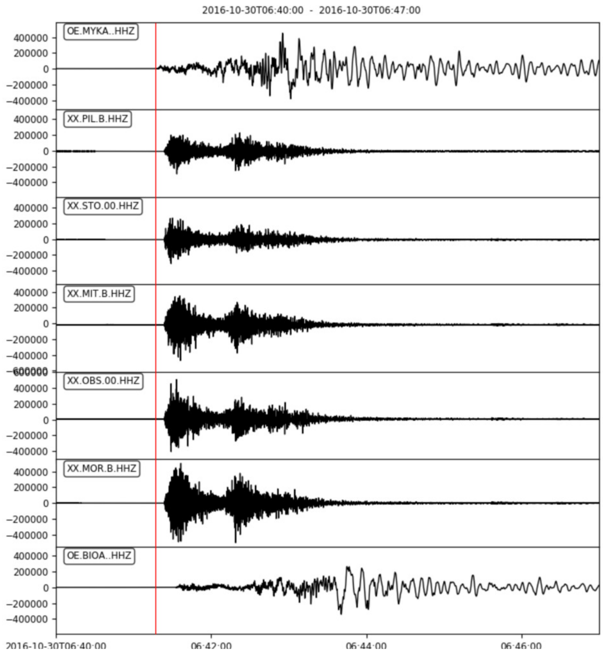

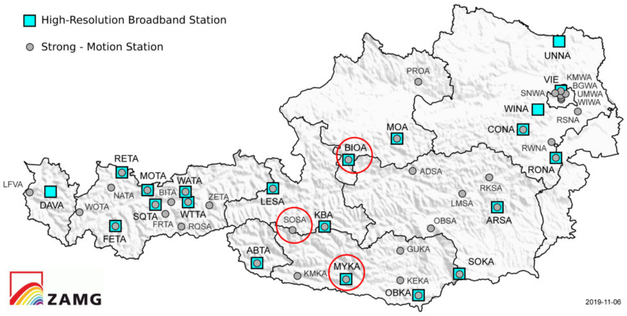

Figure 4.10:
The central Italy earthquake was recorded by the *SeisRockHT* network. Austrian earthquake network stations (right) from which data is shown are encircled in red. The SOSA station indicates the location of the *SeisRockHT* Sonnblick network. The red vertical line in the seismogram plot marks the first arrival of the earthquake event at the southerly MYKA station. Delayed first arrivals in northerly direction confirm the correct timing of the *SeisRockHT* data.

Kitzsteinhorn

As described in section 3.4, all Kitzsteinhorn stations were mains powered. Despite partially different applied sensors, the station setup was identical with the mains powered stations of the Sonnblick network (OBS and STO). During non-charging periods the power cable was physically disconnected for the Kitzsteinhorn stations, which was actually never done for the Sonnblick stations.

However, spurious signals were present throughout all test measurements which eventually made the Kitzsteinhorn data unusable for further analysis. The Kitzsteinhorn site, with the dominant cable car top station and its numerous electric installations, apparently poses a true electric grounding challenge which could not be overcome with the available *SeisRockHT* equipment. Various grounding points were tested throughout the project, but to no avail. Tested grounding points were the top station balustrade, a still extant metal drill rig anchoring rod which was drilled several meters into the rock, and the negative pole of the power supply battery.

Data quality

The central Italy earthquake event from October 30, ∼06:40 UTC, is applied to illustrate the quality of recorded data at the Kitzsteinhorn site. In the following, recorded data of the two different applied sensor types (OMNI-2400 and GS-11D; compare section 3.2) are shown.

Already the calculated PPSDs of the vertical components of the BH1 and BH3 station suggested operational problems of the Kitzsteinhorn network (Figure 4.12), and recorded waveforms of the vertical components of the BH1 and BH3 stations confirm that (Figure 4.13). Due to the prominent electromagnetic interferences, ground motion caused by the central Italy earthquake event was not resolved by the Kitzsteinhorn network.

Figure 4.11: Several grounding strategies were tested to overcome the bad data quality of the Kitzsteinhorn network stations. Photos are taken during an extensive testing session at the BH1 station. However, all the efforts did not lead to better data quality, which left the Kitzsteinhorn unusable for further analysis.

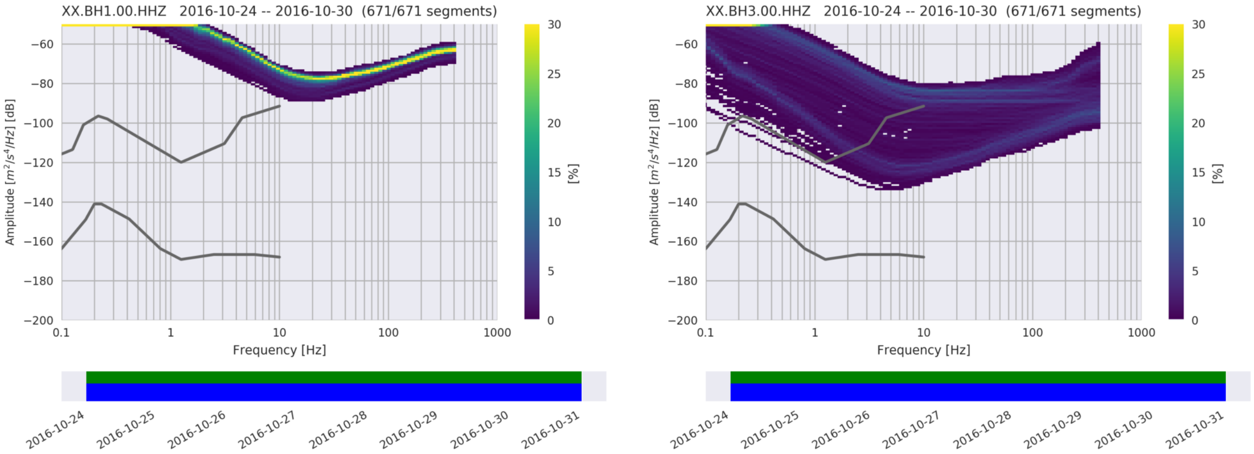

Figure 4.12: Calculated PPSDs for the vertical sensor component of the BH1 and BH3 station for the week 43 (24. - 30. 10.) which included the central Italy main earthquake event from October 30, ~06:40 UTC (compare 4.9).

The recorded BH1 and BH3 waveforms in figure 4.13 appear very similar. The ambient noise exhibits a rather broad amplitude range, and is interrupted by individual distinct broadband events. The largest broadband event at 06:46 UTC is visible on both stations. We hypothesize that the origin of the distinct broadband events is anthropogenic, caused by fluctuations within the Kitzsteinhorn top station electrical network. Figure 4.14 shows 15 seconds of ambient noise data of figure 4.13. The blow-up view revealed different characteristics of the recorded ambient noise. BH1 ambient noise shows a more chaotic behavior with regular step-like amplitude drops, while BH3 ambient noise features a rather constant amplitude cycle with the mains frequency of 50 Hz. Whether this difference in ambient noise characteristics is due to the applied sensor type, and/or a site-specific effect cannot be answered at this stage.

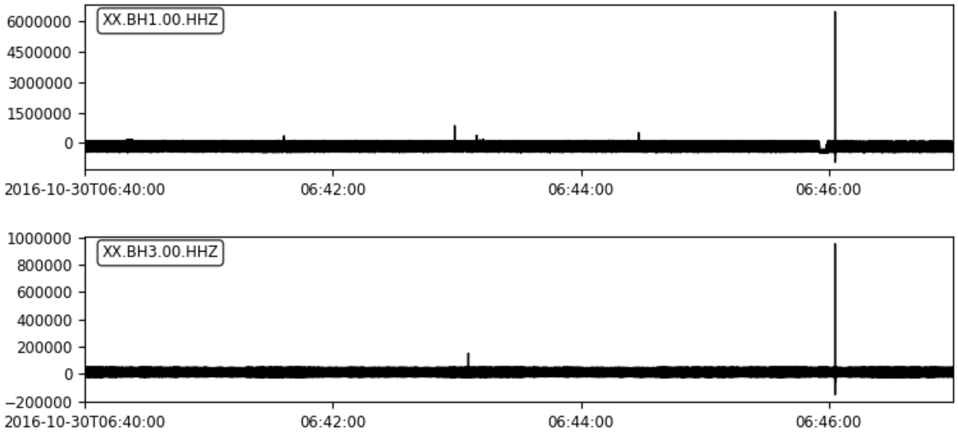

Figure 4.13:
No ground motion of the central Italy main earthquake from October 30, ~06:40 UTC, was recorded by the vertical components of the BH1 and BH3 stations at the Kitzsteinhorn site (compare 4.10).

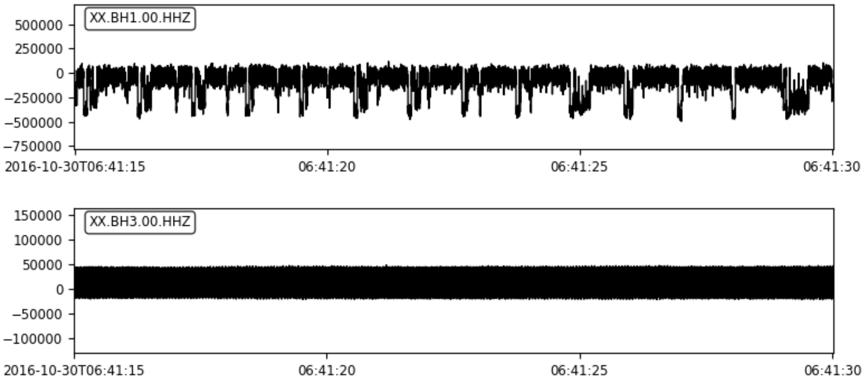

Figure 4.14:
15 seconds of the data shown in figure 4.13 revealed different characteristics of the ambient seismic data. BH1 data shows a more chaotic behavior with regular step-like amplitude drops, whereas BH3 ambient data feature a rather constant amplitude range.

4.3 Complementary Data

A strength of the *SeisRockHT* initiative is the availability of manifold complementary data which were used to interpret recorded seismic data. Both *SeisRockHT* investigation sites are manned year-round and host comprehensive environmental monitoring programs (compare sections 3.3 and 3.4). Exemplary, figure 4.15 shows the mean annual ground temperature series for the period 2010-2018 of a deep borehole (BH3, Figure 3.19) at the Sonnblick summit. Phase changes between water and ice release or uptake latent heat during freezing or thawing, respectively. This latent heat temporarily maintains temperatures near 0°C in freezing or thawing soils which is termed as the zero-curtain effect. In figure 4.15 the zero-curtain effect is nicely visible in the shoulder seasons.

Besides the environmental data provided by the two long-term monitoring sites, meteorological data of the Austrian Weather Service network and river discharge data from the Hydrographic Service of Salzburg (`https://www.salzburg.gv.at/`) were available. Furthermore, data of the *Austrian Lightning Detection and Information System (ALDIS)*, and Sonnblick cable car operation and construction logs were provided for *SeisRockHT* seismic data interpretation.

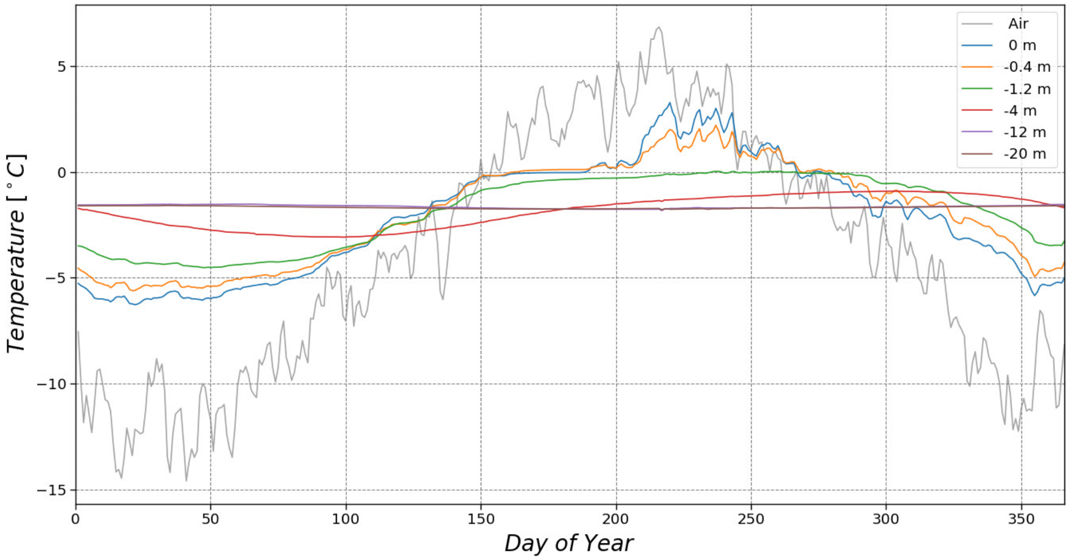

Figure 4.15: The mean annual ground temperature time series for the period 2010-2018 at the Sonnblick summit. In the shoulder seasons the zero-curtain effect is nicely visible.

Visual Rockfall Monitoring

Eyewitness observations generally provide valuable information for the interpretation of corresponding seismic data. A systematic visual rockfall monitoring was initiated at the Sonnblick investigation site with the start of the *SeisRockHT* project in 2015. This ongoing initiative provides a growing database of verified rockfall events which are used to derive characteristic seismic rockfall features, which will be used for the development of an automated rockfall detection algorithm. The visual rockfall monitoring will be continued in the future.

Since 2015 in total 26 rockfall events were observed and documented. Table 4.2 lists all the visually validated rockfall events to date. However, several documented events occurred outside of the *SeisRockHT* network, whereas the recently deglaciated rockwalls adjacent to the glaciers Kleinfleisskees and Goldbergkees represented a regular rockfall release zone. The regular data gaps of the *SeisRockHT* stations reduced the visually validated rockfalls to just two recorded seismic events (→ID 5 and 19). Corresponding seismic data and derived seismic rockfall features are presented in section 6.2.

ID	**Date**	**Time (CET)**	**Rockfall Release Zone**	**Volume [m^3]**	**Observer**
1	2015-07-02	12:00	Nordrinne	1	HS
2	2016-07-24	11:05	Scheisshaeuslrinne	0.5	ND
3	2017-06-15	11:30	Sonnblickgipfel NO	1.5	ND
4	2017-08-03	01:39	Goldbergspitze W	5	MD
5*	2017-08-17	01:00	Nordrinne	1	DB
6	2018-07-20	03:00	Goldbergspitze O	3	ND
7	2018-07-23	12:00	Goldbergspitze O	2.5	ND
8	2018-07-24	06:48	Nordrinne 3030 masl	0.3	ND
9	2018-07-24	11:00	Goldzechkopf		HS
10	2018-07-25	04:15	Nordwand 3050 masl	1	HS/ND
11	2018-08-13	12:35			EL
12	2018-08-19	11:53	Grat Lislstange	0.2	ND
13	2018-08-19	11:30	Goldbergspitze O	0.8	ND
14	2018-08-19	07:00	Nordwand	0.5	ND
15	2018-08-24	09:52	Rojacherspitze W	1.5	ND
16	2018-08-25	09:48		0.2	ND
17	2019-06-18	07:07	Nordrinne	0.3	ND
18	2019-07-31	10:00			HS
19*	2019-09-13	09:12	Nordwand 2800 masl	3	ND
20	2020-07-01	06:00	Goldzechkopf		HS
21	2020-07-24	09:22	Nordrinne		HS
22	2020-07-11	02:30	Goldbergspitze O		WS
23	2020-07-28	10-19:00	OBS SW		HS
24	2020-08-10	04:38	Nordwand	0.2	ND
25	2020-08-20	02:40	Nordwand Pilatus	0.2	ND
26	2020-08-30	03:30	Nordwand Pilatus	150	MD

Table 4.2: All visually registered rockfalls to date. The volume is a visually estimated value. The initials of the individual observer(s) are given. The two visually and by the seismic network observed rockfalls are marked with an asterisk (ID 5 and 19).

5. Analysis Tools and Methods

5.1 Terrain Modeling

Georeferencing was carried out by aligning the acquired TLS point clouds with airborne LiDAR ('Light Detection and Ranging') datasets recorded in 2007/2008 (SAGIS (2007), SAGIS (2008)). Spurious signals like e.g. atmospheric particles were removed from the point clouds prior to the georeferencing process. Point clouds were then coarsely aligned using the GPS location of the scan position, and the recorded azimuth angle of the laserscanner. The referencing was performed with the RiScanPro software applying the robust Iterative-Closest-Point (ICP) method (Chen and Medioni (1992)). The ICP method relies solely on surface geometry comparison, whereas point clouds differences are iteratively minimized by a mean square error approach. Poor fits (e.g. large distances) in the referencing results were gradually eliminated by reducing the 'search radius'- and 'outlier threshold'- parameters. Real surface changes between the annual surveys hence do not affect the surface matching, and rendering alignment errors are negligible (Abellán et al. (2011), Abellán et al. (2010)). Therefore, best-fit algorithms such as the ICP method are particularly suited for surface matching in stable environments (Rosser et al. (2007)). Accordingly, final referencing results with typical errors of 1-2 centimeter could be obtained.

Surface changes are detected through distance differences for sequential point clouds. The two most prominent approaches comprise on the one hand the identification of homologous features in the sequential point clouds to calculate displacement fields (Teza et al. (2007), Monserrat and Crosetto (2008)), and on the other, the direct distance calculation (Rosser et al. (2005)). Due to the fact that the direct distance calculation is well-suited for surfaces modified by erosion or sedimentation between the surveys, we applied the latter approach. Direct comparisons usually either rely on closest Euclidean point distances, or require at least one gridded point cloud product. However, the gridding process introduces limitations for rough surfaces such as heterogenous rockwalls. Eventually, the M3C2 algorithm was applied (Lague et al. (2013)) to calculate the closest Euclidean point distances. This algorithm was specifically designed for orthogonal distance measurement in complex terrain and is implemented in the open source software *CloudCompare*. The M3C2 algorithm performs direct 3D comparisons of two point clouds, whereas it is especially accounting for point cloud heterogeneity. Point cloud differences are measured along local surface normal vectors, whereas local surfaces reproduce the apparent surface roughness in every calculation step. The M3C2 approach represents a robust method for irregular surfaces, varying point densities, and missing data. This makes the M3C2 algorithm particularly suited for multi-annual TLS rockwall surveys with varying data quality.

The M3C2 algorithm does not provide difference volumes of two sequential point clouds directly, but can be derived from the calculated distance differences. As a first step, zones with significant distance differences of the two point clouds are identified and extracted. Subsequently, local grids are calculated for each identified zone. Eventually, volume differences for each zone are determined by subtracting the two local grids. Since the distance uncertainty behind each grid cell is known, the error associated to each volume can be calculated.

5.2 Seismic Processing

5.2.1 pSysmon - a FOSS Project

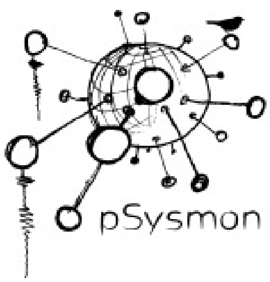

pSysmon is a seismological prototyping and processing software dedicated to non-standard seismological studies. It is written in *Python* and released under the *GNU GPL license*. *pSysmon* documentation and source code is available through the *pSysmon Wiki* and *pSysmon Git repository*, respectively.
Scientific research in seismology often involves new approaches for data collection, unconventional instrumentation and the development of novel algorithms to process the data. The combination of these needs limits the usage of routine software packages. Furthermore, smaller research projects are often constrained by low-budgets and are not able to afford the license fees for proprietary software and the costly services to adapt the software to special needs.
pSysmon tries to fill this gap and provides a free seismological processing and prototyping software. The software is built around a primary graphical user interface using *wxPython*. *pSysmon* provides a modular frameset arranged in collection nodes for data organisation, visualization and signal processing of seismic time series. It is simple to add custom collection nodes to *pSysmon* with a basic knowledge of *Python* programming. No knowledge of *wxPython* graphical user interface programming is required. The *FOSS ObsPy* seismological toolbox (Krischer et al. (2015)) is a central building block of *pSysmon*. *SeisRockHT's* seismic data processing was implemented with *pSysmon*.

5.2.2 Analysis Methods

Spectrograms

Spectrograms visualize the spectral content of the recorded waveform over time and are computed by applying the Short-Time Fourier Transform (STFT). We used the STFT implemented in the Python library *scipy.signal.spectrogram* to compute the spectrograms as power spectral densities (PSD). All these spectrograms are plotted together with the recorded waveforms (seismograms) as presented e.g. in section 6.2.

Long-term spectrograms with timespans of days or weeks to visualize e.g. ambient seismicity were computed by a custom implementation of the STFT available in the *pSysmon* software. Thereby, *pSysmon* splits the timespan to analyze into overlapping windows and computes for each window the power spectral density. The Welch method implemented in the Python library *matplotlib.pyplot.psd* is used for the PSD computation. Finally, the power spectral densities are plotted as spectrograms in a time-frequency plot.

The parameters used to compute the long-term spectrograms for this report are given in table 5.1. The *SeisRockHT* data were sampled with 800 samples per second, thus the applied PSD segment length of 8192 samples is equivalent to a length of 10.24 seconds.

The computation of the Probalistic Power Spectral Density (PPSD) plots used in e.g. section 4.2 to evaluate the installed seismic recording system performance, follows McNamara and Buland (2004).

Parameter	Value
window length	900 s
window overlap	50 %
PSD segment length	8192 samples
PSD segment overlap	50%

Table 5.1: Long-term spectrogram parameters.

Event Detection and Categorization

A STA/LTA detection algorithm implemented in *pSysmon* was used for automated event detection. The STA/LTA algorithm was introduced by R. Allen (1978). It is based on the comparison of a long time average (LTA) and a short time average (STA) of one or more features computed from the seismic time series. R. Allen (1978) named the derived features characteristic functions (CFs). The most basic CFs apply the absolute values, or the squares, of the time series amplitudes. Principally, the LTA of the characteristic function models the seismic noise, whereas seismic noise is regarded as *"that part of the data that we chose not to explain"* (Scales and Snieder (1998)). The STA of the characteristic function represents short-term variations of the data. Whenever the STA exceeds the LTA by a given ratio an event is declared. Besides the timespans over which the LTA and STA are determined, the ratio threshold must be defined by the operator. The selection of the STA/LTA parameters depends on the data as well as the required event detector sensitivity.

The STA/LTA detection is a single trace process and, depending on the analyzed time-span, usually results in a huge amount of detections without any relation to each other. The most important point in declaring a seismic event is the occurrence of related seismic signals on multiple stations with travel time differences that reasonably reflect the local velocity structure. In local- and regional earthquake analysis, the detection-binding (also called event-binding) usually requires a sophisticated algorithm. This includes the localization of possible hypocenters to compute theoretical travel-times to which the first onsets of the detected patterns are compared to.

The gathered *SeisRockHT* data featured many weak events and reliable first onsets were rather rare. A simplified algorithm using the begin times of the extracted patterns to bind the single-trace detections was used to overcome this challenge. Therefore, the detection binding was split into two steps. The first step was binding detections of the individual array stations MOR, PIL and MIT to array-detections, to suspend detections caused by very local sources (e.g. animal activity near an array station). Detections occurring on more than two array locations (A, B, C) within a search window of 0.5 seconds were declared as an array-detection and were assigned to the array station.

The square of the low-pass filtered seismogram was used as a characteristic function for the STA/LTA detection. A cutoff frequency of 200 Hz was used for the applied low-pass filter. The window length for the STA and the LTA was 1 s and 10 s, respectively. A STA/LTA ratio threshold of 5 was applied. Furthermore, a STA/LTA ratio threshold of 2 was chosen for the refinement of the initial detection start. Detections with a event duration smaller than 0.5 s were rejected.

The second step was then binding the array-detections with all the other network stations, whereas each indiviudal array location (A, B, C) was treated as a single station. The array-detection binding is done by comparing the start times of the detections at neighbouring stations. If at least two detections on neighbouring stations are found within the search window of again 0.5 seconds, these detections are bound and considered as a seismic event for further analysis. The final classification of the detected events was done by manual screening in the *pSysmon* software.

6. Results and Discussion

Continuous data availability for the *SeisRockHT* networks and an implemented real-time rockfall detection is still a future challenge. Apart from the realization of real-time data availability, the development of an automated rockfall detection algorithm is indispensable to cope with the amount of continuously gathered data. In the following we will present the results of the terrestrial laser scanning (TLS) terrain monitoring, and the results of two exemplary seismological monitoring periods.

6.1 TLS Terrain Monitoring

TLS monitoring delivered rockwall volume differences in between two survey dates. Regular optic rockwall surveys accurately deliver volume differences, but often show shortcomings in the temporal sampling frequency. It cannot be distinguished, if the determined volume difference was the consequence of a single rockfall event, or a series of adjacent and/or subsequent rockfall events (Barlow et al. (2012)). Consequently, TLS monitoring provided no information about single rockfall events, but accurately determined rockfall release zones and total rockfall volume.

Sonnblick

The TLS surveys were performed on an annual basis in August/September. During the four-year TLS monitoring period (2015-2018) a total number of 71 rockfall release zones with volumes ranging from 1.4 to 584.3 m^3 were detected. However, we defined a volume threshold of 10 m^3 for the main rockfall release zones (MRRZs) of the Sonnblick north-face ($n = 25$; Table 6.1). This cut-off is based on the assumption that the MRRZs were not the result of a quasi-continuous eroding process, but were produced by single rockfall events which could be detected by the seismological network.

Release Zone	**Volume** [m^3]	**Altitude** [m a.s.l.]	**Slope** [°]	**Az** [°]	**FD** [m]	**Survey Period**
1	584.3	2796	67	13	3.5	2015-2016
2	122.7	2775	82	30	3.9	2015-2016
3	118.0	2705	88	314	3.5	2016-2017
4	89.3	2621	77	45	1.3	2016-2017
5	62.7	2633	77	345	2.2	2016-2017
6	57.4	2953	74	32	2.7	2017-2018
7	54.9	2848	59	20	3.1	2015-2016
8	53.9	2600	76	45	1.6	2016-2017
9	46.5	2654	82	44	1.9	2015-2016
10	45.5	2612	74	58	1.8	2015-2016
11	45.4	2864	73	3	2.2	2016-2017
12	32.8	2647	47	37	1.5	2015-2016
13	26.6	2770	78	350	1.7	2017-2018
14	26.3	2751	87	226	2.0	2015-2016
15	24.0	2622	84	53	1.3	2015-2016
16	23.1	2827	82	36	1.8	2016-2017
17	16.1	2875	85	40	1.3	2017-2018
18	14.3	2743	84	30	1.4	2015-2016
19	12.6	2768	74	54	1.3	2015-2016
20	12.5	2742	32	101	1.7	2015-2016
21	11.5	2924	54	28	3.5	2016-2017
22	10.9	2787	82	38	1.1	2015-2016
23	10.9	2980	70	24	1.3	2016-2017
24	10.3	2831	13	13	1.3	2016-2017
25	10.3	2916	52	54	1.5	2017-2018

Table 6.1: Key characteristics of detected rockfall release zones with volumes greater than 10 m^3. Altitude is measured from the lower edge of the individual release zones. **Slope** and **Az** denote the mean local slope and azimuth, respectively. **FD** describes the rockfall release zone failure depth. Survey period shows the corresponding years of the annual surveys from which rockfall release zone volumes are determined.

Figure 6.1 shows the visualization of the gathered TLS data with the red spots indicating detected volume differences above 10 m^3. The blue no-data areas within the north-face are, on the one hand, due to occlusion effects caused by the couloirs in the Sonnblick north-face, and on the other, by glaciers at the north-face foot which did not reflect the TLS signal. The majority of the detected MRRZs, 19 out of 25, is located in the lower half of the Sonnblick north-face (Figure 6.1). Three of the MRRZs exceeded 100 m^3, while five MRRZs ranged between 50 and 100 m^3. The three largest MRRZs on the Sonnblick north-face are found as well in the lower half of the rock-face. The largest MRRZ with a volume of 584.3 m^3 (Figure 6.1) was identified in the survey period 2015-2016 (Table 6.1) and is located above a glacier in a rather steep (∼70°) part of the central rock face. The altitude of the lower edge of the largest MRRZ is 2796 m a.s.l.. The potential rockfall path features a ∼100 meter vertical drop, likely causing sharp seismic impacts of the rockfall fragments, before running out over the glacier. The second largest MRRZ (122.7 m^3) was detected during the same survey period, 2015-2016, and shows similar slope characteristics as the largest detected MRRZ. The third largest MRRZ (118 m^3) was detected at the slope foot right at the current glacier margin. Local terrain characteristics suggest a toppling and sliding of detached rocks over the glacier.

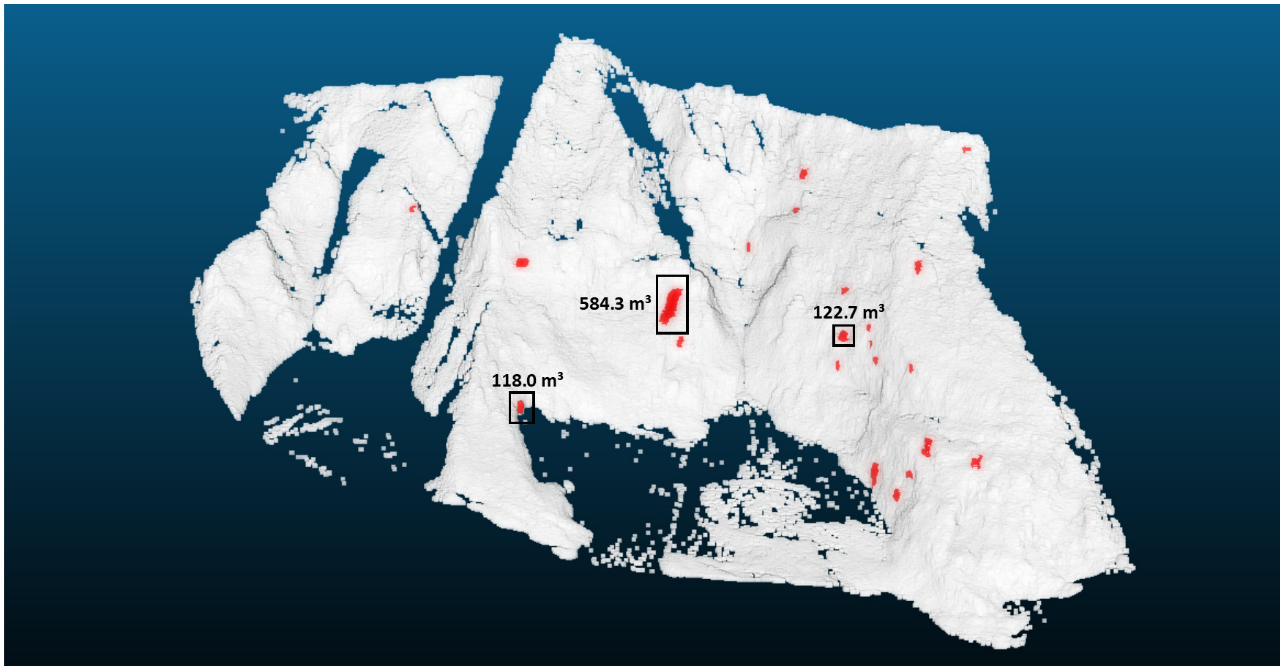

Figure 6.1: Rockfall release zones with volumes greater than 10 m^3 detected during four years (2015-2018) of TLS monitoring at the Sonnblick north-face. The blue, no-data areas within the north-face are due to occlusion effects mainly by the dominant north-face couloirs, as well as by glaciers at the foot of the north-face. 19 out of the 25 identified rockfall release zones are located in the bottom half of the rock face. The three largest rockfall release zones are indicated.

Figure 6.2 shows the MRRZ altitude kernel density estimation (KDE). The KDE is a non-parametric way to estimate the probability density function of a random variable. Unlike a histogram, a KDE represents the data distribution with a smooth curve. The MRRZ altitude KDE reveals a dominant rockfall release altitude of 2800 m for the period 2015-2018.

Principally, the lower sections of the Sonnblick north-face are more susceptible to climate change induced processes like glacier thinning, ice-face and permafrost degradation (Fischer et al. (2006), Magnin et al. (2017), Hartmeyer et al. (2020b)), which is a valid explanation for the observed rockfall release zone disparity in altitude. However, the observed rockfall release zone disparity in altitude is potentially also a consequence of the occlusion effects mainly found in the upper half of the Sonnblick north-face.

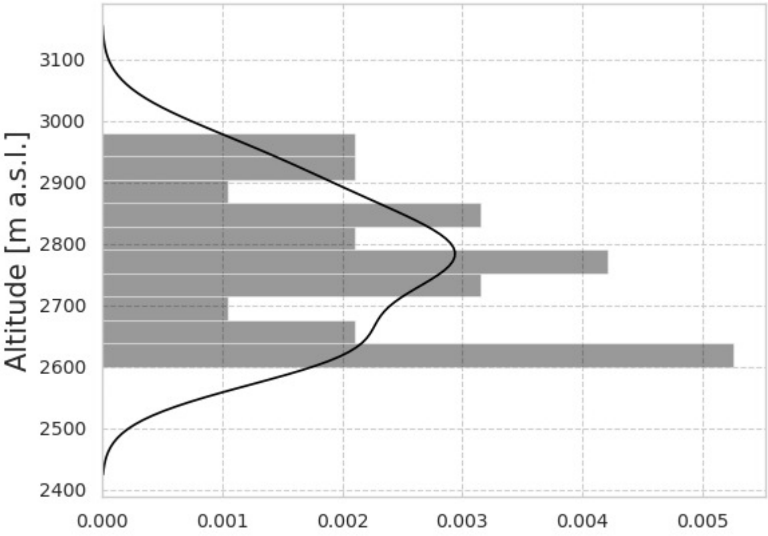

Figure 6.2:
Black line shows the main rockfall release zones (MRRZs) altitudes kernel density estimation (KDE). Gray bars illustrate the MRRZs altitudes histogram. However, x-axis shows KDE probability values. KDE distribution reveals a dominant MRRZ altitude of about 2800 m.

Kitzsteinhorn

The Kitzsteinhorn TLS campaign was a project overarching long-term initiative where the *SeisRockHT* TLS surveys also contributed to the analysed database. The *SeisRockHT* investigation site took up just a minor areal part of the entire TLS campaign. Results of the entire Kitzsteinhorn TLS campaign and the smaller *SeisRockHT* site are briefly summarized in this report. Detailed results, discussion and conclusions can be found in Hartmeyer et al. (2020b) and Hartmeyer et al. (2020a).

During the entire monitoring period (2011-2018) a total number of 678 rockfall release zones were registered ranging from 0.003 to 879.4 m^3. The total rockfall release zone volume equaled 2654.8 m^3. 60% of the rockfall release zone volume detached from less than ten meters above the glacier surface, indicating enhanced rockfall activity in recently deglaciated rockwall sections. Currently, the glacier is wasting down at rates around 0.5 m per year.

Figure 6.3 shows the determined rockfall release zones for the *SeisRockHT* investigation site. A total number of 226 rockfall release zones were registered with a total volume of 1490.2 m^3. Nine rockfall release zones exceeded 10 m^3 and three were larger than 100 m^3. The majority of the rockfall release zones was detected in the lower rockwall sections close to the current glacier surface (Figure 6.4). A mean annual rockwall retreat rate of 10.4 mm a^{-1} was determined for the entire monitoring period (2011-2018). This retreat rate ranks among the highest ever reported for high-alpine cirque headwalls (Benn and Evans (2011), Barr and Spagnolo (2015), Hartmeyer et al. (2020a)), and emphasizes the excellent suitability of the Kitzsteinhorn north-face for seismic rockfall monitoring.

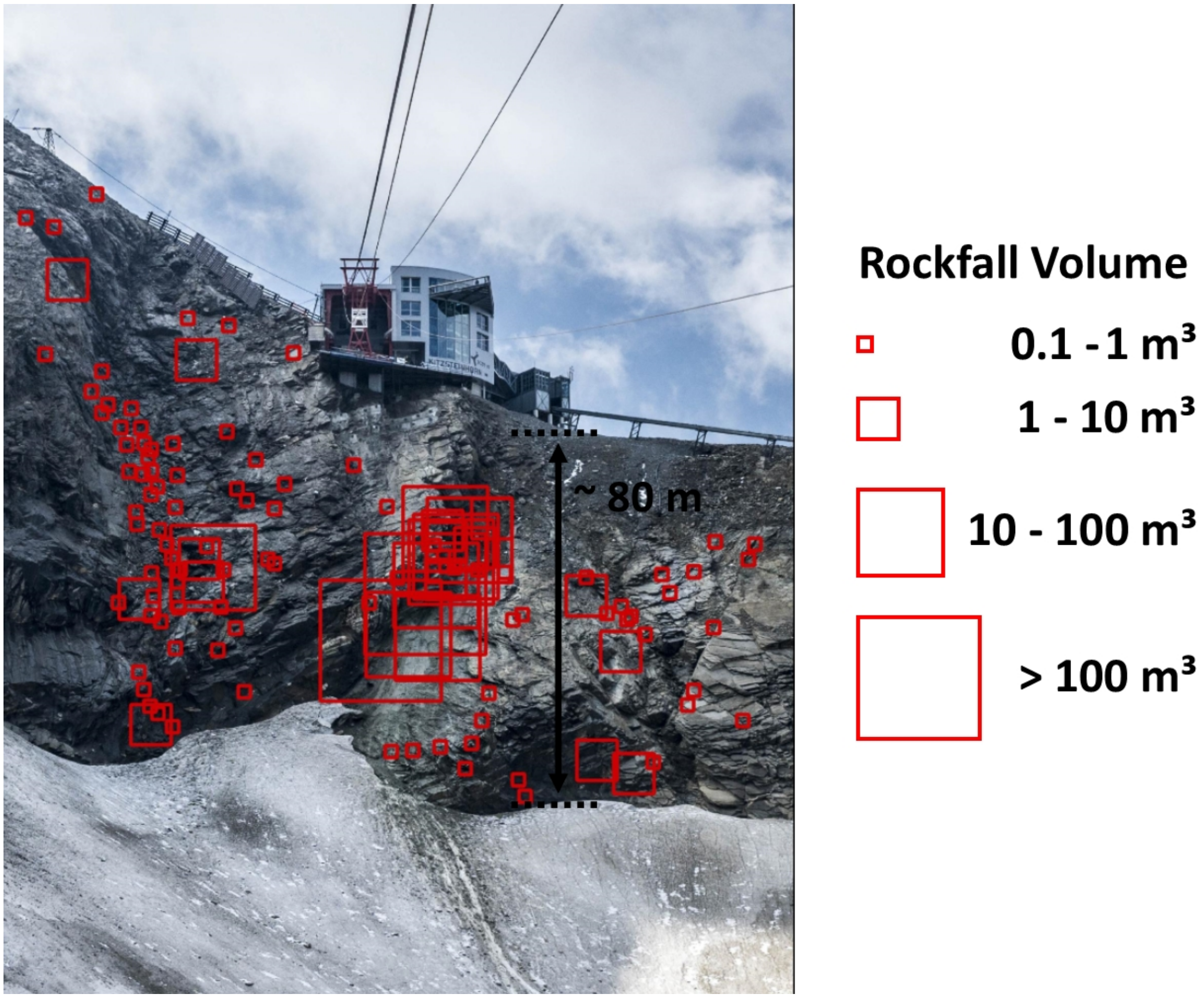

Figure 6.3: Rockfall release zones detected during the entire TLS monitoring period (2011-2018) at the Kitzsteinhorn north-face (n = 226). The majority of the release zones was detected in the lower rockwall sections close to the current glacier surface. A mean annual rockwall retreat rate of 10.4 mm a^{-1} was determined for the entire monitoring period.

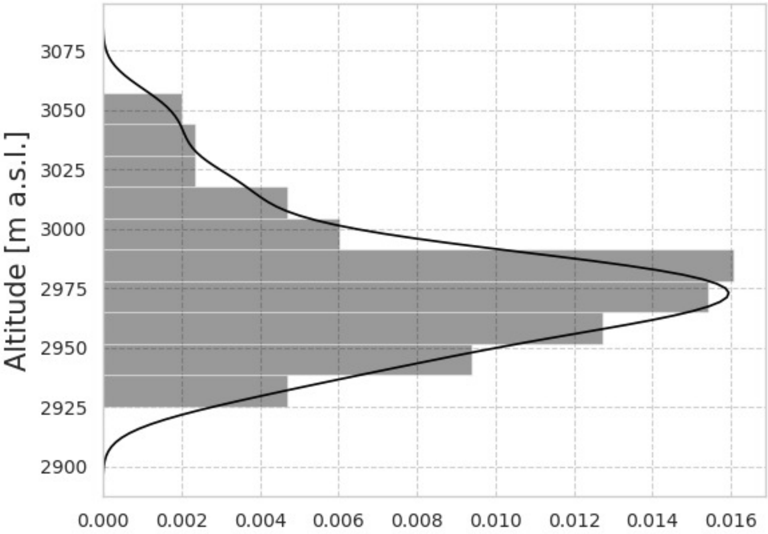

Figure 6.4:
Black line shows the rockfall release zones altitudes kernel density estimation (KDE). Gray bars illustrate the rockfall release zones altitudes histogram. However, x-axis shows KDE probability values. KDE distribution reveals the rockfall release zone majority in the lower rockwall section at about 2970 m a.s.l., adjacent to the current glacier surface.

6.2 Visually Validated Rockfalls

A visual rockfall monitoring was introduced at the Sonnblick observatory (SBO) with the *SeisRockHT* project start in 2015. However, due to reasons discussed in section 4.3, so far just two recorded seismic events could be visually validated as rockfalls. The table 6.2 summarizes the two rockfall events which were also registered by the seismological network. The MIT station in brackets for the rockfall in 2019 indicates that the station was active, but eventually the data was not usable. In summer 2019, the ingress of water into the MIT sensor plug was identified as the source of the spurious data. In the following, we present the available seismic data of all active stations for the two rockfall events. The data is presented in raw waveforms on top of the corresponding spectrograms. Furthermore, we will discuss some key characteristics of the gathered data.

Date	**Time (UTC)**	**Location**	**Volume**	**Observer**	**Active Stations**
2017-08-17	~11:00	Main North Couloir	~0.5-1 m^3	DB	MIT, MOR
2019-09-13	~07:15	North Couloir Pilatuskees	~3 m^3	ND	(MIT), MOR, PIL, SOSA, STO

Table 6.2: Metadata of the two visually validated rockfall events. The rockfall event in 2017 was observed by Daniel Binder (DB), and the one in 2019 by the Sonnblick observatory technician Norbert Daxbacher (ND). The MIT station in brackets indicates spurious data which made the data eventually unusable.

Rockfall Event August 17, 2017

This rockfall was recorded at stations MIT and MOR only. The other stations have not been operating at that time. The data of the three mini-array locations (A,B,C) of the two stations is shown in figure 6.5. The array-locations of the MIT station, however, were at the same position during the time of the recording. The strongest amplitudes were measured at station MOR. They are about one magnitude larger than those recorded at station MIT. The duration of the event is ca. 75 seconds. The frequency content at station MOR is below 100 Hz and at station MIT it is below 50 Hz. A variation of the waveform among the array stations of station MOR is visible. The waveform similarity at station MIT is due to the co-location of the array stations at that time.

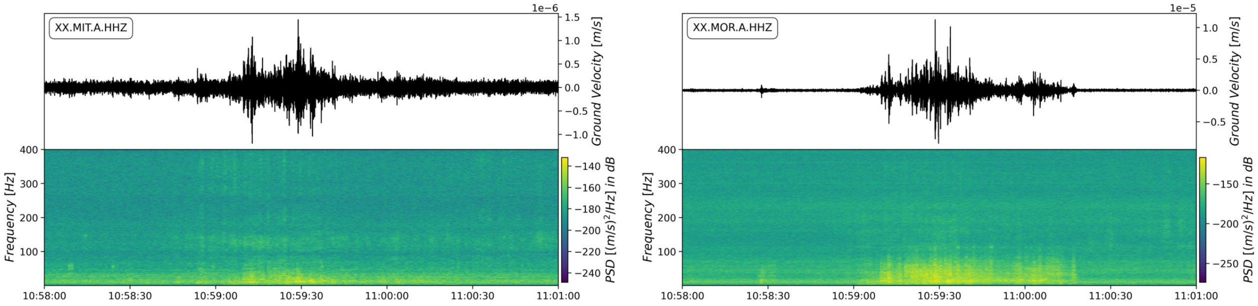

Figure 6.5: The visually observed rockfall from August 17, 2017, recorded at stations MIT and MOR.
...→*Figure continues on the next page.*

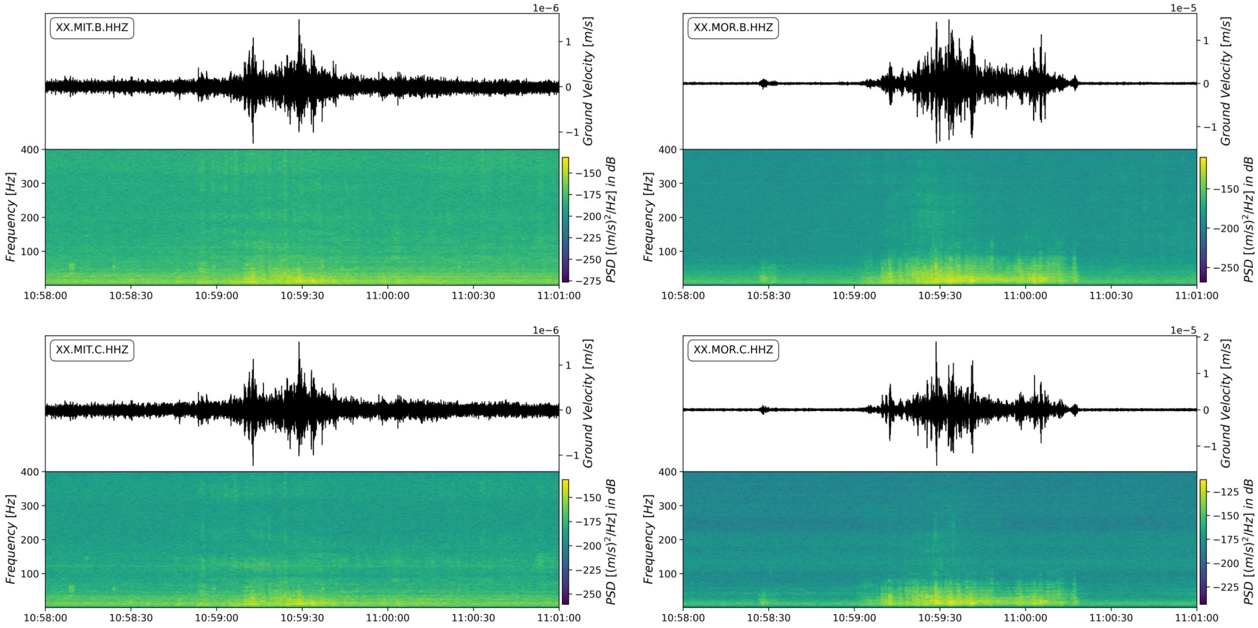

Figure 6.5: The visually observed rockfall from August 17, 2017, recorded at stations MIT and MOR. The data of the three mini-array locations (A,B,C) is shown. The array-locations of station MIT were at the same position during the time of the recording.

Rockfall Event September 13, 2019

This rockfall event has a duration of ca. 120 seconds with a second, impulsive event following at ca. 07:14:44. The amplitudes at stations MOR and PIL are similar. At stations SOSA and STO (see figure 6.6 the seismograms of the event show only small amplitudes. Compared with the rockfall on August 17, 2017, this event featured a broadband frequency content (> 400 Hz).

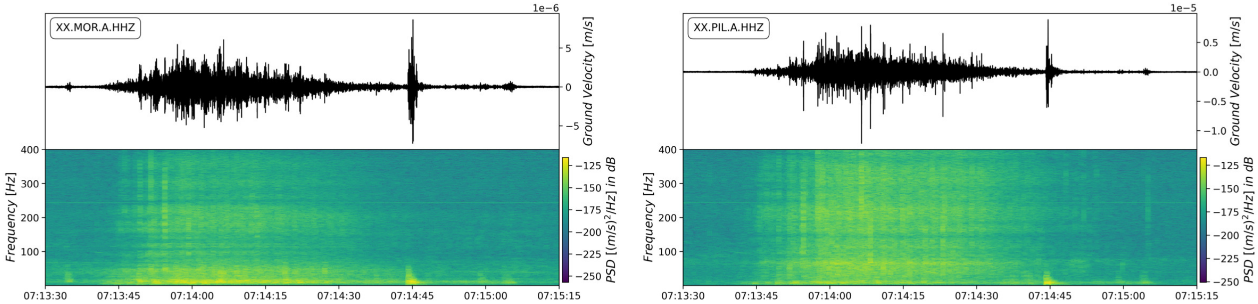

Figure 6.6: The recorded MOR, PIL, STO and SOSA data of the visually observed rockfall from September 13, 2019. ...→*Figure continues on the next page.*

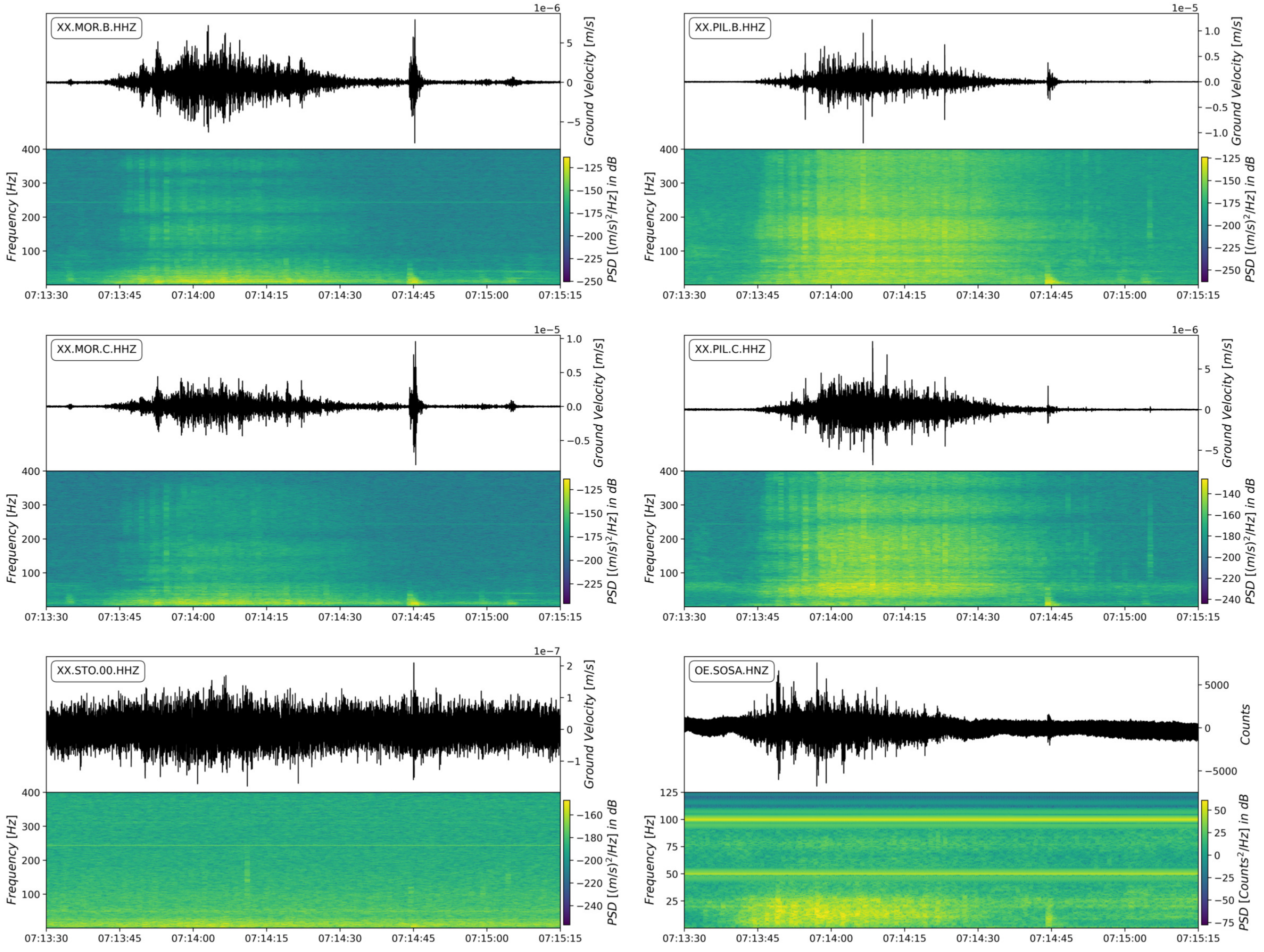

Figure 6.6: The recorded MOR, PIL, STO and SOSA data of the visually observed rockfall from September 13, 2019. While for the mini array stations MOR and PIL every channel (A-C) is shown, just the representative vertical component is shown for the STO and SOSA stations. Due to the SOSA sampling frequency of 250 Hz, the maximum resolvable frequency of the SOSA station is 125 Hz. The prominent 50 and 100 Hz noise is caused by the SOSA power supply by mains. Furthermore, SOSA data is still in [Counts].

6.3 Field Campaign 2017

A *SeisRockHT* field campaign was realized in autumn 2017 to capture the transition period from autumn to winter. During summer 2017 all stations were serviced, and in case technically improved, so that a full operational network was ready in August 2017. Unfortunately, due to an until then unknown software issue with the BeagleBone single board computer of the *Ruwai* data recorder, the MIT station failed just after two weeks (details in section 3.1 - *Routine Operation and System Adaption*). All the other stations delivered data until mid of October, before power shortages due to the lower sun position became more and more an issue for the two stand-alone stations MOR and PIL.

Figure 6.7 illustrates the meteorological data from the Austrian Weather Service stations Kolm Saigurn and Sonnblick throughout the campaign period. The gray background indicates the actual campaign period from August 23 to October 11. Beside regular precipitation events especially in the first half of the shown period, a temperature drop between August 29 to September 5 was observed. The lower temperature level remained throughout the field campaign.

Generally, the seismic data of the field campaign was affected by the ongoing construction work for the new Sonnblick observatory (SBO) cable car. The seismic data gathered during these weeks is presented in the coming sections.

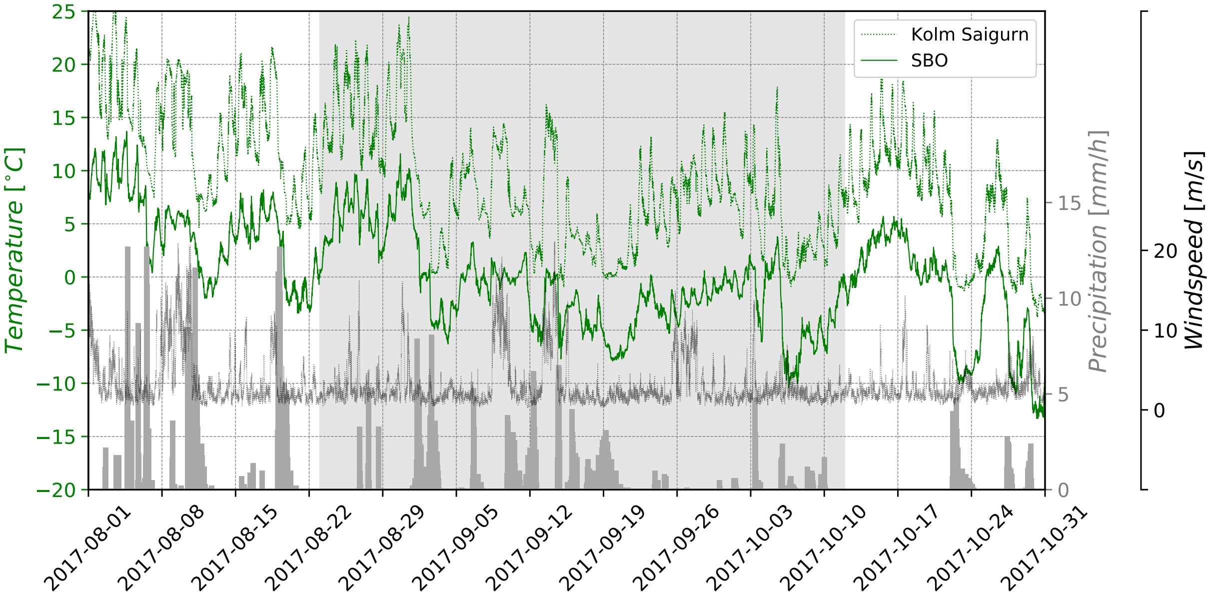

Figure 6.7: Overview of the weather throughout the field campaign 2017. The green lines illustrate the air temperature of the Sonnblick observatory (SBO, 3106 m a.s.l.) and the Kolm Saigurn valley floor (1600 m a.s.l., dashed line). The gray bars indicate the hourly precipitation sums, and the black dotted line the maximum windspeed, both measured at Kolm Saigurn. The gray background marks the field campaign period from August 23 to October 11.

6.3.1 Ambient Seismicity

Spectrograms illustrate the temporal evolution of the signal frequency content of recorded seismic data. Single seismic events are imaged as temporarily sharp vertical stripes of elevated power spectral density (PSD) values, whereas the vertical extent of the event covers the involved frequency range. While earthquakes feature a rather low frequency range, local events like rockfalls feature generally higher frequencies (compare Figure 6.25). Beside distinct seismic events, spectrograms reveal the ambient seismicity over the entire spectrogram time window. All calculated spectrograms for the campaign 2017 period can be found in Appendix B.

Figure 6.8 shows the median spectrograms of the vertical component of all Sonnblick stations for two distinct weeks. The upper spectrogram shows a week with elevated seismicity at the end of August featuring a diurnal pattern. The lower spectrogram represents a more quiet period with lower signal content in the end of September. The two vertical black lines in the lower median spectrogram enclose the daytime 05:00-15:00 UTC (local time: 07:00-17:00 CET) on Wednesday, September 20. The elevated PSD values around 4.5 Hz were also present for the other days of the working week. The arrow in between the two vertical lines points at an interruption from 10:00-10:30 UTC (local time: 12:00-12:30 CET) of the observed elevated PSDs. This pattern was identified in every single spectrogram of all active stations. No correlation between the available environmental data and the described spectrogram features could be identified. Consequently, we propose the SBO cable car construction work with the daily lunch break as the source of the observed ambient seismicity pattern. This 'working week'-pattern is present in all median spectrograms, except for those featuring elevated ambient seismicity with a diurnal pattern as shown in Figure 6.9.

The upper median spectrogram in Figure 6.8 covers the seismically more active week August 21-27, and features a diurnal pattern. The sheltered STO site at the Kolm Saigurn valley floor turned out to be the main contributor of this diurnal ambient seismicity pattern. Figure 6.9 shows STO spectrograms for two consecutive weeks with the most prominent 24 hours cyclicity of ambient seismicity throughout the campaign. Similar ambient seismicity characteristics were observed for all calculated STO spectrograms except for the period September 20-30. This period was characterized by increasing air temperatures and minor precipitation. However, the pronounced 24 hours cyclicity was most evident for the presented two weeks (21.08.-03.09.). The upper STO spectrogram in Figure 6.9 features two vertical black lines which mark the seismicity maxima around 14:00 UTC (local time: 16:00 CET) of the 24 hours cycle between Thursday, 24.08., and Friday, 25.08.. The cyclic ambient seismicity persisted throughout the two weeks with a decaying phase during Sunday, 03.09..

The air temperature (white line) and the hourly precipitation sums (gray bars) of the Kolm Saigurn weather station are shown as well in Figure 6.9. Beside the meteorological data, data of the Bucheben discharge gauge (black dashed line), run by the Hydrographic Service of Salzburg (`https://www.salzburg.gv.at/`), is also available for the period. The Bucheben discharge gauge monitors the 'Hüttwinklache' which rises in the Kolm Saigurn basin. The Bucheben discharge gauging site is about ten kilometers downstream of the STO station.

The precipitation and discharge data did not show any cyclic behavior throughout the considered period, solely, the temperature showed its natural 24 hours cycle with its maximum around 12:00 UTC (local time: 14:00 CET). Generally, ambient seismicity peaked in the afternoon lagging the maximum air temperature a few hours. The elevated ambient seismicity decayed during the night and morning hours, but eventually was clearly present throughout the entire period. Furthermore, ambient seismicity amplitude and cyclicity decayed with falling air temperatures in the end of the second week (Figure 6.9). These observations suggest discharge of a local creek driven by snow and ice melt as a potential cause of the observed ambient seismicity cyclicity. In the vicintiy of the STO station several creeks are coming down the mountain and feed the Hüttwinklache. However, as already stated before, the available discharge of the 10 kilometers distant Bucheben gauging site did not show any 24 hours cyclicity. Nevertheless, this might be due to masking of a potentially cyclic local discharge by the other contributors of the discharge measured at the Bucheben gauging site.

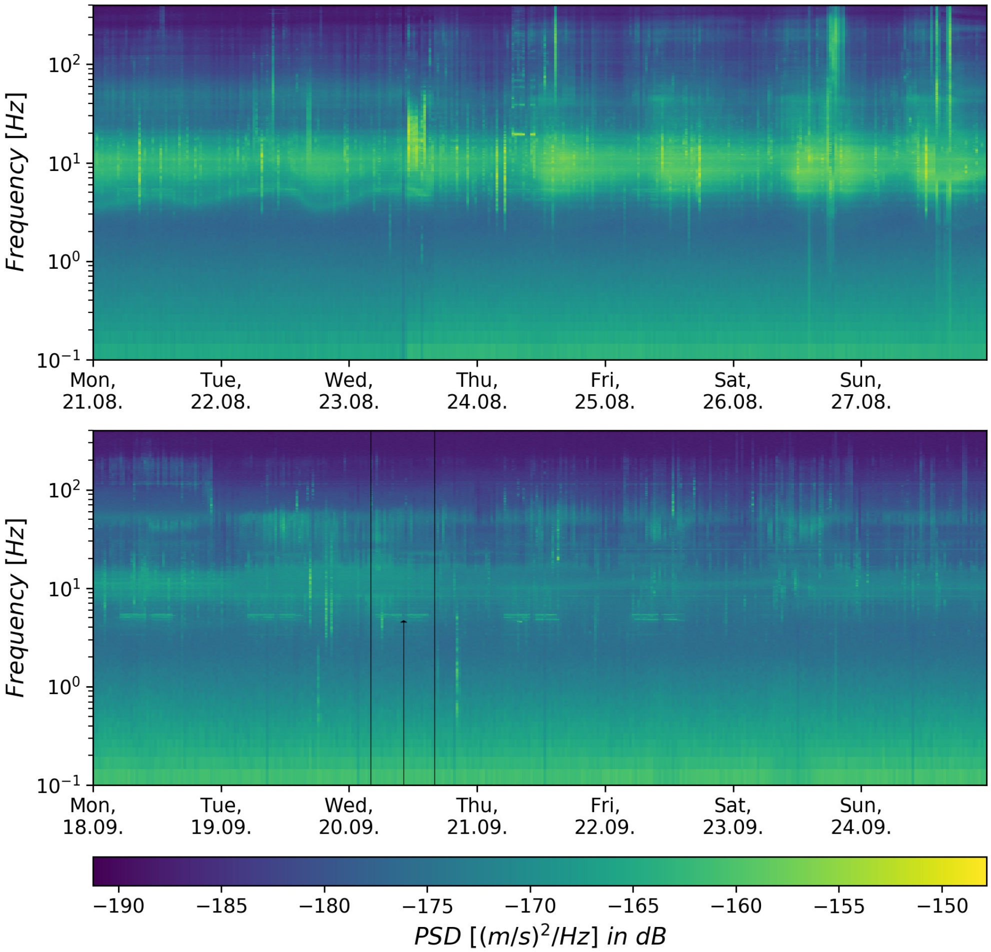

Figure 6.8: Median spectrograms of two weeks calculated from the vertical component of all Sonnblick stations. The upper spectrogram shows a week with elevated seismicity, whereas the lower spectrogram represents a more quiet period with lower signal content. In the upper spectrogram a diurnal ambient seismicity pattern is visible. The diurnal ambient seismicity cyclicity originates from the STO station. In the lower spectrogram the ongoing construction work for the new SBO cable car is clearly visible at a frequency of about 4.5 Hz. The two vertical black lines indicate the working hours (05-15:00 UTC, or 07-17:00 CET) of Wednesday, 20.09.. The arrow points at the lunch break where a gap of the enhanced seismicity is visible. Every day of the working week showed a similar signature, and accordingly the weekend did not.

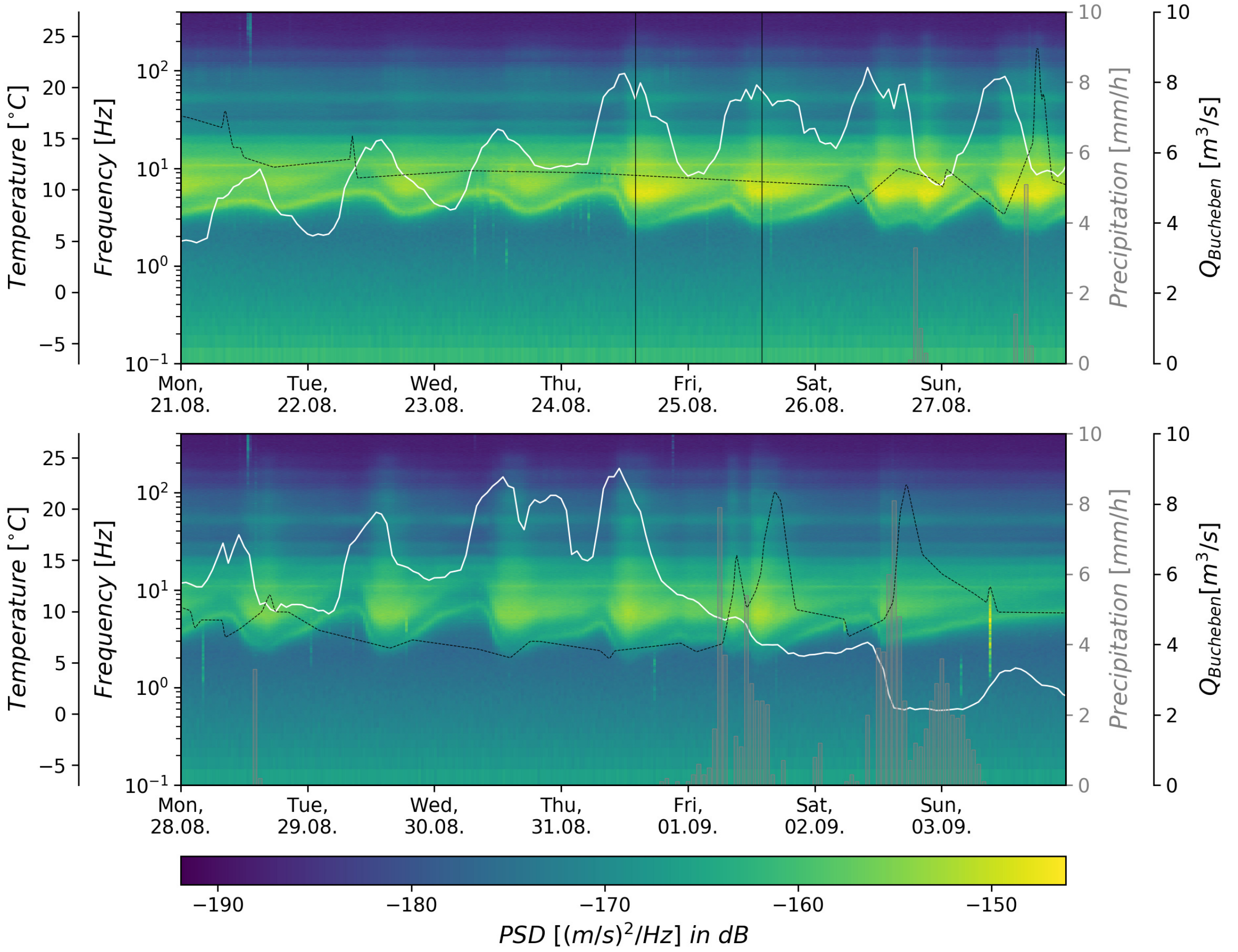

Figure 6.9: Spectrograms of two weeks for the vertical component of the STO station. Both weeks show a cyclic ambient seismicity pattern, whereas one cycle is about 24 hours with maxima located around 14:00 UTC. An exemplary cycle is marked by the two vertical black lines in the upper spectrogram. The vertical lines mark 14:00 UTC on the 24.08. and the 25.08.. The line plots and gray bars show complementary data (white line - air temperature Kolm Saigurn, black dashed line - discharge gauging site Bucheben, gray bars - hourly precipitation sums Kolm Saigurn).

Through the available SBO cable car construction reports it is known that throughout the campaign period anchor drilling work for the new cable car's top station was done. The anchor drilling was also carried on over some weekends. Figure 6.10 shows the STO (top) and OBS spectrograms of the week 28.08. - 03.09.. While the STO spectrogram features the already discussed ambient seismicity cyclicity, the spectrogram of the OBS station situated right at the new cable car's top station does not. The OBS spectrogram shows sharp horizontal features which are rather characteristic for anchor drilling work than a diurnally varying frequency content.

Figure 6.11 shows STO spectrograms for a two-week period in the end of Spetember and beginning of October. The first week is rather quiet with the already discussed 'working week'-pattern. The second half of the week featured a distinct diurnal air temperature variation with an increase in ambient seismicity cyclicity during the weekend. The second week in Figure 6.11 featured a rain event on October 3 which is followed by a clear short-term ambient seismicity and river discharge increase. The frequency characteristics of the short-term ambient seismicity increase strongly recall the elevated ambient seismicity characteristics of Figure 6.9. Based on all the available complementary data, we eventually suggest the discharge of a local, melt-driven creek as the source of the diurnal ambient seismicity variation observed at the STO monitoring station (Figure 6.9).

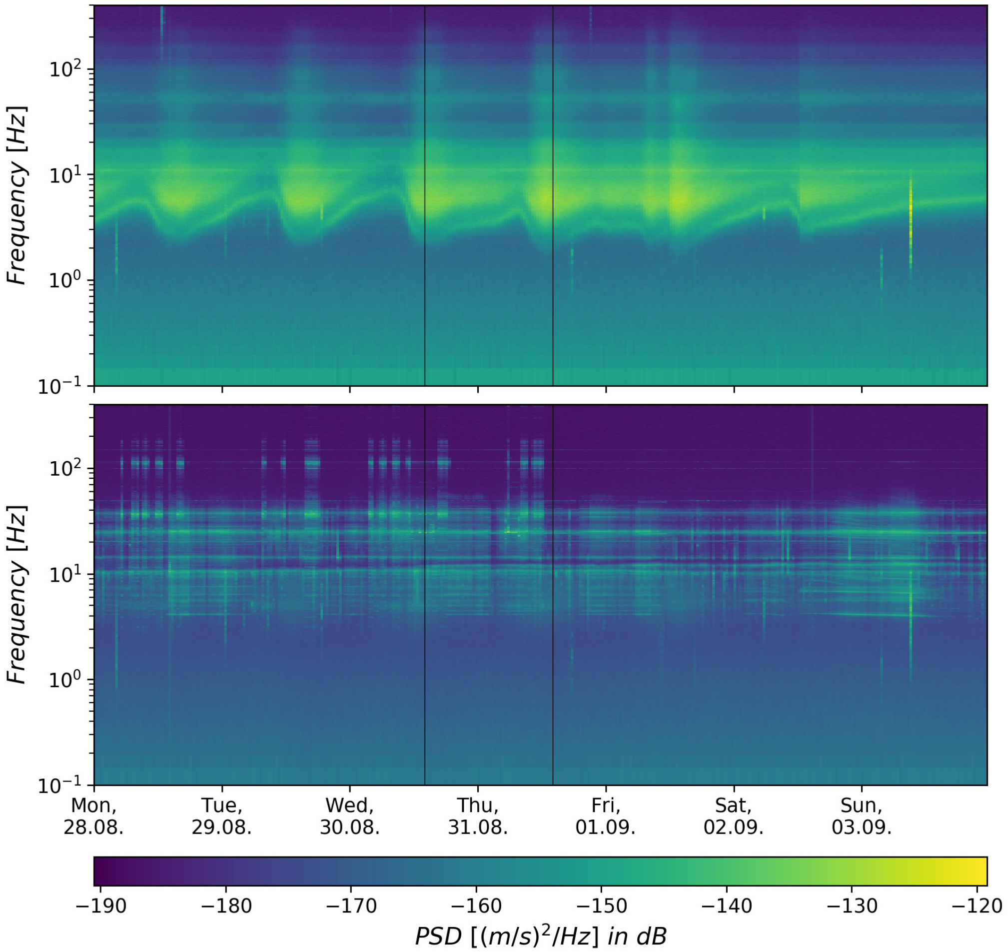

Figure 6.10: Spectrograms of the STO (top) and the OBS station for the seismically active week 28.08. - 03.09.. The vertical lines mark the exemplary 24 hours cycle 24.08. to 25.08. at 14:00 UTC, respectively. No ambient seismicity cylicity was observed for the OBS station data.

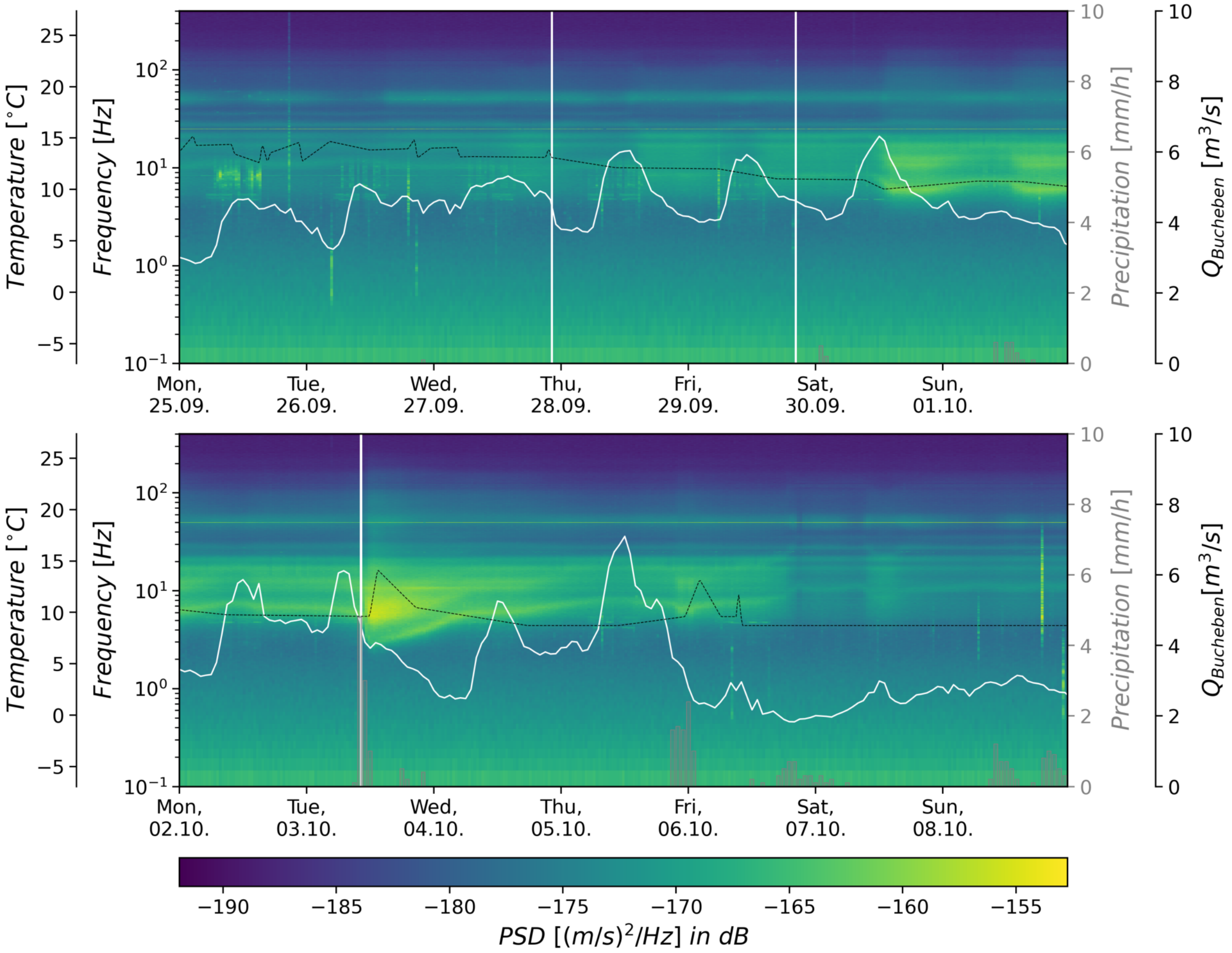

Figure 6.11: STO spectrograms of the last week of September and first week of October. The white vertical stripes indicate data gaps. The line plots and gray bars show complementary data (white line - air temperature Kolm Saigurn, black dashed line - discharge gauging site Bucheben, gray bars - hourly precipitation sums Kolm Saigurn). The rain event on October 3 is followed by an ambient seimicity and river discharge increase.

6.3.2 Detected Events

An automated STA/LTA event detection and event binding (see section 5.2) was applied for the campaign 2017 data set. Detected events with a signal to noise ratio above 20 were then manually categorized. In total 435 events were categorized into 6 different event types, and 101 events were categorized as *Noise* (see table 6.3) which were ignored for further analysis. The complete event catalog of the field campaign in 2017 can be found in Appendix C. In the following exemplary examples of the event catalog are presented.

Event type	**Number of Events**	**Description**
Anthropogenic	3	Events related to human activities like air traffic or cable car operation.
Earthquake	9	Events related to well-known tectonic earthquakes.
Lightning	10	Events related to lightning strikes.
Rockfall Candidate Long	2	Events with a signature suggesting a long-term, flow-like process.
Rockfall Candidate Short	361	Events with a signature suggesting local sources related to rockfalls.
Tremor LF	50	Events with mainly low-frequency (< 50 Hz) signal content with an emerging onset and a duration of several seconds.
Noise	101	Detections with no clear correlation and waveform similarity among the individual stations.

Table 6.3: The classified event types with the associated total number of events detected during the field campaign in 2017.

Rockfall Candidate Short

The *Rockfall Candidate Short* (*RC Short*) events show a clearly visible, impulsive onset. The duration is usually between 1 and 2 seconds. A strong amplitude decay between the individual stations is visible with the largest amplitudes recorded at station MOR or PIL. The presented *RC Short* example has the event catalog ID 19124.

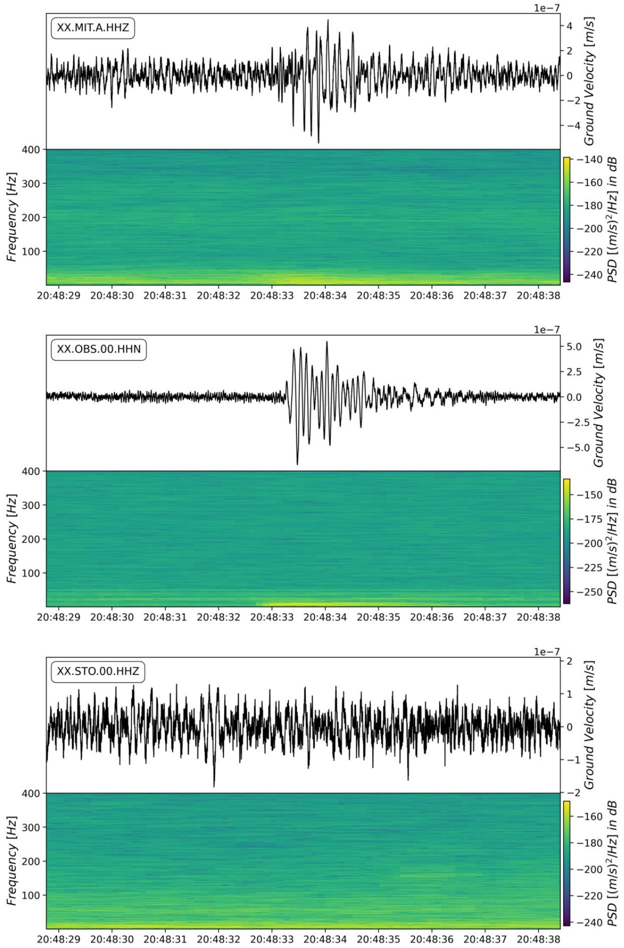

Figure 6.12: A *Rockfall Candidate Short* event recorded in the evening of August 24 (event id 19124).

Rockfall Candidate Long

Rockfall Candidate Long (*RC Long*) events have a long duration of several tens of seconds. The frequency is below 200 Hz with variation between the individual stations. The strongest amplitudes are usually recorded at station MOR. The event has an emerging onset and individual "sub-events" can be seen. There is no clear correlation of individual phases of sub-events among the stations. Also a striking difference of the amplitude envelope is visible between stations MOR and MIT or PIL. At station MOR a concentration of energy is visible at the end of the event, whereas, the strongest amplitudes at station MIT and PIL can be observed in the middle of the event. The presented *RC Long* example has the event catalog ID 19150.

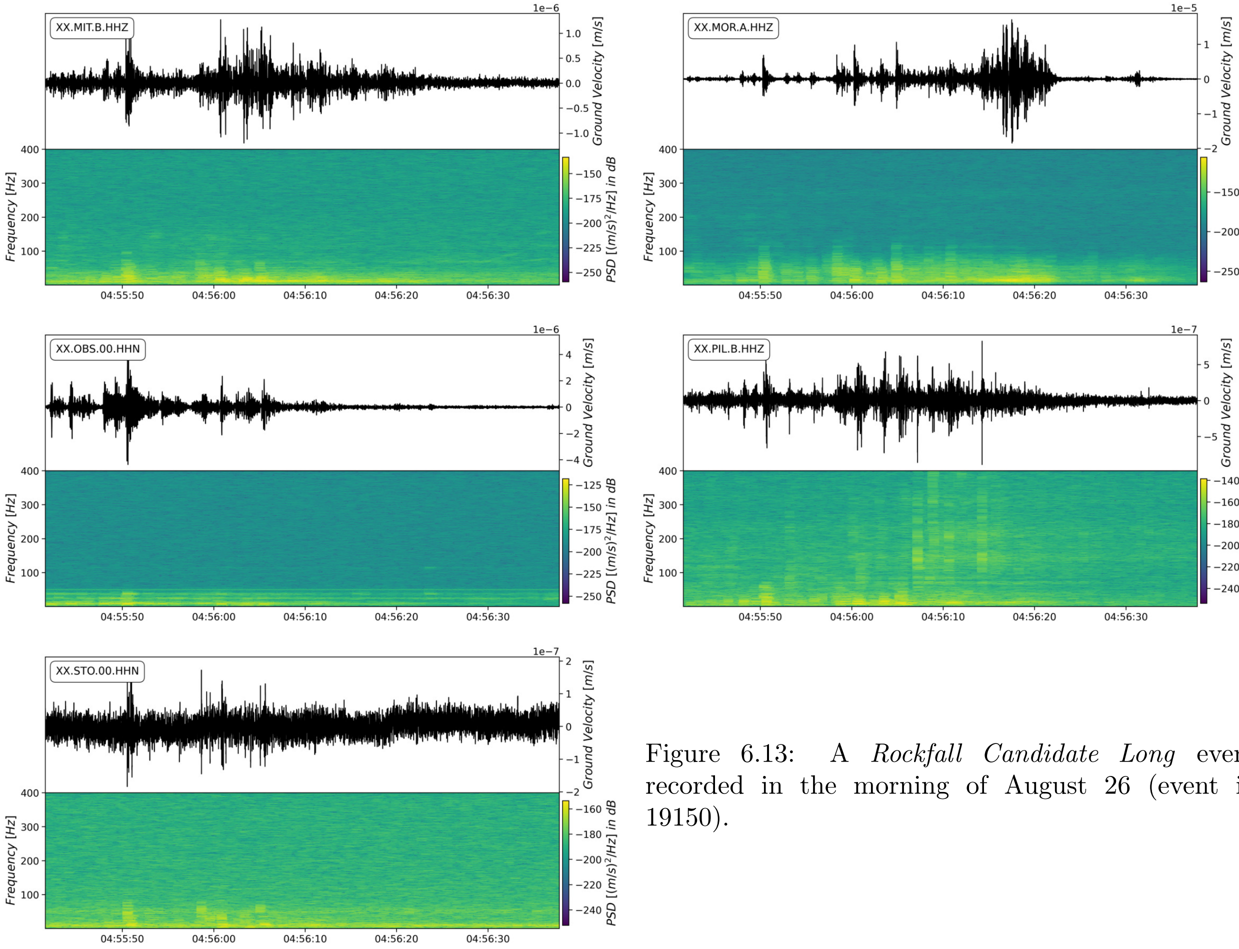

Figure 6.13: A *Rockfall Candidate Long* event recorded in the morning of August 26 (event id 19150).

Tremor LF

Tremor LF are events with a duration of several seconds which are usually visible only at station MOR and PIL. They have an emerging onset and show a low frequency content (< 100 Hz). There is no clear correlation of individual phases among the stations. The presented *Tremor LF* example has the event catalog ID 19173.

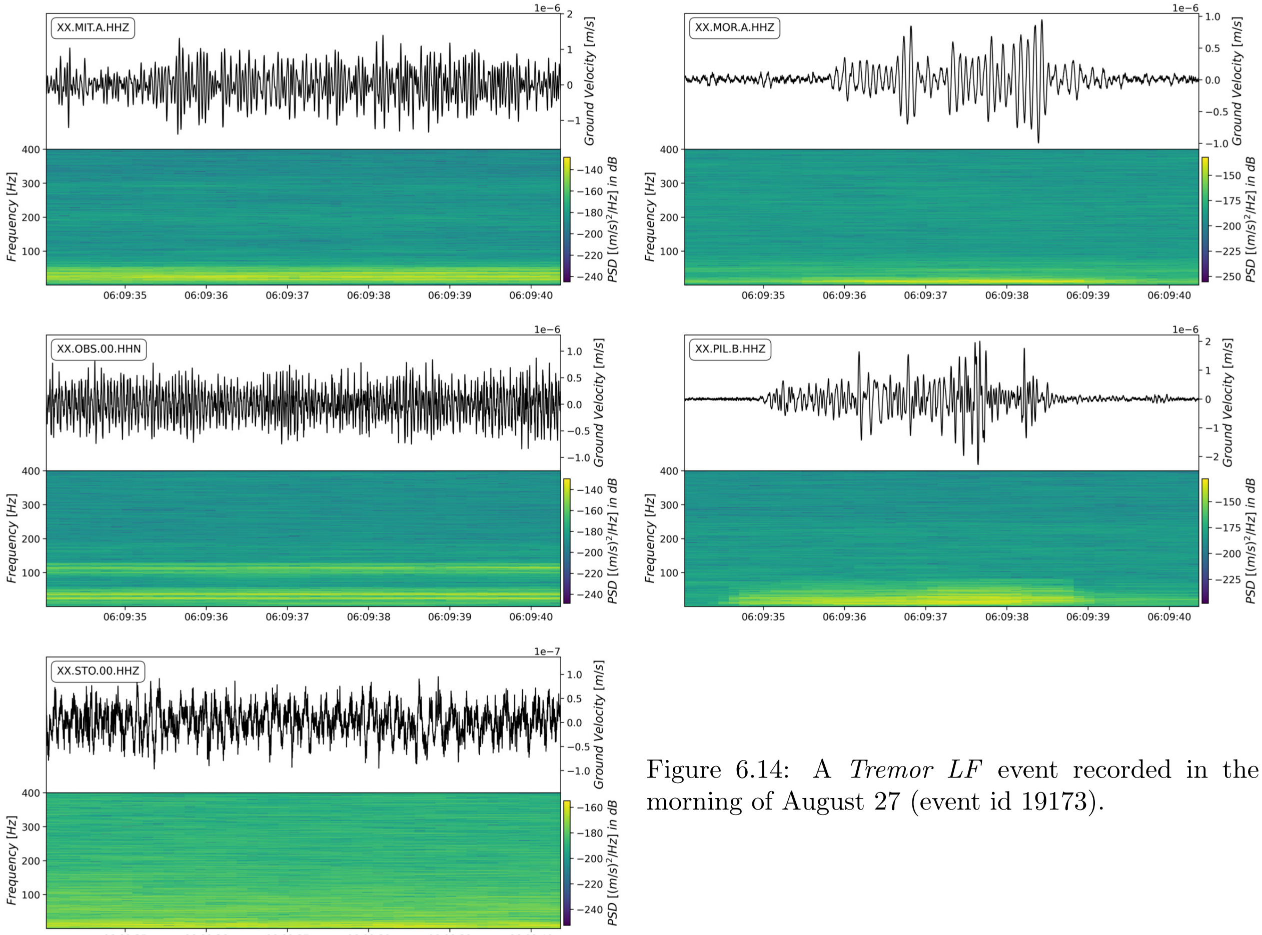

Figure 6.14: A *Tremor LF* event recorded in the morning of August 27 (event id 19173).

6.3.3 Temporal Event Distribution and Correlation with Complementary Data

Figure 6.15 shows the cumulated number of events for each of the six event types, and the complementary meteorological data. The top plot presents the cumulated number of the abundant *RC Short* events with the complementary data. The occurrence rate of the *RC Short* events exhibited a distinct drop around September 6. Before September 6, a *RC Short* occurrence rate of about 20 events per day was observed, after a substantial air temperature drop in the week August 29 to September 5, however, the occurrence rate abruptly dropped to about 7 events per day.

The other striking event type is the *Tremor LF* type which showed maximum occurrence rates during the precipitation event in the night of August 26. Higher occurrence rates were then retained until after the maximum precipitation event on September 2, also throughout the precipitation-less period August 29-31. This precipitation-less period was characterized by rising air temperatures.

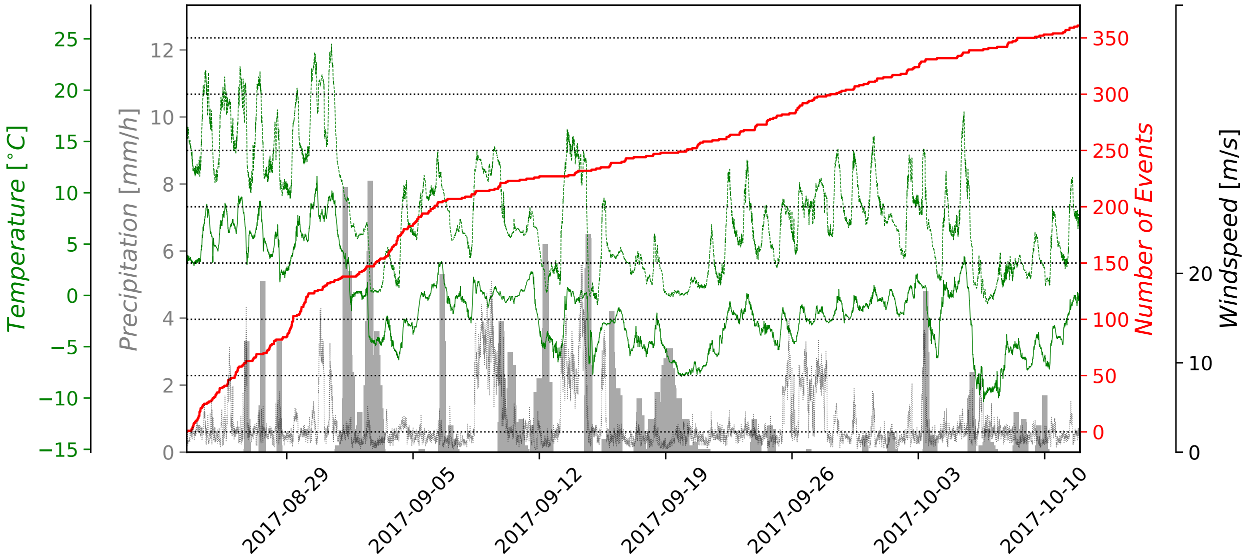

Figure 6.15: Figure shows the cumulated number of events of the six event types versus the complementary meteorological data. The first plot shows the cumulated number just of the abundant *Rockfall Candidate Short* events. The *Rockfall Candidate Short* events clearly exhibited a lower occurrence rate after the apparent temperature drop in week August 29 to September 5. ...→*Figure continues on the next page.*

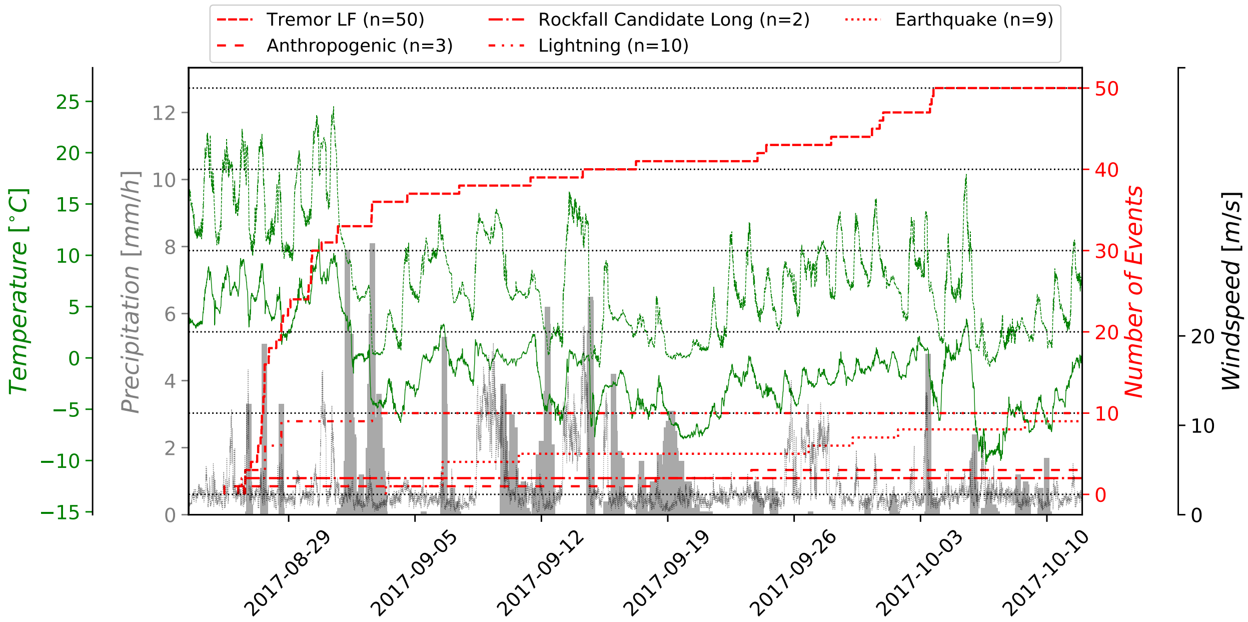

Figure 6.15: ...The second plot shows the number of events for the remaining event types. The *Tremor LF* event type featured maximum occurrence rates during the precipitation event in the night of August 26. The meteorolgical data is from the SBO (air temperature) and the Kolm Saigurn (air temperature (dashed line), precipitation, windspeed) stations.

Figure 6.16 shows the calculated degree day sum (DDS) versus the cumulated number of *RC Short* events. DDS and number of events time series were normalized for a better comparison. DDS was calculated for each temperature time series, whereas SBO and Kolm Saigurn air temperature data, as well as temperature data from a shallow borehole in the upper Sonnblick north face (3090 m a.s.l.) were employed. DDS was calculated as the cumulative sums of the daily mean temperatures. Kolm Saigurn air temperatures did not show below zero temperatures, hence, the calculated DDS values are equivalent with the positive degree day sum (PDD), where just positive daily means are summed up. PDD is often used in glaciology for the parametrization of ice melt (e.g. Hock (2003)). All the other temperature time series exhibited negative daily mean temperatures which resulted in decreasing DDS values, especially after September 6.

Figure 6.16 reveals a clear correlation between the Kolm Saigurn air temperature DDS and the occurrence rate of *RC short* events. However, this correlation might be due to melt of a steep ice face (height ∼10 m) at the terminus of the debris covered Pilatuskees. The ice face is situated between the MOR and the PIL stations (Figure 6.17). As observed during field work, boulders are regularly tumbling down the ice face and collide with other boulders at the foot of the ice face. This process is enhanced by melting of the ice face during periods of higher air temperatures and solar radiation. Eventually, at this stage we do not know to what extent these 'ice face events' are responsible for the observed temperature correlation of the *RC short* events. This has to be investigated in future work.

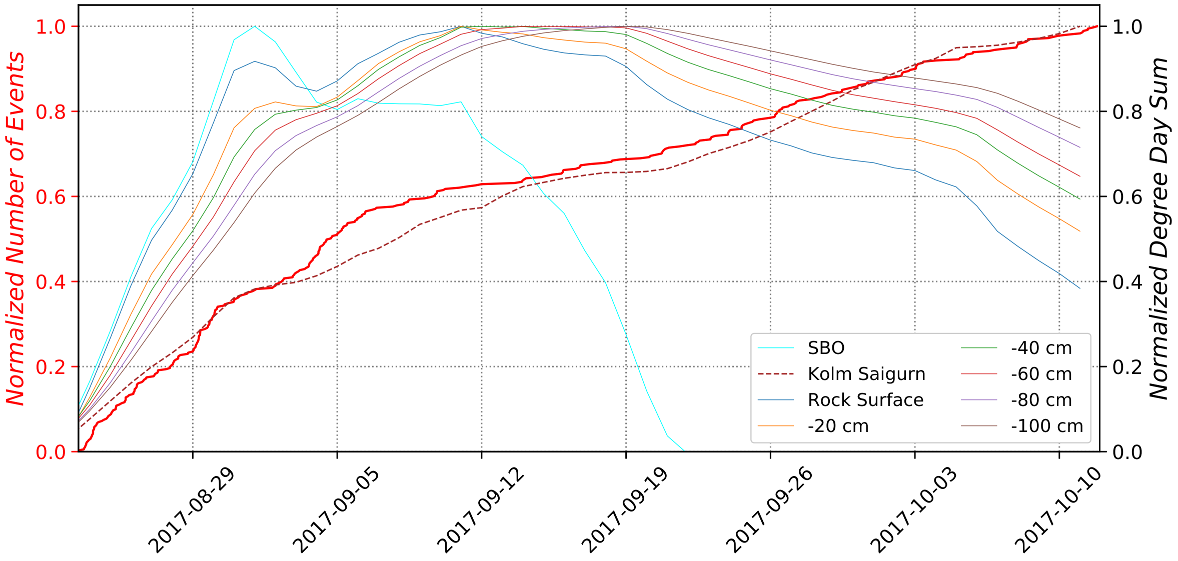

Figure 6.16: The normalized cumulated number of the *Rockfall Candidate Short* events (red line) plotted with normalized degree day sums of air and borehole temperatures. A clear correlation between the number of *Rockfall Candidate Short* events and the air temperature measured in the Kolm Saigurn valley floor is visible.

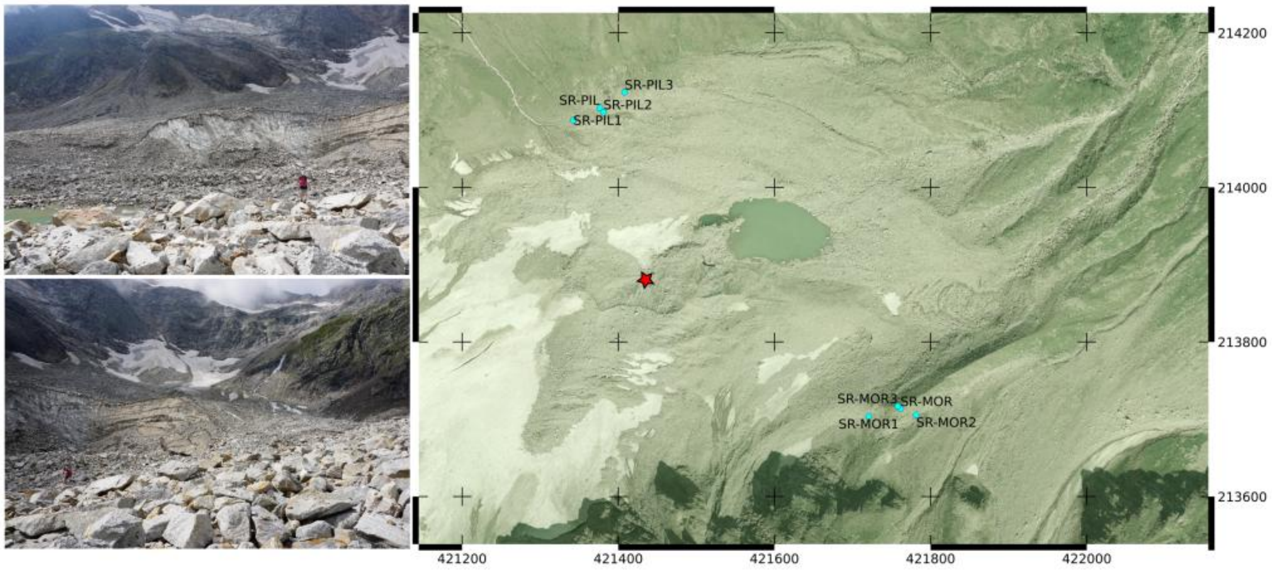

Figure 6.17: The left photos show the ice face at the terminus of the debris covered Pilatuskees. The red star in the right map indicates a potential impact zone of tumbling down rocks at the foot of the ice face. The locations of the PIL (SR-PIL) and MOR (SR-MOR) stations are shown. The individual sensor locations of the two mini array stations are shown as well (SR-PIL1-3, SR-MOR1-3).(Coordinate System: MGI/Austria GK 31, EPSG:31258)

6.4 Extreme Weather Event 2018

In the period October 27-30, 2018, an extreme weather event hit the Alps-Adriatic region. Heavy precipitation along with high winds and occasional thunderstorms caused floodings, mud flows and windthrows in several regions, also in the Sonnblick region. The Austrian Weather Service station at the valley floor of Kolm Saigurn (1600 m a.s.l.) measured 320 mm of total precipitation and maximum wind speeds of 29 m/s within this period (Figure 6.18).

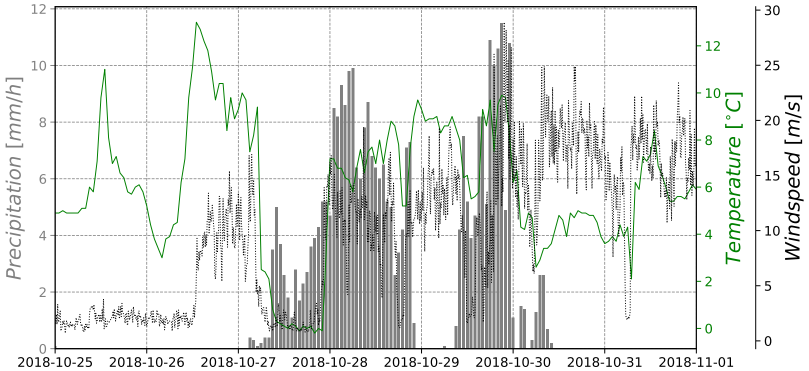

Figure 6.18: The extreme weather event in October 2018 caused floodings, mud flows and windthrows in the Alps-Adriatic region. During this event a total sum of 320 mm of precipitation, as well as maximum wind speeds of 29 m/s were recorded at the valley floor of Kolm Saigurn.

Despite the clear diurnal temperature profile at the Kolm Saigurn valley floor, generally, valley and summit air temperatures showed a steadily uprising trend before the extreme weather event. The Sonnblick observatory (SBO) air temperatures were steadily rising towards zero degrees after a rather short cooling event on October 25. Beside the meteorological data, data of the Bucheben discharge gauge run by the Hydrographic Service of Salzburg (`https://www.salzburg.gv.at/`) is available for the period. The Bucheben discharge gauge monitors the 'Hüttwinklache' which rises in the Kolm Saigurn basin. The Bucheben discharge gauge is about ten kilometers downstream of the Austrian Weather Service station Kolm Saigurn. Furthermore, electric field strength data of the SBO and detected lightnings by the Austria-wide ALDIS network (`https://www.aldis.at/`) are available as complementary data. Figure 6.19 shows the compiled complementary data for the period of the extreme weather event. The lag of the discharge peaks in relation to the two precipitation peaks is likely due to the 10 km distance between the two monitoring stations. However, the lags vary significantly. While the lag of the first event is 5 hours 45 min, which corresponds to a flood propagation velocity of about 0.5 m/s, the second main discharge peak showed a lag of just 1.5 hours, or a flood propagation velocity of 1.8 m/s. Soil moisture saturation and the efficiency of rain water routing into the river, as well as the precipitation intensity are potential drivers for this significant difference of flood propagation velocities. The lower graph shows the electric field strength data of the SBO which shows clearly the electrostatic charging of the atmosphere before the first lightnings discharge. The constant electric field strength values of zero in the second half of the time period is potentially due to icing of the sensor at the Sonnblick summit.

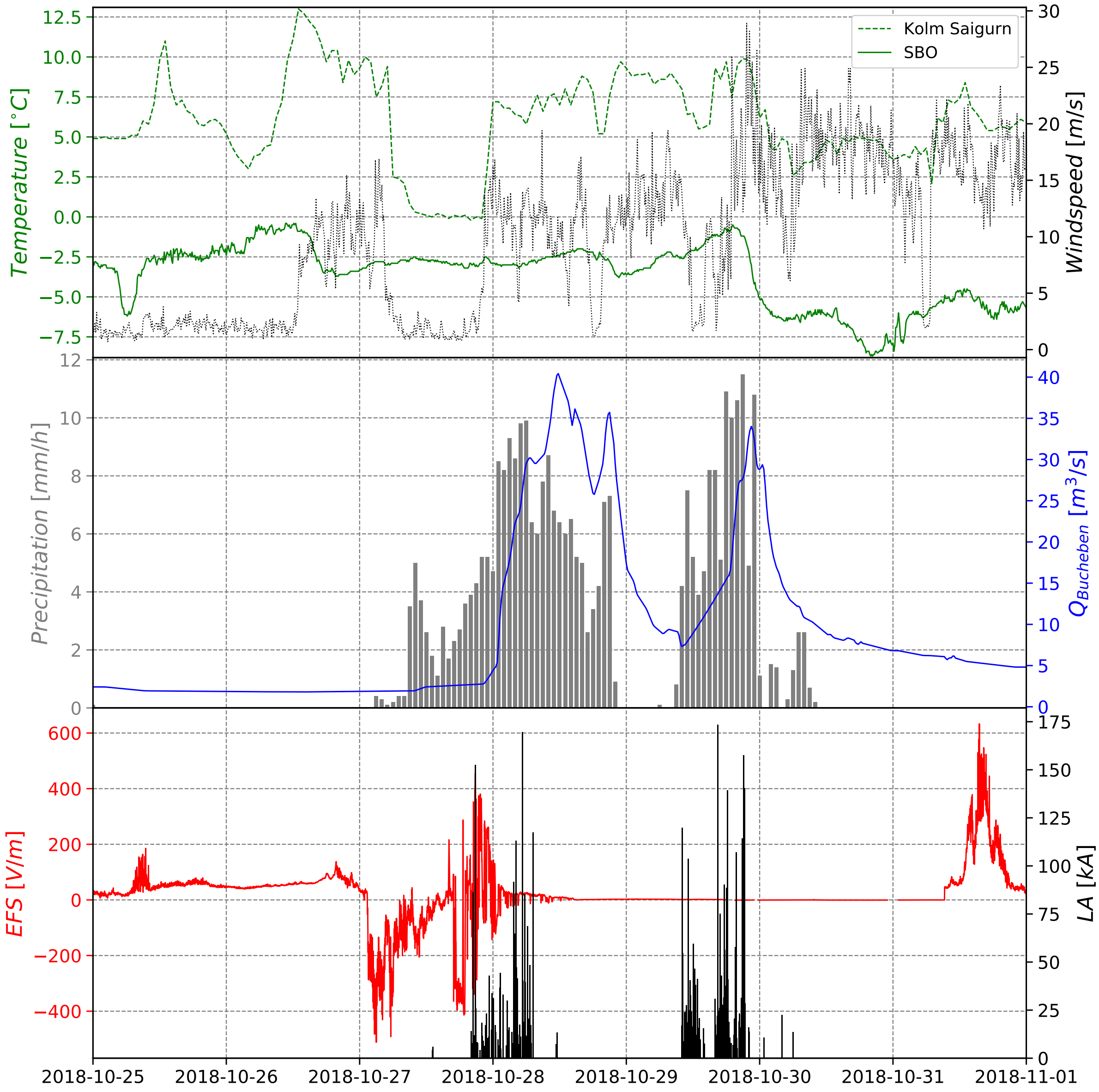

Figure 6.19: The compiled complementary data for the period of the extreme weather event in October 2018. The top graph illustrates the air temperature of the Sonnblick observatory (SBO, 3106 m a.s.l.) and the Kolm Saigurn valley floor (1600 m a.s.l.). The black dotted line indicates the measured maximum windspeeds. The middle graph shows the Kolm Saigurn precipitation versus the Hüttwinklache discharge (Q) measured at the Bucheben gauging site. The lag of the discharge peak is likely due to the distance of about 10 kilometers in between the two monitoring stations. The lower graph compiles electric field strength (EFS) data of the SBO, as well as the amplitudes of lightnings (LA) detected by the Austria-wide ALDIS network. The constant electric field strength values of zero in the second half of the time period is potentially due to icing of the sensor at the Sonnblick summit.

One mud flow coming down the Hüttwinklache river bed was documented by a time lapse camera. The time lapse camera takes a photo every half an hour. Figure 6.20 shows a time series of the mud flow event. In the river bed right in front of the 'Naturfreundehaus' guesthouse, mud flow material was deposited and substantial erosion of the river bank was present. Based on the time lapse photos the mud flow happened in between October 29, 17:00, and October 30, 02:00, which corresponds well with the second precipitation maximum of this weather event (compare Figure 6.18).

Figure 6.20: Photo time series of a mud flow coming down the river bed of the Hüttwinklache. The top photo shows the river bed before the heavy precipitation event, the middle the rising discharge, and the bottom photo documents the mud flow deposit and river bank erosion after the extreme weather event in October 2018. Based on the time lapse photos the mud flow happened in the night 29.-30.10., which corresponds well with the second precipitation maximum of this weather event (compare Figure 6.18). *Source: foto-webcam.eu*

Beside the mud flow documented by the time lapse camera at the Kolm Saigurn valley floor (Figure 6.20), an additional mud flow and two snow slides were observed during field work on November 15, 2018. The debris and snow deposits were found at the foot of the Sonnblick north-face, in between the MIT and the MOR seismic stations. Unfortunately, the *SeisRockHT* network and the observed deposits are not covered by the time lapse camera photos. Figure 6.21 shows the estimated run-out zones (RZs) of the mud flow (RZ1) and snow slides (RZ2,3). All slides came down in dominant north-face gulleys. Figures 6.22, 6.23 and 6.24 show photos of the three RZ deposits. While the RZ1 deposit is a mix of mud, snow, gravel and smaller boulders, the RZ2 and RZ3 deposits consisted of bare snow.

In the following, the derived products of the gathered seismic data recorded during the extreme weather period are presented. Complementary data suggest potential interactions between recorded seismic data and individual weather related processes.

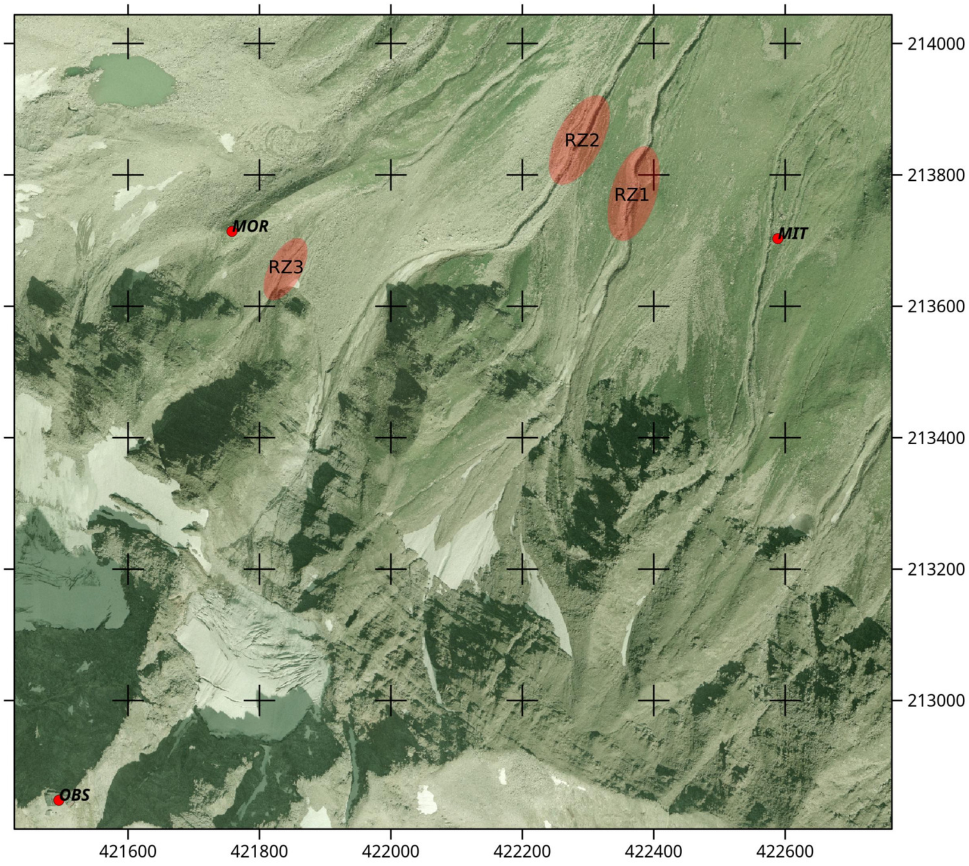

Figure 6.21:
The three run-out zones (RZ1-3) were situated at the Sonnblick north-face foot in between the MIT and the MOR station. All slides came down in dominant gulleys. (COS: MGI/Austria GK M31 (EPSG:31258) with 200 m grid spacing)

Figure 6.22: The run-out zone 1 (RZ1) debris came down in a major Sonnblick north-face gulley. The deposit consisted of a mix of mud, snow, gravel and smaller boulders. In the left background of the right photo the back then still existing red cable car pillar, right at the MIT station, is visible.

Figure 6.23: The snow slide of the run-out zone 2 (RZ2) came down in a major Sonnblick north-face gulley. The deposit consisted of bare snow.

Figure 6.24:
The snow slide of the run-out zone 3 (RZ3) came down in a major Sonnblick north-face gulley. The deposit consisted of bare snow.

6.4.1 Ambient Seismicity

Spectrograms illustrate the temporal evolution of the signal frequency content of the recorded seismic data. Figure 6.25 shows two spectrograms for the period October 25-31, 2018. The top spectrogram illustrates the median power spectral densities (PSDs) calculated from one representative component of each station of the Sonnblick network. The lower spectrogram is calculated from the vertical component of the STO station. Generally, the lack of short term, high frequency content in the STO spectrogram is striking and illustrates the isolation of the STO station from surface processes, as well as environmental and anthropogenic noise. The prominent lower frequent event before midnight on October 25, was caused by a magnitude 6.8 earthquake in the Ionian Sea, Greece. All calculated spectrograms for the extreme weather event in 2018 can be found in Appendix B.

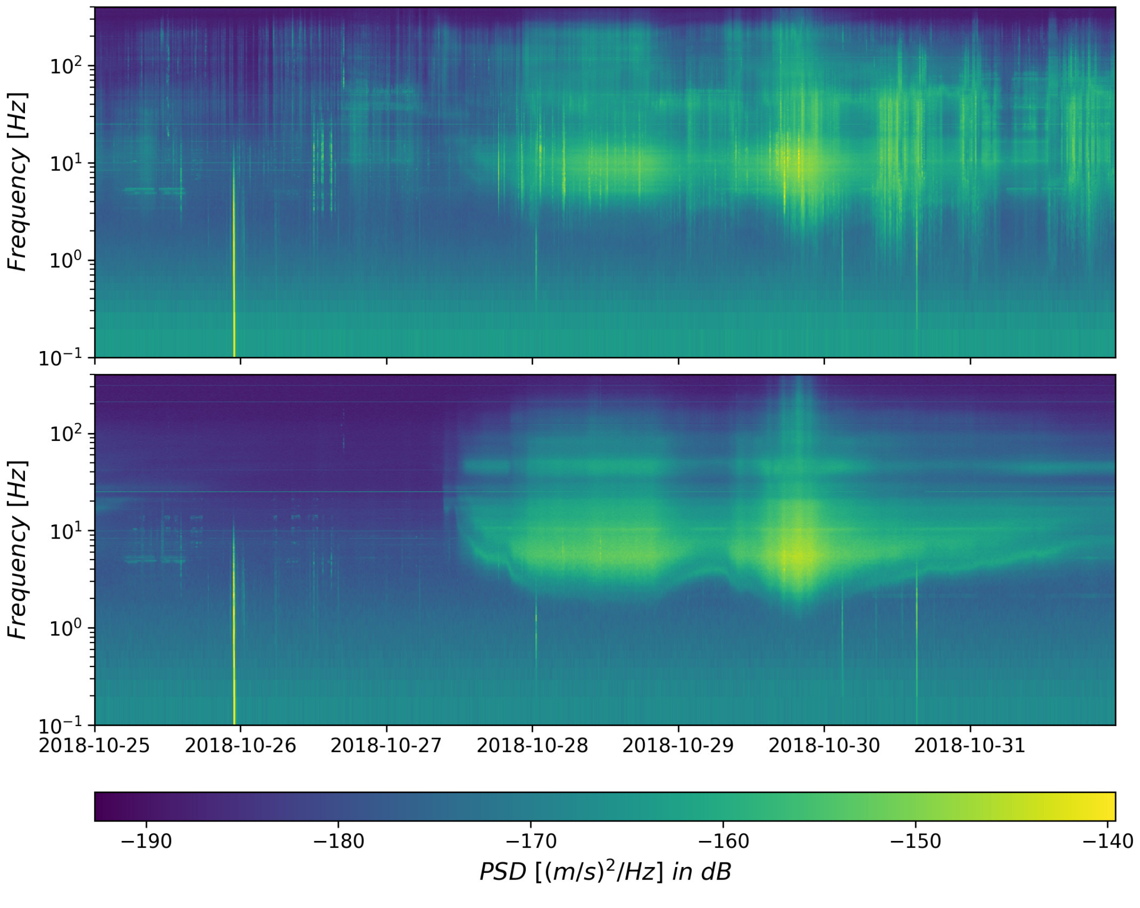

Figure 6.25: Two spectrograms for the period October 25-31, 2018. The top spectrogram illustrates the median power spectral density (PSD) values of all stations of the Sonnblick network. The lower spectrogram shows the calculated PSDs for the STO station. The isolated subsurface location of the STO station significantly reduces the short term, high frequency signal content caused by surface processes, and environmental and anthropogenic noise. The prominent lower frequent event before midnight on October 25, was caused by a magnitude 6.8 earthquake in the Ionian Sea, Greece.

The STO spectrogram features a clear PSD increase for frequencies larger than ∼2 Hz throughout the time period of the extreme weather event. Figure 6.26 shows a clear correlation between the STO PSDs and the available precipitation and discharge data. The STO station is situated at the end of a 50 m deep rock tunnel which makes it relatively isolated from the impact noise of the precipitation droplets. The elevated PSD levels in between the two main precipitation events support that the observed STO PSD distribution is not caused by the precipitation itself. Due to the fact that the STO station at the Kolm Saigurn valley floor is close to creeks coming down the mountain and feeding the Hüttwinklache, we suggest that the course of the STO PSDs is driven by discharge. The black dashed line in Figure 6.26 represents the discharge data of the 10 km distant Bucheben gauge. Despite a likely distance-related temporal lag, the discharge corresponds well with the STO PSD distribution.

Additionally, the frequency characteristics of the elevated ambient seismicity during the extreme weather event are similar to the frequency characteristics of the ambient seismicity cyclicity observed during the field campaign in 2017 (Figure 6.9). This signal similarity further strengthens the suggestion that the discharge of a local, melt-driven creek is the source of the observed ambient seismicity cyclicity during the field campaign in 2017.

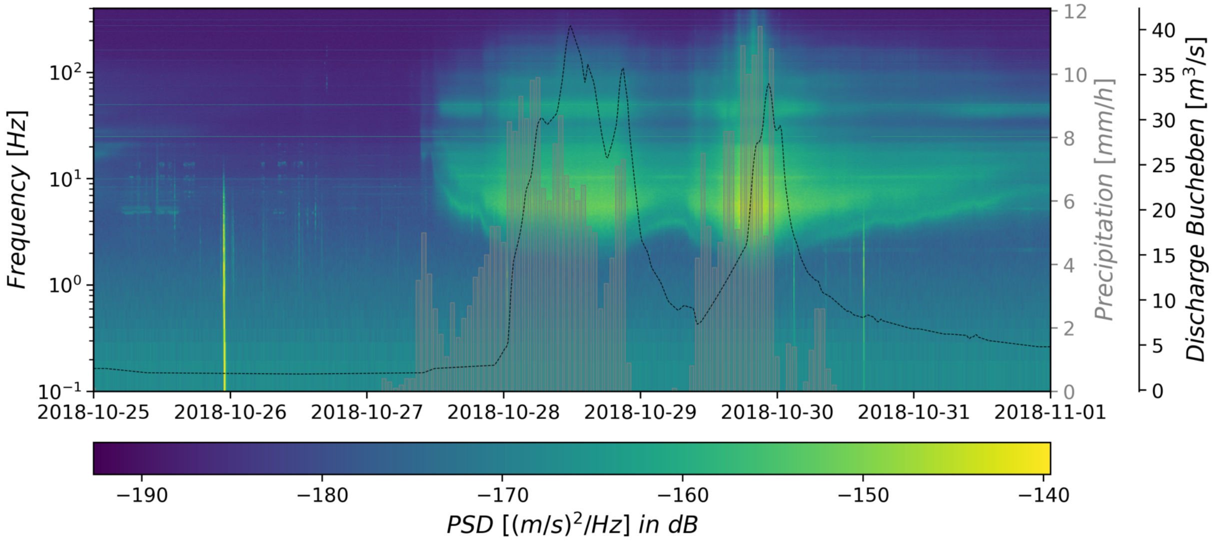

Figure 6.26: The STO spectrogram reveals a clear correlation with the precipitation and the discharge data.

6.4.2 Detected Events

The seismic data of the extreme weather period 2018 was manually screened for seismic events. In total 110 events were categorized into six different event types (see table 6.4). The complete event catalog of the extreme weather event in 2018 can be found in Appendix C. In the following exemplary examples of the event catalog are presented.

Event type	**Number of Events**	**Description**
Anthropogenic	23	Events related to human activities like air traffic or cable car operation.
Earthquake	5	Events related to well-known tectonic earthquakes.
Lightning	6	Events related to lightning strikes.
Rockfall Candidate Long	12	Events with a signature suggesting a long-term, flow-like process.
Rockfall Candidate Short	15	Events with a signature suggesting local sources related to rockfalls.
Tremor	49	Mostly long events ($>$ 20s) recorded on multiple stations but with no clear traceability of individual seismic phases between the stations.

Table 6.4: The classified event types with the associated total number of events detected during the extreme weather event in 2018.

The *Anthropogenic* event type comprise all events which are related to human activities. The most prominent events during the observation period were signals from helicopters, airplanes and the SBO cable car operation. Examples of these events can be found in the following section 6.5.

Another event type occurring throughout the extreme weather period could be identified as lightning events with subsequent rumble of thunder. *Lightning* events are discussed in the following section 6.5.

In the week of the extreme weather event five earthquakes were detected. The most prominent, on October 25, was a magnitude 6.8 earthquake in the Ionian Sea, Greece. The most prominent feature to identify earthquakes is the familiar shape of P-, S- and surface waves and almost similar arrival times on all stations of the network due to the large distance between the earthquake epicenter and the network stations (compare Figure 4.10).

The two event types *Rockfall Candidate Long* (*RC Long*) and *Rockfall Candidate Short* (*RC Short*) are related to local rockfall activity. The events of type *Tremor* are mostly long events ($>$ 20s) with an emerging onset recorded on multiple stations of the network exhibiting a general correlation of the spectrograms among the stations. The source of the *Tremor* events is not yet clear. These three event types are discussed in detail in the following sections.

Rockfall Candidate Long

Figure 6.27 gives a representative example of a *RC Long* event. The events show distinct low frequency content and are most prominent on stations MOR and MIT. A striking feature is the different shape of the amplitude envelopes of station MOR and MIT. This shape suggests a moving mass passing station MOR (amplitude maximum during the middle of the event) and accumulating near station MIT (amplitude maximum towards the end of the event with an abrupt ending). A similar amplitude distribution was observed by Weginger (2012) for rockfalls passing seismic stations at the mass movement Steinlehnen, Tirol, Austria.

Compared to the visually validated rockfall events (see section 6.2), the *RC Long* events show no high frequency content, thus suggesting a different source process than the validated rockfall events. The presented *RC Long* example has the event catalog ID 79.

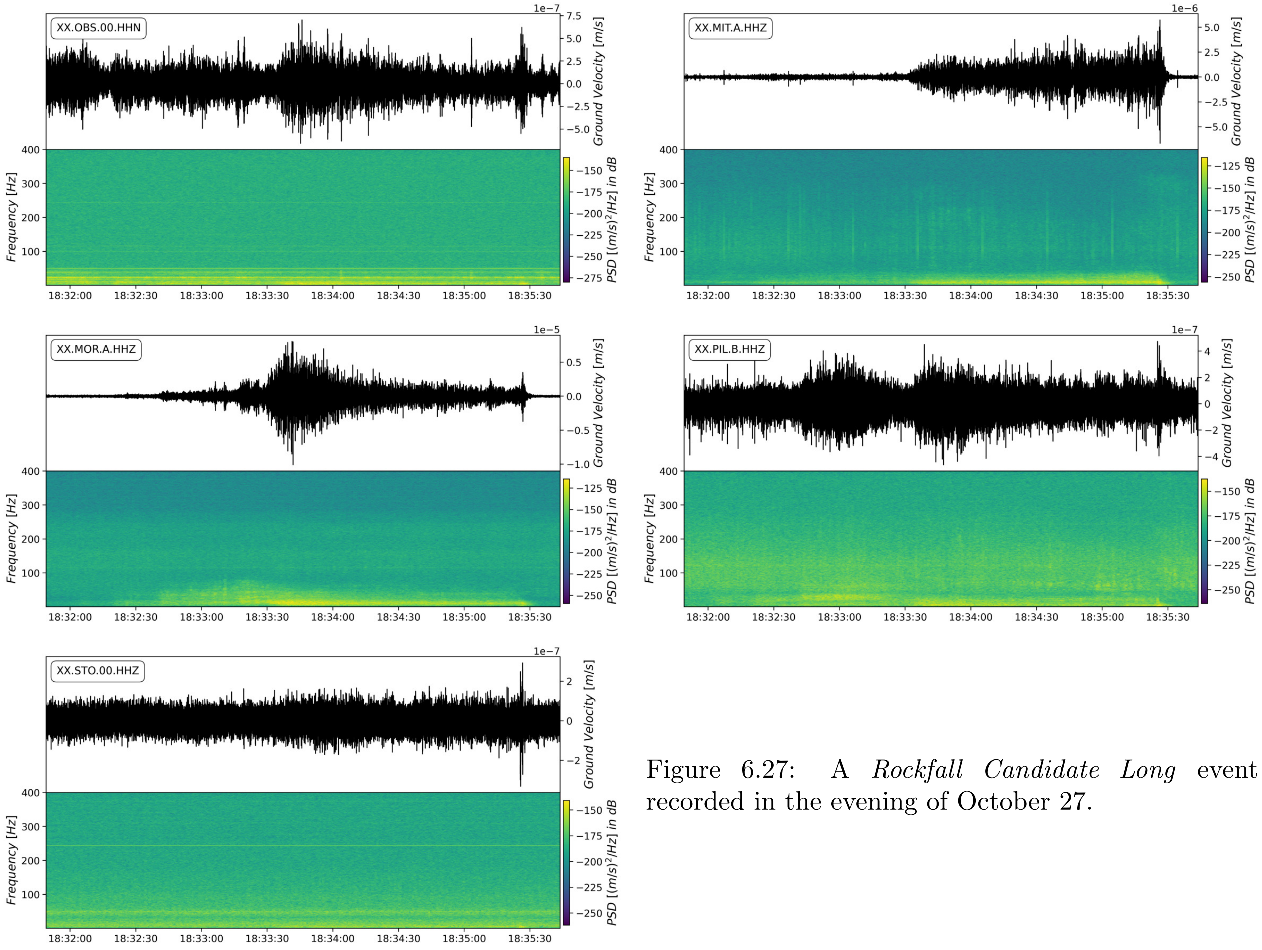

Figure 6.27: A *Rockfall Candidate Long* event recorded in the evening of October 27.

Rockfall Candidate Short

The *RC Short* events are characterised by short-term, impulsive signals with low frequency content (see Figure 6.28). Individual phases can be traced between the stations. Usually, they were recorded at stations MOR and PIL with a clear amplitude variation between the two stations. However, no systematic behaviour of one station showing larger maximum amplitudes was observed. Compared to the visually validated rockfall in section 6.2, where rockfalls with an estimated volume of ∼0.5-1 m^3 showed recordings at all stations, these events seem to be related to short-term, weak energy sources like single rocks falling without further rolling downhill. Possible source regions could be the foot of the Sonnblick north-face, as well as the ice face at the terminus of the debris covered glacier Pilatuskees (Figure 6.17). The presented *RC Short* example has the event catalog ID 59.

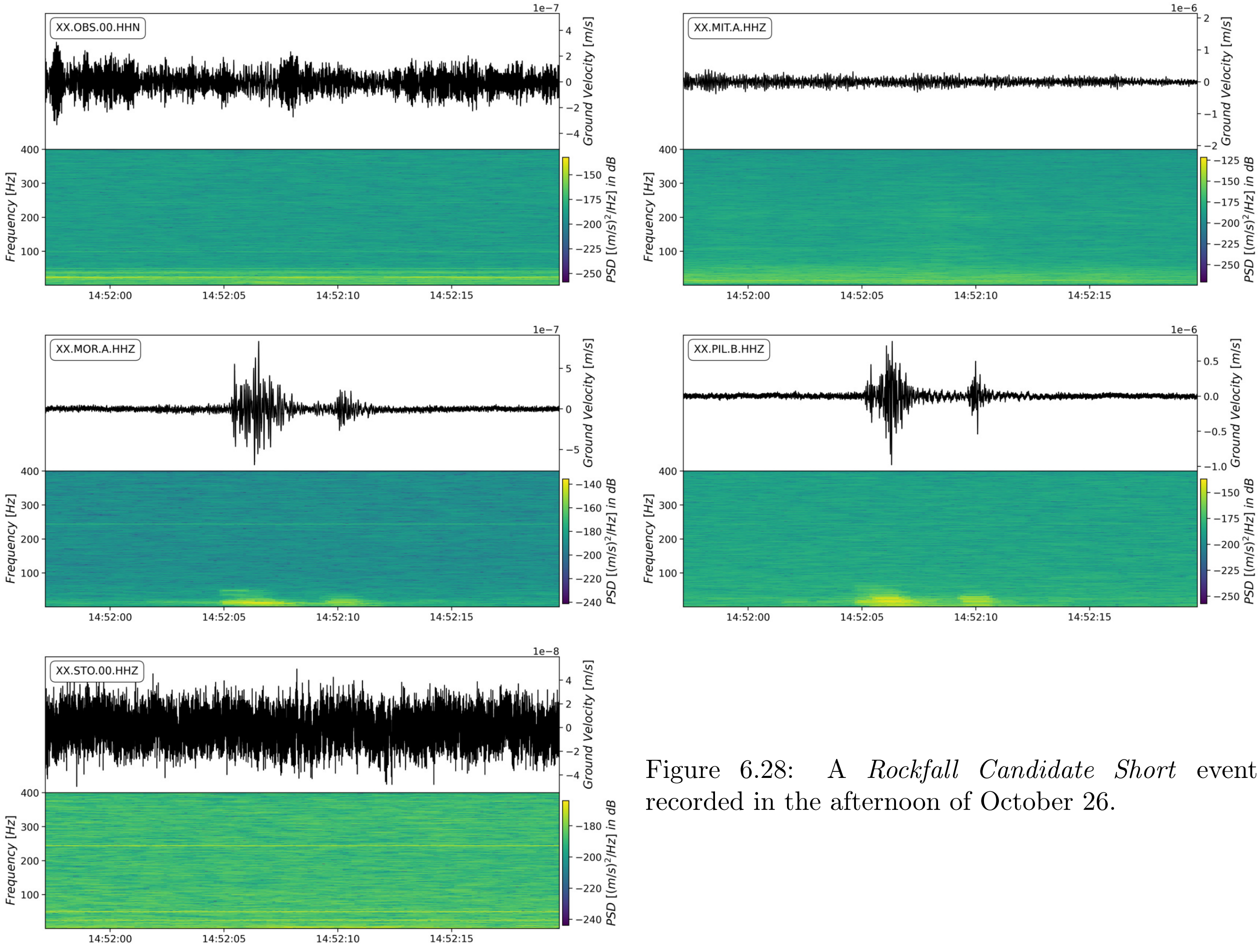

Figure 6.28: A *Rockfall Candidate Short* event recorded in the afternoon of October 26.

Tremor

The observed *Tremor* events feature an emergent onset and no distinct waveform phases which could be traced throughout the network stations. Also the frequency content varies from station to station.These events are usually recorded at stations MIT, MOR and PIL. The presented *Tremor* example has the event catalog ID 30.

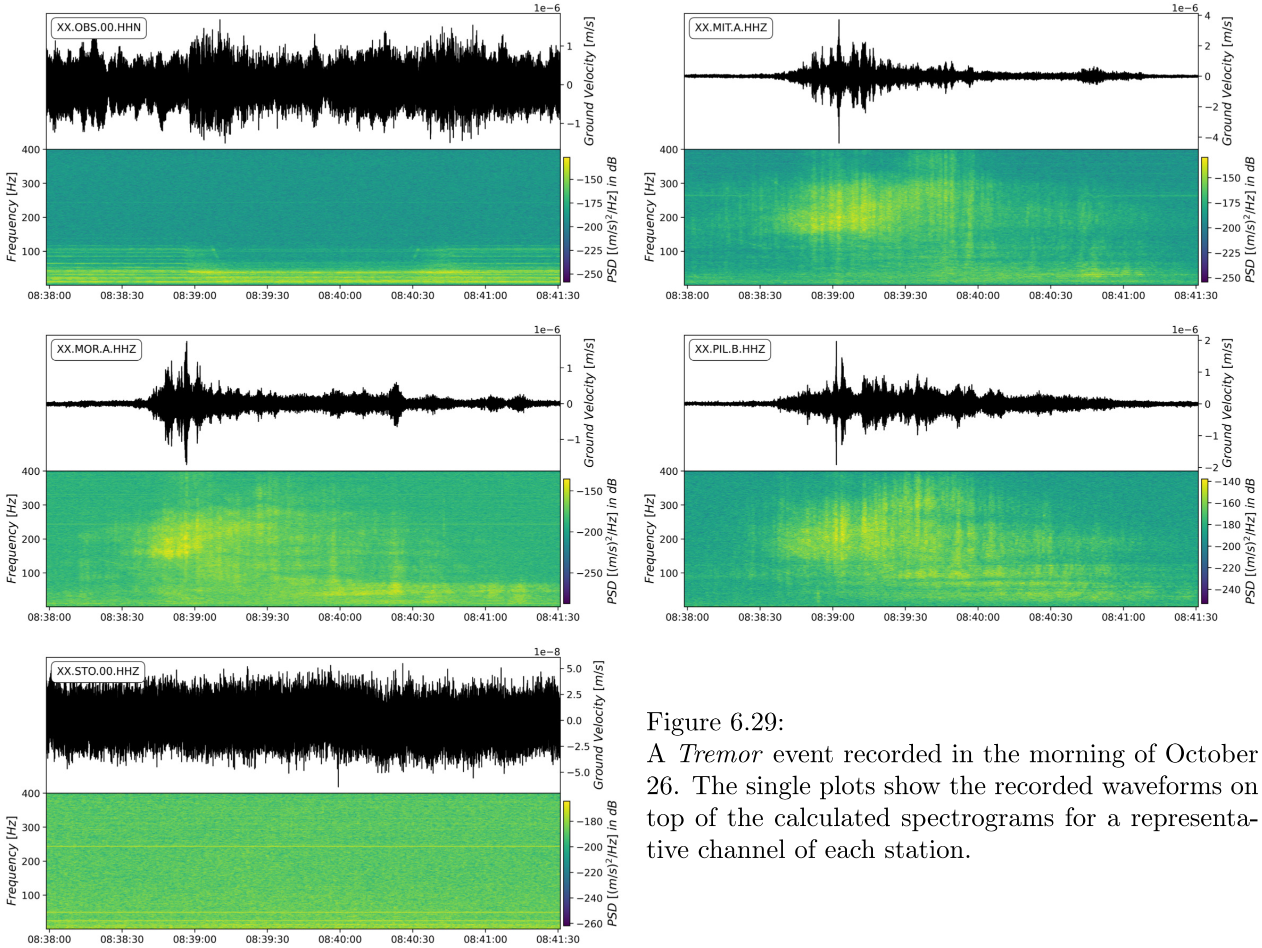

Figure 6.29:
A *Tremor* event recorded in the morning of October 26. The single plots show the recorded waveforms on top of the calculated spectrograms for a representative channel of each station.

6.4.3 Temporal Event Distribution and Correlation with Complementary Data

Figure 6.30 shows the median spectrogram with white line plots of the cumulative number of each event type. Prominent single events like earthquakes, *RC Short* and *RC Long* events can be clearly identified in the spectrogram. Furthermore, rather distant earthquakes and local events can be clearly distinguished by their apparent frequency content. Also a temporal accumulation of *RC Short* on October 26, and *RC Long* mainly within October 28 is revealed. The most abundant *Tremor* events accumulate in the same period as the two rockfall candidate event types (beginning of October 26 and the second half of October 27).

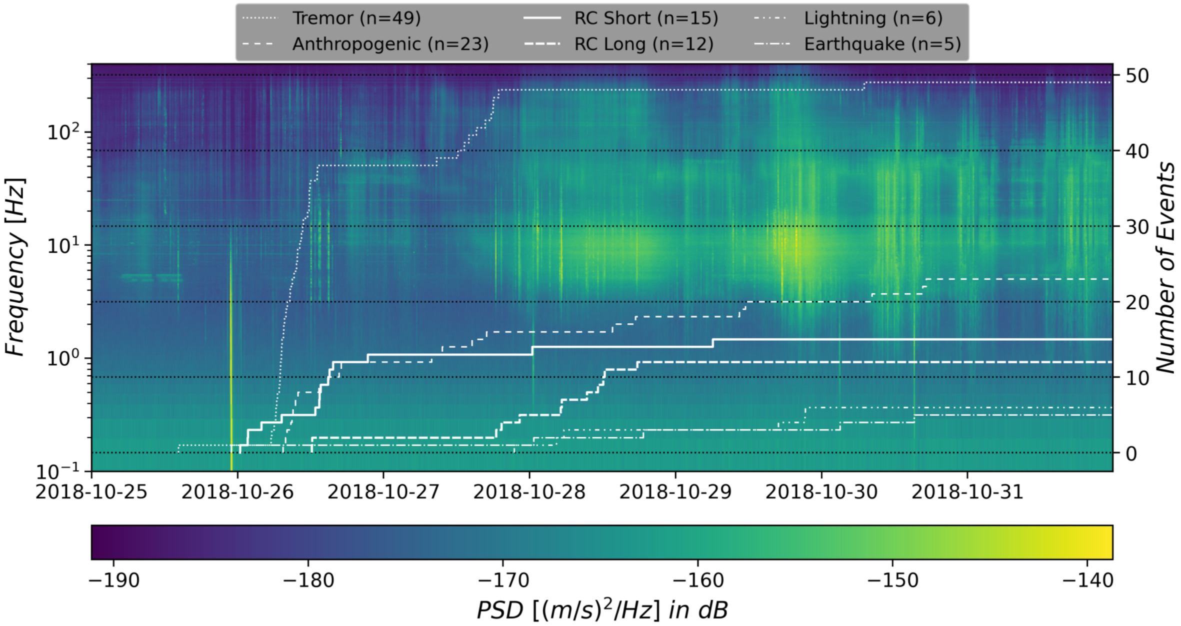

Figure 6.30: Spectrogram of the median PSDs of all Sonnblick stations shown with the over time cumulated number of the six different event types.

Figure 6.31 presents the median spectrogram with the cumulated events from figure 6.30 together with selected meteorological parameters. It shows that all *RC Long* events happened within the first major precipitation event on October 28. Furthermore, the data juxtaposition reveals that 13 of in total 15 detected *RC Short* events occurred within one day, October 26, which was characterized by rising air temperatures and the first episode of higher windspeeds. The first steep increase of *Tremor* events happened within the temporary break of *RC Short* events on October 26, and generally also correlates with the rising air temperatures. The second pronounced increase of *Tremor* events started with the first medium rainfall event in the middle of October 27, and continued until the number of *RC Long* events started to take off during the first main precipitation event on October 28. Interestingly, no comparable increase of rockfall candidate, nor *Tremor* events was detected during the second main precipitation event on October 29-30 which was also accompanied by a distinct temperature drop lasting throughout the end of the extreme weather event.

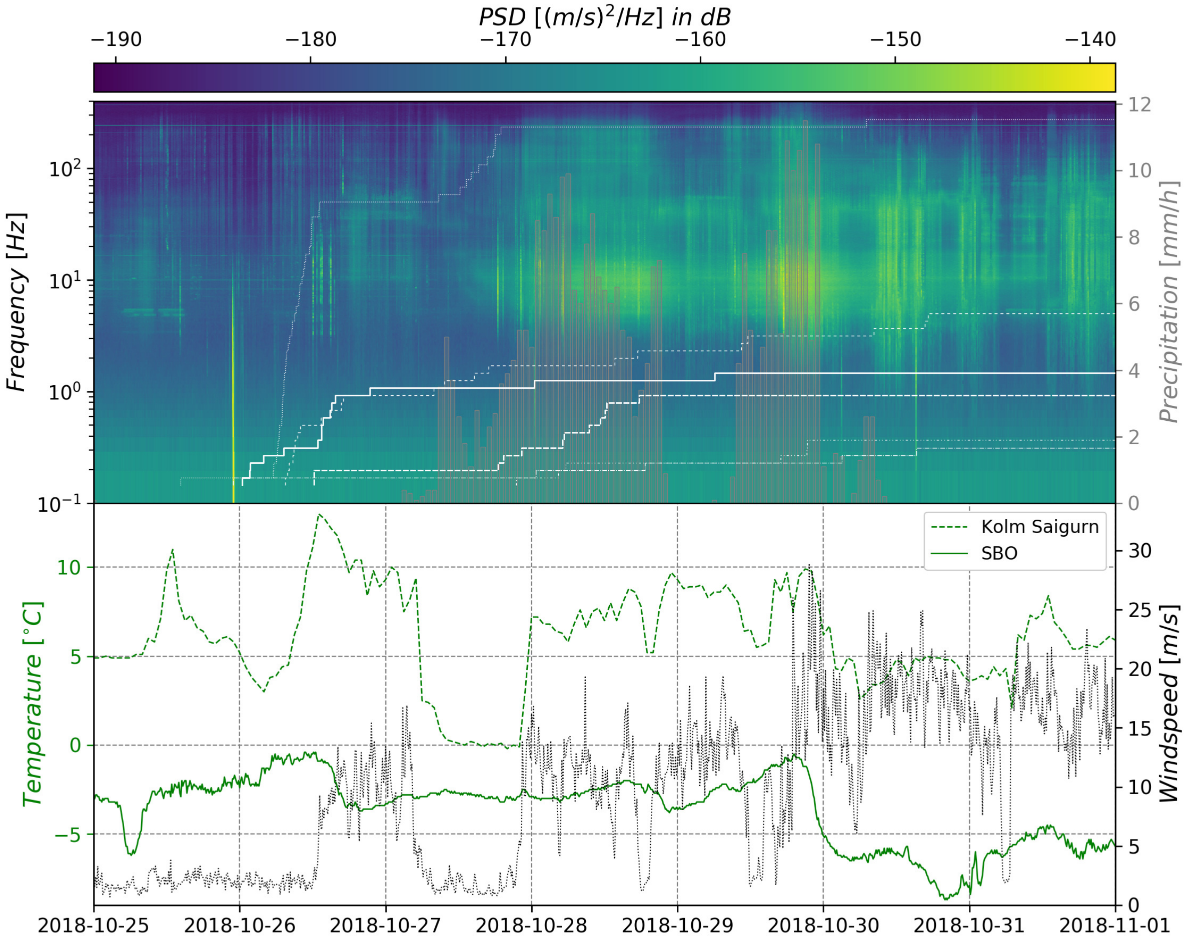

Figure 6.31: The top plot shows the median spectrogram of figure 6.30 with the precipitation data. All events of the rockfall long type happened within the first precipitation peak. The lower plot shows complementary data, whereas the green lines illustrate measured air temperatures at Kolm Saigurn (1600 m a.s.l.; dashed line) and on the Sonnblick summit (3106 m a.s.l.). The black dotted line presents maximum wind speeds at the Kolm Saigurn valley floor.

Figure 6.32 illustrates the measured rock temperatures of a shallow borehole in the upper Sonnblick north face at 3080 m a.s.l.. The presented borehole data already starts on October 15 to uncover the evolution of the rock temperatures before the actual extreme weather period. The first days show a clear diurnal cycle of the rock temperatures with maximum temperatures above 0°C. On October 21 a cooling event significantly lowered the rock temperatures. Thereafter, the rock temperatures were generally rising until the local rock surface temperature maximum of October 26, when the *RC Short* and *Tremor* event sequence was initiated.

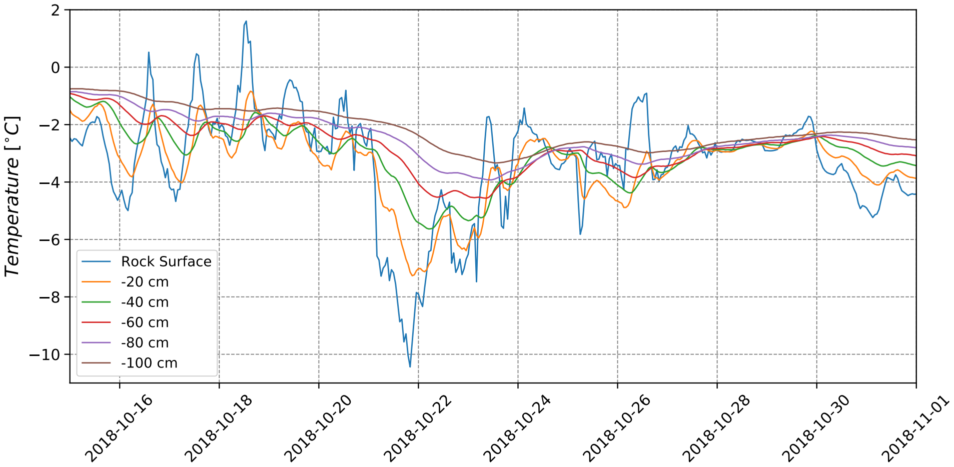

Figure 6.32:
Rock temperature evolution of a shallow borehole in the Sonnblick north face at 3080 m a.s.l.. About one week before the actual extreme weather event the striking cooling event on October 21 caused a significant disturbance of the rock temperatures.

6.5 Miscellaneous Seismic Events

Helicopter

In summer 2018 regular support by helicopter for the construction of the new SBO cable car was operative. Following figures present recorded data from the MIT, MOR and PIL stations where helicopter-triggered signals are clearly visible due to the rather shallow installed sensors. Validation of air-traffic by microphones as shown by Mertl (2014) was not available. However, helicopter as source of the recorded seismic data could be validated through available SBO logs. Furthermore, characteristic helicopter-triggered seismic features like the observed spectral gliding is supported by literature (e.g. Eibl et al. (2017), Eibl et al. (2015)).

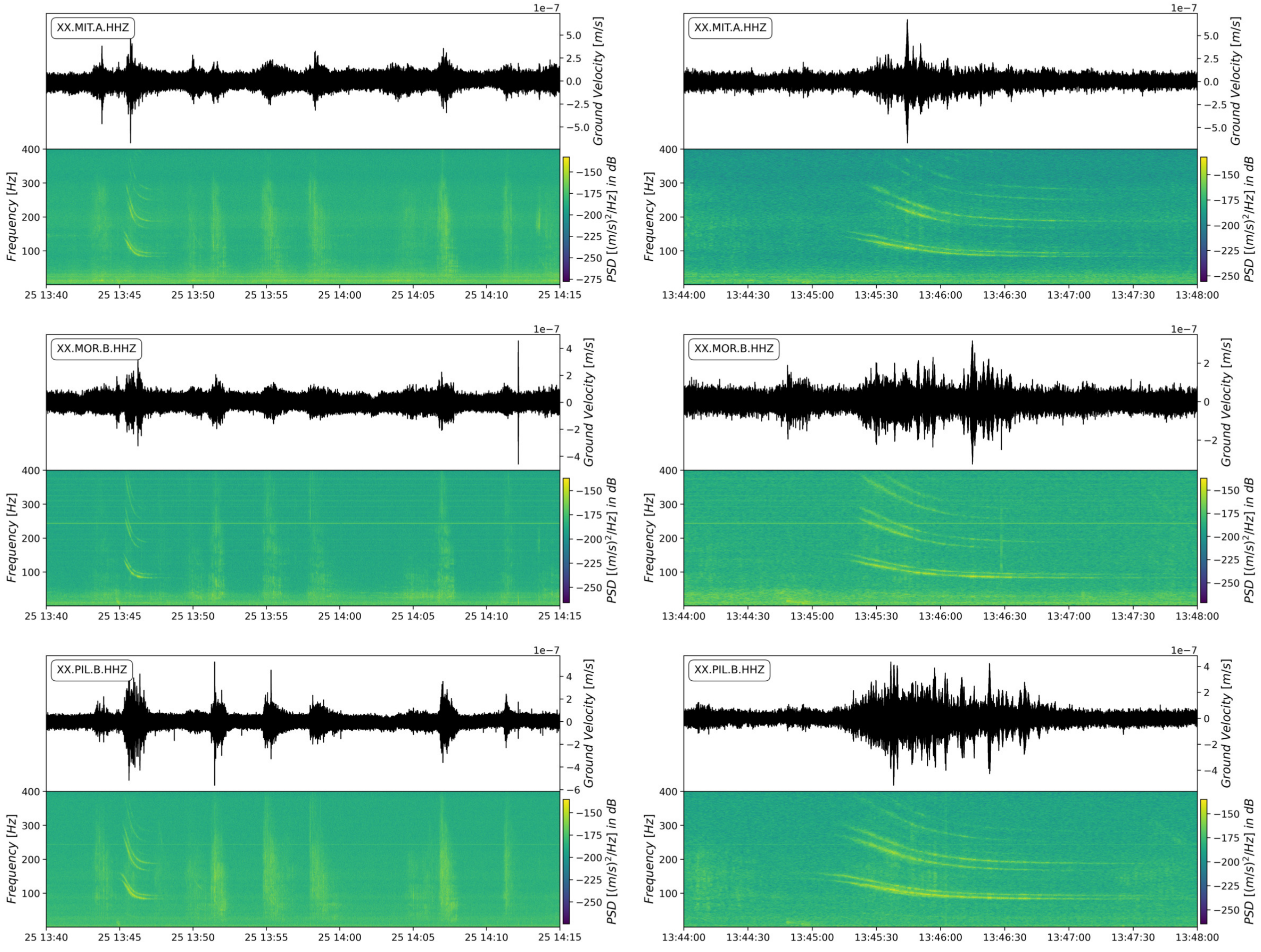

Figure 6.33: The seismic response of an operating helicopter. The left plots show 35 minutes of MIT, MOR and PIL station data with the recorded waveforms on top of the calculated spectrograms. The right plots show 4 minutes of data with details of the observed characteristic spectral gliding.

Sonnblick Observatory Cable Car

An obvious seismic source for the OBS station are the regular SBO cable car rides. The left plot in Figure 6.34 shows OBS data with a dominant wave train caused by the operating SBO cable car which was validated by the SBO cable car logs. Furthermore, the one-way travel time for the old SBO cable car of about 20 minutes perfectly fits the recorded data. The right plot in Figure 6.34 shows seismic data of the MIT station where the cable car operation is also clearly visible. All the other stations did not show a clear seismic response.

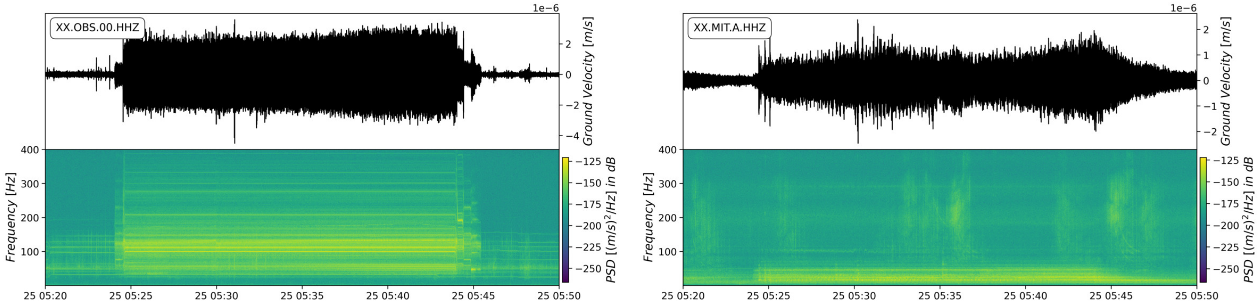

Figure 6.34: Seismic response of the operating old Sonnblick observatory cable car. The cable car signal is clearly visible in the OBS and MIT station data.

Lightning and Thunder Events

In bad weather periods reoccurring events with a broadband spike signature and a following tremor-like signal were observed (see Figure 6.35). The spikes were recorded at all individual stations at the same time. The simultaneous spike arrivals led to the hypothesis of a electromagnetic wave which propagated with speed of light and caused the recorded electrical spike signals by electromagnetic induction in the geophone coil. The most likely source of the electromagnetic wave was lightning strikes during thunderstorms. The following tremor-like signal was related to acoustic waves of the thunder. The available complementary data of the ALDIS lightning detection made it possible to quantitatively verify this hypothesis.

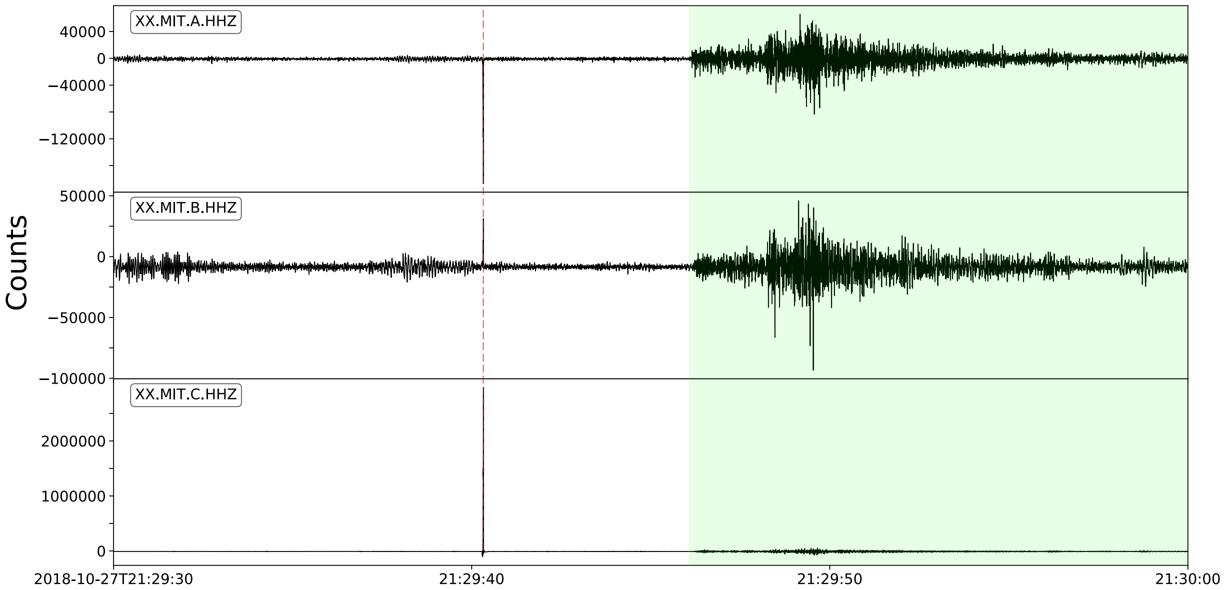

Figure 6.35: Seismograms of the three MIT channels from October 27 in the beginning of the discussed extreme weather event (section 6.4). Each seismogram features a broadband spike (red dashed line) with a subsequent tremor-like signal (highlighted green). The simultaneity of the spike signal is striking.

A correlation of the arrival times of the spike signals with the ALDIS lightning detection revealed a strong correlation of the measured arrival times of the spikes with the ALDIS origin times of the lightning strikes. An example of the strong temporal correlation between the seismograms and the ALDIS origin times is given in Figure 6.36. Eventually, not all lightning strikes reported by ALDIS were recorded by the *SeisRockHT* network and for at least one event vice versa, but for the majority there is a strong correlation of the two data sets.

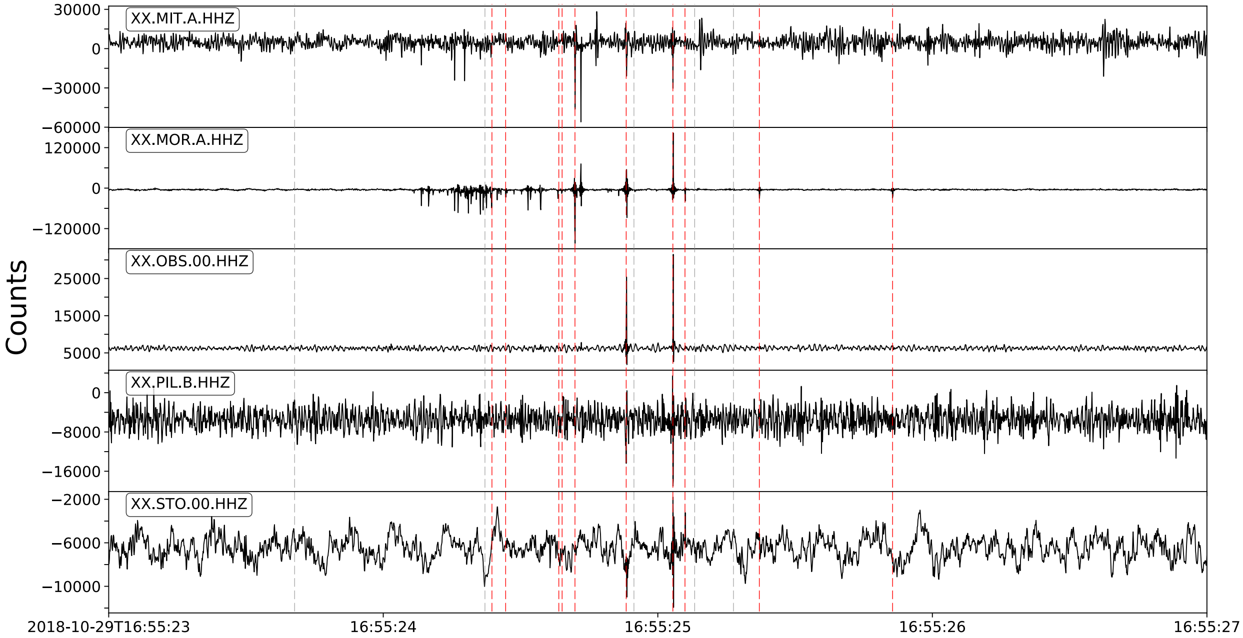

Figure 6.36: Temporal correlation of detected lightnings by the ALDIS network (vertical dashed lines), and seismograms of the Sonnblick network. Red dashed lines highlight lightnings which correspond to discrete events in the seismograms. Simultaneity and signal characteristics of the corresponding events in the seismograms suggest lightnings as event source.

The verification of the tremor signal which follows the spike signals as the acoustic waves related to thunder is ambiguous. ALDIS reports a location of the detected lightning strikes with a location accuracy of 100 - 200 meters (according to their website `https://www.aldis.at/netzwerk/funktionsweise/`). Using this location, the distance to the seismic stations can be computed and the expected arrival time of the acoustic waves can be computed using the speed of sound.

Figure 6.37 shows an example of a good correlation between the seismic arrival of the tremor and the expected arrival time of the acoustic wave. The ALDIS detection of the lightning is at 2018-10-29T16:55:25.0544 at a distance of 6715 m. Multiple lightnings within one second were detected by the seismic network at that time. Assuming a speed of sound of 330 m/s, the expected travel time of the acoustic wave is about 20 seconds. Depending on the individual station, the arrival time of the strongest tremor ranges between about 17 to 20 seconds. A seismic tremor with the source of rumbling thunder after a lightning could be shown for several other examples. Nevertheless, we found as well examples with a clear mismatch between the calculated and observed tremor arrival. However, the role of the seismic ground role still needs to be clarified for these cases, but that is beyond the scope of this report.

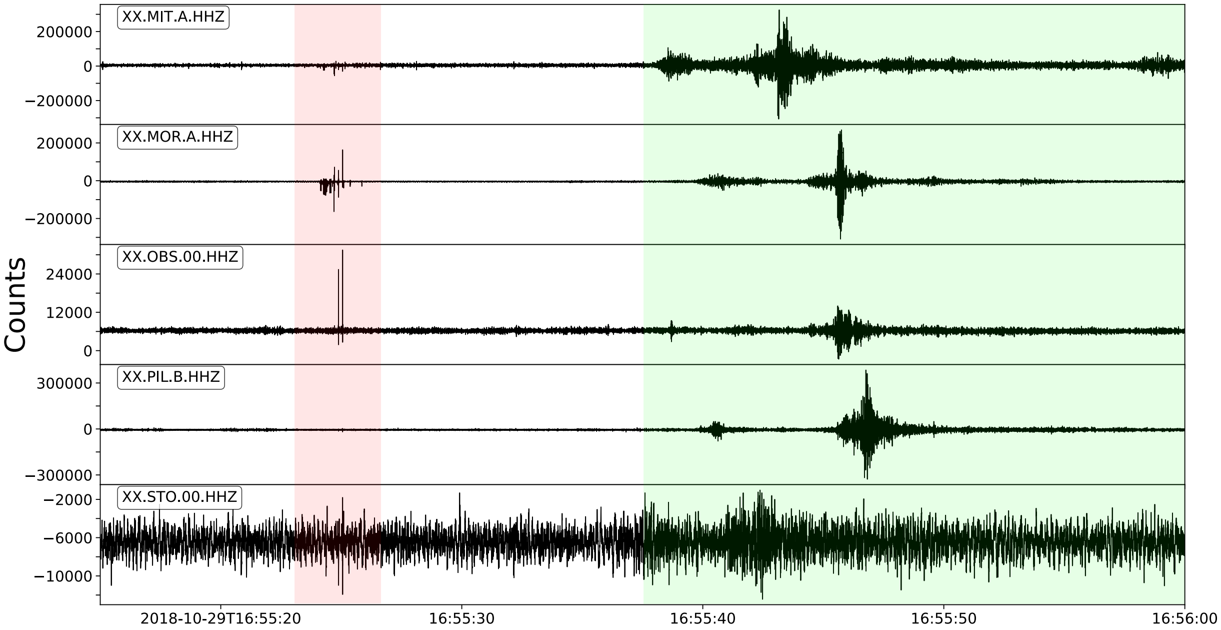

Figure 6.37: Good correlation between the expected arrival time of the acoustic waves and the seismic arrival time of the tremor. Red highlighted is the lightning sequence detected by the seismic network. Green highlighted are the recorded seismic tremors which correlated with the expected arrival time of the rumble of thunder.

Slab Avalanche Event 2017

In the late winter season 2016/17 an extensive snowfall event brought about 0.5 m of fresh snow for the Hohe Tauern region in about two days (08./09.-10. 03.). High winds during the snowfall caused snow redistribution into north-east facing slopes. On Saturday, March 11, the weather improved and numerous self-triggered slab avalanches were visible on north-east faces all along the main alpine ridge of the 'Hohe Tauern' region.

Figure 6.38: The slab avalanche released in between the summits of Hoher Sonnblick and Hocharn. The left photo gives an overview of the avalanche source location. The right photo shows the clearly visible slab avalanche fracture line. The darker area right below the central fracture line is most likely bare ice.

One larger slab avalanche was released at a north-east face between the summits of Hoher Sonnblick and Hocharn (Figure 6.38). The avalanche source terrain is steep and leads to a dominant rock step directly above the end of the Pilatus side valley. This setting indicates a rather hard impact of the snow masses after being discharged over the dominant rock step. Based on the acoustic observations by Sonnblick observatory (SBO) technician N. Daxbacher, we know that several avalanches in the direct vicinity of the SBO discharged during the entire day of March 10. Unfortunately, due to bad sight during that day, we could not pinpoint the exact daytime of the distinct slab avalanche shown in figure 6.38. Furthermore, the closest stations MOR and PIL were not operating during that period. Beside the manual screening of the March 10 datasets, no further analysis was done due to project time limitations. However, for the sake of completeness of this final report, as well as to show alternative applications of the within *SeisRockHT* installed local seismological network, we decided to also present this rather qualitative result.

Figures below show the recorded waveforms on top of the calculated spectrograms for the five slab avalanche candidates. The shown data is from a representative channel of the active OBS, MIT and STO stations. Generally, the observed signals feature a signal duration of about one minute and a lower frequency content which is in accordance with seismic avalanche signals from literature (e.g. Kogelnig et al. (2011), Suriñach et al. (2005), Suriñach et al. (2001)). The OBS data of slab avalanche candidate 4 (Figure 6.42) exhibits clear characteristics of a regional earthquake due to its abrupt signal onset, duration and frequency content. However, especially the different waveform shape of the STO station, as well as the lack of simultaneity of all three stations refute a regional earthquake as seismic source (compare Figure 4.10). Additionally, no matching regional earthquake could be found in the Seismological Service summary of *March 2017*.

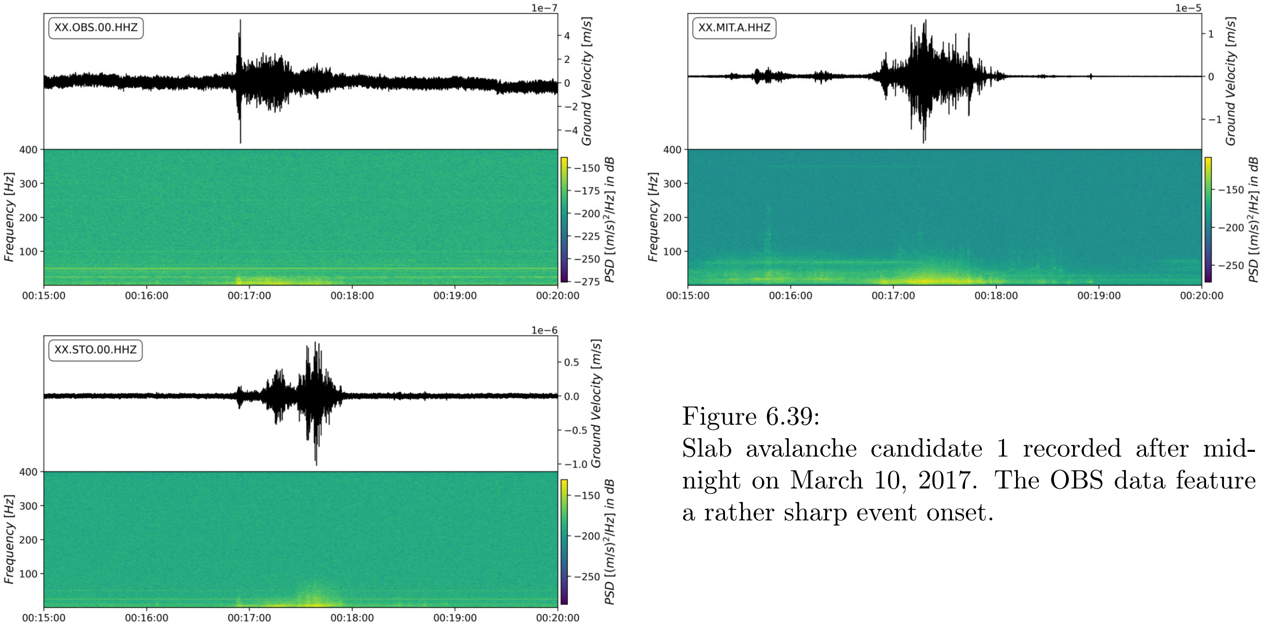

Figure 6.39:
Slab avalanche candidate 1 recorded after midnight on March 10, 2017. The OBS data feature a rather sharp event onset.

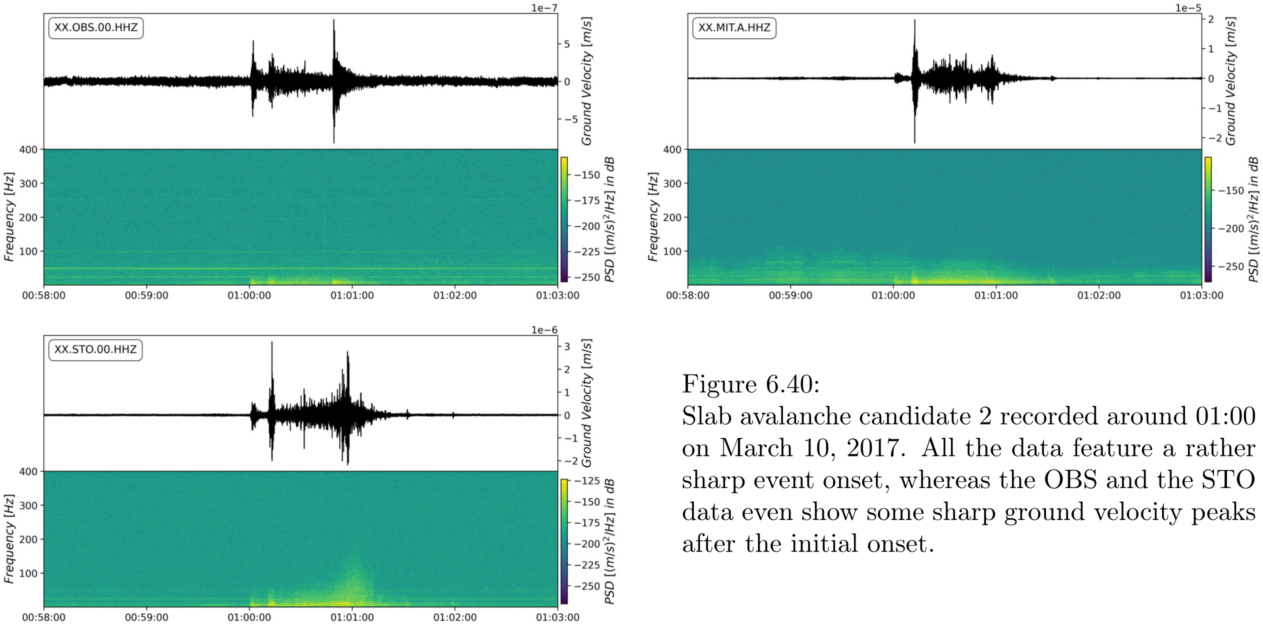

Figure 6.40:
Slab avalanche candidate 2 recorded around 01:00 on March 10, 2017. All the data feature a rather sharp event onset, whereas the OBS and the STO data even show some sharp ground velocity peaks after the initial onset.

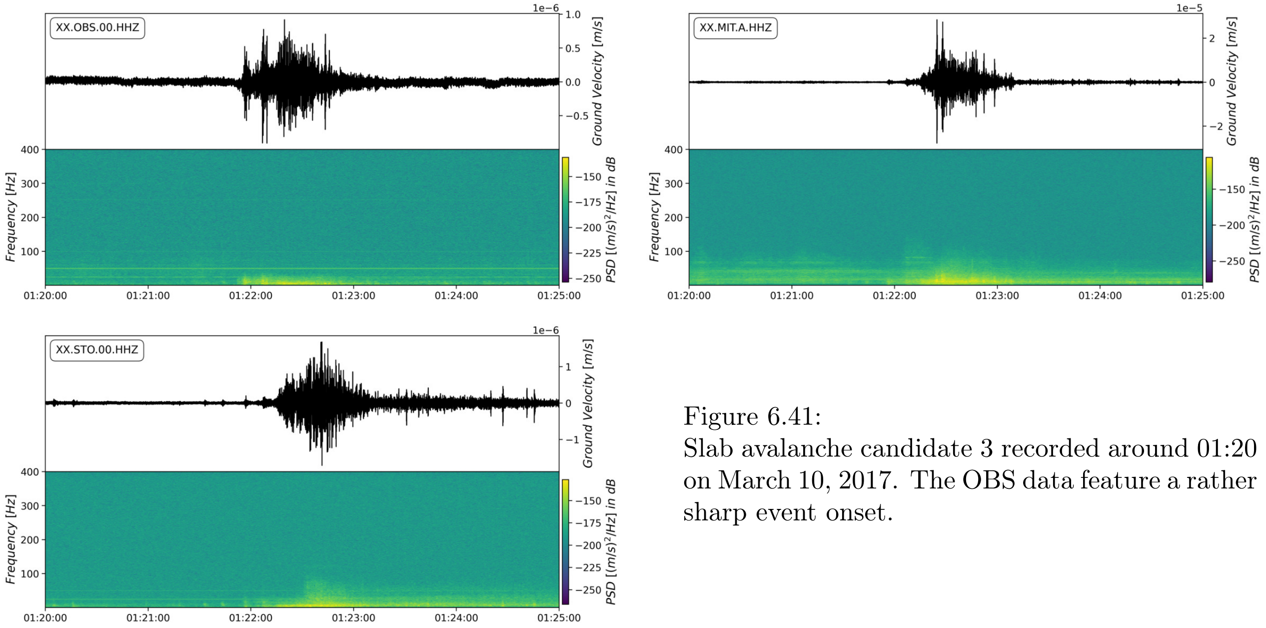

Figure 6.41:
Slab avalanche candidate 3 recorded around 01:20 on March 10, 2017. The OBS data feature a rather sharp event onset.

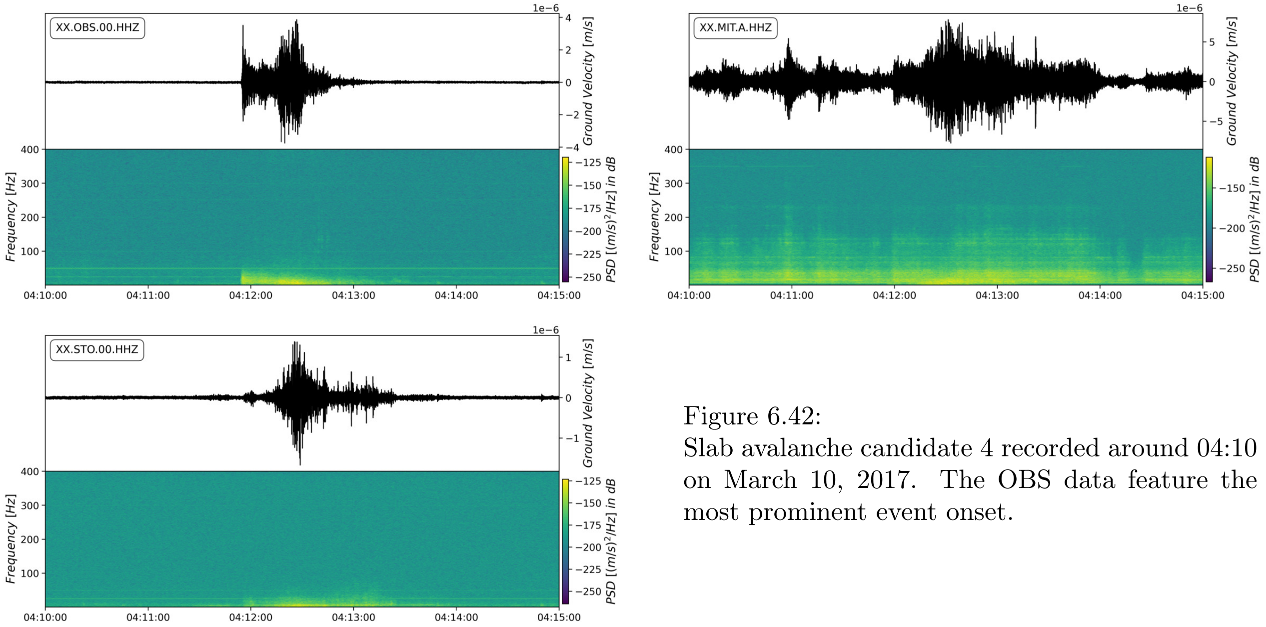

Figure 6.42:
Slab avalanche candidate 4 recorded around 04:10 on March 10, 2017. The OBS data feature the most prominent event onset.

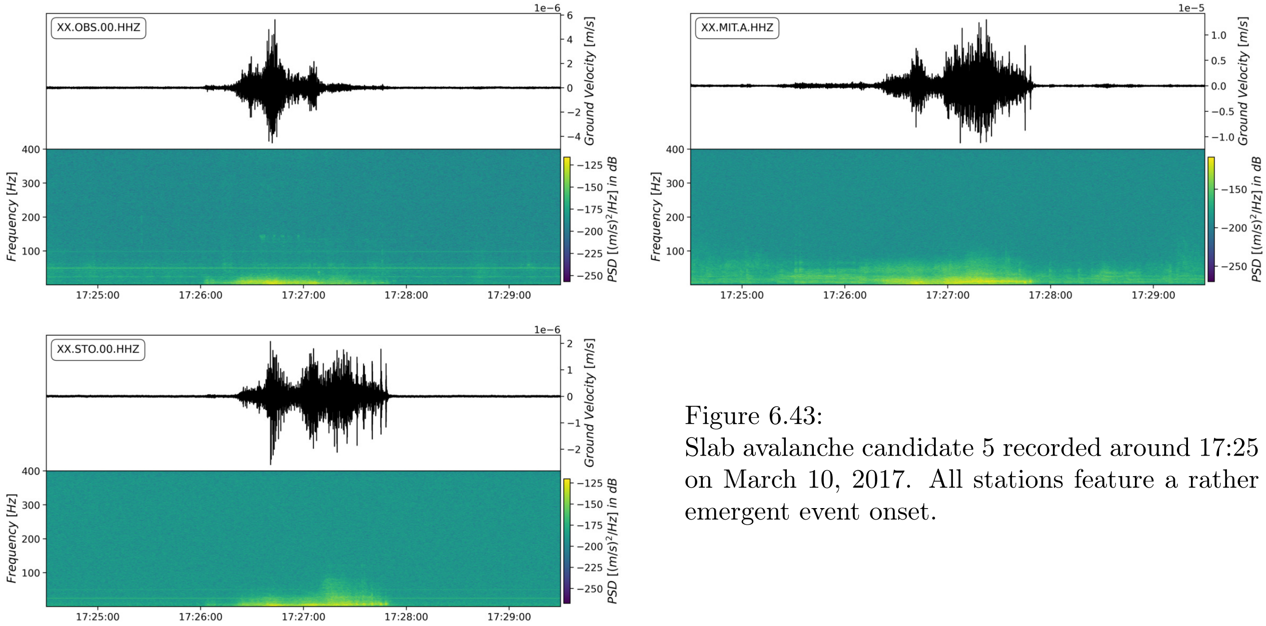

Figure 6.43:
Slab avalanche candidate 5 recorded around 17:25 on March 10, 2017. All stations feature a rather emergent event onset.

6.6 Discussion

In the following the main results of the *SeisRockHT* initiative are briefly discussed. Since no quality seismic data was gathered for the Kitzsteinhorn site, the discussion will focus on the Sonnblick site.

Throughout the five year project the terrestrial laser scanning (TLS) monitoring successfully delivered an overview of rockfall release zones and annually accumulated rockfall volumes. The majority of the detected main rockfall release zones (19 out of 25) was located in the lower half of the Sonnblick north-face ($< \sim 2850$ m a.s.l.), and the three largest in the closer surrounding of a glacier at the foot of the rockwall. The lower half of the Sonnblick north-face is more susceptible to climate change induced processes like glacier thinning, ice-face degradation and permafrost degradation. These are all likely rockfall drivers and potentially explain the altitudinal pattern of rockfall release zones observed by TLS. However, the lower data coverage in the upper half of the Sonnblick north-face is an alternative and artificial cause for the observed altitude disparity of rockfall release zones. Eventually, regular full coverage terrain surveys of the Sonnblick north-face are necessary to examine the role of the biased data coverage.

Visually validated rockfalls are building the base to develop robust seismic rockfall characteristics to (i) automate rockfall categorization algorithms, (ii) evaluate potential relations with rockfall parameters, and (iii) delineate dynamic rockfall phases. So far, however, just two visually validated rockfall events were registered. Consequently, a more solid database still needs to be built up to elaborate on these topics.

Following the environmental seismology approach, *SeisRockHT* data analysis re-affirmed that quality complementary data are indispensable for seismic data interpretation, as well as to suggest potential process chains. The seismic data analysis concentrated on two periods. The first period covered about 7 weeks in the autumn-winter transition in 2017 with regular rainfalls, and a temperature development from autumn towards winter. The other period covered a short-term extreme weather event in October, 2018, with thunderstorms accompanied by heavy rainfall and mud flows.

Ambient seismicity analysis revealed a variety of different seismic episodes. Generally, the STO monitoring site, which is sheltered in a tunnel at the valley floor, was most suited for ambient seismicity monitoring applications. The sheltered STO site naturally resulted in a lower amount of higher frequency single events and a generally reduced noise level. Clear diurnal patterns were present during the field campaign in 2017. Available complementary data suggested a correlation with the discharge of a local, melt-driven creek. Ambient seismicity analysis for the extreme weather event in 2018 showed a clear correlation with the available Bucheben river discharge.

In total 545 seismic events were manually categorized into 7 different event types (*Anthropogenic*, *Earthquake*, *Lightning*, *RC Long*, *RC Short*, *Tremor* and *Tremor LF*). While the event detection in 2017 was realized with an automated STA/LTA event detection and event binding (see section 5.2), the 2018 extreme weather data set was screened manually for events. Seismic characteristics of the detected events from the rockfall candidate categories generally suggest gravitational mass movements, and especially, rockfall events as source.

Generally, a clear increase of *RC Short* events with rising air temperature was observed for both investigation periods. However, this correlation might be due to the melting of a steep ice face at the terminus of the debris covered Pilatuskees glacier which regularly triggered boulders tumbling down the ice face. Dietze et al. (2017b) detected 37 potential rockfall events in a 37-day period. Compared to that, the *RC Short* occurrence rates of 7 to 20 potential rockfalls per day, as observed within the field campaign 2017, were relatively high. This suggests that the Pilatuskees 'ice face events' claimed a substantial proportion of the detected *RC Short* events. Eventually, the extent of the influence of the 'ice face events' needs to be evaluated in future work.

All *RC Long* events within the extreme weather event happened during the first main precipitation event. The seismic characteristics of the *RC Long* events propose a moving mass which passes the involved seismic stations. Generally, the detected tremor events were temporarily correlated with the rockfall candidate events. We suggest, that the mass movements which caused the observed mud and snow slide deposits (Figure 6.21) are amongst the registered *Tremor* or *RC Long* events, consequently, happened during the first main precipitation period of the extreme weather event.

Just two *RC Long* events were registered during the first precipitation event in the 2017 field campaign. However, a steep increase of the *Tremor LF* events was registered within the first precipitation events (August 26-28). Generally, the *Tremor LF* events showed constantly rising numbers throughout the whole campaign 2017 period, but with varying occurrence rates. Interestingly, the number of *Tremor LF* events maintained clear upward trends also throughout the precipitation-less period August 29-31. This precipitation-less period was characterized by rising air temperatures. A similar behavior was observed for the *Tremor* events throughout the extreme weather event in 2018, which also showed rising numbers during periods with rising temperatures, as well as precipitation. Generally, the occurrence of both tremor and rockfall candidate types were correlated and suggest that also the two tremor types are related to gravitational mass movements.

Dietze et al. (2017b) reported that the majority of their registered rockfalls was triggered by rainfall (∼40 %) and diurnal air temperatures changes (∼35 %), whereas they stressed, that the rockfalls were triggered during the coldest hours and during the highest temperature change rates of the day. Generally, we also observed a clear correlation of event occurrence with rainfall, however, not every precipitation event produced an increasing number of registered *RC Long* or tremor events. The observed air temperature correlation of the *RC Short* and both tremor event types was rather linked to steadily rising daily mean air temperatures (Figure 6.16). However, so far we did not thoroughly look into any potential diurnal variations of our detected events, and the role of the Pilatuskess ice face (Figure 6.17) also needs to be quantitatively addressed, before this point of discussion can be further elaborated. Generally, we could not observe any increase in rockfall candidate or tremor events during periods of steadily decreasing temperatures. Eventually, also the fact that the Dietze et al. (2017b) investigation site featured no occurrence of permafrost has to be taken into account.

During the two discussed periods also a suite of event types clearly not related to rockfalls were observed. Through the abundant available complementary data several sources of these non-rockfall event types were identified and demonstrated potential further applications of the installed *SeisRockHT* network (compare section 6.5).

7. Conclusions

The *SeisRockHT* initiative installed seismological networks at two prominent investigation sites in the 'Hohe Tauern' region. An open-design and low-cost approach was followed due to major cuts of the applied project budget. The free and open hardware *Ruwai* data recorder was deployed for the first time under rugged field conditions. In the first project phase a batch of eight *Ruwai* data recorders were built and eight seismic monitoring stations were installed for the two *SeisRockHT* networks. Due to varying site characteristics individual station installation concepts had to be designed and realized. Furthermore, the individual station designs were continuously adapted and improved throughout the course of the project.

The annual terrestrial laser scanning (TLS) surveys delivered an overview of active rockfall release zones (RRZs) and total rockfall volumes. A much higher resolution of RRZs was accomplished for the Kitzsteinhorn site, because of the significantly lower object distances (∼300 m) compared to the Sonnblick site (∼1000 m). During the four-year TLS monitoring period a total number of 71 RRZs with volumes ranging from 1.4 to 584.3 $\mathbf{m^3}$ was detected for the Sonnblick north-face. The dominant RRZ altitude was about 2800 m a.s.l.. A total number of 226 RRZs with a volume of 1490.2 $\mathbf{m^3}$ and a dominant altitude of about 2970 m a.s.l. was determined for the Kitzsteinhorn investigation site. The majority of the Kitzsteinhorn RRZs was detected in the rockwall sections close to the current glacier surface. An altitudinal pattern disparity with higher rockfall activity at the lower elevations was observed for both north-faces. While for the Kitzsteinhorn north-face a higher susceptibility for climate change induced processes at lower elevations is assumed to be the cause, the correlating Sonnblick north-face data coverage disparity in altitude leaves the open question to which extent the altitudinal pattern might be artificial. This needs to be clarified by regular full-coverage terrain surveys of the Sonnblick north-face in future.

The *Ruwai* data recorder delivered high quality seismic data for the Sonnblick site, however, persistent electromagnetic interferences made the Kitzsteinhorn data unusable. The recorded Sonnblick data exhibited several data gaps throughout the five years project duration. The main cause of the data gaps were power shortages during winter. Eventually, the seismic data yield could be more than doubled throughout the project. However, year-round operation especially of the exposed stand-alone stations MIT, MOR and PIL is an incessant task. The continuation of the visual rockfall monitoring on the Sonnblick observatory ensures a continuously growing database of seismic characteristics of validated rockfalls. Robust seismic rockfall characteristics are essential for further software development to test and automate suitable rockfall detection methods. Rockfall detection automation is indispensable to cope with the amount of continuously gathered seismic data and paves the way to a future operational rockfall monitoring.

The *SeisRockHT* seismic data analysis covered two periods. The first period covered about 7 weeks in autumn 2017 with regular rainfalls and a temperature development from autumn towards winter. The other period covered a short-term extreme weather event in October 2018 with thunderstorms accompanied by high rainfall and mud flows. Ambient seismicity analysis revealed correlations with river discharge and ongoing construction works in autumn 2017. Generally, the STO monitoring site in a tunnel at the valley floor was best suited for ambient seismicity monitoring.

In total 545 seismic events were manually categorized into seven different event types for the two chosen periods. Seismic characteristics of the detected events from the two rockfall candidate categories generally suggest gravitational mass movements, and, especially, rockfall events as source. Available complementary data revealed a clear increase of *Rockfall Candidate Short* events with rising temperatures. However, this correlation might be due to melting of a steep ice face at the terminus of the debris covered Pilatuskees glacier which regularly triggered tumbling down boulders. The relatively high *Rockfall Candidate Short* occurrence rates of several detected events per day support that the Pilatuskees 'ice face events' claimed a substantial proportion of the observed events. Eventually, the extent of the influence of the 'ice face events' needs to be evaluated in future work. *Rockfall Candidate Long* events showed a clear correlation with precipitation. We could not observe an increase in rockfall candidate events during periods of low and decreasing temperatures. The two tremor event types were temporarily related to the occurrence of the rockfall candidate events during periods of rising temperatures and rainfall. Thus, we suggest that the majority of the two detected tremor event types are also caused by gravitational mass movements. However, more quantitative analysis on the nature of the tremor events need to be done in future.

During the *SeisRockHT* project a suite of other event types, not related to rockfall activity, were also recorded. Several sources of the recorded seismic signals were identified due to abundant available complementary data and demonstrated further potential applications of the installed *SeisRockHT* networks.

8. Future Perspectives

The *SeisRockHT* initiative built the foundation of a long-term seismological monitoring at the two investigation sites. Currently, the maintenance of the Sonnblick seismological network is assured by the ZAMG-internal project ASBO and the ZAMG-based long-term monitoring project GCW-Permafrost. Furthermore, gathered seismic data is stored at the Austrian Seismological Service based at the ZAMG.

The seismological network at the Kitzsteinhorn is currently not operative. As discussed in section 3.1, the *SeisRockHT Ruwai* version showed persistent electromagnetic interferences for the Kitzsteinhorn site which made the gathered data unusable. Nevertheless, the *SeisRockHT* seismic sensors are still in place and with new funding a fully shielded and improved *Ruwai* data recorder successor will be tested.

Long-Term Monitoring Perspective

A general aim is the continuous improvement of the seismological setup towards an operational monitoring which is depending on several points. The important regular station maintenance work is currently assured by running projects. A solid power supply of each individual station is another fundamental point. Already throughout the *SeisRockHT* project a lot of improvements were successfully implemented which constantly increased the data yield. As a next step a low-power version of the free and open hardware *Ruwai* data recorder is planned which assures another increase in data yield. Additionally, we aim to successfully resume the seismological monitoring at the Kitzsteinhorn site with one of the new *Ruwai* designs.

The continuation of the visual rockfall monitoring is constantly building up the data base to identify more robust seismic rockfall characteristics which will substantially support the development of automated rockfall detection methods. Automated rockfall detection methods are indispensable to cope with the amount of accruing data. In a longer run station status transmissions and subsequently real-time data availability is aimed. Public accessibility of the Sonnblick seismological data will be realized over the homepage `www.sonnblick.net`.

The north-face terrain monitoring will be continued by *Georesearch* at both sites. The Kitzsteinhorn terrain monitoring is funded by the *OpAL* long-term monitoring project. Since 2018 the Sonnblick north-face is surveyed photogrammetrically by unmmanned aerial vehicles (UAVs). Compared to the previous TLS measurements, UAV surveys achieve a homogeneous point density across the entire rockwall and are capable of overcoming the prominent occlusion effects within the main couloirs. This ongoing initiative will deliver the data base to evaluate e.g. if the observed disparity in altitude at the Sonnblick north-face is real or artificial. The UAV surveys are funded by the ZAMG-internal ASBO project.

Scientific Perspective

The main *SeisRockHT* research question, if rockfall activity of permafrost-affected alpine north-faces is increasing in a warming climate, needs a more solid database and is a clear long-term task. The available rock temperature data represents a precious complementary data set which has the potential to reveal rock permafrost-related triggering processes.

The continuation of the visual rockfall monitoring on the Sonnblick observatory is delivering a continuously growing database of seismic rockfall characteristics. Besides the already mentioned support for the necessary automation of rockfall detection methods, such a database also builds the foundation to evaluate potential relations with rockfall parameters, and potentially delineate dynamic rockfall phases. Furthermore, the extension of the *SeisRockHT* networks with an infrasound sensor would provide another source to better validate and characterize rockfalls. An infrasound sensor test is planned for the field season 2021.

The still unsure nature of the observed abundant tremor event types needs to be further investigated. Interferometric methods are potentially able to reveal waveform patterns that can be tracked throughout the installed mini-arrays and/or in between the individual monitoring stations.

Due to the amount of continuously gathered data the implementation of an automated rockfall event localization scheme is indispensable. However, back azimuth calculations would be a starting point to e.g. evaluate the role of the Pilatuskess 'ice face events' and determine rockfall impact directions which can ideally be linked to determined rockfall release zones.

A long-term scientific aim is the quantitative union of the terrain and the seismic monitoring to ideally assign every seismic rockfall event a release zone and volume. A starting point for that is the calculation of magnitudes for the *SeisRockHT* networks which would require an active seismic experiment to determine all necessary seismic parameters for the individual investigation sites.

One of the main advantages of seismic monitoring is the quasi-continuous observation of a region. That makes seismic monitoring especially suited to observe occasional events. Beside the aimed rockfalls, also other occasional events like mudflows and avalanches were potentially detected by the *SeisRockHT* network. Consequently, seismological monitoring can be the base of a comprehensive natural hazards monitoring.

9. Acknowledgements

The establishment of a permanent seismological monitoring within *SeisRockHT* was an ambitious initiative and would not have been possible without the support of other projects, institutions and individuals. The initial network installations, as well as the continuous improvements and adaptations involved elaborate logistics, extra hardware and fieldwork volunteers. Ultimately, keeping the *SeisRockHT* status quo to assure the aimed long-term perspective is crucially dependent on steady basic funding.

The ZAMG project ASBO ('Active Sonnblick Observatory') logistically and financially supported *SeisRockHT*. The ASBO project assures the continuation of long-term monitoring programs at the Sonnblick observatory and is managed by Sonnblick observatory scientific manager Dr. Elke Ludewig. Eventually, the continuation of the within *SeisRockHT* initiated rockfall monitoring at the Sonnblick north-face is not possible without this support. Additionally, Dr. Elke Ludewig provided complementary data.

The Global Cryosphere Watch (GCW) - Permafrost project has been financially supporting *SeisRockHT* and assures the continuation of the *SeisRockHT* initiative. GCW-Permafrost is managed by Mag. Stefan Reisenhofer and funded by the Austrian Ministry for Sustainability and Tourism (`www.bmnt.gov.at`). Mag. Stefan Reisenhofer also provided rock temperature data gathered within the GCW-Permafrost project.

Nikolaus Horn from the Seismological Service of Austria implemented the gathered seismic data into the Seismological Service of Austria data infrastructure. The Seismological Service of Austria is based at the ZAMG.

Hermann, Gerid and Günther from the Sonnblickbasis (`http://sonnblickbasis.at/`) generally supported *SeisRockHT* field activities, and especially through their workshop including all the available hardware and tools. Furthermore, the STO station in the tunnel at the Kolm Saigurn valley floor is supplied with Sonnblickbasis mains power.

The staff of the Sonnblick observatory and the Kitzsteinhorn Bergbahnen greatly supported *SeisRockHT* with material transport and notice in case of visual station damage.

Leo Hettegger, DI Gerhard Schauer, Msc. Christian Maier and Mag. Claudia Riedl from the ZAMG regional office in Salzburg helped out with material, field work and provided complementary data.

Werner Bernhard and DI Hans Wiesenegger from the Hydrological Service of Salzburg provided river discharge data.

Dr. Maier Martin, head of the ZAMG Technology Department, helped out with hardware and the installation of the GPS system for the OBS station at the Sonnblick summit.

Anton Neureiter (ZAMG, Vienna) helped out with digging down meters of snow.

Finally, I want to thank all the fieldworkers who volunteered in their free time: Alexander Naringbauer, Alexander Standteiner, Babis Charalampidis, Bernhard Hynek, Daniel Holleis, Felix Leimböck, Gudrun Bruckner, Kirstine Skov, Roland Mayer, Severin Mayrhofer, Walter Jenner and Willi Köstinger.

10. Author Contributions

B.D. devised the project and the main conceptual ideas in close collaboration with all the other authors. B.D. was responsible for the project application and redesigned with M.S. the project due to the major budget cuts. M.S. and B.D. built the seismic data recorders. Generally, design and realization of the two monitoring networks was done by B.D. and M.S., and for the Kitzsteinhorn site in close collaboration with H.I. and K.M.. Network maintenance and improvement was done by B.D with help from M.S., H.I. and K.M.. L.W. supported network improvements and the seismic data implementation into the Austrian Seismological Service data infrastructure. Developments for the seismic data recorder and seismic processing software were carried out by M.S.. Terrestrial laser scanning surveys and data processing was done by H.I.. Seismic data was processed by M.S. with contributions from B.D.. Data analysis, data interpretation and discussion of the results was done by B.D., M.S. and H.I.. B.D. was responsible for the final report with contributions from M.S. and H.I.. M.S., H.I. and L.W. commented on the report.

11. Dissemination and Outreach

Presentations

Binder, D., Hartmeyer, I., Keuschnig, M., Mertl, S., & Lenhardt, W. (2016). SeisRockHT - Seismic Rockfall Monitoring in the Hohe Tauern region. *Geophysical Research Abstracts, 18, EGU2016-6892.* EGU General Assembly, Vienna (A).

Binder, D., Hartmeyer, I., Keuschnig, M., Mertl, S., & Lenhardt, W. (2016). SeisRockHT - Seismic Rockfall Monitoring in the Hohe Tauern region. Sonnblick Verein General Assembly, Vienna (A).

Binder, D., Hartmeyer, I., Keuschnig, M., Mertl, S., & Lenhardt, W. (2017). SeisRockHT - Seismic Rockfall Monitoring in the Hohe Tauern region. *Geophysical Research Abstracts, 19, EGU2017-17451.* EGU General Assembly, Vienna (A).

Binder, D., Hartmeyer, I., Keuschnig, M., Mertl, S., & Lenhardt, W. (2017). SeisRockHT - Seismic Rockfall Monitoring in the Hohe Tauern region. EGU Galileo Conference *From process to signal – advancing environmental seismology*, Ohlstadt (D), 6-9 June.

Binder, D., Hartmeyer, I., Keuschnig, M., Mertl, S., & Lenhardt, W. (2017). SeisRockHT - Seismic Rockfall Monitoring in the Hohe Tauern region. 6th International Symposium for Research in Protected Areas, Salzburg (A), 2-4 November.

ZAMG Press Release (August 2015)

The *SeisRockHT* project built the basis for the following press release by the Zentralanstalt for Meteorology and Geodynamics about permafrost degradation in the Alps. The press release was covered by 11 newspapers. The full press release as well as the press review can be found in Appendix F.

ZAMG
Zentralanstalt für
Meteorologie und
Geodynamik

11. August 2015

Projekt SeisRockHT:
Steinschlag-Aktivität in den Hohen Tauern

Am Sonnblick-Observatorium der ZAMG dürfte dieser Sommer so wenige Frosttage wie selten zuvor in der mehr als 100jährigen Messgeschichte bringen. Die in den letzten Jahrzehnten stetig steigenden Temperaturen im Hochgebirge führen zum Auftauen des Permafrostes. Das kann zu einem Anstieg alpiner Gefahren führen, wie etwa Steinschlag.

Das von der ZAMG geleitete Projekt SeisRockHT (Seismic Rockfall Monitoring in the Hohe Tauern Region) untersucht die Häufigkeit von Steinschlag und mögliche Zusammenhänge mit Faktoren wie Wetter und Klima.

Der extrem heiße Sommer 2015 bringt auch im Hochgebirge ungewöhnlich hohe Temperaturen. Am Sonnblick-Observatorium der Zentralanstalt für Meteorologie und Geodynamik (ZAMG) wurden heuer seit Anfang Juni nur 22 Frosttage gemessen, also Tage an denen die Temperatur zumindest für kurze Zeit unter 0 °C liegt. Im vieljährigen Mittel liegt die Zahl der Frosttage am Sonnblick im klimatologischen Sommer (Juni, Juli, August) bei 44 Tagen. Momentan zeichnet sich für 2015 sogar einer der zehn extremsten Werte der seit 1886 bestehenden Messgeschichte ab. Den absoluten Rekord verzeichnet weiterhin der Sommer 2003 mit nur 18 Frosttagen am Sonnblick.

Wie sehr beeinflussen die Änderungen im Permafrost die alpine Sicherheit?

Die in den letzten Jahren sinkende Zahl der Frosttage im Hochgebirge entspricht dem Szenario einer langfristigen Klimaerwärmung. Weltweit sind rund 20 bis 25 Prozent der Erdoberfläche von Permafrost beeinflusst. Eine Konsequenz der Klimaerwärmung ist das Auftauen des Permafrostes, was sich auf Steinschlag- und Felssturz Ereignisse auswirkt. Permafrost wird thermisch definiert als Untergrund, der mindestens zwei Jahre Temperaturen kleiner oder gleich 0 °C aufweist. Topographie, Exposition, Höhe oder Untergrundeigenschaften beeinflussen die Permafrostverbreitung. In Österreich ist ab einer Seehöhe von ca. 2.500 m

Ruwai se

Throughout the project the new *Ruwai se* prototype was developed including major software fixes and a better usability in the field. Further details are described in section 3.1.

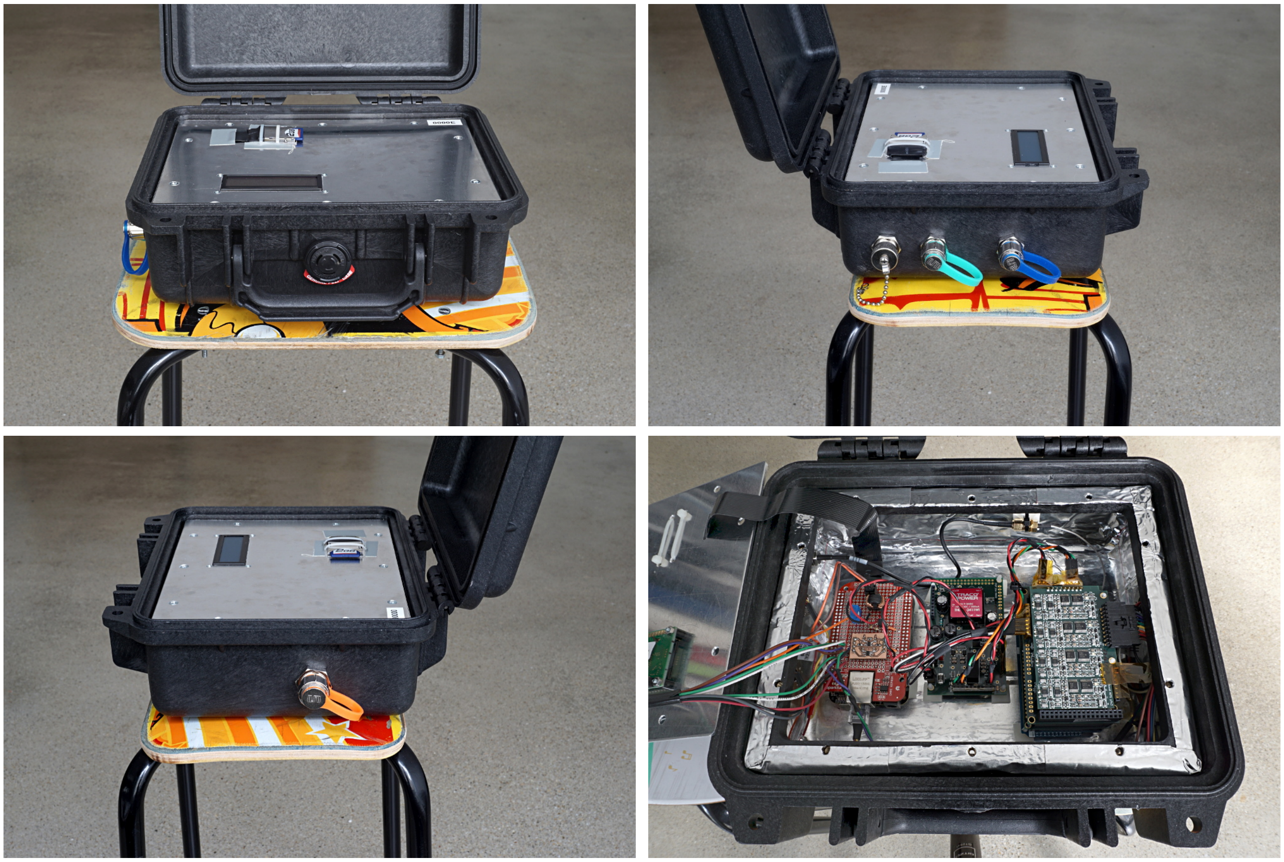

New pSysmon modules

The *pSysmon* software (available from `https://github.com/scientificsteve`) was improved within the *SeisRockHT* project. Besides the enhancement of general software features, several additional software modules have been added:

Array Geometry Support for array station layout in the *pSysmon* data and seismogram display.

STA/LTA Detection Implementation of a STA/LAT detection algorithm.

Detection Binding Implementation of a detection binding dedicated to small extent networks and mini-arrays.

Long Term Spectrograms Implementation of a workflow to compute the power spectral density and create spectrogram images of long timespans (> 1 day).

NOW Project

The within *SeisRockHT* developed open-design seismic monitoring strategy is the base for the successful *NOW (Noise of thaw)* project application. The improved *Ruwai se* datalogger is deployed within the *NOW* project. The *NOW* project is a joint effort of the Geological Survey from Denmark and Greenland (GEUS), *University of Copenhagen*, *University of Oklahoma*, and *Mertl Research GmbH*. *NOW* is funded by *Geocenter*, a center of geoscientific research, education, consulting, innovation and publishing at a high international level based in Denmark. The *NOW* project has a total budget of €127,000.- and started in May 2020. In summer 2020 seismic monitoring stations will be deployed at three investigation sites in Greenland. The full project application can be found in Appendix F.

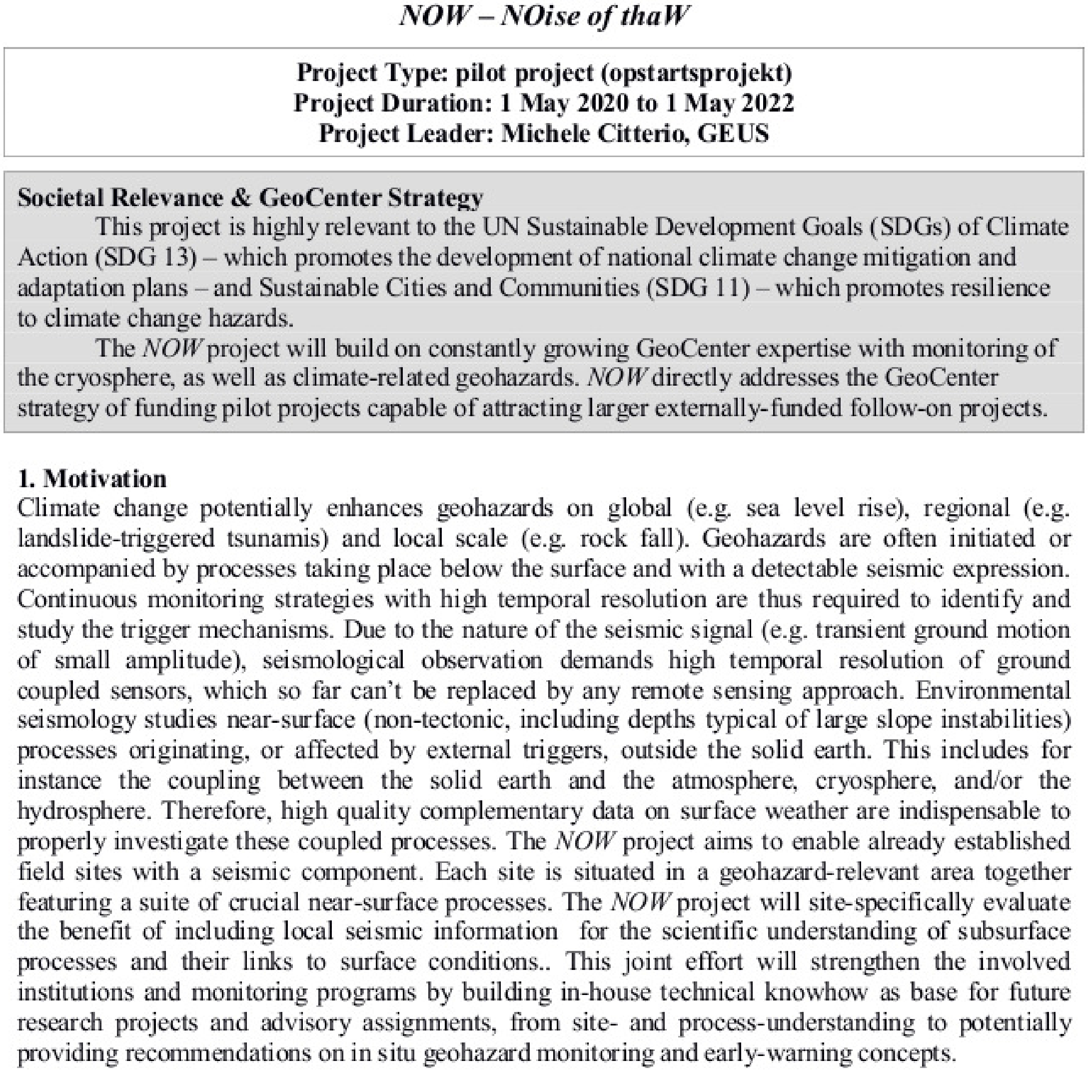

NOW – NOise of thaW

Project Type: pilot project (opstartsprojekt)
Project Duration: 1 May 2020 to 1 May 2022
Project Leader: Michele Citterio, GEUS

Societal Relevance & GeoCenter Strategy

This project is highly relevant to the UN Sustainable Development Goals (SDGs) of Climate Action (SDG 13) – which promotes the development of national climate change mitigation and adaptation plans – and Sustainable Cities and Communities (SDG 11) – which promotes resilience to climate change hazards.

The *NOW* project will build on constantly growing GeoCenter expertise with monitoring of the cryosphere, as well as climate-related geohazards. *NOW* directly addresses the GeoCenter strategy of funding pilot projects capable of attracting larger externally-funded follow-on projects.

1. Motivation

Climate change potentially enhances geohazards on global (e.g. sea level rise), regional (e.g. landslide-triggered tsunamis) and local scale (e.g. rock fall). Geohazards are often initiated or accompanied by processes taking place below the surface and with a detectable seismic expression. Continuous monitoring strategies with high temporal resolution are thus required to identify and study the trigger mechanisms. Due to the nature of the seismic signal (e.g. transient ground motion of small amplitude), seismological observation demands high temporal resolution of ground coupled sensors, which so far can't be replaced by any remote sensing approach. Environmental seismology studies near-surface (non-tectonic, including depths typical of large slope instabilities) processes originating, or affected by external triggers, outside the solid earth. This includes for instance the coupling between the solid earth and the atmosphere, cryosphere, and/or the hydrosphere. Therefore, high quality complementary data on surface weather are indispensable to properly investigate these coupled processes. The *NOW* project aims to enable already established field sites with a seismic component. Each site is situated in a geohazard-relevant area together featuring a suite of crucial near-surface processes. The *NOW* project will site-specifically evaluate the benefit of including local seismic information for the scientific understanding of subsurface processes and their links to surface conditions.. This joint effort will strengthen the involved institutions and monitoring programs by building in-house technical knowhow as base for future research projects and advisory assignments, from site- and process-understanding to potentially providing recommendations on in situ geohazard monitoring and early-warning concepts.

Peer-Reviewed Papers

No peer-reviewed papers based on the *SeisRockHT* seismic monitoring data were published yet. However, *SeisRockHT* project partners recently published results of a project overarching long-term terrestrial laser scanning campaign. *SeisRockHT* terrestrial laser scanning surveys contributed to the analysed database.

Hartmeyer, I., Delleske, R., Keuschnig, M., Krautblatter, M., Lang, A., Schrott, L., & Otto, J.-C. (2020). Current glacier recession causes significant rockfall increase: The immediate paraglacial response of deglaciating cirque walls. *Earth Surface Dynamics*, 8(3), 729–751. doi:https://doi.org/10.5194/esurf-8-729-2020

Hartmeyer, I., Keuschnig, M., Delleske, R., Krautblatter, M., Lang, A., Schrott, L., & Otto, J.-C. (2020). A 6-year lidar survey reveals enhanced rockwall retreat and modified rockfall magnitudes/frequencies in deglaciating cirques. *Earth Surface Dynamics*, 8(3), 753–768. doi:https://doi.org/10.5194/esurf-8-753-2020

References

Abellán, A., Calvet, J., Vilaplana, J. M., & Blanchard, J. (2010, July). Detection and spatial prediction of rockfalls by means of terrestrial laser scanner monitoring. *Geomorphology*, *119*(3), 162–171. Retrieved 2020-03-11, from `http://www.sciencedirect.com/science/article/pii/S0169555X10001224` doi: 10.1016/j.geomorph.2010.03.016

Abellán, A., Vilaplana, J. M., Calvet, J., García-Sellés, D., & Asensio, E. (2011, March). Rockfall monitoring by Terrestrial Laser Scanning – case study of the basaltic rock face at Castellfollit de la Roca (Catalonia, Spain). *Natural Hazards and Earth System Sciences*, *11*(3), 829–841. Retrieved 2020-03-11, from `https://www.nat-hazards-earth-syst-sci.net/11/829/2011/` (Publisher: Copernicus GmbH) doi: https://doi.org/10.5194/nhess-11-829-2011

Allen, R. (1978). Automatic earthquake recognition and timing from single traces. *Bulletin of the Seismological Society of America*, *68*(5), 1521–1532–. (Number: 5)

Allen, S., & Huggel, C. (2013, August). Extremely warm temperatures as a potential cause of recent high mountain rockfall. *Global and Planetary Change*, *107*, 59–69. Retrieved 2020-04-20, from `http://www.sciencedirect.com/science/article/pii/S0921818113001112` doi: 10.1016/j.gloplacha.2013.04.007

Amitrano, D., Arattano, M., Chiarle, M., Mortara, G., Occhiena, C., Pirulli, M., & Scavia, C. (2010, April). Microseismic activity analysis for the study of the rupture mechanisms in unstable rock masses. *Natural Hazards and Earth System Sciences*, *10*(4), 831–841. Retrieved 2020-02-12, from `https://www.nat-hazards-earth-syst-sci.net/10/831/2010/nhess-10-831-2010.html` doi: https://doi.org/10.5194/nhess-10-831-2010

Barlow, J., Lim, M., Rosser, N., Petley, D., Brain, M., Norman, E., & Geer, M. (2012, February). Modeling cliff erosion using negative power law scaling of rockfalls. *Geomorphology*, *139-140*, 416–424. Retrieved 2020-03-11, from `http://www.sciencedirect.com/science/article/pii/S0169555X11005903` doi: 10.1016/j.geomorph.2011.11.006

Barr, I. D., & Spagnolo, M. (2015, December). Glacial cirques as palaeoenvironmental indicators: Their potential and limitations. *Earth-Science Reviews*, *151*, 48–78. Retrieved 2020-03-11, from `http://www.sciencedirect.com/science/article/pii/S0012825215300519` doi: 10.1016/j.earscirev.2015.10.004

Benn, D., & Evans, D. J. A. (2011). *Glaciers and Glaciation, 2nd edition: 2nd Edition (Paperback) - Routledge.* Routledge Taylor & Francis Group. Retrieved 2020-03-11, from `https://www.routledge.com/Glaciers-and-Glaciation-2nd-edition-2nd-Edition/Benn-Evans/p/book/9780340905791`

Brückl, E., & Mertl, S. (2013). Monitoring and Predicting Acceleration and Deceleration of Large Landslides – Part of TU Wien. *OeAW (ISDR) - Final Report*, 71. doi: 10.1553/ISDR-24

Chen, Y., & Medioni, G. (1992, April). Object modelling by registration of multiple range images. *Image and Vision Computing*, *10*(3), 145–155. Retrieved 2020-03-11, from `http://www.sciencedirect.com/science/article/pii/026288569290066C` doi: 10.1016/0262-8856(92)90066-C

Cochran, E. S. (2018, July). To catch a quake. *Nature Communications*, *9*(1), 1–4. Retrieved 2020-04-22, from `https://www.nature.com/articles/s41467-018-04790-9` (Number: 1 Publisher: Nature Publishing Group) doi: 10.1038/s41467-018-04790-9

Dammeier, F., Moore, J. R., Haslinger, F., & Loew, S. (2011). Characterization of alpine rockslides using statistical analysis of seismic signals. *Journal of Geophysical Research: Earth Surface*, *116*(F4). Retrieved 2020-04-20, from `https://agupubs.onlinelibrary.wiley.com/doi/abs/10.1029/2011JF002037` (_eprint: https://agupubs.onlinelibrary.wiley.com/doi/pdf/10.1029/2011JF002037) doi: 10.1029/2011JF002037

Deparis, J., Jongmans, D., Cotton, F., Baillet, L., Thouvenot, F., & Hantz, D. (2008, August). Analysis of Rock-Fall and Rock-Fall Avalanche Seismograms in the French AlpsAnalysis of Rock-Fall and Rock-Fall Avalanche Seismograms in the French Alps. *Bulletin of the Seismological Society of America*, *98*(4), 1781–1796. Retrieved 2020-02-12, from `https://pubs.geoscienceworld.org/bssa/article/98/4/1781/341946/Analysis-of-Rock-Fall-and-Rock-Fall-Avalanche` doi: 10.1785/0120070082

Dietze, M., Mohadjer, S., Turowski, J. M., Ehlers, T. A., & Hovius, N. (2017a, October). Seismic monitoring of small alpine rockfalls – validity, precision and limitations. *Earth Surface Dynamics*, *5*(4), 653–668. Retrieved 2020-02-07, from `https://www.earth-surf-dynam.net/5/653/2017/` doi: https://doi.org/10.5194/esurf-5-653-2017

Dietze, M., Turowski, J. M., Cook, K. L., & Hovius, N. (2017b, November). Spatiotemporal patterns, triggers and anatomies of seismically detected rockfalls. *Earth Surface Dynamics*, *5*(4), 757–779. Retrieved 2020-02-07, from `https://www.earth-surf-dynam.net/5/757/2017/` doi: https://doi.org/10.5194/esurf-5-757-2017

Dramis, F., Govi, M., Guglielmin, M., & Mortara, G. (1995). Mountain permafrost and slope instability in the Italian Alps: The Val Pola Landslide. *Permafrost and Periglacial Processes*, *6*(1), 73–81. Retrieved 2020-02-10, from `https://onlinelibrary.wiley.com/doi/abs/10.1002/ppp.3430060108` doi: 10.1002/ppp.3430060108

Eibl, E. P. S., Lokmer, I., Bean, C. J., & Akerlie, E. (2017, May). Helicopter location and tracking using seismometer recordings. *Geophysical Journal International*, *209*(2), 901–908. Retrieved 2020-10-20, from `https://academic.oup.com/gji/article/209/2/901/2972867` (Publisher: Oxford Academic) doi: 10.1093/gji/ggx048

Eibl, E. P. S., Lokmer, I., Bean, C. J., Akerlie, E., & Vogfjörd, K. S. (2015, October). Helicopter vs. volcanic tremor: Characteristic features of seismic harmonic tremor on volcanoes. *Journal of Volcanology and Geothermal Research*, *304*, 108–117. Retrieved 2020-10-20, from `http://www.sciencedirect.com/science/article/pii/S0377027315002516` doi: 10.1016/j.jvolgeores.2015.08.002

Ewald, A., Hartmeyer, I., Keuschnig, M., Lang, A., & Otto, J.-C. (2019, April). Fracture dynamics in an unstable, deglaciating headwall,Kitzsteinhorn, Austria. In (Vol. 21). Geophysical Research Abstracts. Retrieved 2020-03-11, from `https://meetingorganizer.copernicus.org/EGU2019/EGU2019-3055.pdf` doi: 10.5194/tc-2019-42

Fischer, L., Kääb, A., Huggel, C., & Noetzli, J. (2006, September). Geology, glacier retreat and permafrost degradation as controlling factors of slope instabilities in a high-mountain rock wall: the Monte Rosa east face. *Natural Hazards and Earth System Sciences*, *6*(5), 761–772. Retrieved 2020-02-10, from `https://www.nat-hazards-earth-syst-sci.net/6/761/2006/` doi: https://doi.org/10.5194/nhess-6-761-2006

Fuchs, F., Lenhardt, W., Bokelmann, G., & the AlpArray Working Group. (2018, October). Seismic detection of rockslides at regional scale: examples from the Eastern Alps and feasibility of kurtosis-based event location. *Earth Surface Dynamics*, *6*(4), 955–970. Retrieved 2020-04-20, from `https://www.earth-surf-dynam.net/6/955/2018/` (Publisher: Copernicus GmbH) doi: https://doi.org/10.5194/esurf-6-955-2018

Glade, T., Mergili, M., & Sattler, K. (2020). *ExtremA 2019*. Vandenhoeck & Ruprecht verlage. Retrieved 2020-09-10, from `https://www.vandenhoeck-ruprecht-verlage.com/themen-entdecken/sozial-rechts-und-wirtschaftswissenschaften/natur-landschaft/55101/extrema-2019`

Got, J.-L., Mourot, P., & Grangeon, J. (2010, April). Pre-failure behaviour of an unstable limestone cliff from displacement and seismic data. *Natural Hazards and Earth System Sciences*, *10*(4), 819–829. Retrieved 2020-02-12, from `https://www.nat-hazards-earth-syst-sci.net/10/819/2010/` doi: https://doi.org/10.5194/nhess-10-819-2010

Gruber, S., & Haeberli, W. (2007). Permafrost in steep bedrock slopes and its temperature-related destabilization following climate change. *Journal of Geophysical Research: Earth Surface*, *112*(F2). Retrieved 2020-02-10, from `https://agupubs.onlinelibrary.wiley.com/doi/abs/10.1029/2006JF000547` doi: 10.1029/2006JF000547

Gruber, S., Hoelzle, M., & Haeberli, W. (2004). Permafrost thaw and destabilization of Alpine rock walls in the hot summer of 2003. *Geophysical Research Letters*, *31*(13). Retrieved 2020-02-10, from `https://agupubs.onlinelibrary.wiley.com/doi/abs/10.1029/2004GL020051` doi: 10.1029/2004GL020051

Gruner, U. (2008). Climatic and meteorological influences on rockfall and rockslides. *Interpaevent 2008 - Conference Proceedings*, 12. Retrieved from `http://www.interpraevent.at/?tpl=tagungsbaende_detail.php&band_id=1288&menu=221`

Haeberli, W., Huggel, C., Kääb, A., Zgraggen-Oswald, S., Polkvoj, A., Galushkin, I., … Osokin, N. (2004). The Kolka-Karmadon rock/ice slide of 20 September 2002: an extraordinary event of historical dimensions in North Ossetia, Russian Caucasus. *Journal of Glaciology*, *50*(171), 533–546. Retrieved 2020-02-10, from `https://www.cambridge.org/core/journals/journal-of-glaciology/article/kolkakarmadon-rockice-slide-of-20-september-2002-an-extraordinary-event-of-historical-dimensions-in-north-ossetia-russian-caucasus/7FA91EBF980A35D0235A3A32B13A4FA7` doi: 10.3189/172756504781829710

Haeberli, W., Schaub, Y., & Huggel, C. (2017, September). Increasing risks related to landslides from degrading permafrost into new lakes in de-glaciating mountain ranges. *Geomorphology*, *293*, 405–417. Retrieved 2020-02-10, from `http://www.sciencedirect.com/science/article/pii/S0169555X16300381` doi: 10.1016/j.geomorph.2016.02.009

Hartmeyer, I., Delleske, R., Keuschnig, M., Krautblatter, M., Lang, A., Schrott, L., & Otto, J.-C. (2020b, September). Current glacier recession causes significant rockfall increase: the immediate paraglacial response of deglaciating cirque walls. *Earth Surface Dynamics*, *8*(3), 729–751. Retrieved 2020-10-30, from `https://esurf.copernicus.org/articles/8/729/2020/` (Publisher: Copernicus GmbH) doi: https://doi.org/10.5194/esurf-8-729-2020

Hartmeyer, I., Keuschnig, M., Delleske, R., Krautblatter, M., Lang, A., Schrott, L., … Otto, J.-C. (2020a, September). A 6-year lidar survey reveals enhanced rockwall retreat and modified rockfall magnitudes/frequencies in deglaciating cirques. *Earth Surface Dynamics*, *8*(3), 753–768. Retrieved 2020-10-30, from `https://esurf.copernicus.org/articles/8/753/2020/` (Publisher: Copernicus GmbH) doi: https://doi.org/10.5194/esurf-8-753-2020

Hartmeyer, I., Keuschnig, M., & Schrott, L. (2012). A scale-oriented approach for the long-term monitoring of ground thermal conditions in permafrost-affected rock faces, Kitzsteinhorn, Hohe Tauern Range, Austria. *Austrian Journal of Earth Sciences*, *105*(2), 128–139.

Hasler, A., Gruber, S., & Beutel, J. (2012). Kinematics of steep bedrock permafrost. *Journal of Geophysical Research: Earth Surface*, *117*(F1). Retrieved 2020-02-10, from `https://agupubs.onlinelibrary.wiley.com/doi/abs/10.1029/2011JF001981` doi: 10.1029/2011JF001981

Helmstetter, A., & Garambois, S. (2010). Seismic monitoring of Séchilienne rockslide (French Alps): Analysis of seismic signals and their correlation with rainfalls. *Journal of Geophysical Research: Earth Surface*, *115*(F3). Retrieved 2020-02-12, from `https://agupubs.onlinelibrary.wiley.com/doi/abs/10.1029/2009JF001532` doi: 10.1029/2009JF001532

Hibert, C., Malet, J.-P., Bourrier, F., Provost, F., Berger, F., Bornemann, P., … Mermin, E. (2017, May). Single-block rockfall dynamics inferred from seismic signal analysis. *Earth Surface Dynamics*, *5*(2), 283–292. Retrieved 2020-02-13, from `https://www.earth-surf-dynam.net/5/283/2017/` doi: https://doi.org/10.5194/esurf-5-283-2017

Hibert, C., Mangeney, A., Grandjean, G., & Shapiro, N. M. (2011). Slope instabilities in Dolomieu crater, Réunion Island: From seismic signals to rockfall characteristics. *Journal of Geophysical Research: Earth Surface*, *116*(F4). Retrieved 2020-02-12, from `https://agupubs.onlinelibrary.wiley.com/doi/abs/10.1029/2011JF002038` doi: 10.1029/2011JF002038

Hock, R. (2003, November). Temperature index melt modelling in mountain areas. *Journal of Hydrology*, *282*(1), 104–115. Retrieved 2020-10-28, from `http://www.sciencedirect.com/science/article/pii/S0022169403002579` doi: 10.1016/S0022-1694(03)00257-9

Keuschnig, M., Krautblatter, M., Hartmeyer, I., Fuss, C., & Schrott, L. (2017). Automated Electrical Resistivity Tomography Testing for Early Warning in Unstable Permafrost Rock Walls Around Alpine Infrastructure. *Permafrost and Periglacial Processes*, *28*(1), 158–171. Retrieved 2020-03-11, from `https://onlinelibrary.wiley.com/doi/abs/10.1002/ppp.1916` (_eprint:

https://onlinelibrary.wiley.com/doi/pdf/10.1002/ppp.1916) doi: 10.1002/ppp.1916

Kogelnig, A., Suriñach, E., Vilajosana, I., Hübl, J., Sovilla, B., Hiller, M., & Dufour, F. (2011, August). On the complementariness of infrasound and seismic sensors for monitoring snow avalanches. *Natural Hazards and Earth System Sciences*, *11*(8), 2355–2370. Retrieved 2020-10-22, from `https://nhess.copernicus.org/articles/11/2355/2011/` (Publisher: Copernicus GmbH) doi: https://doi.org/10.5194/nhess-11-2355-2011

Krautblatter, M., Funk, D., & Günzel, F. K. (2013). Why permafrost rocks become unstable: a rock–ice-mechanical model in time and space. *Earth Surface Processes and Landforms*, *38*(8), 876–887. Retrieved 2020-02-10, from `https://onlinelibrary.wiley.com/doi/abs/10.1002/esp.3374` doi: 10.1002/esp.3374

Krautblatter, M., & Leith, K. (2015). Glacier- and permafrost-related slope instabilities. In C. Huggel, M. Carey, J. J. Clague, & A. Kaab (Eds.), *The High-Mountain Cryosphere* (pp. 147–165). Cambridge: Cambridge University Press. Retrieved 2020-02-10, from `https://www.cambridge.org/core/product/identifier/9781107588653%23CT-bp-9/type/book_part` doi: 10.1017/CBO9781107588653.009

Krischer, L., Megies, T., Barsch, R., Beyreuther, M., Lecocq, T., Caudron, C., & Wassermann, J. (2015, May). ObsPy: a bridge for seismology into the scientific Python ecosystem. *Computational Science & Discovery*, *8*(1), 014003. Retrieved 2020-04-29, from `https://doi.org/10.1088%2F1749-4699%2F8%2F1%2F014003` (Publisher: IOP Publishing) doi: 10.1088/1749-4699/8/1/014003

Lague, D., Brodu, N., & Leroux, J. (2013, August). Accurate 3D comparison of complex topography with terrestrial laser scanner: Application to the Rangitikei canyon (N-Z). *ISPRS Journal of Photogrammetry and Remote Sensing*, *82*, 10–26. Retrieved 2020-03-11, from `http://www.sciencedirect.com/science/article/pii/S0924271613001184` doi: 10.1016/j.isprsjprs.2013.04.009

Larose, E., Carrière, S., Voisin, C., Bottelin, P., Baillet, L., Guéguen, P., ... Massey, C. (2015, May). Environmental seismology: What can we learn on earth surface processes with ambient noise? *Journal of Applied Geophysics*, *116*, 62–74. Retrieved 2020-04-22, from `http://www.sciencedirect.com/science/article/pii/S0926985115000403` doi: 10.1016/j.jappgeo.2015.02.001

Le Roy, G., Helmstetter, A., Amitrano, D., Guyoton, F., & Roux-Mallouf, R. L. (2019). Seismic Analysis of the Detachment and Impact Phases of a Rockfall and Application for Estimating Rockfall Volume and Free-Fall Height. *Journal of Geophysical Research: Earth Surface*, *124*(11), 2602–2622. Retrieved 2020-02-13, from `https://agupubs.onlinelibrary.wiley.com/doi/abs/10.1029/2019JF004999` doi: 10.1029/2019JF004999

Lévy, C., Jongmans, D., & Baillet, L. (2011, July). Analysis of seismic signals recorded on a prone-to-fall rock column (Vercors massif, French Alps). *Geophysical Journal International*, *186*(1), 296–310. Retrieved 2020-02-10, from `https://academic.oup.com/gji/article/186/1/296/699018` doi: 10.1111/j.1365-246X.2011.05046.x

Magnin, F., Etzelmüller, B., Westermann, S., Isaksen, K., Hilger, P., & Hermanns, R. L. (2019, October). Permafrost distribution in steep rock slopes in Norway: measurements, statistical modelling and implications for geomorphological processes. *Earth Surface Dynamics*, *7*(4), 1019–1040. Retrieved 2020-02-10, from `https://www.earth-surf-dynam.net/7/1019/2019/` doi: https://doi.org/10.5194/esurf-7-1019-2019

Magnin, F., Josnin, J.-Y., Ravanel, L., Pergaud, J., Pohl, B., & Deline, P. (2017, August). Modelling rock wall permafrost degradation in the Mont Blanc massif from the LIA to the end of the 21st century. *The Cryosphere*, *11*(4), 1813–1834. Retrieved 2020-03-11, from `https://www.the-cryosphere.net/11/1813/2017/` (Publisher: Copernicus GmbH) doi: https://doi.org/10.5194/tc-11-1813-2017

Manconi, A., Coviello, V., Galletti, M., & Seifert, R. (2018, December). Short Communication: Monitoring rockfalls with the Raspberry Shake. *Earth Surface Dynamics*, *6*(4), 1219–1227. Retrieved 2020-04-20, from `https://www.earth-surf-dynam.net/6/1219/2018/` (Publisher: Copernicus GmbH) doi: https://doi.org/10.5194/esurf-6-1219-2018

Manconi, A., Picozzi, M., Coviello, V., Santis, F. D., & Elia, L. (2016). Real-time detection, location, and characterization of rockslides using broadband regional seismic networks. *Geophysical Research Letters*, *43*(13), 6960–6967. Retrieved 2020-04-20, from `https://agupubs.onlinelibrary.wiley.com/doi/abs/10.1002/2016GL069572` (_eprint: https://agupubs.onlinelibrary.wiley.com/doi/pdf/10.1002/2016GL069572) doi: 10.1002/2016GL069572

Matasci, B., Jaboyedoff, M., Loye, A., Pedrazzini, A., Derron, M. H., & Pedrozzi, G. (2015, July). Impacts of fracturing patterns on the rockfall susceptibility and erosion rate of stratified limestone. *Geomorphology*, *241*, 83–97. Retrieved 2020-04-20, from `http://www.sciencedirect.com/science/article/pii/S0169555X15001889` doi: 10.1016/j.geomorph.2015.03.037

McNamara, D. E., & Buland, R. P. (2004, August). Ambient Noise Levels in the Continental United States. *Bulletin of the Seismological Society of America*, *94*(4), 1517–1527. Retrieved 2020-04-13, from `https://pubs.geoscienceworld.org/bssa/article-abstract/94/4/1517/121021/Ambient-Noise-Levels-in-the-Continental-United` (Publisher: GeoScienceWorld) doi: 10.1785/012003001

Mertl, S. (2014). *Characterization of local seismic events on the deep-seated gravitational slope deformation Gradenbach* (Doctoral dissertation, University of Technology, Vienna, Austria). Retrieved from `http://repositum.tuwien.ac.at/urn:nbn:at:at-ubtuw:1-88124`

Mertl, S. (2017a, April). *Assembly of the seismic data recorder Ruwai* (Technical Report). Kienmayergasse 22, 1140 Vienna: Mertl Research GmbH. Retrieved from `https://www.mertl-research.at/`

Mertl, S. (2017b, April). *Electromagnetic Interference and the Ruwai recording system* (Technical Report). Kienmayergasse 22, 1140 Vienna: Mertl Research GmbH. Retrieved from `https://www.mertl-research.at/`

Mertl, S. (2017c, April). *Performance of the seismic data recorder Ruwai* (Technical Report). Kienmayergasse 22, 1140 Vienna: Mertl Research GmbH. Retrieved from `https://www.mertl-research.at/`

Monserrat, O., & Crosetto, M. (2008, January). Deformation measurement using terrestrial laser scanning data and least squares 3D surface matching. *ISPRS Journal of Photogrammetry and Remote Sensing*, *63*(1), 142–154. Retrieved 2020-03-11, from `http://www.sciencedirect.com/science/article/pii/S0924271607000810` doi: 10.1016/j.isprsjprs.2007.07.008

Noetzli, J., Huggel, C., Hoelzle, M., & Haeberli, W. (2006, June). GIS-based modelling of rock-ice avalanches from Alpine permafrost areas. *Computational Geosciences*, *10*(2), 161–178. Retrieved 2020-02-10, from `https://doi.org/10.1007/s10596-005-9017-z` doi: 10.1007/s10596-005-9017-z

Occhiena, C., Coviello, V., Arattano, M., Chiarle, M., Morra di Cella, U., Pirulli, M., … Scavia, C. (2012, July). Analysis of microseismic signals and temperature recordings for rock slope stability investigations in high mountain areas. *Natural Hazards and Earth System Sciences*, *12*(7), 2283–2298. Retrieved 2020-02-12, from `https://www.nat-hazards-earth-syst-sci.net/12/2283/2012/` doi: https://doi.org/10.5194/nhess-12-2283-2012

Paranunzio, R., Laio, F., Chiarle, M., Nigrelli, G., & Guzzetti, F. (2016, September). Climate anomalies associated with the occurrence of rockfalls at high-elevation in the Italian Alps. *Natural Hazards and Earth System Sciences*, *16*(9), 2085–2106. Retrieved 2020-04-22, from `https://www.nat-hazards-earth-syst-sci.net/16/2085/2016/` (Publisher: Copernicus GmbH) doi: https://doi.org/10.5194/nhess-16-2085-2016

Peterson, J. R. (1993). *Observations and modeling of seismic background noise* (USGS Numbered Series No. 93-322). U.S. Geological Survey. Retrieved 2020-04-13, from `http://pubs.er.usgs.gov/publication/ofr93322` (Code Number: 93-322 Code: Observations and modeling of seismic background noise Publication Title: Observations and modeling of seismic background noise Reporter: Observations and modeling of seismic background noise Series: Open-File Report) doi: 10.3133/ofr93322

Pläsken, R., Keuschnig, M., & Krautblatter, M. (2017). Systematic derivation of anchoring forces in permafrost-affected bedrock. In (Vol. 19, p. 1). Geophysical Research Abstracts.

Ravanel, L., & Deline, P. (2011, March). Climate influence on rockfalls in high-Alpine steep rockwalls: The north side of the Aiguilles de Chamonix (Mont Blanc massif) since the end of the 'Little Ice Age'. *The Holocene*, *21*(2), 357–365. Retrieved 2020-04-20, from `https://doi.org/10.1177/0959683610374887` (Publisher: SAGE Publications Ltd) doi: 10.1177/0959683610374887

Ravanel, L., & Deline, P. (2015). Rockfall Hazard in the Mont Blanc Massif Increased by the Current Atmospheric Warming. In G. Lollino, A. Manconi, J. Clague, W. Shan, & M. Chiarle (Eds.), *Engineering Geology for Society and Territory - Volume 1* (pp. 425–428). Cham: Springer International Publishing. doi: 10.1007/978-3-319-09300-0_81

Rosser, N., Lim, M., Petley, D., Dunning, S., & Allison, R. (2007). Patterns of precursory rockfall prior to slope failure. *Journal of Geophysical Research: Earth Surface*, *112*(F4). Retrieved 2020-03-11, from `https://agupubs.onlinelibrary.wiley.com/doi/abs/10.1029/2006JF000642` (_eprint: https://agupubs.onlinelibrary.wiley.com/doi/pdf/10.1029/2006JF000642) doi: 10.1029/2006JF000642

Rosser, N., Petley, D. N., Lim, M., Dunning, S. A., & Allison, R. J. (2005, November). Terrestrial laser scanning for monitoring the process of hard rock coastal cliff erosion. *Quarterly Journal of Engineering Geology and Hydrogeology*, *38*(4), 363–375. Retrieved 2020-03-11, from `https://qjegh.lyellcollection.org/content/38/4/363` (Publisher: Geological Society of London Section: Original Article) doi: 10.1144/1470-9236/05-008

SAGIS. (2007). *Salzburg Airborne Laserscan Survey 2007.* Salzburger Geographisches Informationssystem (SAGIS). Retrieved from `https://www.salzburg.gv.at/themen/bauen-wohnen/raumplanung/geodaten/geodaten-und-karten`

SAGIS. (2008). *Salzburg Airborne Laserscan Survey 2008.* Salzburger Geographisches Informationssystem (SAGIS). Retrieved from `https://www.salzburg.gv.at/themen/bauen-wohnen/raumplanung/geodaten/geodaten-und-karten`

Sass, O., & Oberlechner, M. (2012, November). Is climate change causing increased rockfall frequency in Austria? *Natural Hazards and Earth System Sciences*, *12*(11), 3209–3216. Retrieved 2020-02-10, from `https://www.nat-hazards-earth-syst-sci.net/12/3209/2012/` doi: https://doi.org/10.5194/nhess-12-3209-2012

Scales, J. A., & Snieder, R. (1998). What is noise? *Geophysics*, *63*(4), 1122–1124. (Number: 4)

Schöner, W., Boeckli, L., Hausmann, H., Otto, J.-C., Reisenhofer, S., Riedl, C., & Seren, S. (2012). Spatial Patterns of Permafrost at Hoher Sonnblick (Austrian Alps) - Extensive Field-measurements and Modelling Approaches. *Austrian Journal of Earth Sciences*, *105*(2), 154–168.

Spillmann, T. (2007). *Borehole radar experiments and microseismic monitoring on the unstable Randa rockslide (Switzerland)* (Doctoral Thesis, ETH Zurich). doi: 10.3929/ethz-a-005319606

Stähli, M., Sättele, M., Huggel, C., McArdell, B. W., Lehmann, P., Van Herwijnen, A., ... Springman, S. M. (2015, April). Monitoring and prediction in early warning systems for rapid mass movements. *Natural Hazards and Earth System Sciences*, *15*(4), 905–917. Retrieved 2020-04-22, from `https://www.nat-hazards-earth-syst-sci.net/15/905/2015/nhess-15-905-2015.html` (Publisher: Copernicus GmbH) doi: https://doi.org/10.5194/nhess-15-905-2015

Supper, R., Ottowitz, D., Jochum, B., Römer, A., Pfeiler, S., Gruber, S., ... Ita, A. (2014, February). Geoelectrical monitoring of frozen ground and permafrost in alpine areas: field studies and considerations towards an improved measuring technology. *Near Surface Geophysics*, *12*(1), 93–115. Retrieved 2020-03-11, from `http://nsg.eage.org/publication/publicationdetails/?publication=73124` doi: 10.3997/1873-0604.2013057

Suriñach, E., Furdada, G., Sabot, F., Biesca, B., & Vilaplana, J. M. (2001). On the characterization of seismic signals generated by snow avalanches for monitoring purposes. *Annals of Glaciology*, *32*, 268–274. Retrieved 2020-10-22, from `https://www.cambridge.org/core/journals/annals-of-glaciology/article/on-the-characterization-of-seismic-signals-generated-by-snow-avalanches-for-monitoring-purposes/48CC3CFCC26566CF943211201F8E82E6` (Publisher: Cambridge University Press) doi: 10.3189/172756401781819634

Suriñach, E., Vilajosana, I., Khazaradze, G., Biescas, B., Furdada, G., & Vilaplana, J. M. (2005, October). Seismic detection and characterization of landslides and other mass movements. *Natural Hazards and Earth System Sciences*, *5*(6), 791–798. Retrieved 2020-10-22, from `https://nhess.copernicus.org/articles/5/791/2005/` (Publisher: Copernicus GmbH) doi: https://doi.org/10.5194/nhess-5-791-2005

Teza, G., Galgaro, A., Zaltron, N., & Genevois, R. (2007, August). Terrestrial laser scanner to detect landslide displacement fields: a new approach. *International Journal of Remote Sensing*, *28*(16), 3425–3446. Retrieved 2020-03-11, from `https://doi.org/10.1080/01431160601024234` (Publisher: Taylor & Francis _eprint: https://doi.org/10.1080/01431160601024234) doi: 10.1080/01431160601024234

Volkwein, A., Schellenberg, K., Labiouse, V., Agliardi, F., Berger, F., Bourrier, F., ... Jaboyedoff, M. (2011, September). Rockfall characterisation and structural protection – a review. *Natural Hazards and Earth System Sciences*, *11*(9), 2617–2651. Retrieved 2020-02-10, from `https://www.nat-hazards-earth-syst-sci.net/11/2617/2011/` doi: https://doi.org/10.5194/nhess-11-2617-2011

Walter, M., Arnhardt, C., & Joswig, M. (2012, March). Seismic monitoring of rockfalls, slide quakes, and fissure development at the Super-Sauze mudslide, French Alps. *Engineering Geology*, *128*, 12–22. Retrieved 2020-02-12, from `http://www.sciencedirect.com/science/article/pii/S001379521100281X` doi: 10.1016/j.enggeo.2011.11.002

Walter, M., Schwaderer, U., & Joswig, M. (2012, November). Seismic monitoring of precursory fracture signals from a destructive rockfall in the Vorarlberg Alps, Austria. *Natural Hazards and Earth System Sciences*, *12*(11), 3545–3555. Retrieved 2020-02-12, from `https://www.nat-hazards-earth-syst-sci.net/12/3545/2012/nhess-12-3545-2012.html` doi: https://doi.org/10.5194/nhess-12-3545-2012

Weginger, S. (2012). *Detektion und Lokalisierung seismischer Signale zur Überwachung der Massenbewegung Steinlehnen* (Unpublished master's thesis). University of Technology, Vienna, Austria.

Wikipedia. (2020, April). *Open-design movement.* Wikipedia - The Free Encyclopedia. Retrieved 2020-04-23, from `https://en.wikipedia.org/w/index.php?title=Open-design_movement&oldid=951655626` (accessed 2020-04-23 17:52:09; Page Version ID: 951655626)

List of Figures

3.1 Block diagram of the major *Ruwai* hardware components. 8

3.2 The *Arduino Stack* of the *Ruwai* seismic data recorder. The *Arduino Mega 2560* microcontroller builds the base, with the *GPS Timing Shield*, the *ADC Main shield* with the *Analog Interface PGA Shield*, and the *Power Supply Shield* stacked on top of each other. 9

3.3 The *Arduino Stack* inside the *Pelicase* enclosure with closed and open shielding. The left element is the *BeagleBone Black* single-board computer. 10

3.4 (a) Power spectral density of the *Ruwai* recorder with shorted input channels at a sampling rate of 800 sps. The colored lines represent the average of all 4 channels for various pre-amplification factors. The light grey line represents the noise of channel 1 of the *ADC Main Shield* only. (b) Minimum noise floor of the *SeisRockHT* recording system (*Ruwai* data logger + 4.5 Hz GS-11D seismic sensor) with a sampling rate of 800 sps for various pre-amplification factors. All power spectral densities were smoothed using an 11 samples long moving average filter. 11

3.5 The workplace setup (a) and the tools (b) used for the manual assembly of the PCBs. 12

3.6 Clean printed circuit board (left) and the corresponding metal solder paste stencil (right). . . . 12

3.7 The solder paste applied to the PCB (a) and a close-up (b). 13

3.8 Close-up view of the ADS1274 ADC on the PCB before (a) and after (b) reflow soldering. . . . 13

3.9 The first *Ruwai* recorder version for the *SeisRockHT* project. The *BeagleBone Black* single board computer is mounted next to the unshielded *Arduino Stack*. 14

3.10 Field data recorded with an unshielded *Ruwai* recording system at station STO of the Sonnblick seismological network. 10 seconds of the waveform data (top) and the power spectral density of a 1 hour recording (bottom) are shown. 15

3.11 Field data recorded with the shielded *Ruwai* recording system at station STO of the Sonnblick seismological network. 10 seconds of the waveform data (top) and the power spectral density of a 1 hour recording (bottom) are shown. Note the different magnitude of waveform amplitude (μVolts) compared to Figure 3.10 (Volt). 15

3.12 Throughout the *SeisRockHT* project the new *Ruwai se* prototype was developed including major software fixes and a better usability in the field. 18

3.13 Power spectral density averaged for all four channels with a sampling rate of 800 sps. The light grey line represents the noise of channel 1 of the *ADC Main Shield* only. All power spectral densities were smoothed using an 11 samples long moving average filter. The change of the operational amplifier of the anti aliasing filter significantly improved the 1/f-noise at low frequencies, as can bee seen in the comparison of the old system (a) with the *Ruwai se* (b). . . 19

3.14 Minimum noise floor of the old (a) and the new (b) *Ruwai* systems with a 4.5 Hz GS-11D sensor and a sampling rate of 800 sps. The *Ruwai se* does not show a lower noise floor for gain values larger than 32. This suggests, that the noise source is located before the signal amplifier. 19

3.15 The *Ruwai* mast mount strategy. The core is the custom-built *Pelicase 1200* aluminum mast mount. A tarpaulin cover provides additional protection. 20

3.16 Three component (X Y Z) borehole sensor constructed by *Geosono* for the Sonnblick summit station (OBS). In the foreground of the right picture the thermistor string sinking weight is shown. The sinking weight was replaced by the seismometer. 21

3.17 *Geosono* single component (Z) borehole sensor for the Kitzsteinhorn BH1 station. The sensor is mounted at the bottom of a stiff rod along which the thermistor string is also fixed. 22

3.18 Overview of the *SeisRockHT* monitoring network. The OBS and STO stations are mains powered, whereas MIT, MOR and PIL are stand-alone stations. The stand-alone stations power supply is realized by a combination of solar panels, wind turbines and battery packs. The overview map covers an area of 3x3 km. (Coordinate System: MGI/Austria GK 31, EPSG:31258) 24

3.19 Overview of the 'Hoher Sonnblick' summit (3,106 m a.s.l.). (A) shows the steep summit northface during the summit renovation in 2003/04. (B) shows the summit south-face with the three deep boreholes (BH1-3). The three component borehole seismometer of the *SeisRockHT* OBS station was installed in BH1. In August 2019, the *Seismological Service of Austria* installed a permanent surface seismometer (SOSA). (C) gives an overview of the summit-wide surface and subsurface temperature sensor network. 25

3.20 The OBS three component seismometer is sunk in the 21 m deep BH1. The sensor is situated at the lower end of a thermistor string. 26

3.21 GPS signal tests after the OBS station installation. The GPS antenna (red encircled) was initially mounted on the close by wind tower foundation. 27

3.22 Material for the alternative GPS concept of the OBS station. Numbering follows the way of the incoming GPS signal until the data recorder: (1) GPS antenna, (2) GPS antenna cable, (3) lightning protection, (4) GPS signal amplifier, (5) A/D converter, (6) optic fibre, (7) D/A converter, (8) signal attenuator module. 27

3.23 Snapshots of the installed alternative OBS station GPS concept. Due to the omnipresent lightning risk at the Sonnblick summit, the concept is based on an optic fibre connection. Left picture shows the outdoor switchbox with the installed metal protection conduits for the optic fibre. The optic fibre is guided inside an underground pipe from the borehole to the switchbox (upper arrow), and then continues towards the terrace (lower arrow). The middle picture shows the terrace's anteroom switchbox with the installed devices. Left arrow points at the lightning protection of the incoming antenna cable and the right arrow points at the mounted aluminum board with the GPS signal amplifier (left) and the A/D-converter. The right picture shows the installed GPS antenna on the terrace balustrade. 28

3.24 The tunnel portal and the ∼50 m long tunnel. The GPS antenna is mounted on top of the tunnel portal. 29

3.25 Originally, the GPS antenna was mounted directly on the rockwall. In January 2017, a ∼0.5 m beam was mounted to raise the antenna's sky view percentage which substantially improved the GPS signal strength. 30

3.26 The STO station is located at the face of a 50 m deep tunnel. The left arrow points at the three component sensor, and the right one at the GPS signal repeater. The left box contains the *Ruwai* data recorder and the box to the right the power supply. 30

3.27 The Sonnblick Observatory cable car was used to deliver equipment. 31

3.28 Nice weather, but heavy load. The material for the PIL and MOR stations were partly carried up from the valley via backpack transport. 32

3.29 Geophones and cables were dug into the ground about 0.5 and 0.1 m, respectively, to suppress surface noise and potential damages by rockfall or wildlife. 32

3.30 The first MIT station. The *Ruwai* data recorder and the solar panel were mounted on the SBO cable car pillar 'Mittelstütze'. The battery box was placed in the left corner of the basement's downward side. 33

3.31 The avalanche wall above the old cable car pillar 'Mittelstütze'. The new MIT station was installed on top of the avalanche wall. The original battery box (wrapped in a green tarp) was situated in the lower right corner. The new battery enclosure was mounted right below the original battery box. 33

3.32 The new MIT station is equipped with a wind turbine. The *Ruwai* data recorder and the solar panel are mounted on a trussing element. 34

3.33 In autumn 2019, a new battery enclosure was mounted. The new enclosure hosts two batteries providing a total capacity of 3240 Wh. 34

3.34 The solar panel and the *Ruwai* recorder were mounted on a ground-anchored mast. Red arrows are pointing at a buried geophone cable. 35

3.35 The mast and the solar panel were each stabilized by four guy wires. In summer 2017, a wind turbine was installed. The MOR station exhibits the lowest solar irradiance of all stand-alone stations. 35

3.36 The first version of the PIL station. The solar panel was mounted on a southeast-facing rockwall in a height of about 3 m above ground. The *Ruwai* data recorder was mounted on a $\sim$1 m mast. The battery box is placed below the mast base. 36

3.37 Recovery of the PIL *Ruwai* data recorder in January 2017. 36

3.38 In May 2017 a new solar panel was mounted at about 10 m above ground. In the foreground of the right image the recovered wrecked solar panel can be seen. The background shows the new solar panel mounted on the upper rockwall. Furthermore, the image gives an impression of the snow masses accumulated over winter which had to be removed to actually recover the old solar panel. 37

3.39 Installation of the solar panel power cable in late summer 2017. 37

3.40 The left photo shows the solar panel remains after the winter season 2017/18. The remains of the solar panel frame are encircled in red, the arrow points at the crushed solar cells. The photo also illustrates PIL snow conditions on July 2, 2018. Furthermore, the huge snow load partly sheared off the lid of the battery box (right image). 37

3.41 The temporary PIL station in late summer 2018. The left arrow points at the semi-flexible solar panel (50 W) fixed with cord on the rock. The right arrow points at the with a green tarp covered battery and data recorder boxes. 38

3.42 The new PIL solar panel installation. The GPS antenna is mounted at the lower left corner, next to the solar panel wiring. 39

3.43 Schematic overview of the *Open-Air-Lab Kitzsteinhorn (OpAL)* monitoring network. Seismic monitoring stations were installed within the *SeisRockHT* project. 40

3.44 *SeisRockHT* investigation site at the north-face below the Kitzsteinhorn cable car top station. Deep boreholes 1 (BH1) and 2 (BH2) are normal to the local surface which results in a borehole inclination of about 40°. The 6 m deep borehole 3 (BH3) is vertical (borehole inclination 0°). All boreholes are drilled into solid rock. 41

3.45 Overview map of the *OpAL* seismological station network (BH1-3). The blue shaded area indicates the Schmiedingerkees glacier. The overview map covers an area of 1x1 km, whereas the network blow-up covers an area of 100x100 m. (Coordinate System: MGI/Austria GK 31, EPSG:31258) 42

4.1 TLS surveys at the Sonnblick north-face covered the area between the glaciated slope foot (∼2400 m a.s.l.) and the summit (∼3106 m a.s.l.). Significant occlusion effects within the main north-face couloirs are evident (1, 2). Glaciated areas returned little to no TLS signal (3). The right image shows the three different scan positions (1, 2, 3) used to improve the coverage of the heavily incised Sonnblick north-face. 44

4.2 Aerial view of the two main Kitzsteinhorn cirques that were monitored during the major TLS monitoring campaign. The Kitzsteinhorn north-face ('KN') was the *SeisRockHT* investigation site. Whereas, the extended TLS campaign also included the Kitzsteinhorn northwest-face ('KNW'), Magnetkoepfl east-face ('MKE'), Magnetkoepfl west-face ('MKW'), and Maurergrat east-face ('MGE'). The deployed scan positions were: SMK... Scan Position 'Magnetkoepfl', SCC... Scan Position 'Cable Car Top Station', SG1... Scan Position 'Glacier 1', SG2... Scan Position 'Glacier 2', SMG... Scan Position 'Maurergrat' (modified after Hartmeyer et al. (2020b)) 45

4.3 Comparison of the MIT and MOR data availability for January and February of the years 2017 (top row) and 2019. The difference in sola panel shading of the two stations is striking for the month of January (left column). Whereas, the MIT station exhibited a quasi diurnal cycle, the MOR station showed rather persistent periods without data due to the shading of the close-by north-face. Since summer 2018, both stations are equipped with a wind turbine which led to a general higher data yield for 2019. 47

4.4 Sonnblick seismological network data availability for the month of December compared for the years 2016 (left) and 2019. In December 2019 MIT and MOR stations showed no data loss. The OBS borehole sensor is not operational, but the data of the new SOSA station was used instead. 48

4.5 Calculated probabilistic power spectral density (PPSD) for the mains powered stations OBS (left) and STO for available 2017 data. Mains powered stations feature lower amplitude variations due to their sensor installations in a borehole and in a tunnel. Details about the PPSD calculation are given in each PPSD's title. Horizontal green and blue bar at the bottom indicate data availability. 50

4.6 Probabilistic power spectral density (PPSD) for the two horizontal components of the OBS station for 2017. The distinctively elevated amplitudes for the frequency range 30-40 Hz is presumably caused by regular cable car operations. Details about the PPSD calculation are given in each PPSD's title. Horizontal green and blue bar at the bottom indicate data availability. 50

4.7 Probabilistic power spectral density (PPSD) for the stand-alone stations MIT, MOR and PIL for 2017. The MIT station shows the highest amplitude variations of all stations. Vibrations induced by the close-by cable car pillar is the likely source. All stations feature PPSDs in between the two global ambient noise extremes. Details about the PPSD calculation are given in each PPSD's title. Horizontal green and blue bar at the bottom indicate data availability. 51

4.8 Probabilistic power spectral density (PPSD) for the stand-alone station MIT for October 2019. The PPSD clearly shows that the MIT station was recording spurious data. Details about the PPSD calculation are given in the PPSD title. Horizontal green and blue bar at the bottom indicate data availability. 51

4.9 Comparison of representative PPSDs of the PIL station for the active week 43 (24. - 30. 10.) and the rather quiet week 45 (07. - 13. 11.) in 2016. The active week 43 clearly illustrates the higher PPSD amplitudes for lower frequencies due to the central Italy earthquake sequence. . . 52

4.10 The central Italy earthquake was recorded by the *SeisRockHT* network. Austrian earthquake network stations (right) from which data is shown are encircled in red. The SOSA station indicates the location of the *SeisRockHT* Sonnblick network. The red vertical line in the seismogram plot marks the first arrival of the earthquake event at the southerly MYKA station. Delayed first arrivals in northerly direction confirm the correct timing of the *SeisRockHT* data. 53

4.11 Several grounding strategies were tested to overcome the bad data quality of the Kitzsteinhorn network stations. Photos are taken during an extensive testing session at the BH1 station. However, all the efforts did not lead to better data quality, which left the Kitzsteinhorn unusable for further analysis. 54

4.12 Calculated PPSDs for the vertical sensor component of the BH1 and BH3 station for the week 43 (24. - 30. 10.) which included the central Italy main earthquake event from October 30, ∼06:40 UTC (compare 4.9). 54

4.13 No ground motion of the central Italy main earthquake from October 30, ∼06:40 UTC, was recorded by the vertical components of the BH1 and BH3 stations at the Kitzsteinhorn site (compare 4.10). 55

4.14 15 seconds of the data shown in figure 4.13 revealed different characteristics of the ambient seismic data. BH1 data shows a more chaotic behavior with regular step-like amplitude drops, whereas BH3 ambient data feature a rather constant amplitude range. 55

4.15 The mean annual ground temperature time series for the period 2010-2018 at the Sonnblick summit. In the shoulder seasons the zero-curtain effect is nicely visible. 56

6.1 Rockfall release zones with volumes greater than 10 m^3 detected during four years (2015-2018) of TLS monitoring at the Sonnblick north-face. The blue, no-data areas within the north-face are due to occlusion effects mainly by the dominant north-face couloirs, as well as by glaciers at the foot of the north-face. 19 out of the 25 identified rockfall release zones are located in the bottom half of the rock face. The three largest rockfall release zones are indicated. 63

6.2 Black line shows the main rockfall release zones (MRRZs) altitudes kernel density estimation (KDE). Gray bars illustrate the MRRZs altitudes histogram. However, x-axis shows KDE probability values. KDE distribution reveals a dominant MRRZ altitude of about 2800 m. 64

6.3 Rockfall release zones detected during the entire TLS monitoring period (2011-2018) at the Kitzsteinhorn north-face (n = 226). The majority of the release zones was detected in the lower rockwall sections close to the current glacier surface. A mean annual rockwall retreat rate of 10.4 mm a^{-1} was determined for the entire monitoring period. 65

6.4 Black line shows the rockfall release zones altitudes kernel density estimation (KDE). Gray bars illustrate the rockfall release zones altitudes histogram. However, x-axis shows KDE probability values. KDE distribution reveals the rockfall release zone majority in the lower rockwall section at about 2970 m a.s.l., adjacent to the current glacier surface. 66

6.5 The visually observed rockfall from August 17, 2017, recorded at stations MIT and MOR. ...→*Figure continues on the next page.* 67

6.5 The visually observed rockfall from August 17, 2017, recorded at stations MIT and MOR. The data of the three mini-array locations (A,B,C) is shown. The array-locations of station MIT were at the same position during the time of the recording. 68

6.6 The recorded MOR, PIL, STO and SOSA data of the visually observed rockfall from September 13, 2019. ...→*Figure continues on the next page.* 68

6.6 The recorded MOR, PIL, STO and SOSA data of the visually observed rockfall from September 13, 2019. While for the mini array stations MOR and PIL every channel (A-C) is shown, just the representative vertical component is shown for the STO and SOSA stations. Due to the SOSA sampling frequency of 250 Hz, the maximum resolvable frequency of the SOSA station is 125 Hz. The prominent 50 and 100 Hz noise is caused by the SOSA power supply by mains. Furthermore, SOSA data is still in [Counts]. 69

6.7 Overview of the weather throughout the field campaign 2017. The green lines illustrate the air temperature of the Sonnblick observatory (SBO, 3106 m a.s.l.) and the Kolm Saigurn valley floor (1600 m a.s.l., dashed line). The gray bars indicate the hourly precipitation sums, and the black dotted line the maximum windspeed, both measured at Kolm Saigurn. The gray background marks the field campaign period from August 23 to October 11. 70

6.8 Median spectrograms of two weeks calculated from the vertical component of all Sonnblick stations. The upper spectrogram shows a week with elevated seismicity, whereas the lower spectrogram represents a more quiet period with lower signal content. In the upper spectrogram a diurnal ambient seismicity pattern is visible. The diurnal ambient seismicity cyclicity originates from the STO station. In the lower spectrogram the ongoing construction work for the new SBO cable car is clearly visible at a frequency of about 4.5 Hz. The two vertical black lines indicate the working hours (05-15:00 UTC, or 07-17:00 CET) of Wednesday, 20.09.. The arrow points at the lunch break where a gap of the enhanced seismicity is visible. Every day of the working week showed a similar signature, and accordingly the weekend did not. 72

6.9 Spectrograms of two weeks for the vertical component of the STO station. Both weeks show a cyclic ambient seismicity pattern, whereas one cycle is about 24 hours with maxima located around 14:00 UTC. An exemplary cycle is marked by the two vertical black lines in the upper spectrogram. The vertical lines mark 14:00 UTC on the 24.08. and the 25.08.. The line plots and gray bars show complementary data (white line - air temperature Kolm Saigurn, black dashed line - discharge gauging site Bucheben, gray bars - hourly precipitation sums Kolm Saigurn). . 73

6.10 Spectrograms of the STO (top) and the OBS station for the seismically active week 28.08. - 03.09.. The vertical lines mark the exemplary 24 hours cycle 24.08. to 25.08. at 14:00 UTC, respectively. No ambient seismicity cylicity was observed for the OBS station data. 74

6.11 STO spectrograms of the last week of September and first week of October. The white vertical stripes indicate data gaps. The line plots and gray bars show complementary data (white line - air temperature Kolm Saigurn, black dashed line - discharge gauging site Bucheben, gray bars - hourly precipitation sums Kolm Saigurn). The rain event on October 3 is followed by an ambient seimicity and river discharge increase. 75

6.12 A *Rockfall Candidate Short* event recorded in the evening of August 24 (event id 19124). 77

6.13 A *Rockfall Candidate Long* event recorded in the morning of August 26 (event id 19150). . . . 78

6.14 A *Tremor LF* event recorded in the morning of August 27 (event id 19173). 79

6.15 Figure shows the cumulated number of events of the six event types versus the complementary meteorological data. The first plot shows the cumulated number just of the abundant *Rockfall Candidate Short* events. The *Rockfall Candidate Short* events clearly exhibited a lower occurrence rate after the apparent temperature drop in week August 29 to September 5. ...→*Figure continues on the next page.* 80

6.15 ...The second plot shows the number of events for the remaining event types. The *Tremor LF* event type featured maximum occurrence rates during the precipitation event in the night of August 26. The meteorolgical data is from the SBO (air temperature) and the Kolm Saigurn (air temperature (dashed line), precipitation, windspeed) stations. 81

6.16 The normalized cumulated number of the *Rockfall Candidate Short* events (red line) plotted with normalized degree day sums of air and borehole temperatures. A clear correlation between the number of *Rockfall Candidate Short* events and the air temperature measured in the Kolm Saigurn valley floor is visible. 82

6.17 The left photos show the ice face at the terminus of the debris covered Pilatuskees. The red star in the right map indicates a potential impact zone of tumbling down rocks at the foot of the ice face. The locations of the PIL (SR-PIL) and MOR (SR-MOR) stations are shown. The individual sensor locations of the two mini array stations are shown as well (SR-PIL1-3, SR-MOR1-3).(Coordinate System: MGI/Austria GK 31, EPSG:31258) 82

6.18 The extreme weather event in October 2018 caused floodings, mud flows and windthrows in the Alps-Adriatic region. During this event a total sum of 320 mm of precipitation, as well as maximum wind speeds of 29 m/s were recorded at the valley floor of Kolm Saigurn. 83

6.19 The compiled complementary data for the period of the extreme weather event in October 2018. The top graph illustrates the air temperature of the Sonnblick observatory (SBO, 3106 m a.s.l.) and the Kolm Saigurn valley floor (1600 m a.s.l.). The black dotted line indicates the measured maximum windspeeds. The middle graph shows the Kolm Saigurn precipitation versus the Hüttwinklache discharge (Q) measured at the Bucheben gauging site. The lag of the discharge peak is likely due to the distance of about 10 kilometers in between the two monitoring stations. The lower graph compiles electric field strength (EFS) data of the SBO, as well as the amplitudes of lightnings (LA) detected by the Austria-wide ALDIS network. The constant electric field strength values of zero in the second half of the time period is potentially due to icing of the sensor at the Sonnblick summit. 84

6.20 Photo time series of a mud flow coming down the river bed of the Hüttwinklache. The top photo shows the river bed before the heavy precipitation event, the middle the rising discharge, and the bottom photo documents the mud flow deposit and river bank erosion after the extreme weather event in October 2018. Based on the time lapse photos the mud flow happened in the night 29.-30.10., which corresponds well with the second precipitation maximum of this weather event (compare Figure 6.18). *Source: foto-webcam.eu* 85

6.21 The three run-out zones (RZ1-3) were situated at the Sonnblick north-face foot in between the MIT and the MOR station. All slides came down in dominant gulleys. (COS: MGI/Austria GK M31 (EPSG:31258) with 200 m grid spacing) 86

6.22 The run-out zone 1 (RZ1) debris came down in a major Sonnblick north-face gulley. The deposit consisted of a mix of mud, snow, gravel and smaller boulders. In the left background of the right photo the back then still existing red cable car pillar, right at the MIT station, is visible. . . . 87

6.23 The snow slide of the run-out zone 2 (RZ2) came down in a major Sonnblick north-face gulley. The deposit consisted of bare snow. 87

6.24 The snow slide of the run-out zone 3 (RZ3) came down in a major Sonnblick north-face gulley. The deposit consisted of bare snow. 87

6.25 Two spectrograms for the period October 25-31, 2018. The top spectrogram illustrates the median power spectral density (PSD) values of all stations of the Sonnblick network. The lower spectrogram shows the calculated PSDs for the STO station. The isolated subsurface location of the STO station significantly reduces the short term, high frequency signal content caused by surface processes, and environmental and anthropogenic noise. The prominent lower frequent event before midnight on October 25, was caused by a magnitude 6.8 earthquake in the Ionian Sea, Greece. 88

6.26 The STO spectrogram reveals a clear correlation with the precipitation and the discharge data. 89

6.27 A *Rockfall Candidate Long* event recorded in the evening of October 27. 91

6.28 A *Rockfall Candidate Short* event recorded in the afternoon of October 26. 92

6.29 A *Tremor* event recorded in the morning of October 26. The single plots show the recorded waveforms on top of the calculated spectrograms for a representative channel of each station. . 93

6.30 Spectrogram of the median PSDs of all Sonnblick stations shown with the over time cumulated number of the six different event types. 94

6.31 The top plot shows the median spectrogram of figure 6.30 with the precipitation data. All events of the rockfall long type happened within the first precipitation peak. The lower plot shows complementary data, whereas the green lines illustrate measured air temperatures at Kolm Saigurn (1600 m a.s.l.; dashed line) and on the Sonnblick summit (3106 m a.s.l.). The black dotted line presents maximum wind speeds at the Kolm Saigurn valley floor. 95

6.32 Rock temperature evolution of a shallow borehole in the Sonnblick north face at 3080 m a.s.l.. About one week before the actual extreme weather event the striking cooling event on October 21 caused a significant disturbance of the rock temperatures. 96

6.33 The seismic response of an operating helicopter. The left plots show 35 minutes of MIT, MOR and PIL station data with the recorded waveforms on top of the calculated spectrograms. The right plots show 4 minutes of data with details of the observed characteristic spectral gliding. . 97

6.34 Seismic response of the operating old Sonnblick observatory cable car. The cable car signal is clearly visible in the OBS and MIT station data. 98

6.35 Seismograms of the three MIT channels from October 27 in the beginning of the discussed extreme weather event (section 6.4). Each seismogram features a broadband spike (red dashed line) with a subsequent tremor-like signal (highlighted green). The simultaneity of the spike signal is striking. 99

6.36 Temporal correlation of detected lightnings by the ALDIS network (vertical dashed lines), and seismograms of the Sonnblick network. Red dashed lines highlight lightnings which correspond to discrete events in the seismograms. Simultaneity and signal characteristics of the corresponding events in the seismograms suggest lightnings as event source. 100

6.37 Good correlation between the expected arrival time of the acoustic waves and the seismic arrival time of the tremor. Red highlighted is the lightning sequence detected by the seismic network. Green highlighted are the recorded seismic tremors which correlated with the expected arrival time of the rumble of thunder. 101

6.38 The slab avalanche released in between the summits of Hoher Sonnblick and Hocharn. The left photo gives an overview of the avalanche source location. The right photo shows the clearly visible slab avalanche fracture line. The darker area right below the central fracture line is most likely bare ice. 102

6.39 Slab avalanche candidate 1 recorded after midnight on March 10, 2017. The OBS data feature a rather sharp event onset. 103

6.40 Slab avalanche candidate 2 recorded around 01:00 on March 10, 2017. All the data feature a rather sharp event onset, whereas the OBS and the STO data even show some sharp ground velocity peaks after the initial onset. 103

6.41 Slab avalanche candidate 3 recorded around 01:20 on March 10, 2017. The OBS data feature a rather sharp event onset. 104

6.42 Slab avalanche candidate 4 recorded around 04:10 on March 10, 2017. The OBS data feature the most prominent event onset. 104

6.43 Slab avalanche candidate 5 recorded around 17:25 on March 10, 2017. All stations feature a rather emergent event onset. 105

List of Tables

3.1 Station characteristics of the Sonnblick seismological network. OBS sensor is situated at the bottom of a 21 m deep borehole. MIT, MOR and PIL stations feature a mini array ('MA') deployment type. STO station is located at the face of a ∼50 m long tunnel close to the valley floor. 23
3.2 Borehole and sensor characteristics of the *OpAL* seismological network. 41

4.1 Percentages of the annual data yield for the single stations of the Sonnblick seismological network. The mean percentages ('mean') and monthly equivalents ('ME') describe annual data output of the entire network. 2019* takes into account SOSA data instead of the non-operational OBS station. 47
4.2 All visually registered rockfalls to date. The volume is a visually estimated value. The initials of the individual observer(s) are given. The two visually and by the seismic network observed rockfalls are marked with an asterisk (ID 5 and 19). 57

5.1 Long-term spectrogram parameters. 60

6.1 Key characteristics of detected rockfall release zones with volumes greater than 10 m^3. Altitude is measured from the lower edge of the individual release zones. **Slope** and **Az** denote the mean local slope and azimuth, respectively. **FD** describes the rockfall release zone failure depth. Survey period shows the corresponding years of the annual surveys from which rockfall release zone volumes are determined. 62
6.2 Metadata of the two visually validated rockfall events. The rockfall event in 2017 was observed by Daniel Binder (DB), and the one in 2019 by the Sonnblick observatory technician Norbert Daxbacher (ND). The MIT station in brackets indicates spurious data which made the data eventually unusable. 67
6.3 The classified event types with the associated total number of events detected during the field campaign in 2017. 76
6.4 The classified event types with the associated total number of events detected during the extreme weather event in 2018. 90

11.1 Detected and categorized seismic events of the campaign in 2017. **Nr** indicates the number of stations where the event was detected 152
11.2 Detected and categorized seismic events of the extreme weather event in 2018. 163

Appendix A: Seismic Data Availability

Full months without data are not shown.

2016 - Sonnblick Seismological Network

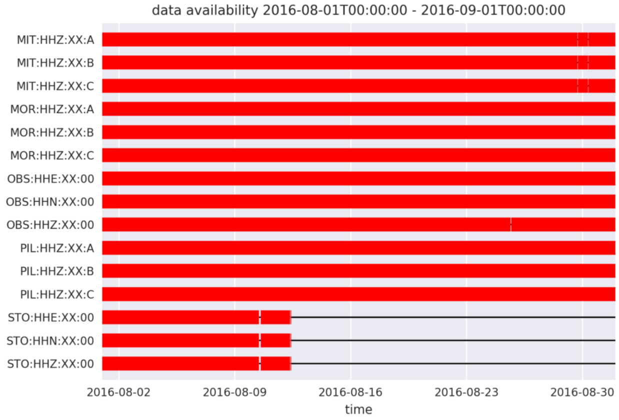

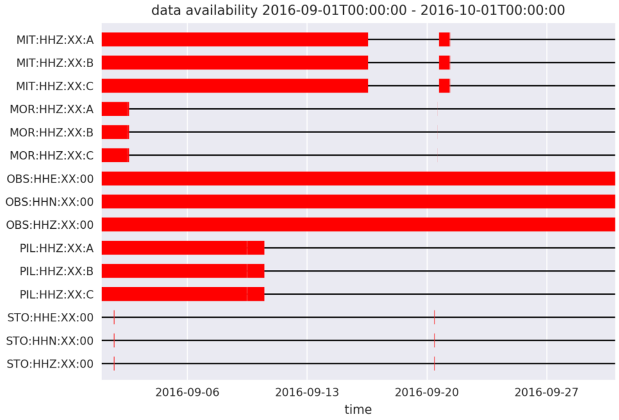

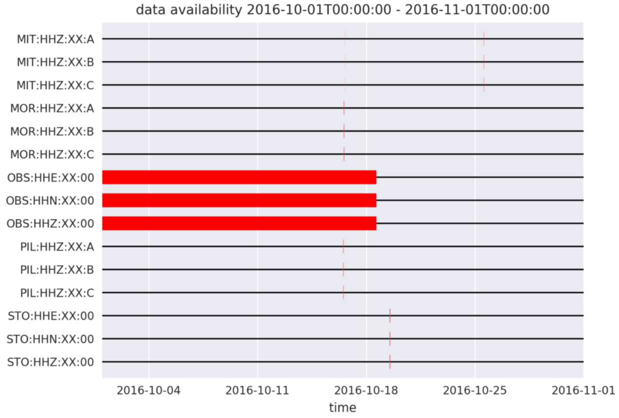

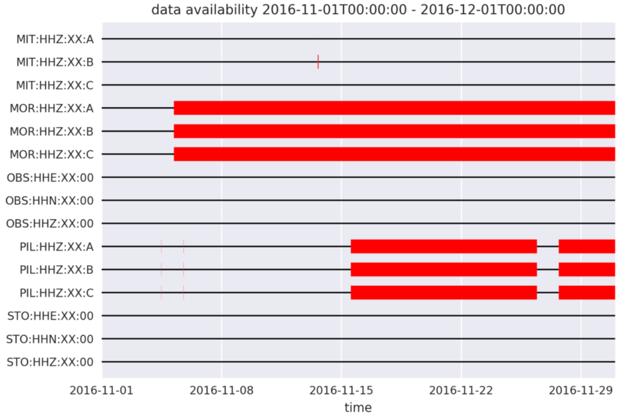

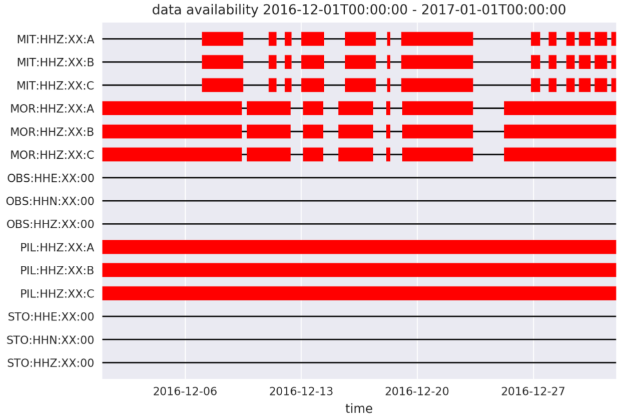

2017 - Sonnblick Seismological Network

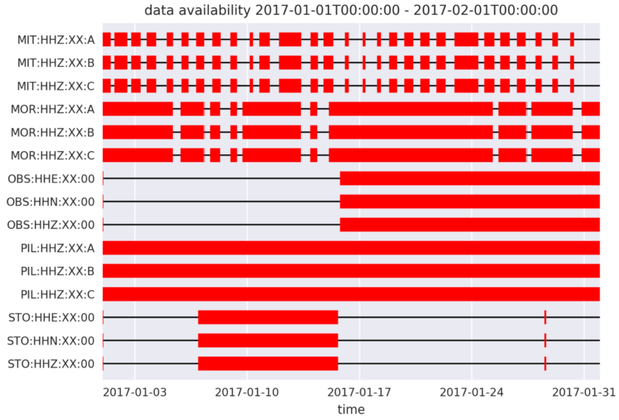

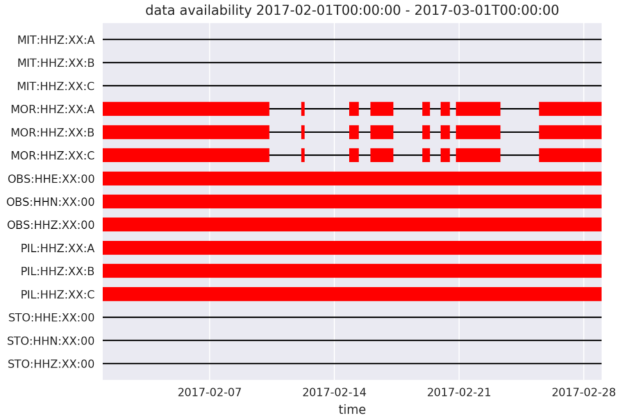

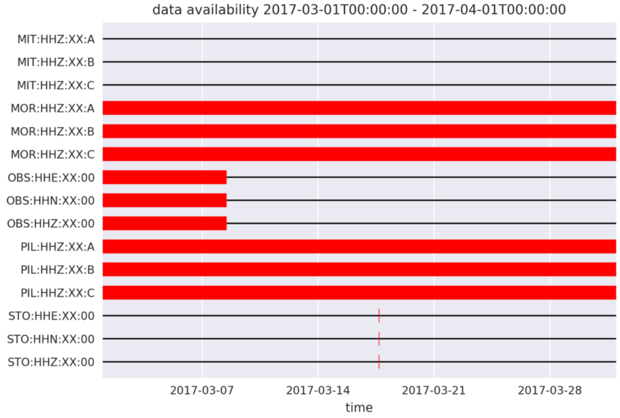

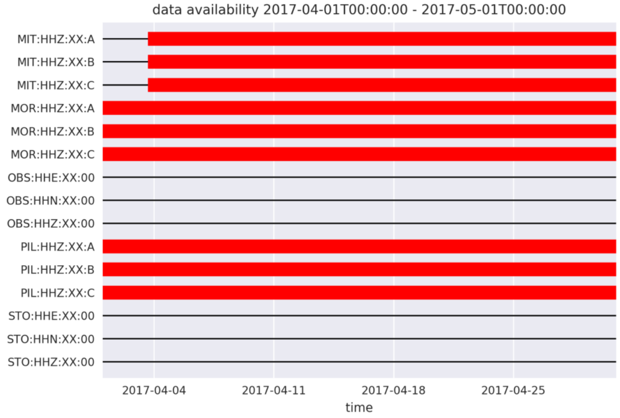

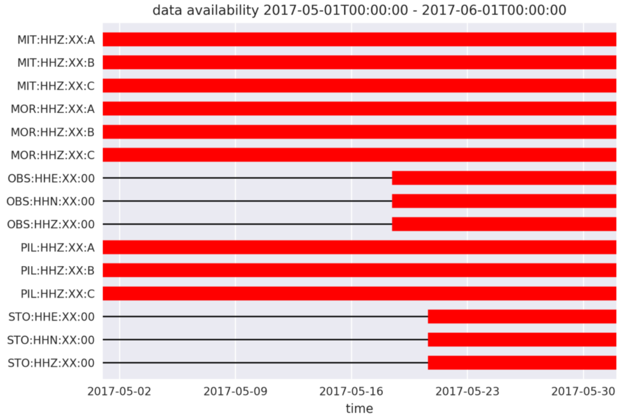

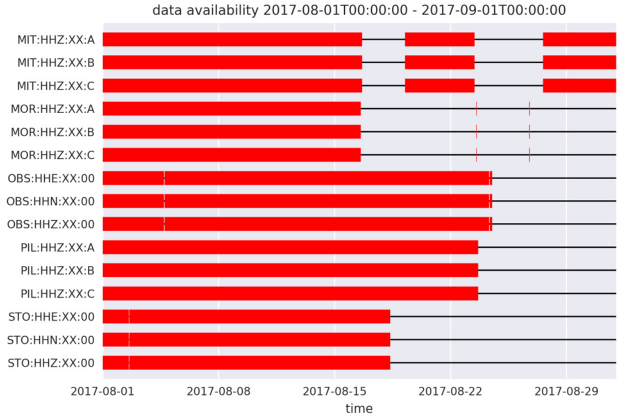

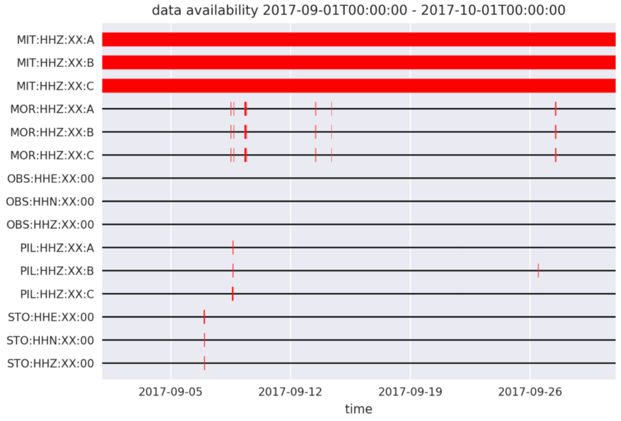
data availability 2017-09-01T00:00:00 - 2017-10-01T00:00:00

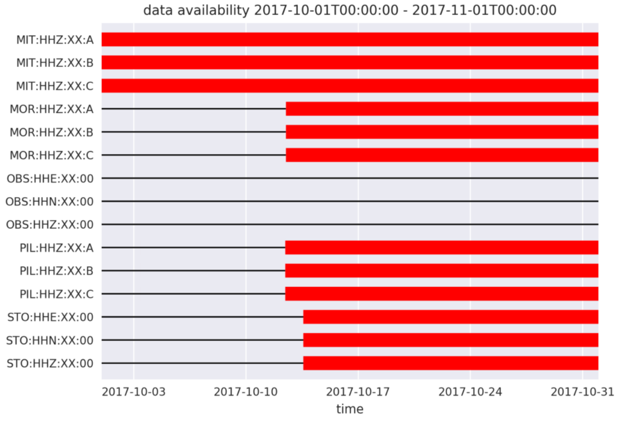
data availability 2017-10-01T00:00:00 - 2017-11-01T00:00:00

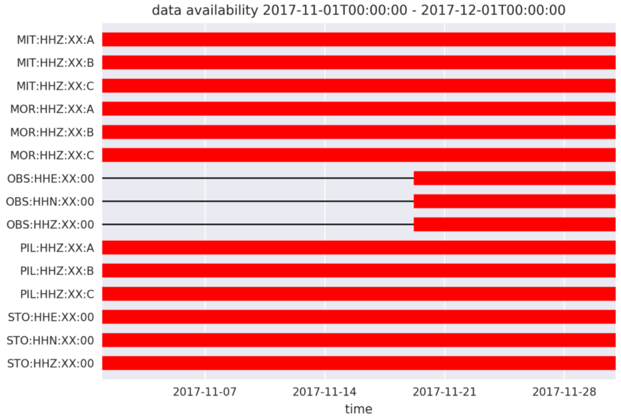
data availability 2017-11-01T00:00:00 - 2017-12-01T00:00:00

2018 - Sonnblick Seismological Network

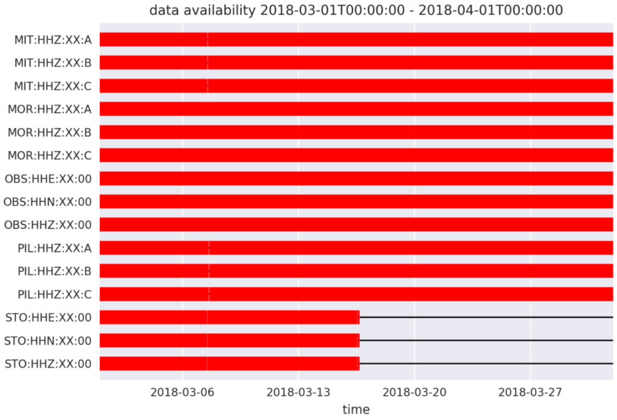

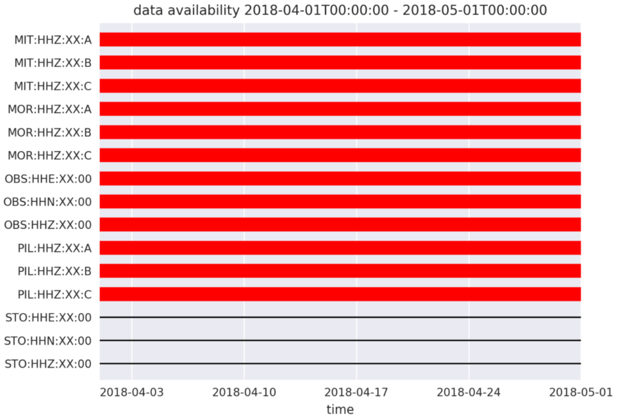

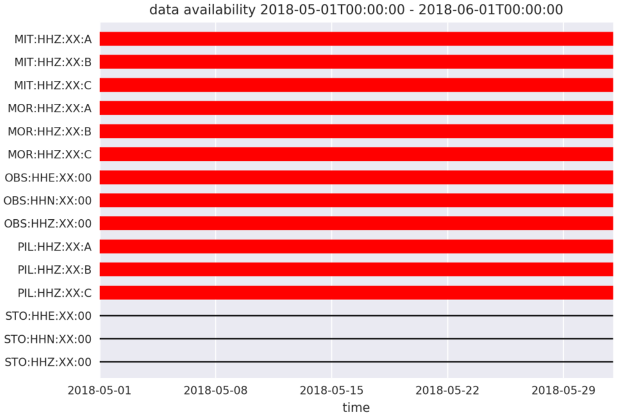

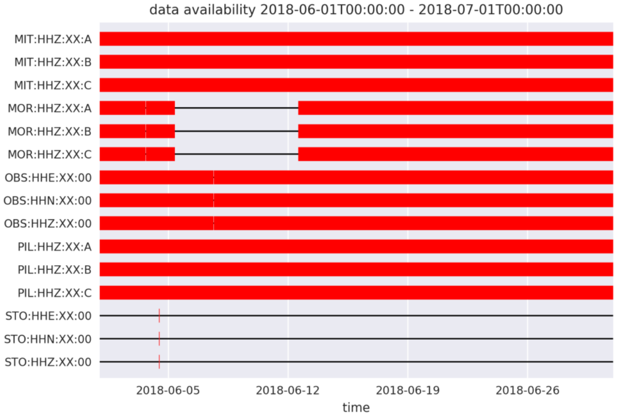

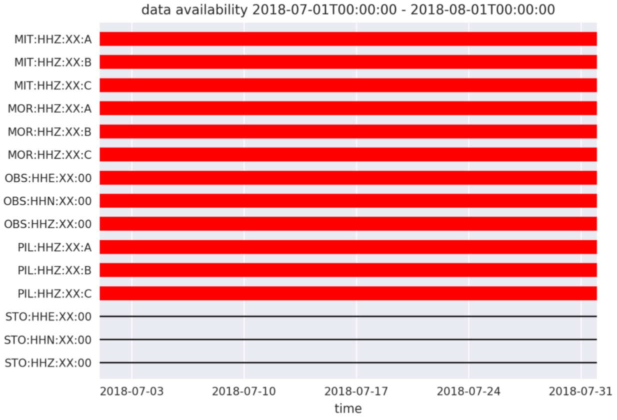

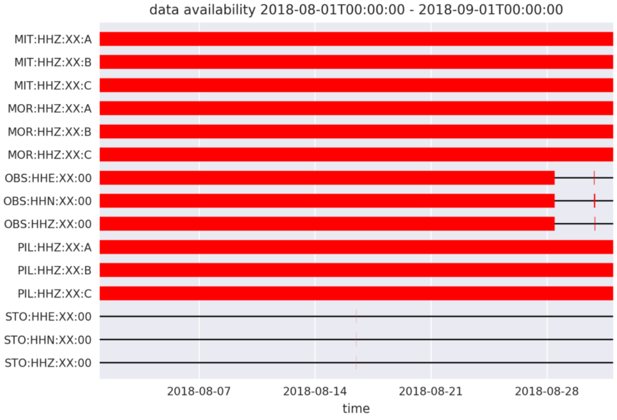

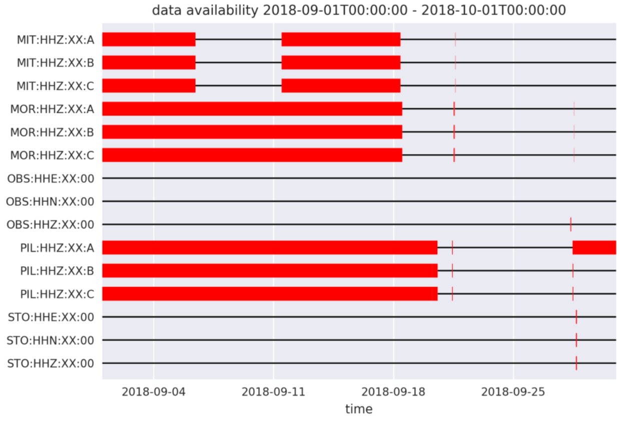
data availability 2018-09-01T00:00:00 - 2018-10-01T00:00:00
MIT:HHZ:XX:A
MIT:HHZ:XX:B
MIT:HHZ:XX:C
MOR:HHZ:XX:A
MOR:HHZ:XX:B
MOR:HHZ:XX:C
OBS:HHE:XX:00
OBS:HHN:XX:00
OBS:HHZ:XX:00
PIL:HHZ:XX:A
PIL:HHZ:XX:B
PIL:HHZ:XX:C
STO:HHE:XX:00
STO:HHN:XX:00
STO:HHZ:XX:00
2018-09-04
2018-09-11
2018-09-18
2018-09-25
time

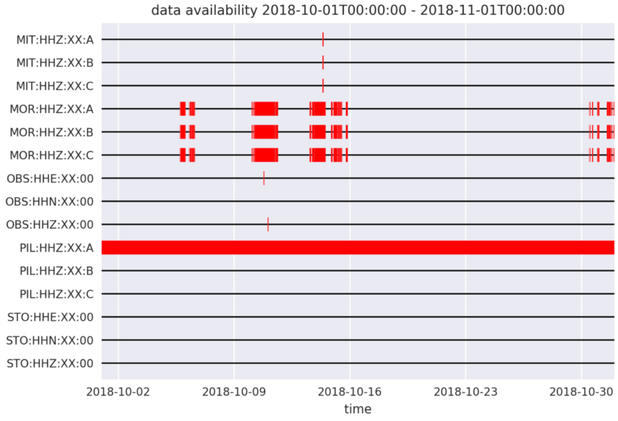
data availability 2018-10-01T00:00:00 - 2018-11-01T00:00:00
MIT:HHZ:XX:A
MIT:HHZ:XX:B
MIT:HHZ:XX:C
MOR:HHZ:XX:A
MOR:HHZ:XX:B
MOR:HHZ:XX:C
OBS:HHE:XX:00
OBS:HHN:XX:00
OBS:HHZ:XX:00
PIL:HHZ:XX:A
PIL:HHZ:XX:B
PIL:HHZ:XX:C
STO:HHE:XX:00
STO:HHN:XX:00
STO:HHZ:XX:00
2018-10-02
2018-10-09
2018-10-16
2018-10-23
2018-10-30
time

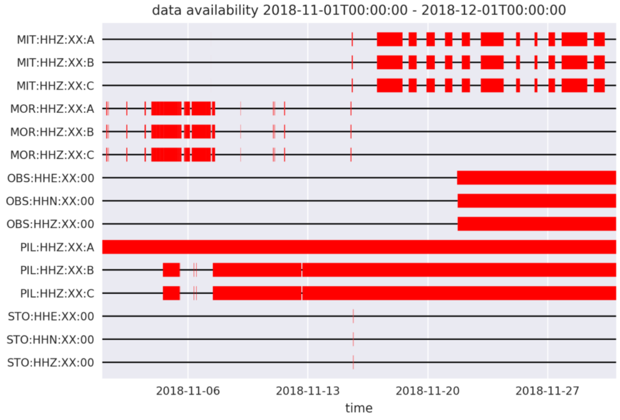
data availability 2018-11-01T00:00:00 - 2018-12-01T00:00:00
MIT:HHZ:XX:A
MIT:HHZ:XX:B
MIT:HHZ:XX:C
MOR:HHZ:XX:A
MOR:HHZ:XX:B
MOR:HHZ:XX:C
OBS:HHE:XX:00
OBS:HHN:XX:00
OBS:HHZ:XX:00
PIL:HHZ:XX:A
PIL:HHZ:XX:B
PIL:HHZ:XX:C
STO:HHE:XX:00
STO:HHN:XX:00
STO:HHZ:XX:00
2018-11-06
2018-11-13
2018-11-20
2018-11-27
time

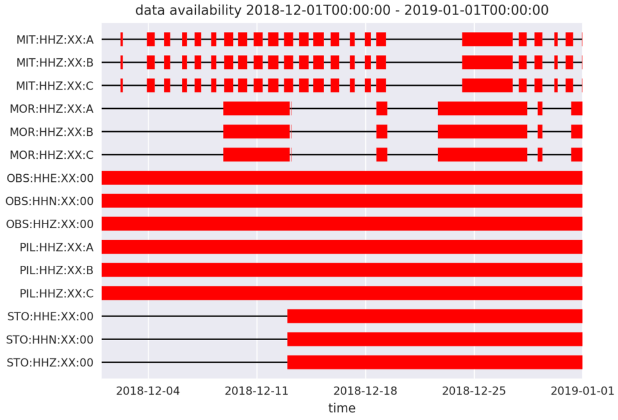
data availability 2018-12-01T00:00:00 - 2019-01-01T00:00:00
MIT:HHZ:XX:A
MIT:HHZ:XX:B
MIT:HHZ:XX:C
MOR:HHZ:XX:A
MOR:HHZ:XX:B
MOR:HHZ:XX:C
OBS:HHE:XX:00
OBS:HHN:XX:00
OBS:HHZ:XX:00
PIL:HHZ:XX:A
PIL:HHZ:XX:B
PIL:HHZ:XX:C
STO:HHE:XX:00
STO:HHN:XX:00
STO:HHZ:XX:00
2018-12-04
2018-12-11
2018-12-18
2018-12-25
2019-01-01
time

2019 - Sonnblick Seismological Network

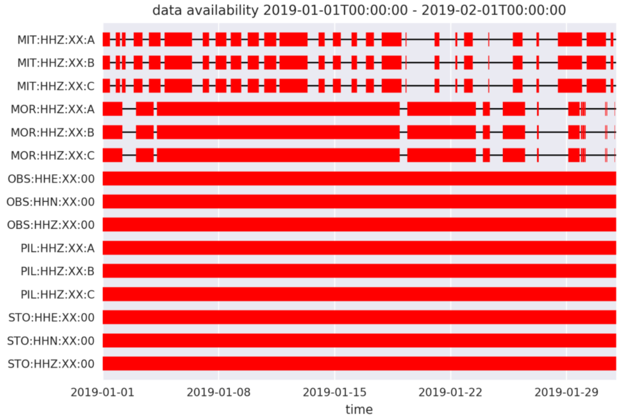
data availability 2019-01-01T00:00:00 - 2019-02-01T00:00:00

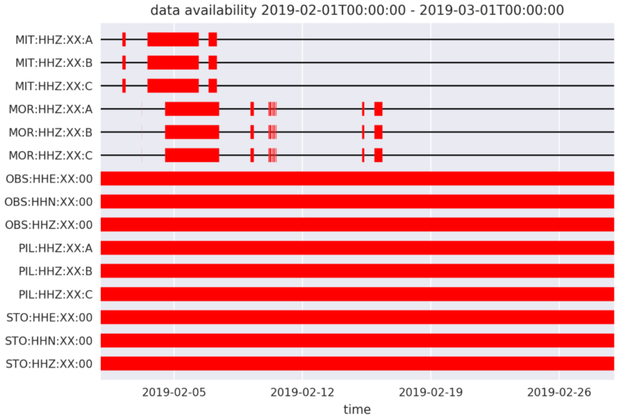
data availability 2019-02-01T00:00:00 - 2019-03-01T00:00:00

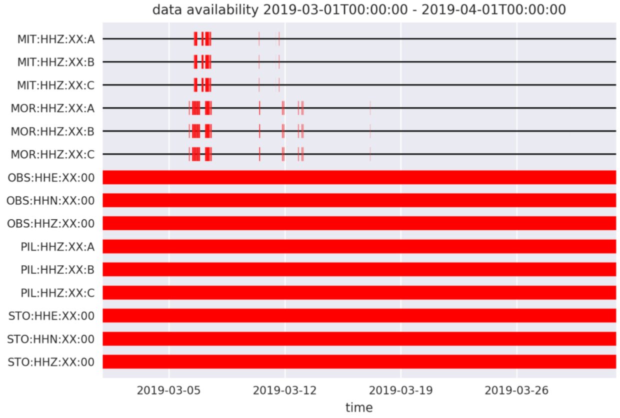
data availability 2019-03-01T00:00:00 - 2019-04-01T00:00:00

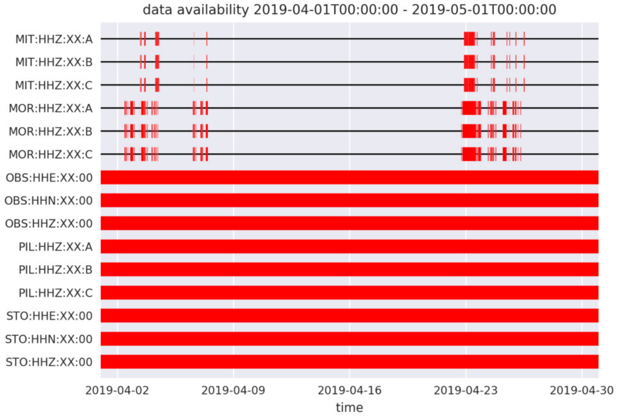
data availability 2019-04-01T00:00:00 - 2019-05-01T00:00:00

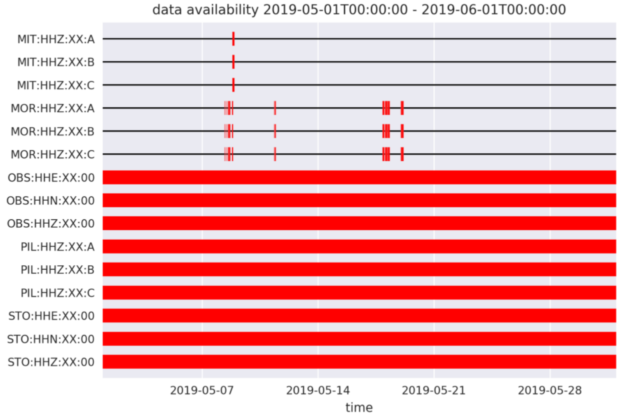
data availability 2019-05-01T00:00:00 - 2019-06-01T00:00:00

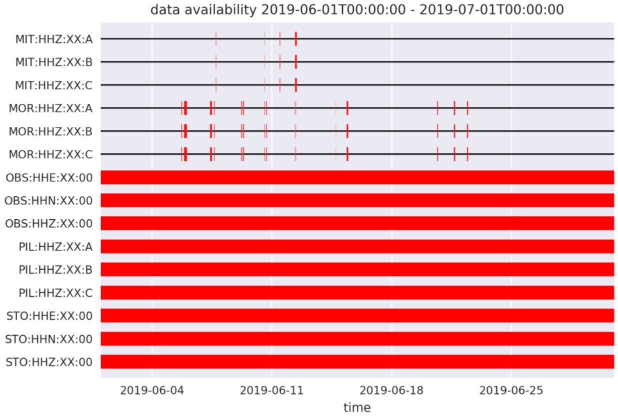
data availability 2019-06-01T00:00:00 - 2019-07-01T00:00:00

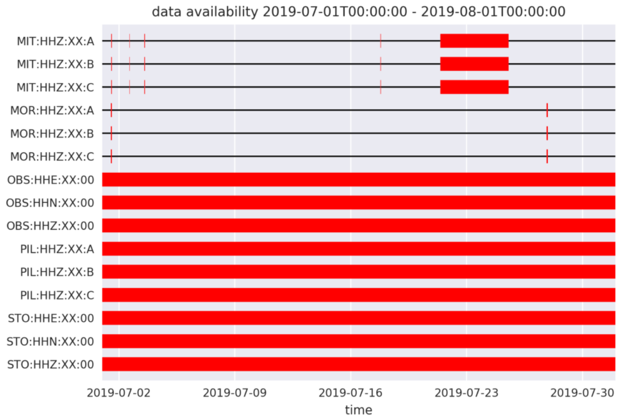
data availability 2019-07-01T00:00:00 - 2019-08-01T00:00:00

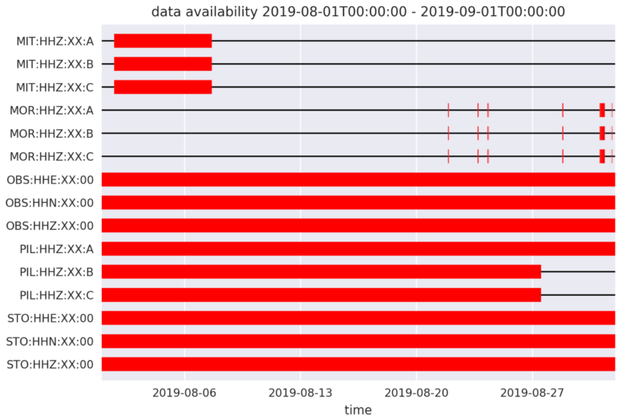
data availability 2019-08-01T00:00:00 - 2019-09-01T00:00:00

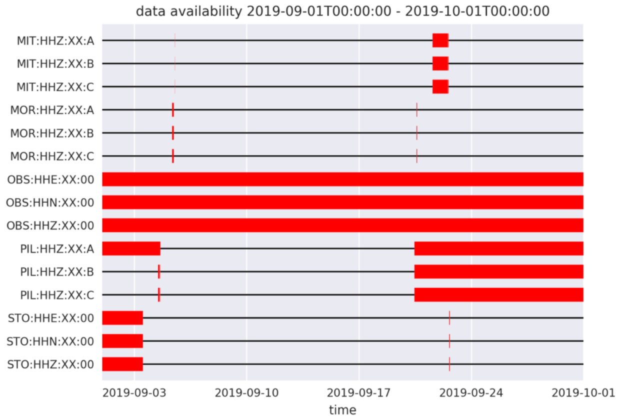
data availability 2019-09-01T00:00:00 - 2019-10-01T00:00:00

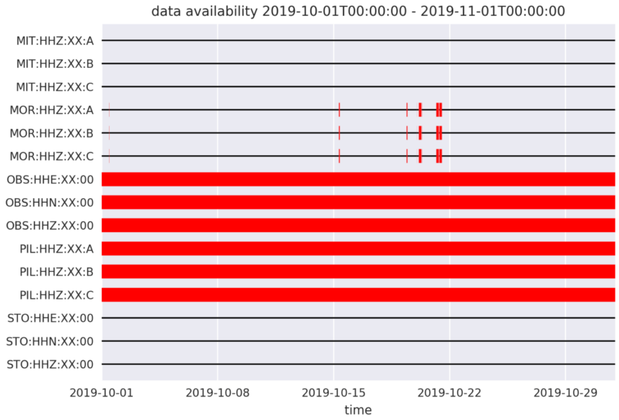
data availability 2019-10-01T00:00:00 - 2019-11-01T00:00:00

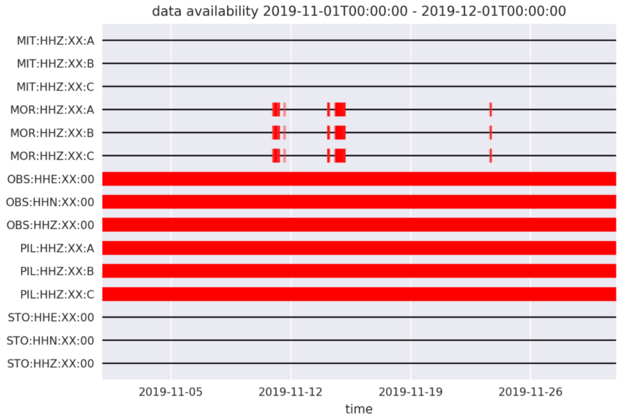
data availability 2019-11-01T00:00:00 - 2019-12-01T00:00:00

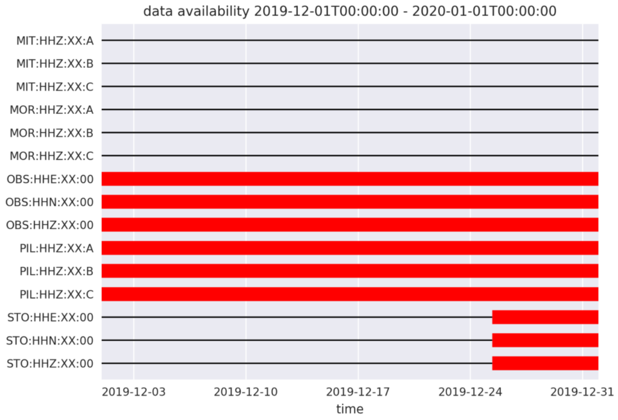
data availability 2019-12-01T00:00:00 - 2020-01-01T00:00:00

Appendix B: Weekly Spectrograms

Field Campaign 2017

In the following all calculated spectrograms for the campaign period in 2017 are shown. The time period of the single spectrograms can be distinguished by the title or the x-axis. In case of the individual spectrograms the title informs about the actual network station (OBS, MIT, MOR, PIL, STO). In the individual spectrograms just one representative channel per station is shown. The representative channel is also stated in the title.

Median Spectrograms

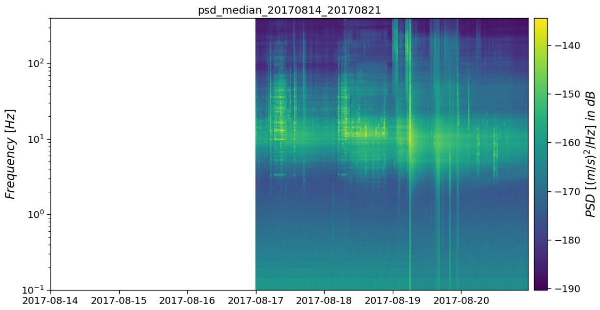

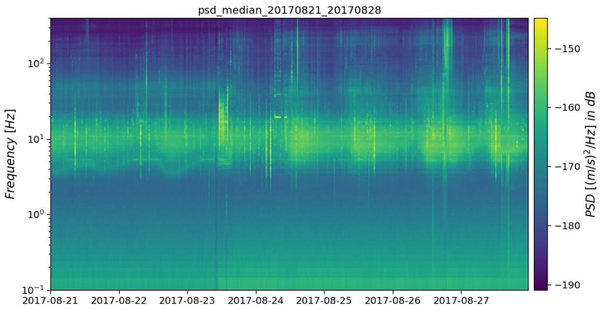

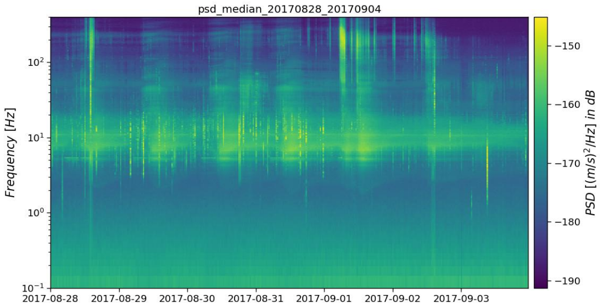

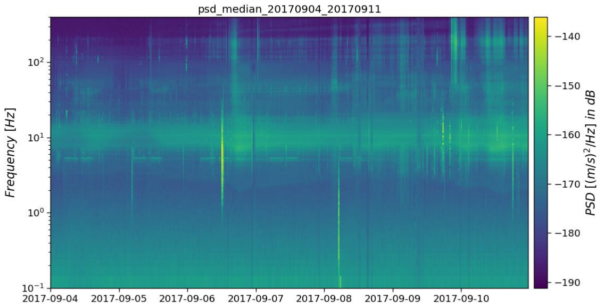

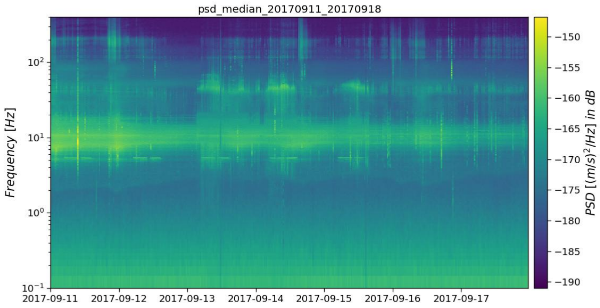

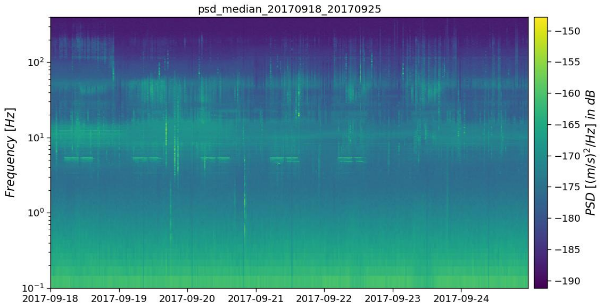

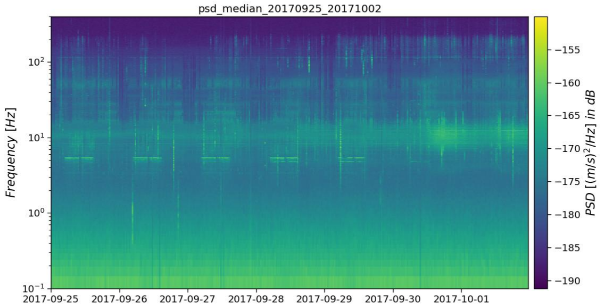
psd_median_20170925_20171002

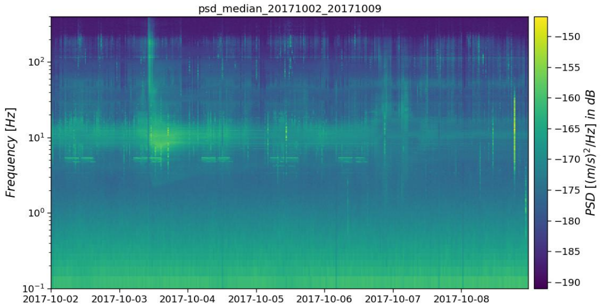
psd_median_20171002_20171009

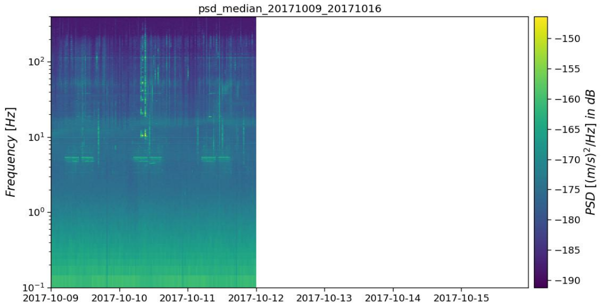
psd_median_20171009_20171016

Individual Spectrograms

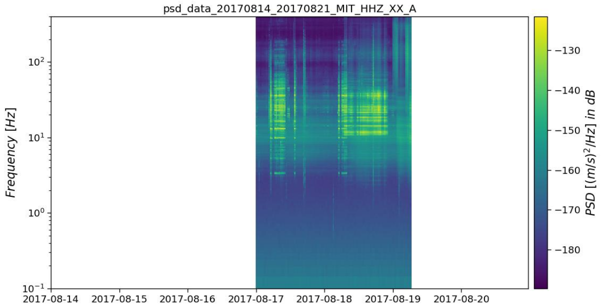
psd_data_20170814_20170821_MIT_HHZ_XX_A

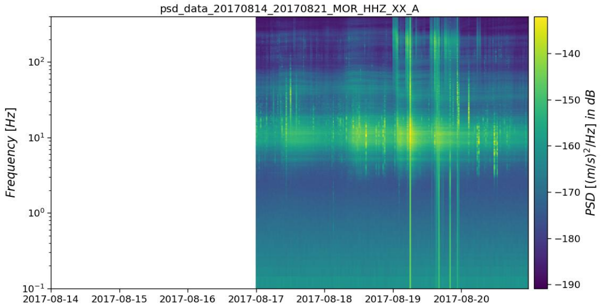
psd_data_20170814_20170821_MOR_HHZ_XX_A

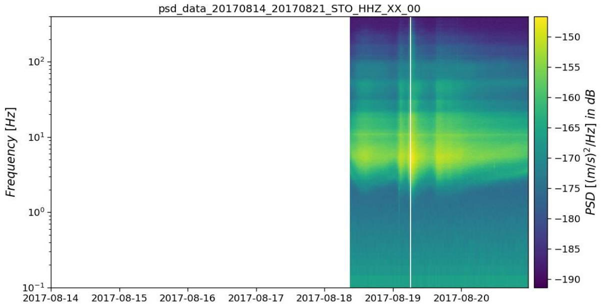
psd_data_20170814_20170821_STO_HHZ_XX_00

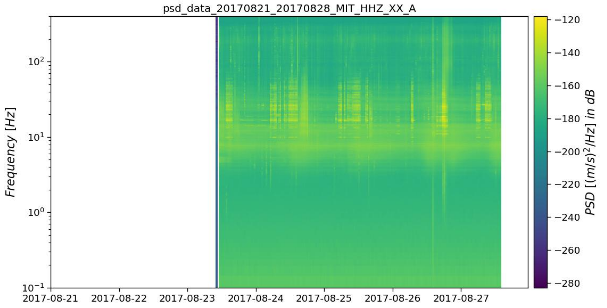
psd_data_20170821_20170828_MIT_HHZ_XX_A

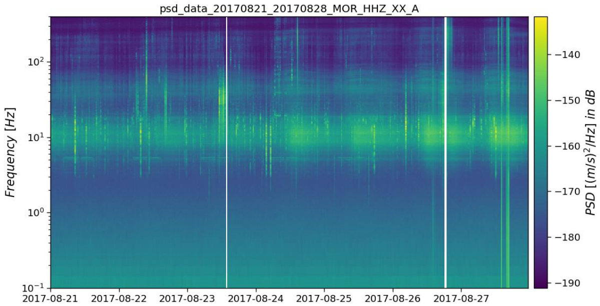
psd_data_20170821_20170828_MOR_HHZ_XX_A
Frequency [Hz]
10^2
10^1
10^0
10^-1
2017-08-21
2017-08-22
2017-08-23
2017-08-24
2017-08-25
2017-08-26
2017-08-27
PSD [(m/s)^2/Hz] in dB
−140
−150
−160
−170
−180
−190

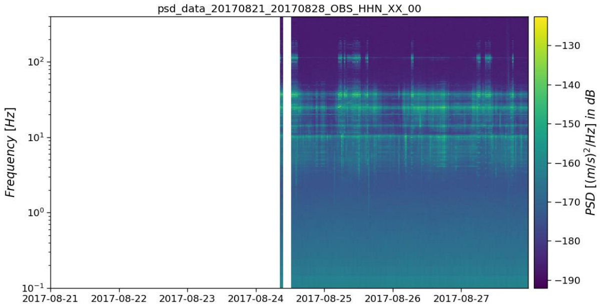
psd_data_20170821_20170828_OBS_HHN_XX_00
Frequency [Hz]
10^2
10^1
10^0
10^-1
2017-08-21
2017-08-22
2017-08-23
2017-08-24
2017-08-25
2017-08-26
2017-08-27
PSD [(m/s)^2/Hz] in dB
−130
−140
−150
−160
−170
−180
−190

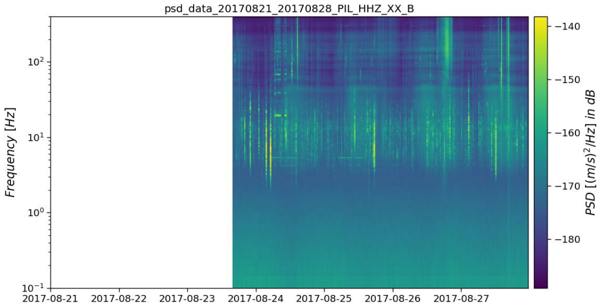
psd_data_20170821_20170828_PIL_HHZ_XX_B
Frequency [Hz]
10^2
10^1
10^0
10^-1
2017-08-21
2017-08-22
2017-08-23
2017-08-24
2017-08-25
2017-08-26
2017-08-27
PSD [(m/s)^2/Hz] in dB
−140
−150
−160
−170
−180

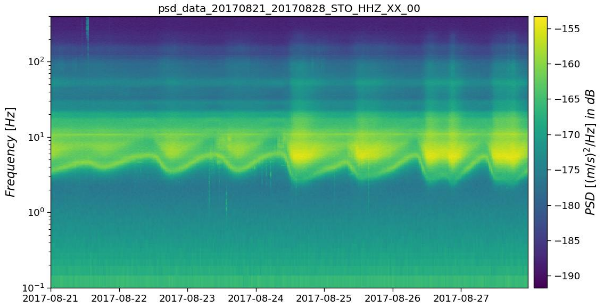
psd_data_20170821_20170828_STO_HHZ_XX_00
Frequency [Hz]
10^2
10^1
10^0
10^-1
2017-08-21
2017-08-22
2017-08-23
2017-08-24
2017-08-25
2017-08-26
2017-08-27
PSD [(m/s)^2/Hz] in dB
−155
−160
−165
−170
−175
−180
−185
−190

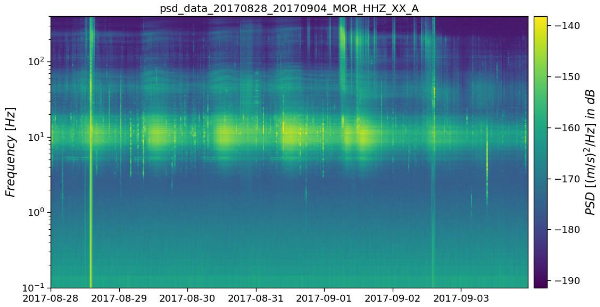
psd_data_20170828_20170904_MOR_HHZ_XX_A
Frequency [Hz]
10^2
10^1
10^0
10^-1
2017-08-28
2017-08-29
2017-08-30
2017-08-31
2017-09-01
2017-09-02
2017-09-03
PSD [(m/s)^2/Hz] in dB
−140
−150
−160
−170
−180
−190

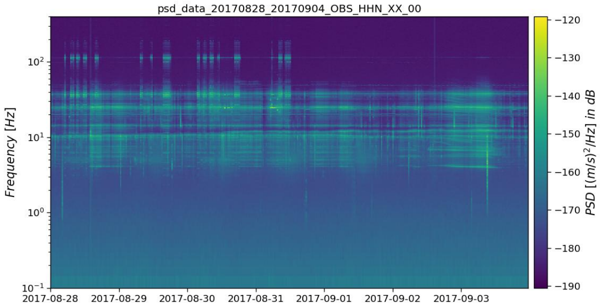
psd_data_20170828_20170904_OBS_HHN_XX_00
Frequency [Hz]
10^2
10^1
10^0
10^-1
2017-08-28
2017-08-29
2017-08-30
2017-08-31
2017-09-01
2017-09-02
2017-09-03
PSD [(m/s)^2/Hz] in dB
−120
−130
−140
−150
−160
−170
−180
−190

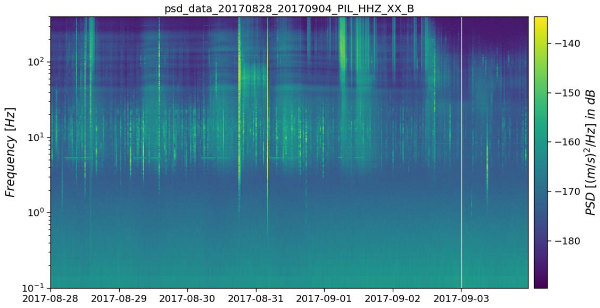
psd_data_20170828_20170904_PIL_HHZ_XX_B
Frequency [Hz]
10^2
10^1
10^0
10^-1
2017-08-28
2017-08-29
2017-08-30
2017-08-31
2017-09-01
2017-09-02
2017-09-03
PSD [(m/s)^2/Hz] in dB
−140
−150
−160
−170
−180

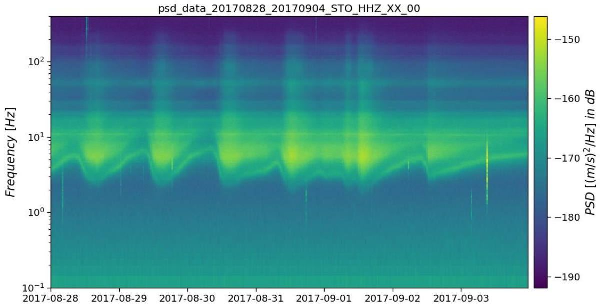
psd_data_20170828_20170904_STO_HHZ_XX_00
Frequency [Hz]
10^2
10^1
10^0
10^-1
2017-08-28
2017-08-29
2017-08-30
2017-08-31
2017-09-01
2017-09-02
2017-09-03
PSD [(m/s)^2/Hz] in dB
−150
−160
−170
−180
−190

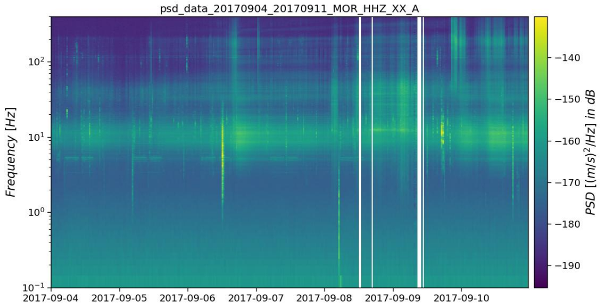
psd_data_20170904_20170911_MOR_HHZ_XX_A
Frequency [Hz]
10^2
10^1
10^0
10^{-1}
2017-09-04
2017-09-05
2017-09-06
2017-09-07
2017-09-08
2017-09-09
2017-09-10
PSD [(m/s)²/Hz] in dB
−140
−150
−160
−170
−180
−190

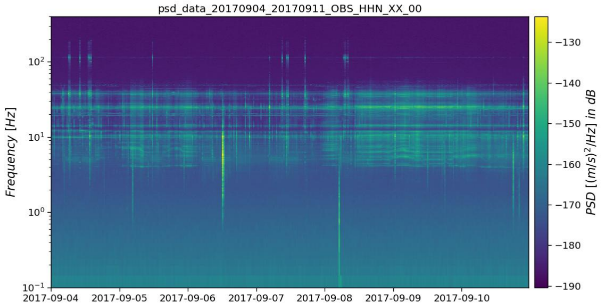
psd_data_20170904_20170911_OBS_HHN_XX_00
Frequency [Hz]
10^2
10^1
10^0
10^{-1}
2017-09-04
2017-09-05
2017-09-06
2017-09-07
2017-09-08
2017-09-09
2017-09-10
PSD [(m/s)²/Hz] in dB
−130
−140
−150
−160
−170
−180
−190

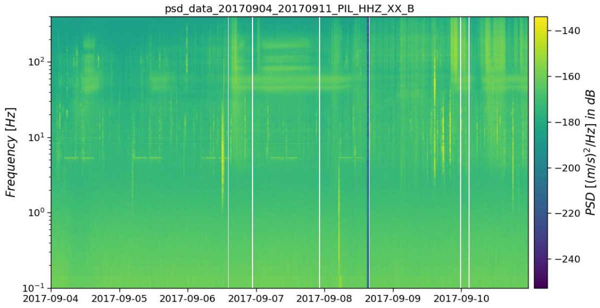
psd_data_20170904_20170911_PIL_HHZ_XX_B
Frequency [Hz]
10^2
10^1
10^0
10^{-1}
2017-09-04
2017-09-05
2017-09-06
2017-09-07
2017-09-08
2017-09-09
2017-09-10
PSD [(m/s)²/Hz] in dB
−140
−160
−180
−200
−220
−240

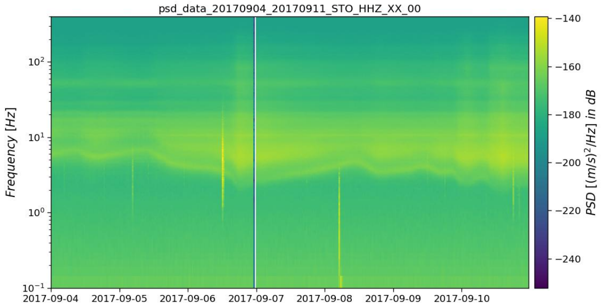
psd_data_20170904_20170911_STO_HHZ_XX_00
Frequency [Hz]
10^2
10^1
10^0
10^{-1}
2017-09-04
2017-09-05
2017-09-06
2017-09-07
2017-09-08
2017-09-09
2017-09-10
PSD [(m/s)²/Hz] in dB
−140
−160
−180
−200
−220
−240

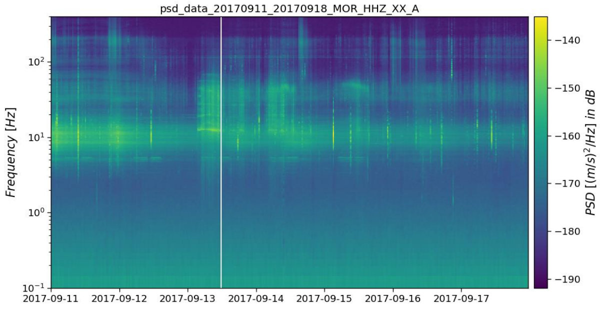
psd_data_20170911_20170918_MOR_HHZ_XX_A
Frequency [Hz]
10^2
10^1
10^0
10^{-1}
2017-09-11
2017-09-12
2017-09-13
2017-09-14
2017-09-15
2017-09-16
2017-09-17
PSD [(m/s)²/Hz] in dB
−140
−150
−160
−170
−180
−190

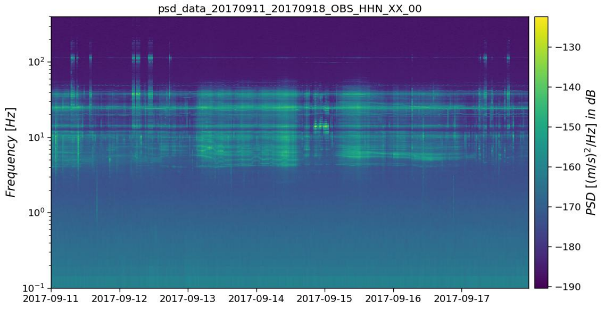
psd_data_20170911_20170918_OBS_HHN_XX_00
Frequency [Hz]
10^2
10^1
10^0
10^{-1}
2017-09-11
2017-09-12
2017-09-13
2017-09-14
2017-09-15
2017-09-16
2017-09-17
PSD [(m/s)²/Hz] in dB
−130
−140
−150
−160
−170
−180
−190

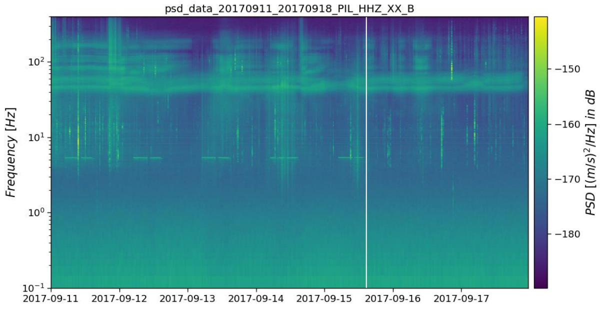
psd_data_20170911_20170918_PIL_HHZ_XX_B
Frequency [Hz]
10^2
10^1
10^0
10^{-1}
2017-09-11
2017-09-12
2017-09-13
2017-09-14
2017-09-15
2017-09-16
2017-09-17
PSD [(m/s)²/Hz] in dB
−150
−160
−170
−180

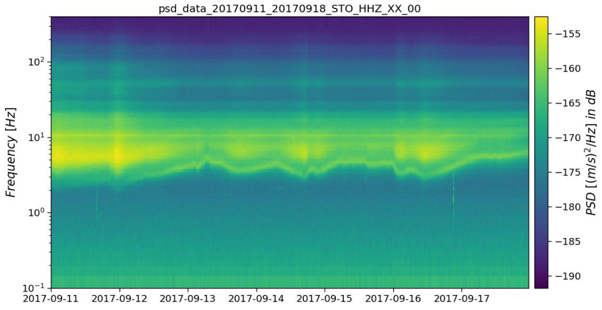
psd_data_20170911_20170918_STO_HHZ_XX_00
Frequency [Hz]
10^2
10^1
10^0
10^{-1}
2017-09-11
2017-09-12
2017-09-13
2017-09-14
2017-09-15
2017-09-16
2017-09-17
PSD [(m/s)²/Hz] in dB
−155
−160
−165
−170
−175
−180
−185
−190

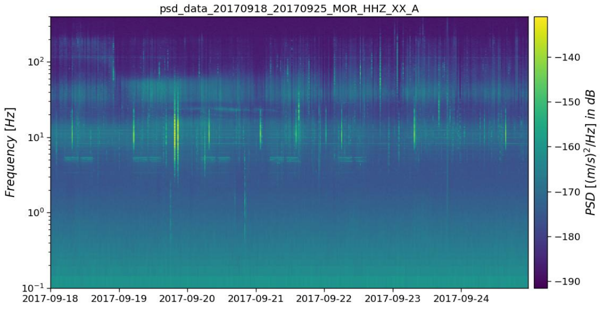
psd_data_20170918_20170925_MOR_HHZ_XX_A
Frequency [Hz]
10^{-1}
10^0
10^1
10^2
2017-09-18
2017-09-19
2017-09-20
2017-09-21
2017-09-22
2017-09-23
2017-09-24
PSD [(m/s)^2/Hz] in dB
−140
−150
−160
−170
−180
−190

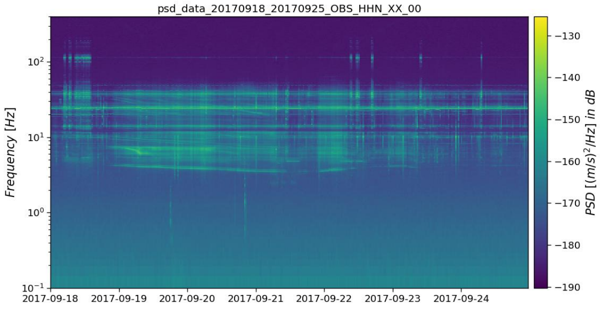
psd_data_20170918_20170925_OBS_HHN_XX_00
Frequency [Hz]
10^{-1}
10^0
10^1
10^2
2017-09-18
2017-09-19
2017-09-20
2017-09-21
2017-09-22
2017-09-23
2017-09-24
PSD [(m/s)^2/Hz] in dB
−130
−140
−150
−160
−170
−180
−190

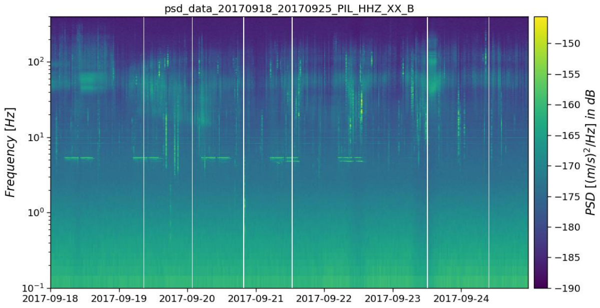
psd_data_20170918_20170925_PIL_HHZ_XX_B
Frequency [Hz]
10^{-1}
10^0
10^1
10^2
2017-09-18
2017-09-19
2017-09-20
2017-09-21
2017-09-22
2017-09-23
2017-09-24
PSD [(m/s)^2/Hz] in dB
−150
−155
−160
−165
−170
−175
−180
−185
−190

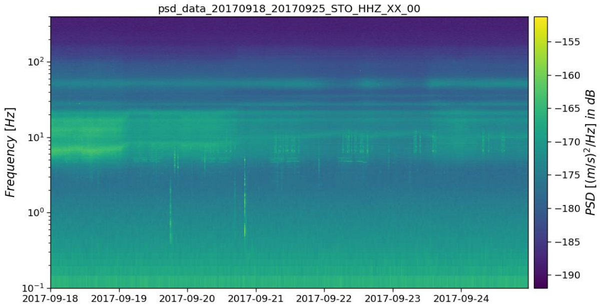
psd_data_20170918_20170925_STO_HHZ_XX_00
Frequency [Hz]
10^{-1}
10^0
10^1
10^2
2017-09-18
2017-09-19
2017-09-20
2017-09-21
2017-09-22
2017-09-23
2017-09-24
PSD [(m/s)^2/Hz] in dB
−155
−160
−165
−170
−175
−180
−185
−190

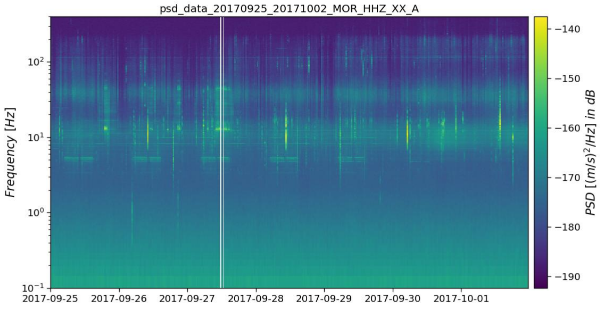
psd_data_20170925_20171002_MOR_HHZ_XX_A
Frequency [Hz]
10^{-1}
10^0
10^1
10^2
2017-09-25
2017-09-26
2017-09-27
2017-09-28
2017-09-29
2017-09-30
2017-10-01
PSD [(m/s)^2/Hz] in dB
−140
−150
−160
−170
−180
−190

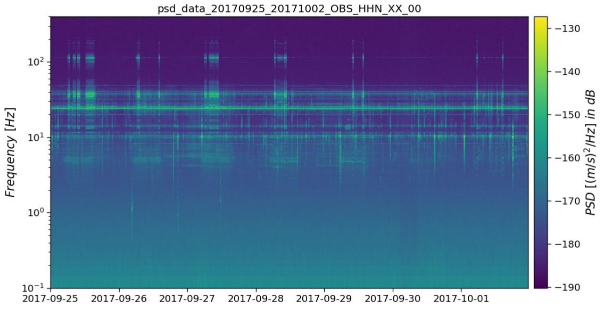
psd_data_20170925_20171002_OBS_HHN_XX_00
Frequency [Hz]
10^{-1}
10^0
10^1
10^2
2017-09-25
2017-09-26
2017-09-27
2017-09-28
2017-09-29
2017-09-30
2017-10-01
PSD [(m/s)^2/Hz] in dB
−130
−140
−150
−160
−170
−180
−190

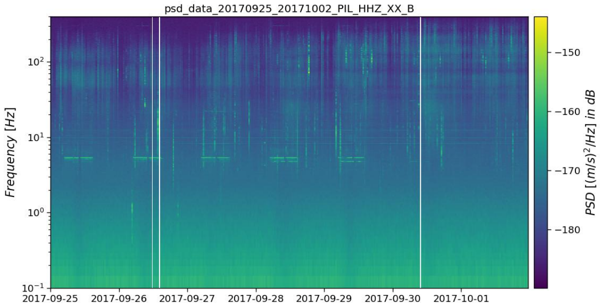
psd_data_20170925_20171002_PIL_HHZ_XX_B
Frequency [Hz]
10^{-1}
10^0
10^1
10^2
2017-09-25
2017-09-26
2017-09-27
2017-09-28
2017-09-29
2017-09-30
2017-10-01
PSD [(m/s)^2/Hz] in dB
−150
−160
−170
−180

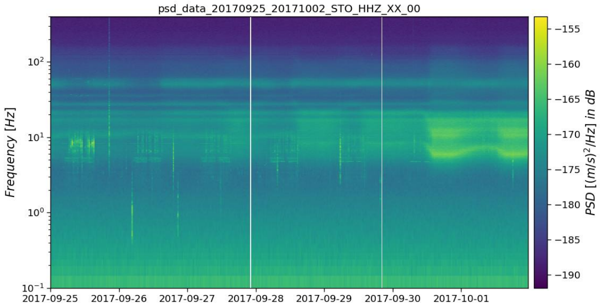
psd_data_20170925_20171002_STO_HHZ_XX_00
Frequency [Hz]
10^{-1}
10^0
10^1
10^2
2017-09-25
2017-09-26
2017-09-27
2017-09-28
2017-09-29
2017-09-30
2017-10-01
PSD [(m/s)^2/Hz] in dB
−155
−160
−165
−170
−175
−180
−185
−190

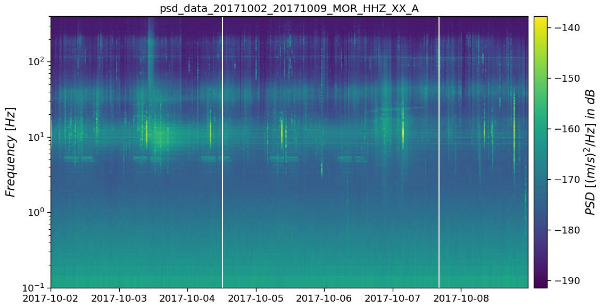

psd_data_20171002_20171009_MOR_HHZ_XX_A

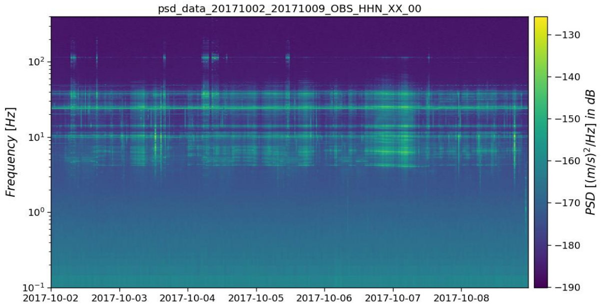

psd_data_20171002_20171009_OBS_HHN_XX_00

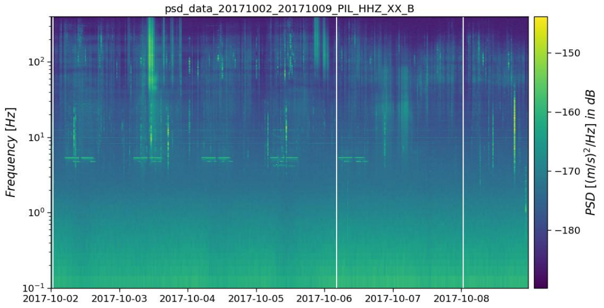

psd_data_20171002_20171009_PIL_HHZ_XX_B

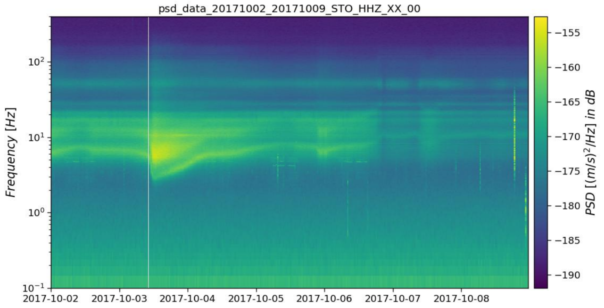

psd_data_20171002_20171009_STO_HHZ_XX_00

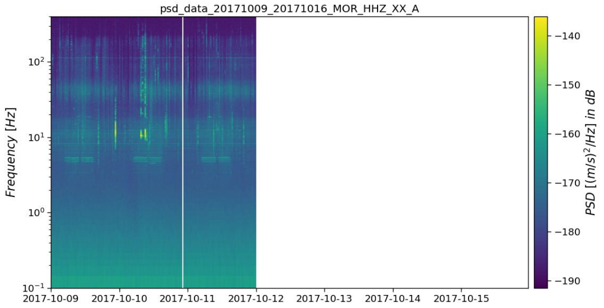

psd_data_20171009_20171016_MOR_HHZ_XX_A

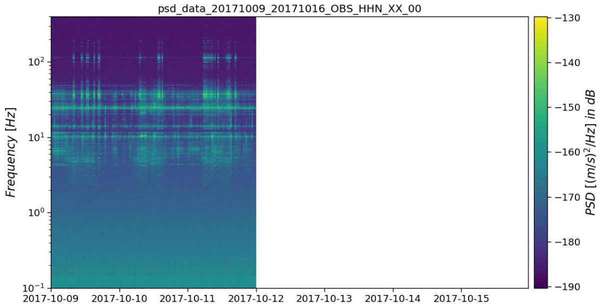

psd_data_20171009_20171016_OBS_HHN_XX_00

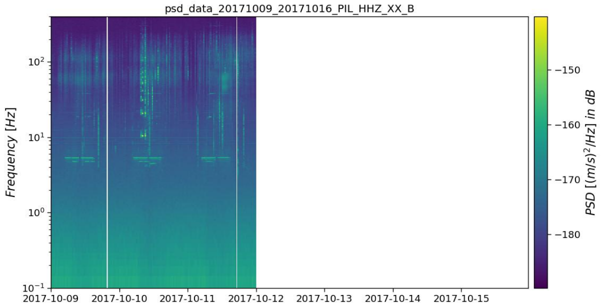

psd_data_20171009_20171016_PIL_HHZ_XX_B

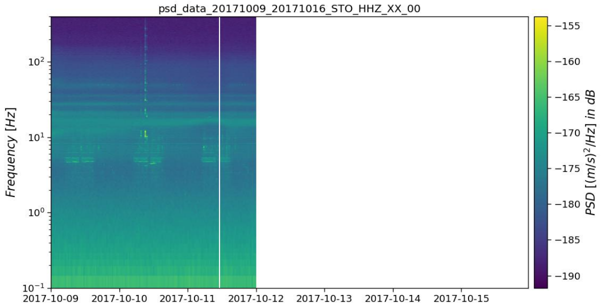

psd_data_20171009_20171016_STO_HHZ_XX_00

Severe Weather Event 2018

In the folllowing all calculated spectrograms for the severe weather event in 2018 are shown. The time period of the single spectrograms can be distinguished by the x-axis. In case of the individual spectrograms the title informs about the actual network station (OBS, MIT, MOR, PIL, STO). In the individual spectrograms just one representative channel per station is shown. The representative channel is also stated in the title.

Median Spectrogram

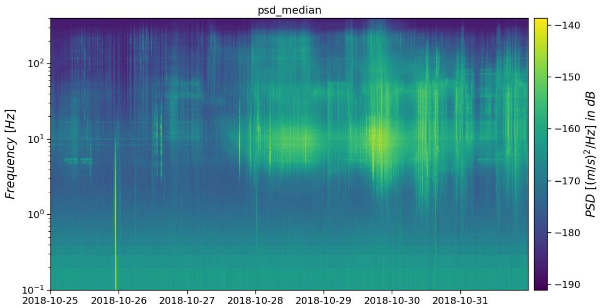

Individual Spectrograms

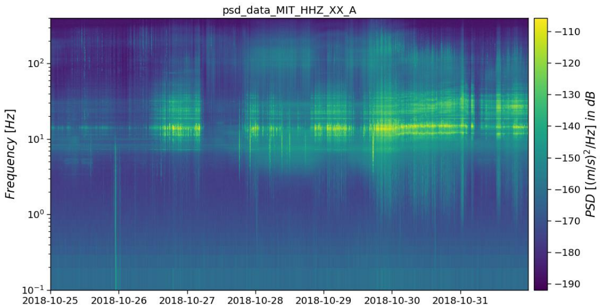

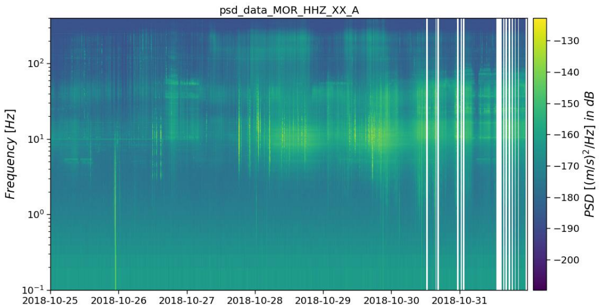

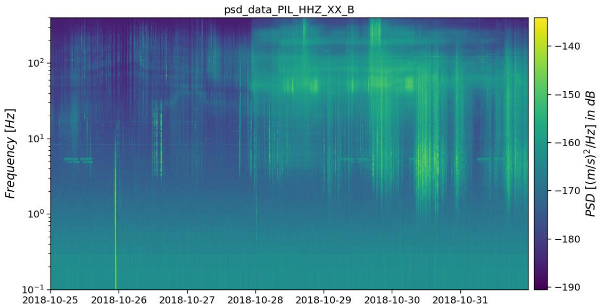

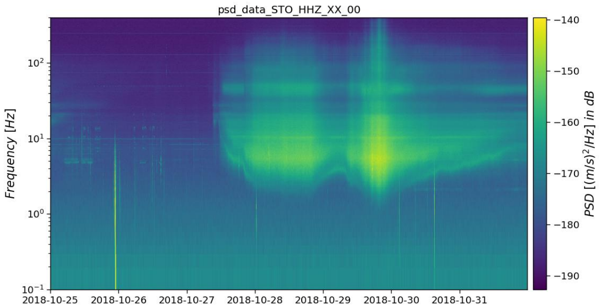

Appendix C: Seismic Event Catalogs

Field Campaign 2017

Table 11.1: Detected and categorized seismic events of the campaign in 2017. **Nr** indicates the number of stations where the event was detected

ID	Event Start Time	Event End Time	Nr	Event Type
19094	2017-08-23T11:01:33.892499	2017-08-23T11:01:33.892499	2	rockfall candidate short
19095	2017-08-23T11:35:27.597500	2017-08-23T11:35:27.597500	2	noise
19096	2017-08-23T17:17:27.960000	2017-08-23T17:17:27.960000	2	rockfall candidate short
19097	2017-08-23T17:40:41.562500	2017-08-23T17:40:41.562500	2	rockfall candidate short
19098	2017-08-23T18:47:35.080000	2017-08-23T18:47:35.080000	2	rockfall candidate short
19099	2017-08-23T19:05:53.069999	2017-08-23T19:05:53.069999	2	rockfall candidate short
19100	2017-08-23T19:56:43.033750	2017-08-23T19:56:43.033750	2	rockfall candidate short
19101	2017-08-23T20:04:07.687500	2017-08-23T20:04:07.687500	3	rockfall candidate short
19102	2017-08-23T20:43:53.801250	2017-08-23T20:43:53.801250	2	rockfall candidate short
19103	2017-08-23T22:11:06.608750	2017-08-23T22:11:06.608750	2	rockfall candidate short
19104	2017-08-23T23:11:07.204999	2017-08-23T23:11:07.204999	2	rockfall candidate short
19105	2017-08-24T01:12:41.327500	2017-08-24T01:12:41.327500	2	rockfall candidate short
19106	2017-08-24T01:33:13.636250	2017-08-24T01:33:13.636250	2	rockfall candidate short
19107	2017-08-24T02:31:45.473750	2017-08-24T02:31:45.473750	2	rockfall candidate short
19108	2017-08-24T02:47:41.571249	2017-08-24T02:47:41.571249	2	rockfall candidate short
19109	2017-08-24T03:44:49.461250	2017-08-24T03:44:49.461250	2	rockfall candidate short
19110	2017-08-24T03:57:26.184999	2017-08-24T03:57:26.184999	2	rockfall candidate short
19111	2017-08-24T03:57:38.953750	2017-08-24T03:57:38.953750	3	rockfall candidate short
19112	2017-08-24T03:59:41.467500	2017-08-24T03:59:41.467500	2	rockfall candidate short
19113	2017-08-24T05:06:36.511249	2017-08-24T05:06:36.511249	2	rockfall candidate short
19114	2017-08-24T05:14:24.658749	2017-08-24T05:14:24.658749	3	rockfall candidate short
19115	2017-08-24T05:25:00.917499	2017-08-24T05:25:00.917499	2	rockfall candidate short
19116	2017-08-24T07:06:57.132499	2017-08-24T07:06:57.132499	2	rockfall candidate short
19117	2017-08-24T08:04:47.293750	2017-08-24T08:04:47.293750	2	rockfall candidate short
19118	2017-08-24T08:30:59.613750	2017-08-24T08:30:59.613750	2	rockfall candidate short
19119	2017-08-24T10:02:52.851249	2017-08-24T10:02:52.851249	2	rockfall candidate short
19120	2017-08-24T13:34:21.364999	2017-08-24T13:34:21.364999	2	noise
19121	2017-08-24T14:05:41.269999	2017-08-24T14:05:41.269999	2	rockfall candidate short
19122	2017-08-24T16:27:00.143749	2017-08-24T16:27:00.143749	2	rockfall candidate short
19123	2017-08-24T19:31:39.700000	2017-08-24T19:31:39.700000	2	rockfall candidate short
19124	2017-08-24T20:48:32.768750	2017-08-24T20:48:32.768750	3	rockfall candidate short
19125	2017-08-24T21:32:28.256249	2017-08-24T21:32:28.256249	2	rockfall candidate short
19126	2017-08-24T23:22:30.037499	2017-08-24T23:22:30.037499	2	rockfall candidate short
19127	2017-08-25T01:04:17.309999	2017-08-25T01:04:17.309999	3	rockfall candidate short
19128	2017-08-25T01:21:43.943749	2017-08-25T01:21:43.943749	2	rockfall candidate short
19129	2017-08-25T02:27:33.214999	2017-08-25T02:27:33.214999	2	rockfall candidate short
19130	2017-08-25T03:11:44.341250	2017-08-25T03:11:44.341250	3	rockfall candidate short
19131	2017-08-25T06:20:13.408750	2017-08-25T06:20:13.408750	3	rockfall candidate short
19132	2017-08-25T06:26:21.173750	2017-08-25T06:26:21.173750	2	rockfall candidate short
19133	2017-08-25T06:44:35.864999	2017-08-25T06:44:35.864999	3	rockfall candidate short
19134	2017-08-25T07:02:53.916250	2017-08-25T07:02:53.916250	3	rockfall candidate short
19135	2017-08-25T10:34:13.086249	2017-08-25T10:34:13.086249	2	anthropogenic

19136	2017-08-25T10:38:42.482500	2017-08-25T10:38:42.482500	2	rockfall candidate short
19137	2017-08-25T12:57:53.698749	2017-08-25T12:57:53.698749	2	rockfall candidate short
19138	2017-08-25T16:40:47.675000	2017-08-25T16:40:47.675000	3	rockfall candidate short
19139	2017-08-25T17:18:20.513750	2017-08-25T17:18:20.513750	3	rockfall candidate short
19140	2017-08-25T17:55:35.128750	2017-08-25T17:55:35.128750	2	rockfall candidate short
19141	2017-08-25T17:56:02.037499	2017-08-25T17:56:02.037499	3	rockfall candidate short
19142	2017-08-25T17:56:13.933750	2017-08-25T17:56:13.933750	4	rockfall candidate short
19143	2017-08-25T20:32:44.752499	2017-08-25T20:32:44.752499	2	rockfall candidate short
19144	2017-08-25T21:59:19.416250	2017-08-25T21:59:19.416250	2	rockfall candidate short
19145	2017-08-26T02:52:02.391249	2017-08-26T02:52:02.391249	2	rockfall candidate short
19146	2017-08-26T02:54:20.666249	2017-08-26T02:54:20.666249	2	rockfall candidate short
19147	2017-08-26T03:57:09.898749	2017-08-26T03:57:09.898749	2	rockfall candidate short
19148	2017-08-26T04:19:26.656250	2017-08-26T04:19:26.656250	2	rockfall candidate short
19149	2017-08-26T04:19:32.109999	2017-08-26T04:19:32.109999	2	rockfall candidate short
19150	2017-08-26T04:55:41.576250	2017-08-26T04:55:41.576250	3	rockfall candidate long
19151	2017-08-26T05:58:10.157499	2017-08-26T05:58:10.157499	3	rockfall candidate short
19152	2017-08-26T06:39:27.376250	2017-08-26T06:39:27.376250	2	rockfall candidate short
19153	2017-08-26T06:59:19.948750	2017-08-26T06:59:19.948750	3	rockfall candidate short
19154	2017-08-26T07:03:44.336250	2017-08-26T07:03:44.336250	2	rockfall candidate short
19155	2017-08-26T08:28:26.573750	2017-08-26T08:28:26.573750	2	rockfall candidate short
19156	2017-08-26T09:26:21.022500	2017-08-26T09:26:21.022500	2	rockfall candidate long
19157	2017-08-26T12:18:16.931250	2017-08-26T12:18:16.931250	2	noise
19158	2017-08-26T12:31:16.678749	2017-08-26T12:31:16.678749	2	tremor lf
19159	2017-08-26T12:36:11.241250	2017-08-26T12:36:11.241250	3	rockfall candidate short
19160	2017-08-26T14:05:27.180000	2017-08-26T14:05:27.180000	2	lightning
19161	2017-08-26T14:13:39.951250	2017-08-26T14:13:39.951250	2	lightning
19162	2017-08-26T14:14:06.468750	2017-08-26T14:14:06.468750	2	tremor lf
19163	2017-08-26T14:15:34.482500	2017-08-26T14:15:34.482500	2	tremor lf
19164	2017-08-26T14:21:26.748750	2017-08-26T14:21:26.748750	2	rockfall candidate short
19165	2017-08-26T14:32:14.780000	2017-08-26T14:32:14.780000	2	lightning
19166	2017-08-26T15:13:20.849999	2017-08-26T15:13:20.849999	2	rockfall candidate short
19167	2017-08-26T17:31:55.403749	2017-08-26T17:31:55.403749	3	rockfall candidate short
19168	2017-08-26T18:04:05.181250	2017-08-26T18:04:05.181250	2	rockfall candidate short
19169	2017-08-26T21:51:19.838749	2017-08-26T21:51:19.838749	2	tremor lf
19170	2017-08-27T02:34:14.842500	2017-08-27T02:34:14.842500	2	rockfall candidate short
19171	2017-08-27T03:25:14.052499	2017-08-27T03:25:14.052499	4	rockfall candidate short
19172	2017-08-27T04:16:58.942500	2017-08-27T04:16:58.942500	2	rockfall candidate short
19173	2017-08-27T06:09:35.029999	2017-08-27T06:09:35.029999	2	tremor lf
19174	2017-08-27T06:51:00.210000	2017-08-27T06:51:00.210000	2	rockfall candidate short
19175	2017-08-27T07:26:31.586249	2017-08-27T07:26:31.586249	2	rockfall candidate short
19176	2017-08-27T07:27:22.238749	2017-08-27T07:27:22.238749	2	tremor lf
19177	2017-08-27T07:34:32.311249	2017-08-27T07:34:32.311249	2	rockfall candidate short
19178	2017-08-27T10:39:44.200000	2017-08-27T10:39:44.200000	2	tremor lf
19179	2017-08-27T11:54:27.237499	2017-08-27T11:54:27.237499	2	tremor lf
19180	2017-08-27T12:13:44.153750	2017-08-27T12:13:44.153750	2	tremor lf
19181	2017-08-27T12:26:49.698749	2017-08-27T12:26:49.698749	3	tremor lf
19182	2017-08-27T14:11:24.002500	2017-08-27T14:11:24.002500	2	tremor lf
19183	2017-08-27T14:28:13.678749	2017-08-27T14:28:13.678749	2	tremor lf
19184	2017-08-27T15:40:42.101250	2017-08-27T15:40:42.101250	2	tremor lf

19185	2017-08-27T15:52:39.063750	2017-08-27T15:52:39.063750	2	tremor lf
19186	2017-08-27T16:00:02.558749	2017-08-27T16:00:02.558749	2	tremor lf
19187	2017-08-27T16:06:22.857500	2017-08-27T16:06:22.857500	2	tremor lf
19188	2017-08-27T16:27:40.782500	2017-08-27T16:27:40.782500	2	lightning
19189	2017-08-27T16:33:04.842500	2017-08-27T16:33:04.842500	3	lightning
19190	2017-08-27T16:41:27.651249	2017-08-27T16:41:27.651249	2	lightning
19191	2017-08-27T16:52:53.438749	2017-08-27T16:52:53.438749	2	rockfall candidate short
19192	2017-08-27T21:24:16.527500	2017-08-27T21:24:16.527500	2	rockfall candidate short
19193	2017-08-27T21:26:32.184999	2017-08-27T21:26:32.184999	2	tremor lf
19194	2017-08-27T21:42:37.470000	2017-08-27T21:42:37.470000	3	rockfall candidate short
19195	2017-08-27T21:54:00.502500	2017-08-27T21:54:00.502500	2	tremor lf
19196	2017-08-27T22:41:09.193750	2017-08-27T22:41:09.193750	2	rockfall candidate short
19197	2017-08-28T00:46:36.456249	2017-08-28T00:46:36.456249	3	rockfall candidate short
19198	2017-08-28T01:04:43.155000	2017-08-28T01:04:43.155000	2	rockfall candidate short
19199	2017-08-28T01:43:24.487500	2017-08-28T01:43:24.487500	2	rockfall candidate short
19200	2017-08-28T02:21:21.227500	2017-08-28T02:21:21.227500	3	rockfall candidate short
19201	2017-08-28T04:06:24.638749	2017-08-28T04:06:24.638749	3	rockfall candidate short
19202	2017-08-28T05:06:41.503750	2017-08-28T05:06:41.503750	2	noise
19203	2017-08-28T06:57:45.718749	2017-08-28T06:57:45.718749	3	rockfall candidate short
19204	2017-08-28T07:00:47.866249	2017-08-28T07:00:47.866249	2	rockfall candidate short
19205	2017-08-28T07:18:41.910000	2017-08-28T07:18:41.910000	2	rockfall candidate short
19206	2017-08-28T07:35:45.577500	2017-08-28T07:35:45.577500	2	tremor lf
19207	2017-08-28T07:57:34.573750	2017-08-28T07:57:34.573750	2	noise
19208	2017-08-28T09:37:06.007500	2017-08-28T09:37:06.007500	2	rockfall candidate short
19209	2017-08-28T13:49:38.744999	2017-08-28T13:49:38.744999	2	tremor lf
19210	2017-08-28T13:55:00.381249	2017-08-28T13:55:00.381249	2	lightning
19211	2017-08-28T14:16:18.541250	2017-08-28T14:16:18.541250	2	lightning
19212	2017-08-28T14:16:28.923749	2017-08-28T14:16:28.923749	3	tremor lf
19213	2017-08-28T14:23:18.526249	2017-08-28T14:23:18.526249	3	lightning
19214	2017-08-28T16:20:48.271249	2017-08-28T16:20:48.271249	2	tremor lf
19215	2017-08-28T18:09:03.732499	2017-08-28T18:09:03.732499	3	rockfall candidate short
19216	2017-08-28T18:38:54.436249	2017-08-28T18:38:54.436249	2	rockfall candidate short
19217	2017-08-28T20:44:02.707500	2017-08-28T20:44:02.707500	2	noise
19218	2017-08-28T23:13:06.940000	2017-08-28T23:13:06.940000	2	tremor lf
19219	2017-08-28T23:56:39.913750	2017-08-28T23:56:39.913750	2	rockfall candidate short
19220	2017-08-29T00:52:19.321250	2017-08-29T00:52:19.321250	2	rockfall candidate short
19221	2017-08-29T00:58:49.942500	2017-08-29T00:58:49.942500	3	rockfall candidate short
19222	2017-08-29T02:04:51.482500	2017-08-29T02:04:51.482500	2	rockfall candidate short
19223	2017-08-29T02:23:08.612499	2017-08-29T02:23:08.612499	2	tremor lf
19224	2017-08-29T02:56:19.078749	2017-08-29T02:56:19.078749	2	noise
19225	2017-08-29T03:23:04.636250	2017-08-29T03:23:04.636250	3	rockfall candidate short
19226	2017-08-29T03:26:00.751249	2017-08-29T03:26:00.751249	2	rockfall candidate short
19227	2017-08-29T04:13:19.807499	2017-08-29T04:13:19.807499	3	rockfall candidate short
19228	2017-08-29T04:48:38.217499	2017-08-29T04:48:38.217499	2	rockfall candidate short
19229	2017-08-29T05:29:10.778749	2017-08-29T05:29:10.778749	3	rockfall candidate short
19230	2017-08-29T06:14:53.613750	2017-08-29T06:14:53.613750	3	rockfall candidate short
19231	2017-08-29T06:37:16.093750	2017-08-29T06:37:16.093750	2	rockfall candidate short
19232	2017-08-29T06:55:53.613750	2017-08-29T06:55:53.613750	3	rockfall candidate short
19233	2017-08-29T06:58:38.207500	2017-08-29T06:58:38.207500	2	rockfall candidate short

19234	2017-08-29T07:05:20.861250	2017-08-29T07:05:20.861250	2	rockfall candidate short
19235	2017-08-29T08:23:38.815000	2017-08-29T08:23:38.815000	3	rockfall candidate short
19236	2017-08-29T08:24:13.564999	2017-08-29T08:24:13.564999	3	rockfall candidate short
19237	2017-08-29T08:35:37.783750	2017-08-29T08:35:37.783750	2	rockfall candidate short
19238	2017-08-29T08:37:27.557499	2017-08-29T08:37:27.557499	2	rockfall candidate short
19239	2017-08-29T08:39:47.124999	2017-08-29T08:39:47.124999	3	rockfall candidate short
19240	2017-08-29T13:36:04.698749	2017-08-29T13:36:04.698749	2	rockfall candidate short
19241	2017-08-29T16:40:51.302500	2017-08-29T16:40:51.302500	2	rockfall candidate short
19242	2017-08-29T17:18:18.643749	2017-08-29T17:18:18.643749	2	noise
19243	2017-08-29T17:39:19.806249	2017-08-29T17:39:19.806249	2	rockfall candidate short
19244	2017-08-29T17:48:48.622499	2017-08-29T17:48:48.622499	2	rockfall candidate short
19245	2017-08-29T18:28:02.106249	2017-08-29T18:28:02.106249	2	noise
19246	2017-08-29T19:08:03.843749	2017-08-29T19:08:03.843749	3	rockfall candidate short
19247	2017-08-29T19:17:41.603749	2017-08-29T19:17:41.603749	2	rockfall candidate short
19248	2017-08-29T19:31:36.320000	2017-08-29T19:31:36.320000	2	rockfall candidate short
19249	2017-08-29T19:44:45.253750	2017-08-29T19:44:45.253750	3	rockfall candidate short
19250	2017-08-29T19:49:07.422499	2017-08-29T19:49:07.422499	2	noise
19251	2017-08-29T22:11:50.212499	2017-08-29T22:11:50.212499	2	rockfall candidate short
19252	2017-08-29T22:14:47.212499	2017-08-29T22:14:47.212499	3	rockfall candidate short
19253	2017-08-29T23:03:50.101250	2017-08-29T23:03:50.101250	2	rockfall candidate short
19254	2017-08-29T23:35:33.491249	2017-08-29T23:35:33.491249	2	rockfall candidate short
19255	2017-08-30T00:45:32.908750	2017-08-30T00:45:32.908750	2	noise
19256	2017-08-30T01:06:46.651249	2017-08-30T01:06:46.651249	2	rockfall candidate short
19257	2017-08-30T01:07:16.813750	2017-08-30T01:07:16.813750	2	rockfall candidate short
19258	2017-08-30T01:15:31.340000	2017-08-30T01:15:31.340000	2	noise
19259	2017-08-30T01:19:08.502500	2017-08-30T01:19:08.502500	2	rockfall candidate short
19260	2017-08-30T01:56:50.535000	2017-08-30T01:56:50.535000	3	rockfall candidate short
19261	2017-08-30T01:58:03.900000	2017-08-30T01:58:03.900000	3	rockfall candidate short
19262	2017-08-30T02:08:08.263750	2017-08-30T02:08:08.263750	2	tremor lf
19263	2017-08-30T02:41:00.807499	2017-08-30T02:41:00.807499	2	tremor lf
19264	2017-08-30T03:53:40.453750	2017-08-30T03:53:40.453750	2	rockfall candidate short
19265	2017-08-30T04:19:53.298749	2017-08-30T04:19:53.298749	2	rockfall candidate short
19266	2017-08-30T04:51:58.587500	2017-08-30T04:51:58.587500	3	rockfall candidate short
19267	2017-08-30T05:43:21.470000	2017-08-30T05:43:21.470000	2	tremor lf
19268	2017-08-30T05:56:09.027500	2017-08-30T05:56:09.027500	2	tremor lf
19269	2017-08-30T06:21:12.240000	2017-08-30T06:21:12.240000	2	tremor lf
19270	2017-08-30T07:10:54.765000	2017-08-30T07:10:54.765000	3	tremor lf
19271	2017-08-30T07:32:50.204999	2017-08-30T07:32:50.204999	2	noise
19272	2017-08-30T07:40:18.271249	2017-08-30T07:40:18.271249	2	noise
19273	2017-08-30T12:36:21.531249	2017-08-30T12:36:21.531249	2	rockfall candidate short
19274	2017-08-30T12:59:40.841250	2017-08-30T12:59:40.841250	2	rockfall candidate short
19275	2017-08-30T15:57:22.875000	2017-08-30T15:57:22.875000	2	noise
19276	2017-08-30T17:17:08.993750	2017-08-30T17:17:08.993750	2	rockfall candidate short
19277	2017-08-30T19:47:06.540000	2017-08-30T19:47:06.540000	2	tremor lf
19278	2017-08-30T23:20:55.974999	2017-08-30T23:20:55.974999	2	rockfall candidate short
19279	2017-08-31T00:00:10.808749	2017-08-31T00:00:10.808749	2	rockfall candidate short
19280	2017-08-31T00:04:08.981250	2017-08-31T00:04:08.981250	3	rockfall candidate short
19281	2017-08-31T02:39:00.431250	2017-08-31T02:39:00.431250	2	rockfall candidate short
19282	2017-08-31T05:21:18.440000	2017-08-31T05:21:18.440000	2	rockfall candidate short

19283	2017-08-31T05:54:25.936249	2017-08-31T05:54:25.936249	2	rockfall candidate short
19284	2017-08-31T09:58:28.847500	2017-08-31T09:58:28.847500	3	rockfall candidate short
19285	2017-08-31T12:51:21.904999	2017-08-31T12:51:21.904999	2	noise
19286	2017-08-31T14:55:41.029999	2017-08-31T14:55:41.029999	2	rockfall candidate short
19287	2017-08-31T15:50:17.266249	2017-08-31T15:50:17.266249	2	rockfall candidate short
19288	2017-08-31T15:51:35.436249	2017-08-31T15:51:35.436249	2	tremor lf
19289	2017-08-31T17:31:00.986249	2017-08-31T17:31:00.986249	2	tremor lf
19290	2017-08-31T20:49:20.336250	2017-08-31T20:49:20.336250	3	rockfall candidate short
19291	2017-08-31T23:41:38.588749	2017-08-31T23:41:38.588749	2	rockfall candidate short
19292	2017-09-01T01:48:50.223750	2017-09-01T01:48:50.223750	2	rockfall candidate short
19293	2017-09-01T20:25:26.552499	2017-09-01T20:25:26.552499	2	rockfall candidate short
19294	2017-09-01T22:08:07.983750	2017-09-01T22:08:07.983750	2	rockfall candidate short
19295	2017-09-02T00:19:54.186249	2017-09-02T00:19:54.186249	2	noise
19296	2017-09-02T00:24:10.551249	2017-09-02T00:24:10.551249	3	rockfall candidate short
19297	2017-09-02T00:29:12.740000	2017-09-02T00:29:12.740000	3	rockfall candidate short
19298	2017-09-02T03:54:03.536250	2017-09-02T03:54:03.536250	3	rockfall candidate short
19299	2017-09-02T06:36:41.908750	2017-09-02T06:36:41.908750	2	rockfall candidate short
19300	2017-09-02T08:13:06.233750	2017-09-02T08:13:06.233750	3	rockfall candidate short
19301	2017-09-02T08:39:51.329999	2017-09-02T08:39:51.329999	2	noise
19302	2017-09-02T09:23:37.533750	2017-09-02T09:23:37.533750	2	rockfall candidate short
19303	2017-09-02T10:05:49.584999	2017-09-02T10:05:49.584999	2	rockfall candidate short
19304	2017-09-02T14:02:43.508750	2017-09-02T14:02:43.508750	2	tremor lf
19305	2017-09-02T14:21:40.693750	2017-09-02T14:21:40.693750	2	tremor lf
19306	2017-09-02T14:52:49.860000	2017-09-02T14:52:49.860000	3	lightning
19307	2017-09-02T14:53:00.647500	2017-09-02T14:53:00.647500	2	tremor lf
19308	2017-09-02T20:04:15.258749	2017-09-02T20:04:15.258749	2	rockfall candidate short
19309	2017-09-02T20:16:24.493750	2017-09-02T20:16:24.493750	3	rockfall candidate short
19310	2017-09-02T21:45:39.172499	2017-09-02T21:45:39.172499	2	rockfall candidate short
19311	2017-09-02T22:30:05.291249	2017-09-02T22:30:05.291249	2	rockfall candidate short
19312	2017-09-03T00:22:43.387500	2017-09-03T00:22:43.387500	2	rockfall candidate short
19313	2017-09-03T02:53:34.686249	2017-09-03T02:53:34.686249	2	rockfall candidate short
19314	2017-09-03T04:19:29.001250	2017-09-03T04:19:29.001250	2	rockfall candidate short
19315	2017-09-03T09:16:25.517499	2017-09-03T09:16:25.517499	4	earthquake
19316	2017-09-03T10:02:51.172499	2017-09-03T10:02:51.172499	2	rockfall candidate short
19317	2017-09-03T12:00:45.184999	2017-09-03T12:00:45.184999	2	rockfall candidate short
19318	2017-09-03T14:37:33.408750	2017-09-03T14:37:33.408750	3	rockfall candidate short
19319	2017-09-03T15:03:44.962500	2017-09-03T15:03:44.962500	2	rockfall candidate short
19320	2017-09-03T15:24:55.142499	2017-09-03T15:24:55.142499	2	rockfall candidate short
19321	2017-09-03T15:51:26.824999	2017-09-03T15:51:26.824999	2	rockfall candidate short
19322	2017-09-03T17:07:32.038749	2017-09-03T17:07:32.038749	2	rockfall candidate short
19323	2017-09-03T18:24:20.746249	2017-09-03T18:24:20.746249	2	rockfall candidate short
19324	2017-09-03T19:46:57.688750	2017-09-03T19:46:57.688750	2	rockfall candidate short
19325	2017-09-03T19:55:50.312499	2017-09-03T19:55:50.312499	2	rockfall candidate short
19326	2017-09-03T21:35:43.349999	2017-09-03T21:35:43.349999	3	rockfall candidate short
19327	2017-09-03T22:45:55.292499	2017-09-03T22:45:55.292499	3	rockfall candidate short
19328	2017-09-04T01:02:22.866249	2017-09-04T01:02:22.866249	3	rockfall candidate short
19329	2017-09-04T01:23:32.282500	2017-09-04T01:23:32.282500	2	noise
19330	2017-09-04T02:06:56.531249	2017-09-04T02:06:56.531249	2	rockfall candidate short
19331	2017-09-04T02:09:31.135000	2017-09-04T02:09:31.135000	3	rockfall candidate short

19332	2017-09-04T02:13:41.843749	2017-09-04T02:13:41.843749	2	rockfall candidate short
19333	2017-09-04T03:17:08.863749	2017-09-04T03:17:08.863749	2	rockfall candidate short
19334	2017-09-04T03:29:09.732499	2017-09-04T03:29:09.732499	2	rockfall candidate short
19335	2017-09-04T03:38:08.116250	2017-09-04T03:38:08.116250	3	rockfall candidate short
19336	2017-09-04T03:39:44.893750	2017-09-04T03:39:44.893750	2	noise
19337	2017-09-04T04:24:17.309999	2017-09-04T04:24:17.309999	2	rockfall candidate short
19338	2017-09-04T06:49:09.097500	2017-09-04T06:49:09.097500	2	rockfall candidate short
19339	2017-09-04T08:11:51.257499	2017-09-04T08:11:51.257499	2	rockfall candidate short
19340	2017-09-04T08:47:10.466249	2017-09-04T08:47:10.466249	2	rockfall candidate short
19341	2017-09-04T10:25:56.098750	2017-09-04T10:25:56.098750	2	rockfall candidate short
19342	2017-09-04T11:20:15.896250	2017-09-04T11:20:15.896250	2	rockfall candidate short
19343	2017-09-04T11:30:11.042500	2017-09-04T11:30:11.042500	3	rockfall candidate short
19344	2017-09-04T13:45:06.193750	2017-09-04T13:45:06.193750	2	tremor lf
19345	2017-09-04T15:47:37.970000	2017-09-04T15:47:37.970000	2	noise
19346	2017-09-04T16:41:21.820000	2017-09-04T16:41:21.820000	2	rockfall candidate short
19347	2017-09-04T17:28:38.707500	2017-09-04T17:28:38.707500	2	rockfall candidate short
19348	2017-09-04T17:45:19.431250	2017-09-04T17:45:19.431250	2	noise
19349	2017-09-04T18:18:05.768750	2017-09-04T18:18:05.768750	2	rockfall candidate short
19350	2017-09-04T23:45:27.877500	2017-09-04T23:45:27.877500	2	rockfall candidate short
19351	2017-09-05T00:18:29.203749	2017-09-05T00:18:29.203749	2	rockfall candidate short
19352	2017-09-05T01:58:01.589999	2017-09-05T01:58:01.589999	2	rockfall candidate short
19353	2017-09-05T03:26:29.638749	2017-09-05T03:26:29.638749	3	rockfall candidate short
19354	2017-09-05T05:16:05.648750	2017-09-05T05:16:05.648750	3	rockfall candidate short
19355	2017-09-05T05:20:40.382499	2017-09-05T05:20:40.382499	3	rockfall candidate short
19356	2017-09-05T07:00:28.537499	2017-09-05T07:00:28.537499	2	rockfall candidate short
19357	2017-09-05T07:13:03.563750	2017-09-05T07:13:03.563750	2	rockfall candidate short
19358	2017-09-05T10:41:52.390000	2017-09-05T10:41:52.390000	2	rockfall candidate short
19359	2017-09-05T11:39:24.222500	2017-09-05T11:39:24.222500	2	rockfall candidate short
19360	2017-09-05T11:58:47.997499	2017-09-05T11:58:47.997499	2	rockfall candidate short
19361	2017-09-05T20:20:13.946249	2017-09-05T20:20:13.946249	2	rockfall candidate short
19362	2017-09-05T20:45:30.133750	2017-09-05T20:45:30.133750	2	rockfall candidate short
19363	2017-09-05T21:00:16.492499	2017-09-05T21:00:16.492499	2	noise
19364	2017-09-05T23:22:10.829999	2017-09-05T23:22:10.829999	2	rockfall candidate short
19365	2017-09-05T23:22:18.996249	2017-09-05T23:22:18.996249	2	rockfall candidate short
19366	2017-09-06T01:53:31.332499	2017-09-06T01:53:31.332499	2	noise
19367	2017-09-06T02:24:50.681250	2017-09-06T02:24:50.681250	2	rockfall candidate short
19368	2017-09-06T04:45:56.562500	2017-09-06T04:45:56.562500	3	rockfall candidate short
19369	2017-09-06T04:54:35.772499	2017-09-06T04:54:35.772499	3	rockfall candidate short
19370	2017-09-06T08:15:11.162499	2017-09-06T08:15:11.162499	2	rockfall candidate short
19371	2017-09-06T08:22:35.628750	2017-09-06T08:22:35.628750	3	rockfall candidate short
19372	2017-09-06T09:08:59.497499	2017-09-06T09:08:59.497499	3	rockfall candidate short
19373	2017-09-06T12:22:49.951250	2017-09-06T12:22:49.951250	4	earthquake
19374	2017-09-06T12:26:37.597500	2017-09-06T12:26:37.597500	4	earthquake
19375	2017-09-06T12:30:52.613750	2017-09-06T12:30:52.613750	4	earthquake
19376	2017-09-06T15:13:53.698749	2017-09-06T15:13:53.698749	3	rockfall candidate short
19377	2017-09-06T20:03:21.008750	2017-09-06T20:03:21.008750	3	rockfall candidate short
19378	2017-09-06T20:16:25.402499	2017-09-06T20:16:25.402499	2	noise
19379	2017-09-06T21:49:54.155000	2017-09-06T21:49:54.155000	2	rockfall candidate short
19380	2017-09-07T08:05:16.228750	2017-09-07T08:05:16.228750	2	noise

19381	2017-09-07T10:18:28.633750	2017-09-07T10:18:28.633750	2	noise
19382	2017-09-07T10:44:38.316250	2017-09-07T10:44:38.316250	2	tremor lf
19383	2017-09-07T11:20:05.910000	2017-09-07T11:20:05.910000	2	noise
19384	2017-09-07T16:50:46.377500	2017-09-07T16:50:46.377500	3	rockfall candidate short
19385	2017-09-07T19:47:16.998749	2017-09-07T19:47:16.998749	2	noise
19386	2017-09-07T21:16:08.783750	2017-09-07T21:16:08.783750	3	rockfall candidate short
19387	2017-09-08T05:33:27.713749	2017-09-08T05:33:27.713749	2	rockfall candidate short
19388	2017-09-08T05:42:52.682499	2017-09-08T05:42:52.682499	3	rockfall candidate short
19389	2017-09-08T10:22:53.018749	2017-09-08T10:22:53.018749	2	rockfall candidate short
19390	2017-09-08T10:53:29.564999	2017-09-08T10:53:29.564999	3	rockfall candidate short
19391	2017-09-08T10:58:07.561250	2017-09-08T10:58:07.561250	2	noise
19392	2017-09-08T11:54:57.642499	2017-09-08T11:54:57.642499	2	rockfall candidate short
19393	2017-09-09T05:39:11.648750	2017-09-09T05:39:11.648750	2	rockfall candidate short
19394	2017-09-09T12:21:56.636250	2017-09-09T12:21:56.636250	2	rockfall candidate short
19395	2017-09-09T17:15:36.948750	2017-09-09T17:15:36.948750	2	rockfall candidate short
19396	2017-09-09T17:37:01.984999	2017-09-09T17:37:01.984999	2	rockfall candidate short
19397	2017-09-09T19:16:23.983750	2017-09-09T19:16:23.983750	2	rockfall candidate short
19398	2017-09-09T20:05:53.723750	2017-09-09T20:05:53.723750	2	rockfall candidate short
19399	2017-09-09T20:06:17.438749	2017-09-09T20:06:17.438749	2	rockfall candidate short
19400	2017-09-10T03:19:08.025000	2017-09-10T03:19:08.025000	2	rockfall candidate short
19401	2017-09-10T05:49:02.161250	2017-09-10T05:49:02.161250	2	rockfall candidate short
19402	2017-09-10T18:01:46.480000	2017-09-10T18:01:46.480000	2	earthquake
19403	2017-09-10T21:50:43.800000	2017-09-10T21:50:43.800000	2	rockfall candidate short
19404	2017-09-11T06:46:11.344999	2017-09-11T06:46:11.344999	2	rockfall candidate short
19405	2017-09-11T09:33:01.196249	2017-09-11T09:33:01.196249	3	tremor lf
19406	2017-09-11T13:00:21.315000	2017-09-11T13:00:21.315000	2	noise
19407	2017-09-11T14:50:38.143749	2017-09-11T14:50:38.143749	2	noise
19408	2017-09-11T15:38:43.712499	2017-09-11T15:38:43.712499	2	noise
19409	2017-09-11T17:01:26.005000	2017-09-11T17:01:26.005000	3	rockfall candidate short
19410	2017-09-11T18:04:51.349999	2017-09-11T18:04:51.349999	2	noise
19411	2017-09-11T23:52:50.577500	2017-09-11T23:52:50.577500	3	rockfall candidate short
19412	2017-09-12T07:37:38.880000	2017-09-12T07:37:38.880000	2	noise
19413	2017-09-12T13:59:00.220000	2017-09-12T13:59:00.220000	2	noise
19414	2017-09-12T20:25:12.061250	2017-09-12T20:25:12.061250	2	noise
19415	2017-09-13T03:19:03.592499	2017-09-13T03:19:03.592499	2	noise
19416	2017-09-13T14:24:46.738749	2017-09-13T14:24:46.738749	2	rockfall candidate short
19417	2017-09-13T16:21:15.251249	2017-09-13T16:21:15.251249	2	noise
19418	2017-09-13T22:42:33.476249	2017-09-13T22:42:33.476249	3	rockfall candidate short
19419	2017-09-13T23:31:41.961250	2017-09-13T23:31:41.961250	2	rockfall candidate short
19420	2017-09-14T01:21:57.603749	2017-09-14T01:21:57.603749	2	rockfall candidate short
19421	2017-09-14T03:34:33.542500	2017-09-14T03:34:33.542500	2	rockfall candidate short
19422	2017-09-14T06:59:43.863749	2017-09-14T06:59:43.863749	2	tremor lf
19423	2017-09-14T07:31:43.349999	2017-09-14T07:31:43.349999	2	noise
19424	2017-09-14T21:17:53.838749	2017-09-14T21:17:53.838749	2	rockfall candidate short
19425	2017-09-15T02:44:01.170000	2017-09-15T02:44:01.170000	2	noise
19426	2017-09-15T03:23:20.941250	2017-09-15T03:23:20.941250	3	rockfall candidate short
19427	2017-09-15T09:21:24.720000	2017-09-15T09:21:24.720000	2	rockfall candidate short
19428	2017-09-15T14:21:14.198749	2017-09-15T14:21:14.198749	2	noise
19429	2017-09-15T20:50:33.343749	2017-09-15T20:50:33.343749	3	rockfall candidate short

19430	2017-09-15T22:08:54.988750	2017-09-15T22:08:54.988750	3	rockfall candidate short
19431	2017-09-15T22:35:50.402499	2017-09-15T22:35:50.402499	2	rockfall candidate short
19432	2017-09-15T23:15:45.483750	2017-09-15T23:15:45.483750	2	rockfall candidate short
19433	2017-09-16T10:50:17.440000	2017-09-16T10:50:17.440000	2	noise
19434	2017-09-16T13:16:25.927500	2017-09-16T13:16:25.927500	2	rockfall candidate short
19435	2017-09-16T17:24:12.302500	2017-09-16T17:24:12.302500	3	rockfall candidate short
19436	2017-09-16T18:42:54.880000	2017-09-16T18:42:54.880000	2	rockfall candidate short
19437	2017-09-16T19:00:23.746249	2017-09-16T19:00:23.746249	2	rockfall candidate short
19438	2017-09-16T21:29:15.208750	2017-09-16T21:29:15.208750	2	noise
19439	2017-09-16T21:57:18.172499	2017-09-16T21:57:18.172499	2	noise
19440	2017-09-17T05:20:08.828749	2017-09-17T05:20:08.828749	2	rockfall candidate short
19441	2017-09-17T05:28:36.482500	2017-09-17T05:28:36.482500	2	noise
19442	2017-09-17T05:44:21.450000	2017-09-17T05:44:21.450000	2	tremor lf
19443	2017-09-17T13:27:42.936249	2017-09-17T13:27:42.936249	2	noise
19444	2017-09-17T18:04:57.598750	2017-09-17T18:04:57.598750	2	noise
19445	2017-09-17T18:16:06.402499	2017-09-17T18:16:06.402499	2	noise
19446	2017-09-17T21:45:01.827500	2017-09-17T21:45:01.827500	2	rockfall candidate short
19447	2017-09-18T04:06:43.948750	2017-09-18T04:06:43.948750	2	noise
19448	2017-09-18T07:01:02.643749	2017-09-18T07:01:02.643749	2	rockfall candidate short
19449	2017-09-18T07:49:16.176249	2017-09-18T07:49:16.176249	2	rockfall candidate short
19450	2017-09-18T07:50:29.762500	2017-09-18T07:50:29.762500	2	anthropogenic
19451	2017-09-18T14:05:17.930000	2017-09-18T14:05:17.930000	2	noise
19452	2017-09-18T17:06:10.861250	2017-09-18T17:06:10.861250	2	rockfall candidate short
19453	2017-09-19T16:46:51.558749	2017-09-19T16:46:51.558749	3	rockfall candidate short
19454	2017-09-20T03:13:18.635000	2017-09-20T03:13:18.635000	4	rockfall candidate short
19455	2017-09-20T04:17:34.626249	2017-09-20T04:17:34.626249	2	rockfall candidate short
19456	2017-09-20T11:10:18.568749	2017-09-20T11:10:18.568749	2	rockfall candidate short
19457	2017-09-20T17:18:10.558749	2017-09-20T17:18:10.558749	2	rockfall candidate short
19458	2017-09-20T18:02:53.760000	2017-09-20T18:02:53.760000	3	rockfall candidate short
19459	2017-09-20T18:43:47.275000	2017-09-20T18:43:47.275000	2	rockfall candidate short
19460	2017-09-20T19:56:16.156250	2017-09-20T19:56:16.156250	2	rockfall candidate short
19461	2017-09-20T21:46:52.180000	2017-09-20T21:46:52.180000	2	rockfall candidate short
19462	2017-09-21T01:41:05.373750	2017-09-21T01:41:05.373750	2	rockfall candidate short
19463	2017-09-21T13:49:47.713749	2017-09-21T13:49:47.713749	2	rockfall candidate short
19464	2017-09-21T22:35:23.036250	2017-09-21T22:35:23.036250	2	rockfall candidate short
19465	2017-09-22T00:43:33.802500	2017-09-22T00:43:33.802500	2	noise
19466	2017-09-22T06:10:43.631249	2017-09-22T06:10:43.631249	2	noise
19467	2017-09-22T08:44:18.318749	2017-09-22T08:44:18.318749	2	rockfall candidate short
19468	2017-09-22T08:55:14.756249	2017-09-22T08:55:14.756249	3	rockfall candidate short
19469	2017-09-22T11:43:07.315000	2017-09-22T11:43:07.315000	2	noise
19470	2017-09-22T11:59:44.505000	2017-09-22T11:59:44.505000	2	rockfall candidate short
19471	2017-09-22T13:42:51.084999	2017-09-22T13:42:51.084999	2	rockfall candidate short
19472	2017-09-22T20:44:48.782500	2017-09-22T20:44:48.782500	2	noise
19473	2017-09-22T23:48:15.976249	2017-09-22T23:48:15.976249	2	noise
19474	2017-09-23T02:11:20.057499	2017-09-23T02:11:20.057499	3	rockfall candidate short
19475	2017-09-23T02:20:15.846249	2017-09-23T02:20:15.846249	2	rockfall candidate short
19476	2017-09-23T03:28:43.450000	2017-09-23T03:28:43.450000	2	rockfall candidate short
19477	2017-09-23T03:48:02.265000	2017-09-23T03:48:02.265000	2	noise
19478	2017-09-23T07:41:52.142499	2017-09-23T07:41:52.142499	2	rockfall candidate short

19479	2017-09-23T08:50:34.230000	2017-09-23T08:50:34.230000	2	noise
19480	2017-09-23T08:51:33.928750	2017-09-23T08:51:33.928750	2	noise
19481	2017-09-23T15:02:38.732499	2017-09-23T15:02:38.732499	2	anthropogenic
19482	2017-09-23T19:17:14.836250	2017-09-23T19:17:14.836250	2	noise
19483	2017-09-23T22:20:38.573750	2017-09-23T22:20:38.573750	2	rockfall candidate short
19484	2017-09-23T22:49:19.022500	2017-09-23T22:49:19.022500	2	rockfall candidate short
19485	2017-09-23T23:01:11.224999	2017-09-23T23:01:11.224999	2	rockfall candidate short
19486	2017-09-23T23:16:30.587500	2017-09-23T23:16:30.587500	2	tremor lf
19487	2017-09-23T23:51:46.072499	2017-09-23T23:51:46.072499	2	rockfall candidate short
19488	2017-09-24T01:27:16.232499	2017-09-24T01:27:16.232499	2	rockfall candidate short
19489	2017-09-24T10:56:08.027500	2017-09-24T10:56:08.027500	2	tremor lf
19490	2017-09-24T14:22:09.682499	2017-09-24T14:22:09.682499	2	rockfall candidate short
19491	2017-09-24T14:24:30.022500	2017-09-24T14:24:30.022500	2	rockfall candidate short
19492	2017-09-24T14:28:37.740000	2017-09-24T14:28:37.740000	2	rockfall candidate short
19493	2017-09-24T15:43:26.589999	2017-09-24T15:43:26.589999	2	rockfall candidate short
19494	2017-09-24T18:34:48.012499	2017-09-24T18:34:48.012499	2	rockfall candidate short
19495	2017-09-24T22:15:15.936249	2017-09-24T22:15:15.936249	2	noise
19496	2017-09-24T23:03:00.046249	2017-09-24T23:03:00.046249	2	rockfall candidate short
19497	2017-09-25T00:43:33.515000	2017-09-25T00:43:33.515000	2	noise
19498	2017-09-25T02:32:42.897500	2017-09-25T02:32:42.897500	2	noise
19499	2017-09-25T03:08:27.973750	2017-09-25T03:08:27.973750	2	rockfall candidate short
19500	2017-09-25T04:02:45.432499	2017-09-25T04:02:45.432499	2	rockfall candidate short
19501	2017-09-25T10:28:33.508750	2017-09-25T10:28:33.508750	3	rockfall candidate short
19502	2017-09-25T20:19:38.453750	2017-09-25T20:19:38.453750	3	rockfall candidate short
19503	2017-09-26T04:27:57.650000	2017-09-26T04:27:57.650000	2	rockfall candidate short
19504	2017-09-26T05:22:47.746249	2017-09-26T05:22:47.746249	2	rockfall candidate short
19505	2017-09-26T05:35:37.472499	2017-09-26T05:35:37.472499	3	rockfall candidate short
19506	2017-09-26T07:15:16.497499	2017-09-26T07:15:16.497499	2	rockfall candidate short
19507	2017-09-26T07:29:46.824999	2017-09-26T07:29:46.824999	2	rockfall candidate short
19508	2017-09-26T09:33:18.268750	2017-09-26T09:33:18.268750	2	rockfall candidate short
19509	2017-09-26T10:25:50.812499	2017-09-26T10:25:50.812499	2	rockfall candidate short
19510	2017-09-26T13:42:11.672499	2017-09-26T13:42:11.672499	2	rockfall candidate short
19511	2017-09-26T13:56:12.683749	2017-09-26T13:56:12.683749	2	rockfall candidate short
19512	2017-09-26T19:14:59.578749	2017-09-26T19:14:59.578749	4	earthquake
19513	2017-09-26T20:35:22.931250	2017-09-26T20:35:22.931250	2	rockfall candidate short
19514	2017-09-26T22:18:33.417499	2017-09-26T22:18:33.417499	2	rockfall candidate short
19515	2017-09-27T03:13:00.332499	2017-09-27T03:13:00.332499	2	rockfall candidate short
19516	2017-09-27T04:28:44.704999	2017-09-27T04:28:44.704999	2	noise
19517	2017-09-27T05:20:12.442500	2017-09-27T05:20:12.442500	2	noise
19518	2017-09-27T05:30:30.777499	2017-09-27T05:30:30.777499	2	rockfall candidate short
19519	2017-09-27T05:53:15.753750	2017-09-27T05:53:15.753750	3	rockfall candidate short
19520	2017-09-27T09:40:02.160000	2017-09-27T09:40:02.160000	2	rockfall candidate short
19521	2017-09-27T21:45:15.561250	2017-09-27T21:45:15.561250	2	rockfall candidate short
19522	2017-09-27T21:54:22.980000	2017-09-27T21:54:22.980000	2	noise
19523	2017-09-27T23:25:59.847500	2017-09-27T23:25:59.847500	2	noise
19524	2017-09-28T01:13:28.066249	2017-09-28T01:13:28.066249	2	tremor lf
19525	2017-09-28T02:41:52.124999	2017-09-28T02:41:52.124999	2	noise
19526	2017-09-28T03:03:02.942500	2017-09-28T03:03:02.942500	2	rockfall candidate short
19527	2017-09-28T09:14:24.827500	2017-09-28T09:14:24.827500	2	noise

19528	2017-09-28T10:58:20.506249	2017-09-28T10:58:20.506249	3	rockfall candidate short
19529	2017-09-28T11:17:12.055000	2017-09-28T11:17:12.055000	2	noise
19530	2017-09-28T14:56:12.778749	2017-09-28T14:56:12.778749	2	rockfall candidate short
19531	2017-09-28T17:49:28.324999	2017-09-28T17:49:28.324999	3	rockfall candidate short
19532	2017-09-28T23:29:41.661250	2017-09-28T23:29:41.661250	2	rockfall candidate short
19533	2017-09-28T23:32:38.032499	2017-09-28T23:32:38.032499	2	noise
19534	2017-09-29T00:54:20.241250	2017-09-29T00:54:20.241250	2	noise
19535	2017-09-29T04:09:31.631249	2017-09-29T04:09:31.631249	2	noise
19536	2017-09-29T05:25:29.675000	2017-09-29T05:25:29.675000	2	noise
19537	2017-09-29T05:47:52.335000	2017-09-29T05:47:52.335000	4	earthquake
19538	2017-09-29T09:06:17.137500	2017-09-29T09:06:17.137500	2	noise
19539	2017-09-29T09:47:41.752499	2017-09-29T09:47:41.752499	2	rockfall candidate short
19540	2017-09-29T11:04:24.623749	2017-09-29T11:04:24.623749	2	rockfall candidate short
19541	2017-09-29T11:07:19.932499	2017-09-29T11:07:19.932499	3	rockfall candidate short
19542	2017-09-29T17:08:39.962500	2017-09-29T17:08:39.962500	2	rockfall candidate short
19543	2017-09-29T23:08:52.232499	2017-09-29T23:08:52.232499	2	rockfall candidate short
19544	2017-09-30T05:00:46.912499	2017-09-30T05:00:46.912499	3	rockfall candidate short
19545	2017-09-30T06:15:03.525000	2017-09-30T06:15:03.525000	3	rockfall candidate short
19546	2017-09-30T07:30:44.744999	2017-09-30T07:30:44.744999	2	tremor lf
19547	2017-09-30T09:12:40.471250	2017-09-30T09:12:40.471250	2	noise
19548	2017-09-30T10:04:18.947500	2017-09-30T10:04:18.947500	2	noise
19549	2017-09-30T11:24:37.324999	2017-09-30T11:24:37.324999	2	noise
19550	2017-09-30T14:38:47.395000	2017-09-30T14:38:47.395000	2	rockfall candidate short
19551	2017-09-30T17:09:16.776249	2017-09-30T17:09:16.776249	2	rockfall candidate short
19552	2017-09-30T17:11:07.089999	2017-09-30T17:11:07.089999	2	rockfall candidate short
19553	2017-09-30T17:44:56.071249	2017-09-30T17:44:56.071249	2	tremor lf
19554	2017-09-30T22:24:08.958749	2017-09-30T22:24:08.958749	2	tremor lf
19555	2017-10-01T01:19:12.172499	2017-10-01T01:19:12.172499	2	rockfall candidate short
19556	2017-10-01T08:40:47.078749	2017-10-01T08:40:47.078749	2	noise
19557	2017-10-01T10:12:48.537499	2017-10-01T10:12:48.537499	2	noise
19558	2017-10-01T10:42:38.990000	2017-10-01T10:42:38.990000	2	noise
19559	2017-10-01T12:34:19.886249	2017-10-01T12:34:19.886249	3	rockfall candidate short
19560	2017-10-01T13:30:12.827500	2017-10-01T13:30:12.827500	2	rockfall candidate short
19561	2017-10-01T17:18:25.289999	2017-10-01T17:18:25.289999	2	noise
19562	2017-10-01T18:10:30.424999	2017-10-01T18:10:30.424999	4	earthquake
19563	2017-10-01T19:59:49.964999	2017-10-01T19:59:49.964999	2	noise
19564	2017-10-01T22:26:44.560000	2017-10-01T22:26:44.560000	2	noise
19565	2017-10-01T23:24:37.144999	2017-10-01T23:24:37.144999	2	noise
19566	2017-10-01T23:46:43.933750	2017-10-01T23:46:43.933750	2	noise
19567	2017-10-02T00:28:06.680000	2017-10-02T00:28:06.680000	3	rockfall candidate short
19568	2017-10-02T08:12:03.964999	2017-10-02T08:12:03.964999	2	rockfall candidate short
19569	2017-10-02T08:48:04.747500	2017-10-02T08:48:04.747500	3	rockfall candidate short
19570	2017-10-02T08:50:49.538749	2017-10-02T08:50:49.538749	2	rockfall candidate short
19571	2017-10-02T10:30:28.321250	2017-10-02T10:30:28.321250	2	rockfall candidate short
19572	2017-10-02T16:30:05.427500	2017-10-02T16:30:05.427500	2	rockfall candidate short
19573	2017-10-02T18:37:53.996249	2017-10-02T18:37:53.996249	2	rockfall candidate short
19574	2017-10-03T00:51:59.687500	2017-10-03T00:51:59.687500	2	rockfall candidate short
19575	2017-10-03T01:14:58.432499	2017-10-03T01:14:58.432499	2	rockfall candidate short
19576	2017-10-03T01:15:15.998749	2017-10-03T01:15:15.998749	2	rockfall candidate short

19577	2017-10-03T02:34:58.641249	2017-10-03T02:34:58.641249	3	rockfall candidate short
19578	2017-10-03T03:41:28.086249	2017-10-03T03:41:28.086249	2	rockfall candidate short
19579	2017-10-03T08:52:30.109999	2017-10-03T08:52:30.109999	2	noise
19580	2017-10-03T09:03:18.472499	2017-10-03T09:03:18.472499	2	rockfall candidate short
19581	2017-10-03T09:45:42.121249	2017-10-03T09:45:42.121249	2	rockfall candidate short
19582	2017-10-03T12:36:50.413750	2017-10-03T12:36:50.413750	2	tremor lf
19583	2017-10-03T14:46:15.193750	2017-10-03T14:46:15.193750	2	tremor lf
19584	2017-10-03T17:14:51.282500	2017-10-03T17:14:51.282500	2	tremor lf
19585	2017-10-04T00:37:25.043750	2017-10-04T00:37:25.043750	3	rockfall candidate short
19586	2017-10-05T03:25:28.421250	2017-10-05T03:25:28.421250	2	rockfall candidate short
19587	2017-10-05T04:24:09.572499	2017-10-05T04:24:09.572499	3	rockfall candidate short
19588	2017-10-05T09:27:12.392499	2017-10-05T09:27:12.392499	2	rockfall candidate short
19589	2017-10-05T10:39:15.564999	2017-10-05T10:39:15.564999	3	rockfall candidate short
19590	2017-10-05T11:25:06.829999	2017-10-05T11:25:06.829999	2	rockfall candidate short
19591	2017-10-05T19:11:42.360000	2017-10-05T19:11:42.360000	2	rockfall candidate short
19592	2017-10-05T19:26:32.962500	2017-10-05T19:26:32.962500	2	rockfall candidate short
19593	2017-10-05T21:04:54.964999	2017-10-05T21:04:54.964999	2	noise
19594	2017-10-06T14:15:04.086249	2017-10-06T14:15:04.086249	2	rockfall candidate short
19595	2017-10-06T21:01:04.337500	2017-10-06T21:01:04.337500	3	rockfall candidate short
19596	2017-10-07T08:40:10.503750	2017-10-07T08:40:10.503750	2	rockfall candidate short
19597	2017-10-07T22:06:57.923749	2017-10-07T22:06:57.923749	3	rockfall candidate short
19598	2017-10-07T22:22:33.224999	2017-10-07T22:22:33.224999	2	rockfall candidate short
19599	2017-10-07T23:05:08.481250	2017-10-07T23:05:08.481250	2	rockfall candidate short
19600	2017-10-07T23:58:41.970000	2017-10-07T23:58:41.970000	2	rockfall candidate short
19601	2017-10-08T05:12:40.300000	2017-10-08T05:12:40.300000	2	rockfall candidate short
19602	2017-10-08T06:04:30.598750	2017-10-08T06:04:30.598750	2	noise
19603	2017-10-08T09:31:45.549999	2017-10-08T09:31:45.549999	3	rockfall candidate short
19604	2017-10-08T11:28:25.353750	2017-10-08T11:28:25.353750	3	rockfall candidate short
19605	2017-10-08T11:33:29.311249	2017-10-08T11:33:29.311249	2	rockfall candidate short
19606	2017-10-08T18:48:33.974999	2017-10-08T18:48:33.974999	4	earthquake
19607	2017-10-09T01:22:33.168750	2017-10-09T01:22:33.168750	2	noise
19608	2017-10-09T05:47:38.128750	2017-10-09T05:47:38.128750	2	noise
19609	2017-10-09T05:54:20.942500	2017-10-09T05:54:20.942500	2	noise
19610	2017-10-09T11:09:44.116250	2017-10-09T11:09:44.116250	2	rockfall candidate short
19611	2017-10-09T14:41:10.368750	2017-10-09T14:41:10.368750	2	noise
19612	2017-10-09T16:59:24.734999	2017-10-09T16:59:24.734999	3	rockfall candidate short
19613	2017-10-09T19:22:46.015000	2017-10-09T19:22:46.015000	2	noise
19614	2017-10-09T22:47:27.797499	2017-10-09T22:47:27.797499	2	rockfall candidate short
19615	2017-10-10T02:06:18.444999	2017-10-10T02:06:18.444999	2	noise
19616	2017-10-10T10:43:16.785000	2017-10-10T10:43:16.785000	3	rockfall candidate short
19617	2017-10-10T16:25:35.222500	2017-10-10T16:25:35.222500	2	noise
19618	2017-10-10T20:48:58.893750	2017-10-10T20:48:58.893750	2	noise
19619	2017-10-11T00:21:20.816250	2017-10-11T00:21:20.816250	2	rockfall candidate short
19620	2017-10-11T01:07:24.612499	2017-10-11T01:07:24.612499	2	noise
19621	2017-10-11T03:01:24.420000	2017-10-11T03:01:24.420000	2	rockfall candidate short
19622	2017-10-11T03:47:34.703749	2017-10-11T03:47:34.703749	3	rockfall candidate short
19623	2017-10-11T08:56:34.766249	2017-10-11T08:56:34.766249	2	noise
19624	2017-10-11T09:00:26.701250	2017-10-11T09:00:26.701250	3	rockfall candidate short
19625	2017-10-11T09:09:04.200000	2017-10-11T09:09:04.200000	2	rockfall candidate short

19626	2017-10-11T15:13:42.918749	2017-10-11T15:13:42.918749	2	rockfall candidate short
19627	2017-10-11T17:07:51.714999	2017-10-11T17:07:51.714999	2	noise
19628	2017-10-11T19:42:49.861250	2017-10-11T19:42:49.861250	3	rockfall candidate short
19629	2017-10-11T22:57:47.769999	2017-10-11T22:57:47.769999	2	noise

Extreme Weather Event 2018

Table 11.2: Detected and categorized seismic events of the extreme weather event in 2018.

ID	Event Start Time	Event End Time	Event Type
1	2018-10-25T14:17:49.212470	2018-10-25T14:17:49.212470	tremor
2	2018-10-26T00:24:10.701839	2018-10-26T00:24:10.701839	rockfall candidate short
3	2018-10-26T01:40:16.718589	2018-10-26T01:40:16.718589	rockfall candidate short
4	2018-10-26T01:42:05.733629	2018-10-26T01:42:05.733629	rockfall candidate short
5	2018-10-26T03:56:36.597650	2018-10-26T03:56:36.597650	rockfall candidate short
6	2018-10-26T05:31:11.331830	2018-10-26T05:31:11.331830	tremor
7	2018-10-26T05:35:54.401809	2018-10-26T05:35:54.401809	tremor
8	2018-10-26T06:01:40.677200	2018-10-26T06:01:40.677200	tremor
9	2018-10-26T06:13:32.753950	2018-10-26T06:13:32.753950	tremor
10	2018-10-26T06:17:03.589159	2018-10-26T06:17:03.589159	tremor
11	2018-10-26T06:25:24.266370	2018-10-26T06:25:24.266370	tremor
12	2018-10-26T06:33:26.433410	2018-10-26T06:33:26.433410	tremor
13	2018-10-26T06:51:07.720089	2018-10-26T06:51:07.720089	tremor
14	2018-10-26T06:57:03.927769	2018-10-26T06:57:03.927769	tremor
15	2018-10-26T07:00:54.176069	2018-10-26T07:00:54.176069	tremor
16	2018-10-26T07:05:05.643340	2018-10-26T07:05:05.643340	tremor
17	2018-10-26T07:12:31.241529	2018-10-26T07:12:31.241529	tremor
18	2018-10-26T07:17:11.264110	2018-10-26T07:17:11.264110	tremor
19	2018-10-26T07:14:34.604969	2018-10-26T07:14:34.604969	tremor
20	2018-10-26T07:14:09.322799	2018-10-26T07:14:09.322799	rockfall candidate short
21	2018-10-26T07:27:39.480809	2018-10-26T07:27:39.480809	anthropogenic
22	2018-10-26T07:30:22.009030	2018-10-26T07:30:22.009030	tremor
23	2018-10-26T07:35:44.018060	2018-10-26T07:35:44.018060	tremor
24	2018-10-26T07:42:16.794579	2018-10-26T07:42:16.794579	tremor
25	2018-10-26T07:52:50.654629	2018-10-26T07:52:50.654629	anthropogenic
26	2018-10-26T07:57:26.614000	2018-10-26T07:57:26.614000	tremor
27	2018-10-26T08:05:36.568849	2018-10-26T08:05:36.568849	anthropogenic
28	2018-10-26T08:10:32.279910	2018-10-26T08:10:32.279910	tremor
29	2018-10-26T08:33:39.706549	2018-10-26T08:33:39.706549	tremor
30	2018-10-26T08:37:58.735889	2018-10-26T08:37:58.735889	tremor
31	2018-10-26T08:44:18.194129	2018-10-26T08:44:18.194129	anthropogenic
32	2018-10-26T08:54:20.451469	2018-10-26T08:54:20.451469	anthropogenic
33	2018-10-26T08:58:00.767489	2018-10-26T08:58:00.767489	tremor
34	2018-10-26T09:07:00.383749	2018-10-26T09:07:00.383749	anthropogenic
35	2018-10-26T09:16:23.363430	2018-10-26T09:16:23.363430	tremor
36	2018-10-26T09:32:19.458240	2018-10-26T09:32:19.458240	anthropogenic
37	2018-10-26T09:42:51.963879	2018-10-26T09:42:51.963879	tremor

38	2018-10-26T09:48:05.282170	2018-10-26T09:48:05.282170	tremor
39	2018-10-26T09:51:02.257339	2018-10-26T09:51:02.257339	tremor
40	2018-10-26T09:55:41.264110	2018-10-26T09:55:41.264110	anthropogenic
41	2018-10-26T10:11:51.241529	2018-10-26T10:11:51.241529	tremor
42	2018-10-26T10:28:57.878099	2018-10-26T10:28:57.878099	tremor
43	2018-10-26T10:40:39.683970	2018-10-26T10:40:39.683970	tremor
44	2018-10-26T10:47:56.252819	2018-10-26T10:47:56.252819	tremor
45	2018-10-26T11:28:13.408580	2018-10-26T11:28:13.408580	tremor
46	2018-10-26T11:43:28.081260	2018-10-26T11:43:28.081260	tremor
47	2018-10-26T11:46:46.726860	2018-10-26T11:46:46.726860	tremor
48	2018-10-26T11:49:05.778779	2018-10-26T11:49:05.778779	tremor
49	2018-10-26T11:54:29.029350	2018-10-26T11:54:29.029350	tremor
50	2018-10-26T12:11:33.453720	2018-10-26T12:11:33.453720	rockfall candidate long
51	2018-10-26T12:14:32.234759	2018-10-26T12:14:32.234759	rockfall candidate long
52	2018-10-26T12:48:01.264110	2018-10-26T12:48:01.264110	rockfall candidate short
53	2018-10-26T13:03:03.295710	2018-10-26T13:03:03.295710	tremor
54	2018-10-26T13:08:07.584649	2018-10-26T13:08:07.584649	tremor
55	2018-10-26T13:20:58.690740	2018-10-26T13:20:58.690740	anthropogenic
56	2018-10-26T13:26:07.494360	2018-10-26T13:26:07.494360	rockfall candidate short
57	2018-10-26T13:27:44.108349	2018-10-26T13:27:44.108349	rockfall candidate short
58	2018-10-26T13:40:40.632049	2018-10-26T13:40:40.632049	rockfall candidate short
59	2018-10-26T14:51:57.155760	2018-10-26T14:51:57.155760	rockfall candidate short
60	2018-10-26T15:01:23.521440	2018-10-26T15:01:23.521440	anthropogenic
61	2018-10-26T15:06:04.334089	2018-10-26T15:06:04.334089	rockfall candidate short
62	2018-10-26T15:42:48.397289	2018-10-26T15:42:48.397289	rockfall candidate short
63	2018-10-26T16:42:05.282170	2018-10-26T16:42:05.282170	anthropogenic
64	2018-10-26T17:00:37.697520	2018-10-26T17:00:37.697520	anthropogenic
65	2018-10-26T21:23:30.158010	2018-10-26T21:23:30.158010	rockfall candidate short
66	2018-10-27T07:54:40.812640	2018-10-27T07:54:40.812640	anthropogenic
67	2018-10-27T08:41:27.133179	2018-10-27T08:41:27.133179	tremor
68	2018-10-27T09:38:08.487580	2018-10-27T09:38:08.487580	anthropogenic
69	2018-10-27T12:12:15.440179	2018-10-27T12:12:15.440179	tremor
70	2018-10-27T13:14:52.550790	2018-10-27T13:14:52.550790	tremor
71	2018-10-27T14:01:42.483069	2018-10-27T14:01:42.483069	tremor
72	2018-10-27T14:32:02.799099	2018-10-27T14:32:02.799099	anthropogenic
73	2018-10-27T15:13:35.801350	2018-10-27T15:13:35.801350	tremor
74	2018-10-27T16:41:16.297970	2018-10-27T16:41:16.297970	tremor
75	2018-10-27T16:56:46.320539	2018-10-27T16:56:46.320539	anthropogenic
76	2018-10-27T17:41:52.415350	2018-10-27T17:41:52.415350	tremor
77	2018-10-27T17:59:46.907449	2018-10-27T17:59:46.907449	tremor
78	2018-10-27T18:02:26.726860	2018-10-27T18:02:26.726860	tremor
79	2018-10-27T18:31:49.029350	2018-10-27T18:31:49.029350	rockfall candidate long
80	2018-10-27T18:55:19.413090	2018-10-27T18:55:19.413090	tremor
81	2018-10-27T19:23:00.361170	2018-10-27T19:23:00.361170	rockfall candidate long
82	2018-10-27T21:29:30.654629	2018-10-27T21:29:30.654629	ligthtning
83	2018-10-28T00:26:05.688489	2018-10-28T00:26:05.688489	rockfall candidate short
84	2018-10-28T04:24:32.686230	2018-10-28T04:24:32.686230	ligthtning
85	2018-10-28T05:06:23.464630	2018-10-28T05:06:23.464630	rockfall candidate long
86	2018-10-28T05:19:09.548530	2018-10-28T05:19:09.548530	rockfall candidate long

87	2018-10-28T05:38:34.334089	2018-10-28T05:38:34.334089	ligthtning
88	2018-10-28T09:27:20.666189	2018-10-28T09:27:20.666189	rockfall candidate long
89	2018-10-28T11:15:26.202939	2018-10-28T11:15:26.202939	rockfall candidate long
90	2018-10-28T12:06:48.577879	2018-10-28T12:06:48.577879	rockfall candidate long
91	2018-10-28T12:21:32.550790	2018-10-28T12:21:32.550790	rockfall candidate long
92	2018-10-28T13:38:36.478560	2018-10-28T13:38:36.478560	anthropogenic
93	2018-10-28T17:25:53.498870	2018-10-28T17:25:53.498870	anthropogenic
94	2018-10-28T17:41:14.492100	2018-10-28T17:41:14.492100	rockfall candidate long
95	2018-10-28T18:40:57.360800	2018-10-28T18:40:57.360800	earthquakes
96	2018-10-29T06:07:39.142210	2018-10-29T06:07:39.142210	rockfall candidate short
97	2018-10-29T10:28:25.477060	2018-10-29T10:28:25.477060	anthropogenic
98	2018-10-29T11:30:13.829200	2018-10-29T11:30:13.829200	anthropogenic
99	2018-10-29T16:55:15.281949	2018-10-29T16:55:15.281949	ligthtning
100	2018-10-29T21:16:45.454440	2018-10-29T21:16:45.454440	ligthtning
101	2018-10-29T21:20:08.614710	2018-10-29T21:20:08.614710	ligthtning
102	2018-10-30T07:01:40.875059	2018-10-30T07:01:40.875059	tremor
103	2018-10-30T08:18:54.269200	2018-10-30T08:18:54.269200	anthropogenic
104	2018-10-30T16:38:14.540080	2018-10-30T16:38:14.540080	anthropogenic
105	2018-10-30T17:13:04.833529	2018-10-30T17:13:04.833529	anthropogenic
106	2018-10-25T22:57:07.118639	2018-10-25T22:57:07.118639	earthquakes
107	2018-10-27T22:20:34.369869	2018-10-27T22:20:34.369869	rockfall candidate long
108	2018-10-30T15:14:18.352140	2018-10-30T15:14:18.352140	earthquakes
109	2018-10-30T03:01:56.817159	2018-10-30T03:01:56.817159	earthquakes
110	2018-10-28T00:40:10.496610	2018-10-28T00:40:10.496610	earthquakes

Appendix D: Ruwai Technical Reports

→Assembly of the seismic data recorder Ruwai

→Performance of the seismic data recorder Ruwai

→Electromagnetic interference and the Ruwai recording system

Assembly of the seismic data recorder Ruwai

Stefan Mertl

Version 1.0 , April 4, 2017.

Technical report number 20170227-01

Mertl Research GmbH

The Ruwai seismic data recorder was design to allow the construction and assembly of the system in a do-it-yourself style. This includes the layout of the printed circuit boards using free software, the publication of the hardware documentation and the software with copyleft licenses, easy access to all hardware parts and needed tools and a full documentation of the construction steps.

This guide provides step-by-step instructions to build a Ruwai data recorder from scratch.

Ruwai as a DIY project

In figure 1 the inside of a Ruwai data recorder is shown. It mainly consist of the Arduino stack given in figure 2 placed in an aluminum box to shield it against electromagnetic emission and a single board computer. Both electronic components are placed inside a rugged case with connectors. The seismic data recorder Ruwai was built to work as a do-it-yourself project. This report documents the steps needed to build a Ruwai data recorder.

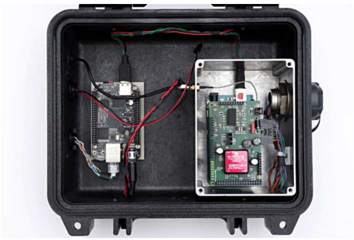

Figure 1: The Ruwai data recorder. The BeagleBoneBlack single board computer is to the left. The Arduino stack is mounted in an aluminum box. Both are placed inside a Peli 1200 case.

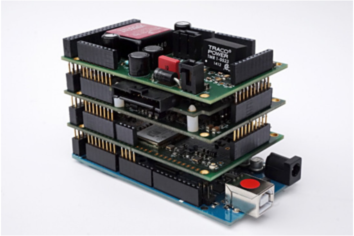

Figure 2: The Ruwai Arduino stack.

The complete hardware documentation is released under the CERN Open Hardware License 1.2[1]. The hardware documentation is available online from a Git repository[2]. It includes the design files of the printed circuit boards, lists of the needed electronic components, connectors and other assembly material, and technical drawings needed for the cases.

The layout of the printed circuit boards (PCB) and the selection of the electronic components was done to facilitate the soldering of the surface mount devices (SMD) using DIY methods. Moreover the replacement of the SMD devices by hand in case of a failure of one of the electronic components was an important design rule.

The printed circuit boards were designed using the free software KiCad[3]. The software for creating the bill of materials, organizing the electronic components and managing the placement of the components is written in the Python programming language and also available in the Ruwai Git repository. All input and output files are formatted as CSV text files to ensure general readability of the data files.

Ordering the printed circuit boards

The Arduino Stack consists of four stacked printed circuit boards which are called shields[4]. For each shield the according PCB has to be manufactured.

The Ruwai PCBs are designed as 4 layer PCBs which is not

---

[1] `http://www.ohwr.org/projects/cernohl/wiki`

[2] `http://www.repo.or.cz/ruwai.git`

[3] `http://www.kicad-pcb.org`

[4] The Ruwai shields:

- the power supply shield (PSS),
- the GPS timing shield (GTS),
- the ADC main shield (AMS),
- and the Analog Interface PGA shield (AIPS).

yet suitable for simple DIY production. Thus, the service of PCB prototype manufacturers has to be used. Several manufacturers offer the production of small numbers of PCBs at a reasonable price. The PCBs of the Ruwais were ordered from Würth Elektronik[5].

Depending on the manufacturer, various file formats of the PCB layout are accepted and the KiCad file format is already supported by several manufacturers. If the KiCad file format is not an option, the Gerber file format should be supported by every manufacturer. Gerber files can be exported by KiCad using the *File → Plot* command.

It is important to include one SMD stencil for each shield of the Arduino Stack. It is needed to apply the solder paste to the PCBs.

Preparing the bill of material

For the Ruwai project, the KiCad library *ruwai.lib* containing all electronic components used for the Ruwai was created. All components contain the custom fields given in table 1 which specify the electronic component.

name	description
Manu	The name of the manufacturer of the component.
Manu#	The part number used by the manufacturer.
Package	The electronic package of the component.
Description	The description of the electronic component.

Table 1: The custom fields of the components in the Ruwai KiCad library.

These fields are used to create the bill of material (BOM) from the schematic files using a KiCad plugin. The BOM plugin is named *bom_csv_grouped_components.py* and located in the folder *software/python/kicad_util* of the git repository.

The creation of the BOM is done in KiCad by opening the schematic of a PCB and selecting the menu *Tools → Generate Bill of Materials*. In the BOM dialog window shown in figure 3, the plugin described above has to be added. Once the plugin was added to KiCad, the BOM can be generated using the *generate* button. The command line field in the dialog contains the execution command of the plugin with the processor command (e.g. python), the complete path to the plugin file and the *"%I"* and *"%O"* parameters. *"%I"* represents the automatically generated name of the netlist file and *"%O"* is the automatically generated name of the output file. These two parameters are used by the *bom_csv_grouped_components.py* plugin.

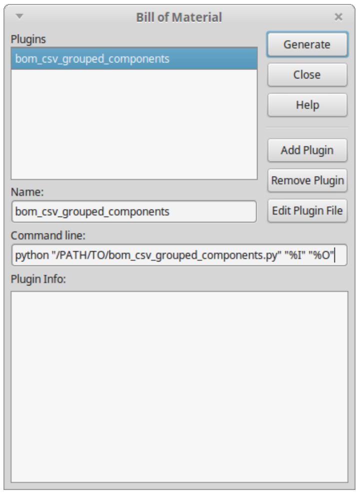

Plugins: bom_csv_grouped_components

Name: bom_csv_grouped_components

Command line: python "/PATH/TO/bom_csv_grouped_components.py" "%I" "%O"

Plugin Info:

Figure 3: The KiCad bill of material dialog.

The plugin creates a BOM in CSV format with the columns given in table 2[6].

Ordering the electronic components

The basic document for ordering the electronic components is the Ruwai inventory file *ruwai_component_inventory.csv* located in the

[5] http://www.we-online.at

[6] Find the tables in section File format description.

folder *hardware/inventory* of the git repository. It contains the description of all components used for the Ruwai project including the order number of a selected distributor (see table 3 in section File format description). Currently, only one distributor which was the best choice at the time the Ruwai was assembled is listed, no alternative distributors are available. When starting your own project, make sure to adapt the inventory to your distributor preferences or to search for better prices, as the price of the components might vary with time and distributor.

The column *stock* of the inventory file can be used to manage the personal stock of the components. The stock is taken into account when creating the order lists.

The fields manufacturer and manufacturer part number are used to link the inventory to the bill of materials. The python program *rw_orderlist_from_bom.py* (located in *software/python/kicad_util*) can be used to create an order list for a CSV BOM file described in section . The program accepts options to specify the number of PCBs and to ignore the stock of the inventory.

rw_orderlist_from_bom.py selects the inventory information of the components listed in the BOM, computes the number of needed components and derives the number of components to order using the stock information of the inventory. The program creates a set of CSV formatted order-list files with all the information needed to order the electronic component (see table 4). One file holds the information of all components. The other files are split depending on the distributor. Use these order list files to order the electronic components for the preferred distributor.

Preparing for assembly

The 4 PCBs of the Arduino Stack include a large number of different electronic components. For the assembly it is crucial to have a well prepared system for the placement of the components to avoid any problems due to the assembly of wrong components or the wrong orientation of the components.

The preparation for the assembly of the Ruwai Arduino Stack PCBs includes the following steps:

1. organize the ordered components according to their inventory number;
2. create the pick-and-place map;
3. create the pick-and-place checklist;
4. and create the pick-and-place boards.

To organize the electronic components I'm keeping the parts in their original packaging which makes sure not to loose the manufacturer information which is usually printed on the packaging label. I add a custom label with the inventory number. I then put the components into plastic bags grouped by decades of the inventory number (see figure 4). With this system it is easy to select the correct component using the inventory number only.

The pick-and-place maps (pnp-maps) are used as a visual reference where to place the components on the PCBs (see figure 5). They highlight the positions of the components on the the silk screen layer of the according PCB. To create the pnp-maps, the program *rw_pnp_map_from_pos.py* located in *software/python/kicad_util* can be used. This program requires a KiCad position file (.pos) and the silk screen layer of the PCB in Gerber file format. The position file can be created in KiCad Pcbnew using the menu File → Fabrication Outputs → Footprint Position (.pos) File.

To create the pnp-map, the program *gerbv*, which is part of most Linux distributions, is used. Make sure, that this program is installed on the computer when creating the pnp-maps.

The pnp-checklist file is used to select the needed components from the inventory, to check the correct part and to track the changes in the inventory once the parts were assembled. The description of the columns of the pnp-checklist is given table 5. The pnp-checklist files can be created using the program *rw_pnp_checklist_from_bom.py* located in *software/python/kicad_util* can be used.

The last step in the preparation of the assembly is the creation of the pick-and-place boards (pnp-boards). These boards hold the right amount of components of the PCB to assemble in the correct order. I'm using simple wooden boards with holes drilled in a raster to mount the components using small pieces of wire (see figure 6).

The components are mounted onto the pnp-board in the order of their appearance in the pnp-checklist. When selecting and mounting the components to the pnp-boards, the pnp-checklist should be used to verify that the correct component is used. On the pnp-boards I'm using small stickers to label the components using their inventory number, the first PCB reference number (e.g. C1) and the number of components used per PCB. When assembling more than one board, I additionally mark the number of components per board on the component packaging (e.g. strokes using a permanent marker). It's recommended to mount exactly the amount of components needed for the scheduled PCBs. This adds an additional check. If at the end some parts are missing, or there are still parts on the pnp-boards, it's an indication to check the PCBs for any wrong component placements.

Once all pnp-boards are assembled, everything is prepared for an effective placement of the components. Only the pnp-boards and pnp-maps are needed.

Figure 4: The organization of the electronic components using labeled plastic bags.

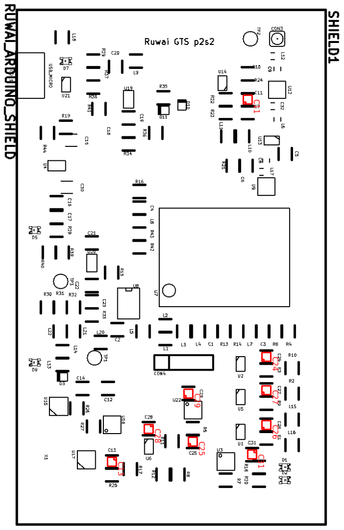

Figure 5: Example pnp-map of the GPS Timing Shield. The red markers specify the positions where to place the components.

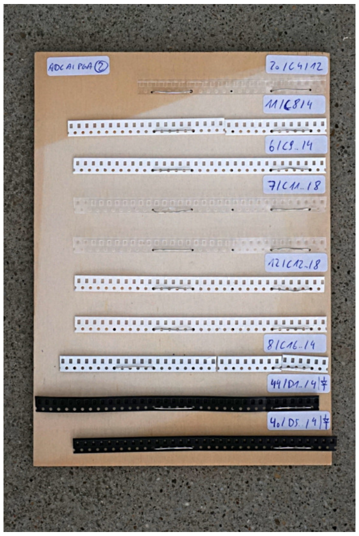

Figure 6: A pnp-board.

Assembly and soldering

The assembly of the PCBs is done manually using simple tools only. The major steps are:

1. application of the solder paste to the PCB using the SMD stencil,
2. placement of the electronic components onto the PCB, and
3. reflow soldering using a desktop oven and a temperature controller kit.

The tools used for the application of the solder paste and the reflow soldering are shown in figure 7. The reflow soldering kit offered by Beta Layout[7] was used. It includes an oven, a temperature controller for the oven and a SMD stencil printer. Furthermore, a digital microscope[8] was used for the assembly. This is not mandatory, but it facilitates the placement of the electronic components, especially when assembling multiple PCBs.

The first step is the application of the solder paste to the PCB. This is done using the SMD stencil and the stencil printer tool. The SMD stencil is a thin metal sheet were the contact pads of the PCB are cut out (see figure 8). Similar to a screenprint, the solder paste is applied to the PCB using a squeegee.

After the printing of the solder paste, all electronic contacts of the PCB are covered with a thin layer of solder paste (see figure 9). In the closeup in figure 10 the exact placement of the solder paste as well as its structure can bee seen. The solder paste consists of a mixture of solder powder and flux. When heating, the solder melts and creates the conductive strong physical connection between the electronic components and the PCB.

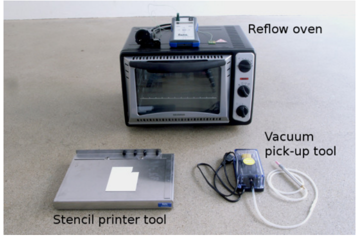

Figure 7: The tools needed for reflow soldering.

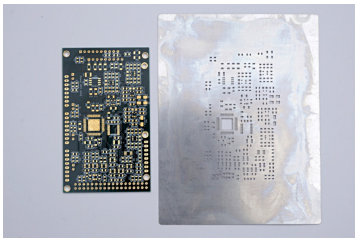

Figure 8: A Ruwai PCB and the according SMD stencil.

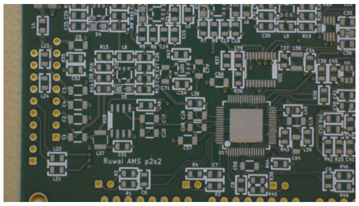

Figure 9: A PCB with applied solder paste.

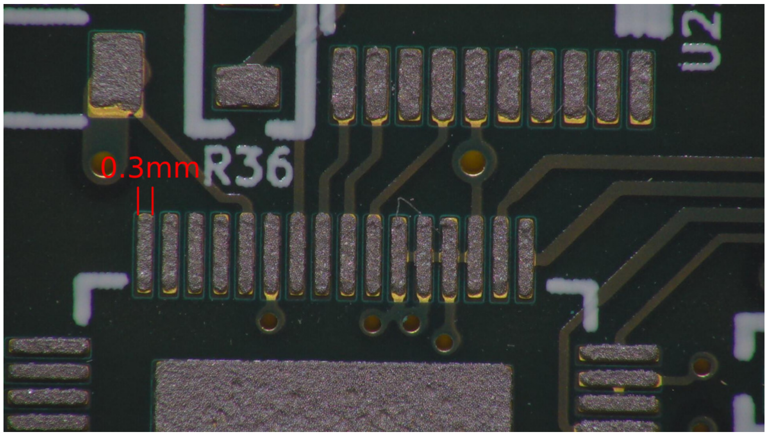

Figure 10: Magnified view of the applied solder paste.

The placement of the SMD components onto the PCB with the applied solder paste is done using a vacuum pickup tool. The used tool is a modified aquarium pump which is a low-cost, but good working alternative to professional tools. To place the compo-

[7] `https://www.beta-estore.com/`

[8] Tagarno Magnus FHD ZIP

nents, the pnp-maps and pnp-boards are used. An overview of the desktop setup for the placement is shown in figure 11.

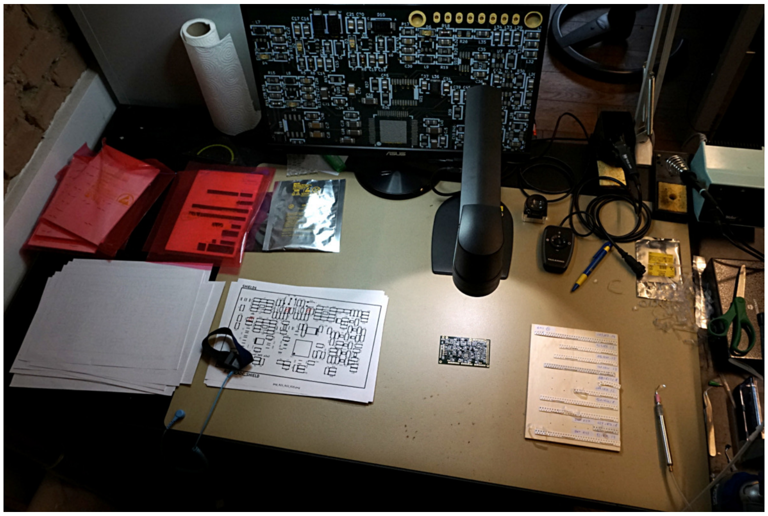

Figure 11: The desktop setup for the placement of the SMD components.

The PCB with the applied solder paste is in the middle and magnified by the digital microscope. On the screen of the microscope it can be seen, that some components already have been placed. The pnp-maps are on the left and the pnp-board with the prepared components on the right. The SMD components are picked up from the pnp-board with the vacuum pickup tool and placed onto the PCB at the position identified by the pnp-map (see figure 12). The solder paste is sticky and holds the SMD components in place until they are soldered.

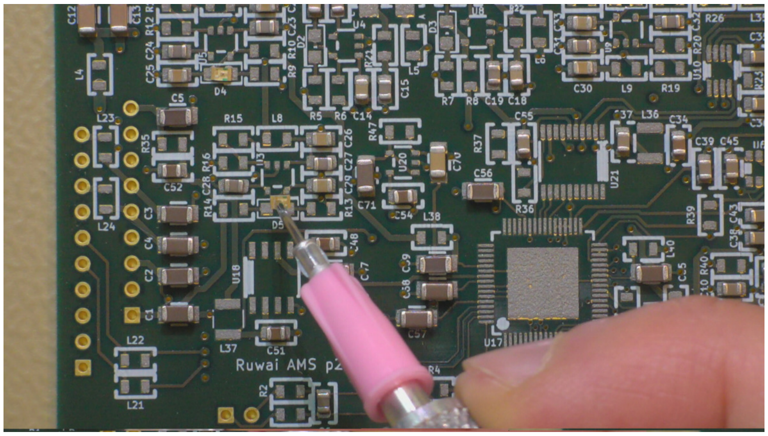

Figure 12: Example of the placement of a LED in 0805 package using the vacuum pickup tool.

After all components have been placed correctly, the PCB is soldered using the oven and the reflow controller. The controller has a temperature sensor, which is put inside the oven. The controller turns the oven on an off, so that the oven temperature follows the temperature curve needed for reflow soldering. The results of the reflow soldering using this low-cost approach are very good. As an example, the soldering of the ADS1274 in a HTQFP-64 package on the ADC main shield is given in figure 13. The pins of this package are at a raster of 0.5 mm.

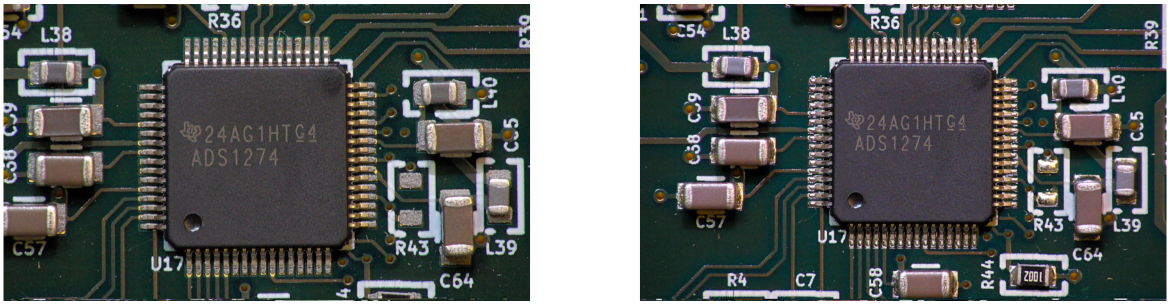

Figure 13: Reflow soldering of a the ADS1274 in a HTQFP-64 package. Left is unsoldered, right after the reflow soldering.

Some problems with shorted pins of components with a dense pin raster occurred. This errors could be avoided by a clean application of the solder paste which required the cleaning of the SMD stencil after every second print using a flux remover[9].

After the soldering of the PCBs in the reflow oven, they are visually inspected for possible failures like shorted pins and misplaced or misaligned components. Figure 14 shows the four soldered PCBs of the Arduino stack.

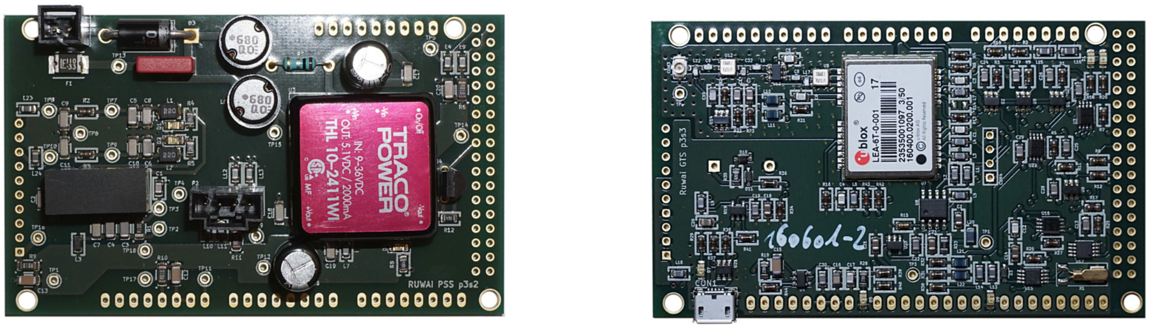

Power Supply Shield (PSS)

GPS Timing Shield (GTS)

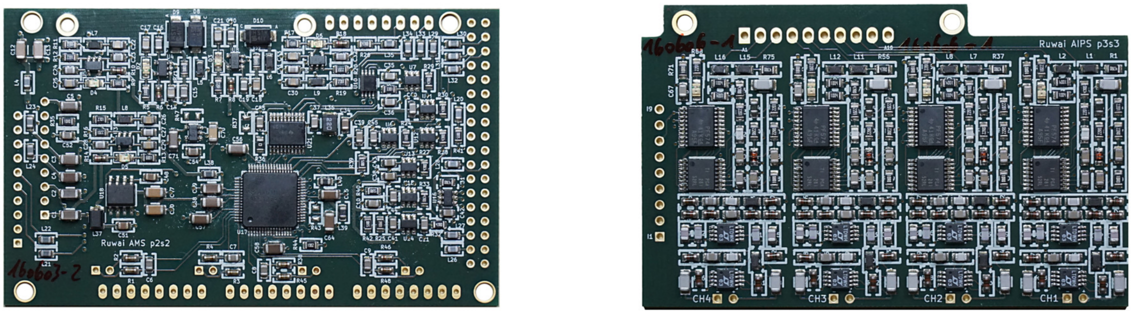

ADC Main Shield (AMS)

Analog Interface PGA Shield (AIPS)

Figure 14: The shields of the Ruwai Arduino stack.

[9] Chemtronics Flux-Off Lead Free

The final step is to solder the header connectors to the shields, mount the spacers on the AMS, add the analog input connector to the AIPS and connect the GPS UF-L to SMA cable to the GTS. The bill of material for the headers is given in the files *stackable_header_bom_total.csv* and *stackable_header_bom_by_shield.csv* in the folder *hardware/bom* of the Git project. The first gives the total number of headers per stack, the second file lists the headers used for each shield. The used headers are from the Samtec SSQ series[10]. The finished shields are shown in figure 15.

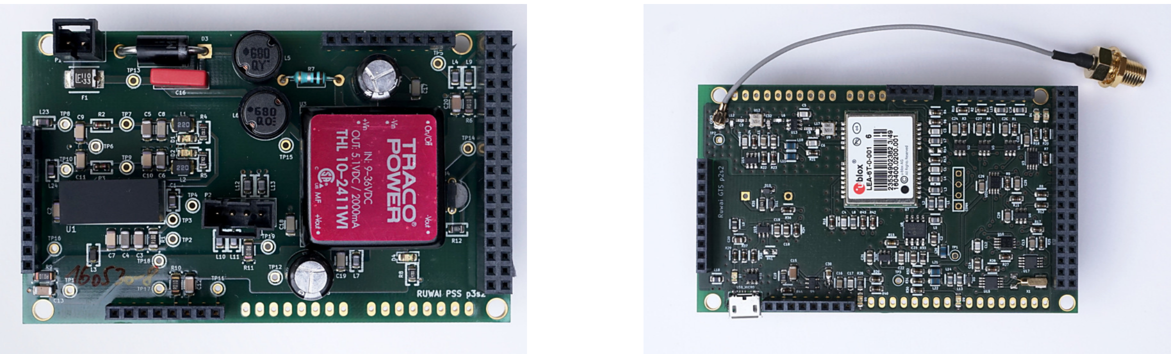

Power Supply Shield (PSS)

GPS Timing Shield (GTS)

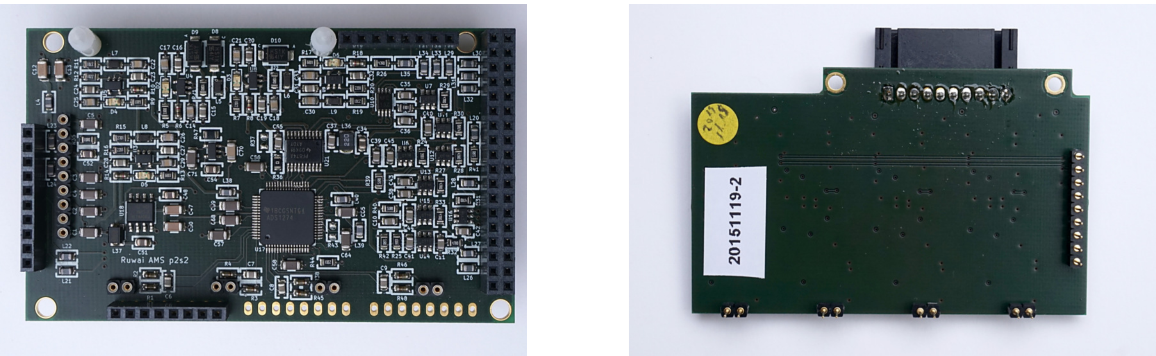

ADC Main Shield (AMS)

Analog Interface PGA Shield (AIPS)

Figure 15: The shields of the Ruwai Arduino stack with the mounted headers, spacers and connectors.

To finalize the Ruwai Arduino stack, stack the shields onto the Arduino Mega 2560 in the following order from bottom to top: GTS, AMS, AIPS and PSS. The whole stack mounted on the Arduino is shown in figure 16.

---

[10] `https://www.samtec.com/products/ssq`

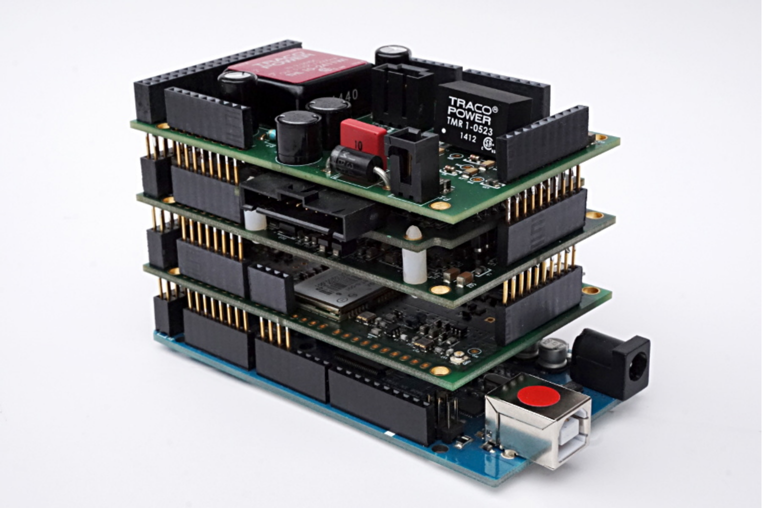

Figure 16: The Ruwai Arduino stack mounted on the Arduino Mega 2560.

The Ruwai case

For the Ruwai case a Peli 1200 case is used. For the shielding of the Arduino stack the Hammond 1550k aluminum case is used. The connectors are Bulgin Buccaneer 400 for the digital-, GPS- and power supply connections and Bulgin Buccaneer 7000 for the analog sensor connector. The BOM of the case is listed in the file *case_peli1200_shielded_bom.csv* in the folder *hardware/bom* of the Git project.

The Arduino stack shield First, the Hammond 1550k aluminum box is prepared to mount the Arduino stack inside. The technical drawings for the mounting and connector holes can be found in the files *hammond_1550_drilling_lid_top_view.dxf* and *hammond_1550_drilling_bottom_and_side_view.dxf* in the folder *hardware/case/peli_1200_shielded* of the Git repository. The drawings can be printed out and used as a drilling pattern.

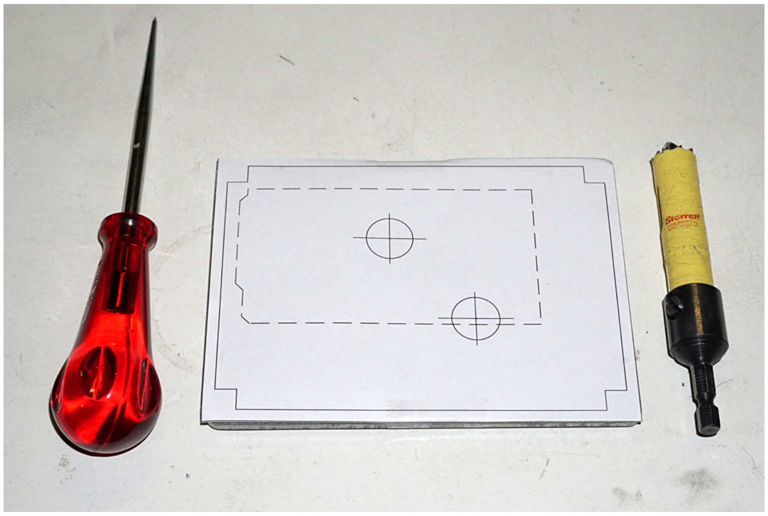

Figure 17: First, the holes for the power supply inlets in the lid of the box are drilled. Fix the pattern with sticky tape and use a piercing awl to mark the drill centers. Remove the drilling pattern and drill the holes using a holesaw. A diameter of 16 mm is used for the holes.

Figure 18: The drilled holes in the lid of the aluminum box. Deburr the edges to avoid cable damages.

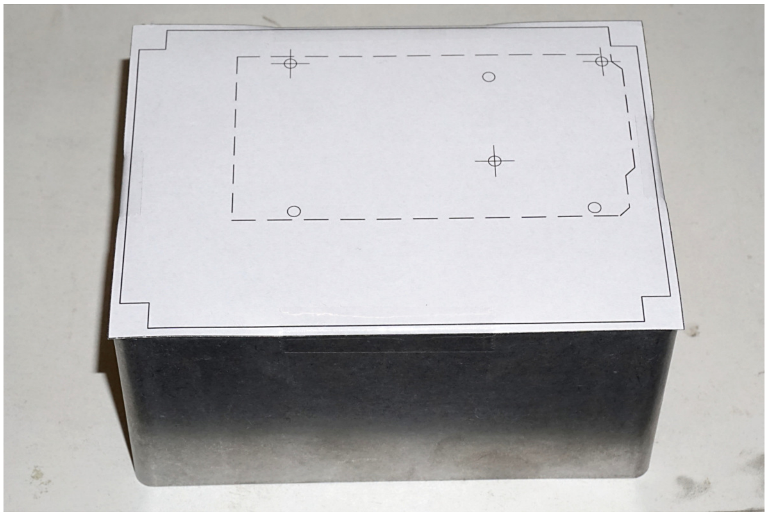

Figure 19: Fix the pattern for the Arduino mount holes to the bottom of the aluminum box and mount the centers of the three holes indicated with a cross with the piercing awl. Only the three holes are used because for the other holes the screw heads don't fit onto the Arduino. Use a 3.5 mm diameter drill.

Figure 20: The three drilled Arduino mount holes.

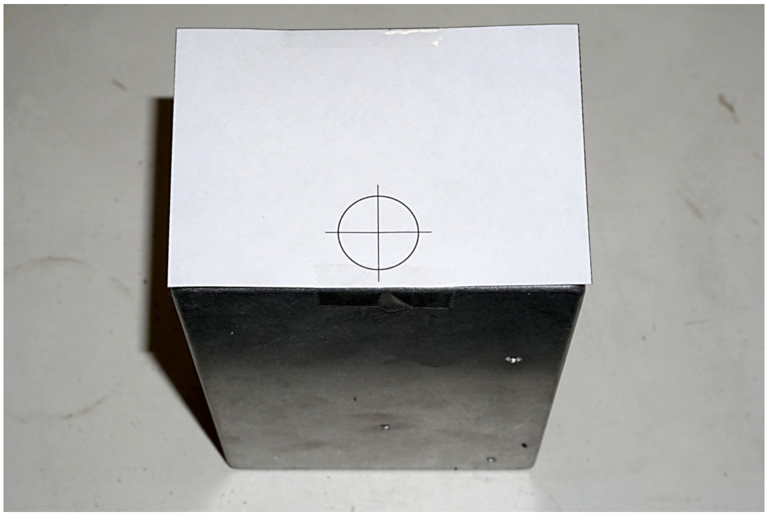

Figure 21: The pattern for the USB cable inlet hole. Make sure to check that the hole is drilled on the correct side of the box. When viewed from top as in the photo, the two Arduino mount holes have to be on the right side. Use a 19 mm diameter holesaw to drill the USB cable inlet.

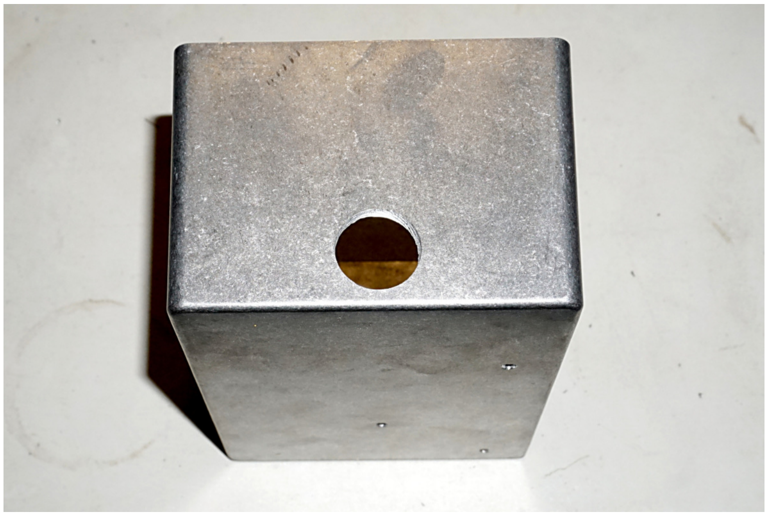

Figure 22: The USB cable inlet hole.

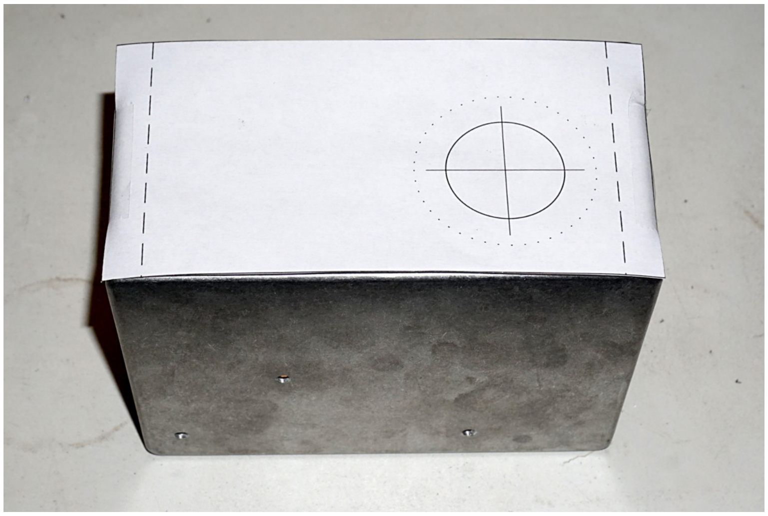

Figure 23: Place the pattern of the analog sensor input hole onto the box. Make sure, that it is on the correct side (check the placement of the Arduino holes). Mark the center of the hole using a piercing awl. Use a 30 mm diameter holesaw to drill the hole. The dotted line marks the outer diameter of the mounting nut of the Buccaneer 7000 connector.

Figure 24: The analog sensor input hole.

Figure 25: Use the same technique with placing the paper pattern on the box and marking the center of the hole for the GPS SMA connector hole. Use a 6.5 mm diameter drill for this hole.

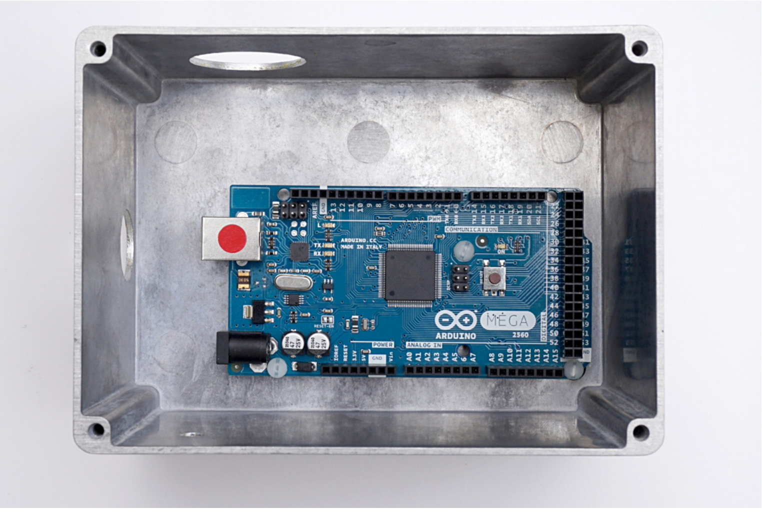

Figure 26: The final step is to mount the Arduino in the shielding box. Use nylon screws (187), nylon nuts (188) and a 5 mm spacer (171) to mount the Arduino. The numbers in the brackets are the inventory number of the parts.

Figure 27: Strip the excessive part of the screws using a wire cutter.

Peli 1200 case To prepare the Peli 1200 case for the Ruwai montage, 4 holes have to be drilled. Similar to the Arduino stack shielding box, technical drawings that can be used as a pattern to mark the drill centers can be found in the folder *hardware/case/peli_1200_shielded*. The filenames are *peli_drilling_analog.dxf* and *peli_drilling_gps_power_net.dxf*.

Figure 28: The pattern for the analog connector hole. Use a 30 mm holesaw for this hole. Align the pattern with the top fillets of the Peli case. Make sure, to place the pattern on the correct side. Use the handle bar of the Peli case as a reference.

Figure 29: The drilled hole for the analog connector.

Figure 30: The pattern for the GPS, power supply and network connector. Align the pattern with the top fillets of the Peli case. Make sure, to place the pattern on the correct side. Use the handle bar of the Peli case as a reference. Use 19 mm diameter hole-saw for the power and network holes. **The GPS hole needs special treatment. The Peli case wall thickness has to be reduced on the inside by ca. 2 mm before drilling the hole. See the next figures for details.**

Figure 31: The GPS connector doesn't fit the wall thickness of 5mm of the Peli case. The wall thickness has to be reduced for this connector. First drill a small hole in the center of the GPS connector hole to transfer the center to the inside of the case. Than use a 30 mm diameter Forstner drill to create an inlay with a depth of ca. 2 mm on the inside of the Peli case to reduce the wall thickness to ca. 3 mm. I marked the needed depth on the drill using a permanent marker. Drilling this inlay from the inside was a little bit tricky. The Forstner drill mounted onto the drilling machine barely fit into the Peli case. Finally drill the hole using a 16 mm holesaw from the outside.

Figure 32: The drilled GPS, power supply and network connector holes.

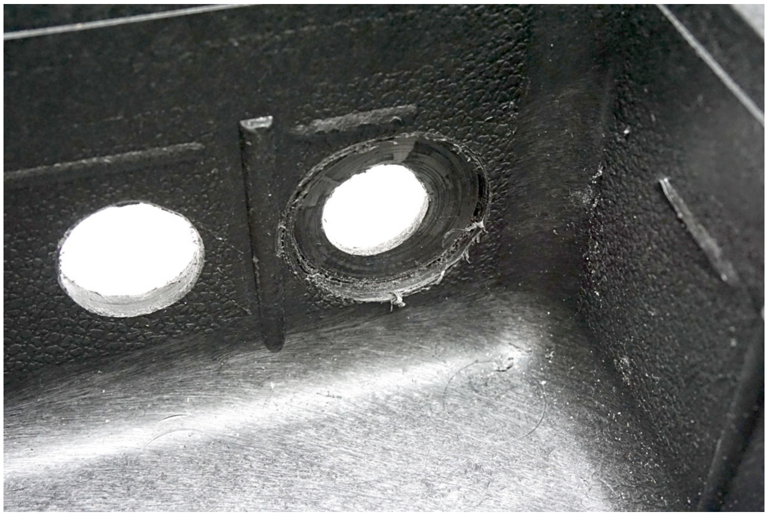

Figure 33: The inlay for the GPS connector created with the Forstner drill.

Peli 1200 connectors The next step is to prepare the connectors and cables needed for the Ruwai case. This includes the connector for GPS, power supply, Ethernet and analog sensor input connector shown in figure 34 and the internal USB and BeagleBone Black power supply cable shown in figure 35.

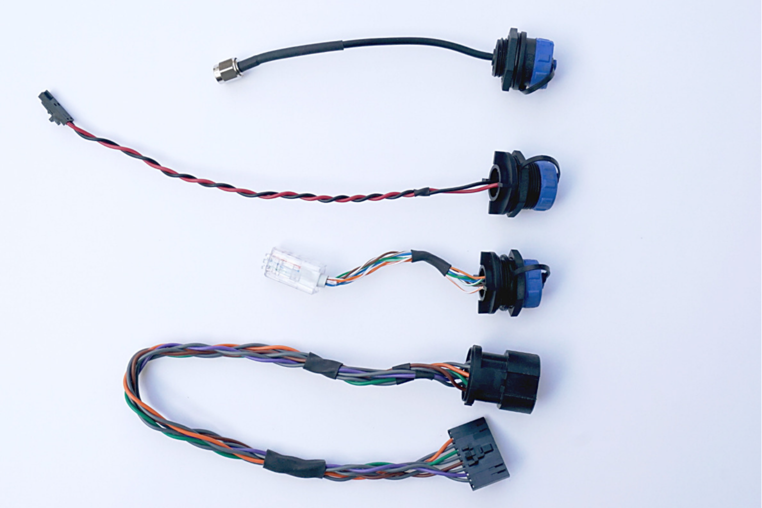

Figure 34: The connector cables from top to bottom: GPS, power supply, Ethernet and analog sensor connector.

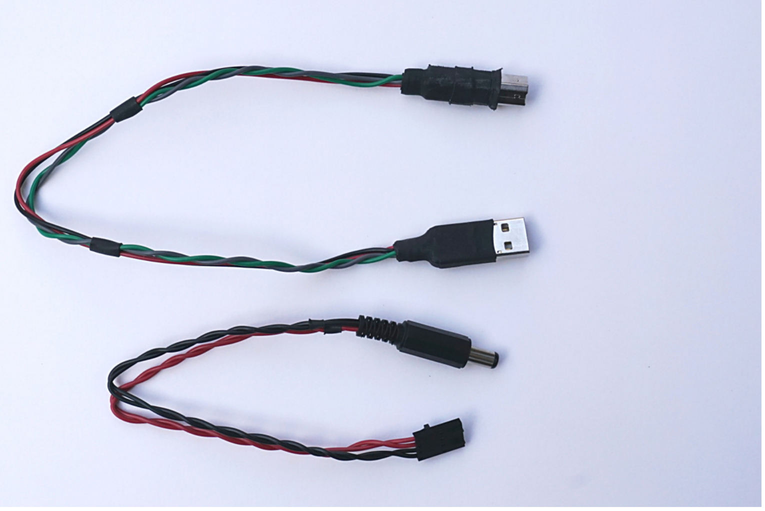

Figure 35: The internal cables from top to bottom: USB and BeagleBone power supply.

The needed material is given in the BOM files in the folder *hardware/bom* and the pin assignment of the connectors is listed in section Connector pin assignment.

The final steps are to mount the Hammond 1550k aluminum box in the Peli case and assemble all connectors. Mount the GPS, power supply and Ethernet connector to the Peli case and continue with the aluminum box and the analog sensor connector.

Figure 36: Mount the Hammond 1550k aluminum box using the Bulgin 7000 analog sensor input connector. Stick the connector through both holes in the Peli case and the aluminum box and fix the aluminum box using the screw of the Bulgin 7000 connector. Put the Arduino stack onto the Arduino and fix the GPS SMA connector as well.

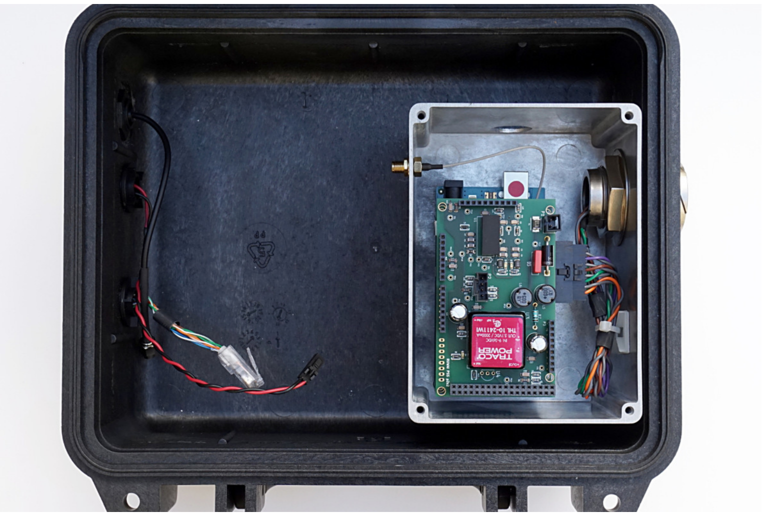

Figure 37: Put the analog sensor input cable with the pin cage in the Bulgin 7000 connector and connect the C-Grid connector on the Arduino stack. Fix the cable to the box using an adhesive base and a cable tie. If the position of the adhesive base is already known it's easier to mount the adhesive base and to fix the cable if the Arduino stack has not been put onto the Arduino.

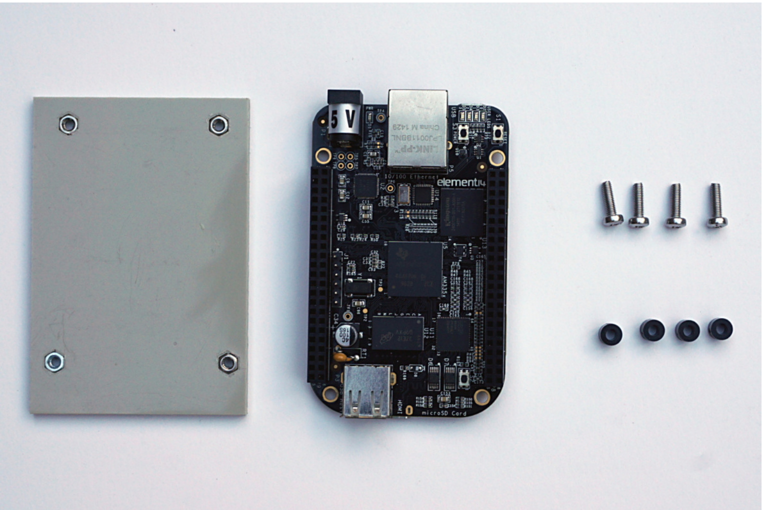

Figure 38: Mount the Beaglebone Black on a baseplate using 5 mm spacers. The baseplate was cut out of a Polypropylene-board and 4 hexagon cuts were milled on the bottom side of the baseplate to hold the hex-nuts. If milling the cuts is not an option other methods should also work: the cuts can also be drilled and the nuts glued in afterwards; the screw thread can be cut directly into the base plate; counter sunk nuts can be used. The technical drawing of the baseplate is given in the file *baseplate_beaglebone_black.dxf* in the folder *hardware/case/peli_1200_shielded* folder.

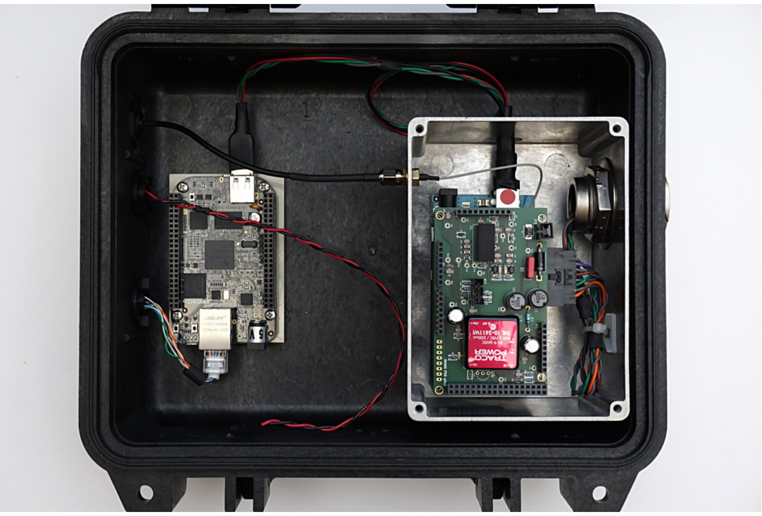

Figure 39: Glue the Beaglebone mounted on the baseplate to the Peli case using a glue suitable for the used material of the baseplate. Connect the GPS, USB and Ethernet cable. Use a heat shrink tube or a self bonding tape to fix the USB connector to the Arduino stack. This USB connector is a little bit loose and might cause problems.

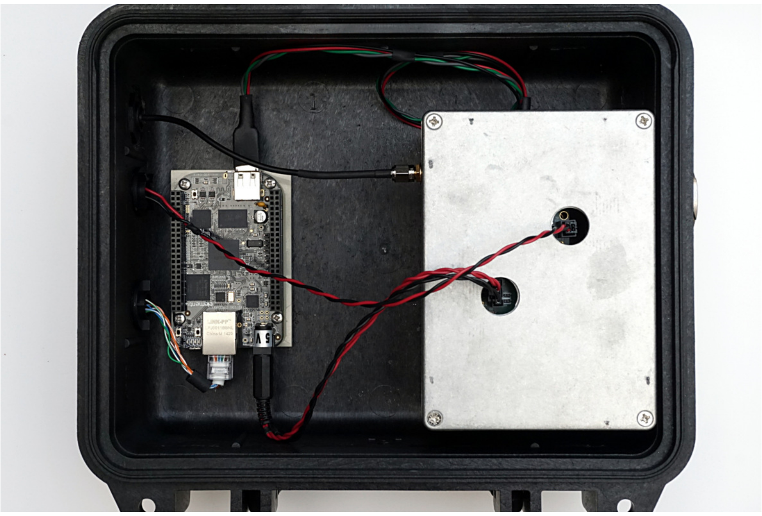

Figure 40: Close the lid of the aluminum box and connect the two power supply cables.

External cables

The last steps to finalize the assembly of the Ruwai data recorder is to assemble the external cables. These are the power supply cable, the GPS antenna cable and the Ethernet cable.

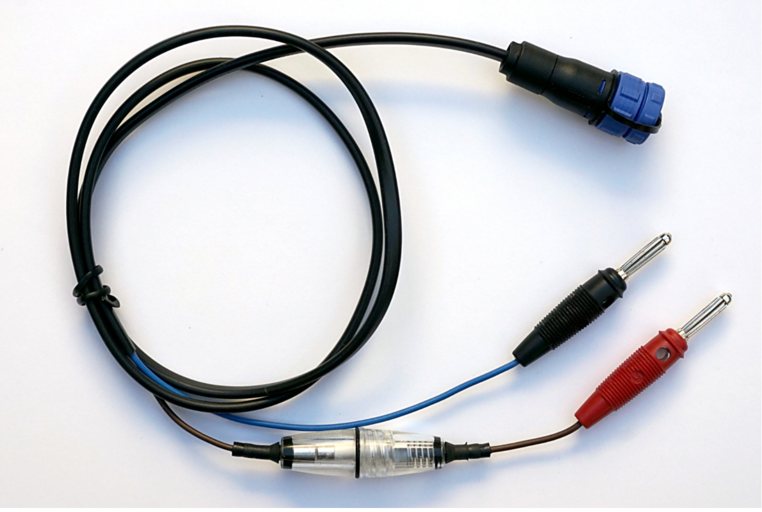

Figure 41: The power supply cable. Select the connector type of the second ending according to the power supply used. Always add a replaceable fuse near to the external power source (the battery) to protect the equipment from any damage due to high currents. Although the Arduino itself protects the input with a resettable fuse, it is advisable to protect whole system as near as possible at the power source. A 10 Ampere fuse should work fine for most applications.

Figure 42: Assemble the Bulgin SMB cable connector to the GPS antenna which should be used together with the Ruwai data recorder.

Figure 43: Assemble a crossed Ethernet cable if the Ruwai is connected directly to a computer or a straight Ethernet cable if the Ruwai is connected to a router or switch.

File format description

The bill of materials file.

name	description
ref	The component reference used in the schematic.
value	The value of the component.
quantity	Number of components used in the design.
manufacturer	The name of the manufacturer. This is the value of the Manu custom field.
manufacturer part number	The part number used by the manufacturer. This is the value of the Manu# custom field.
package	The code of the package of the component (e.g. 0805, SOT23). This is the value of the Package custom field.
description	The description of the component. This is the value of the Description custom field.
footprint	The name of the KiCad footprint used for this component.
library	The name of the library containing the component.
part name	The name of the component in the KiCad library.

Table 2: The columns of the BOM file.

The inventory file.

name	description
number	A unique number identifying the component in the inventory.
type	The type of the component (e.g. resistor, capacitor, ic).
manufacturer	The name of the manufacturer. This is the value of the Manu custom field.
manufacturer part number	The part number used by the manufacturer. This is the value of the Manu# custom field.
mount	The type of mount (e.g. THM, SMD, CON)
package	The code of the package of the component (e.g. 0805, SOT23).
description	The description of the component.
distributor	The distributor selling the component.
distributor part number	The distributor part number of the component.
minimum order qty	The minimum quantity to order.
packaging	The type of packaging.
cost per unit	The cost per unit.
stock	Number of components available in the stock.

Table 3: The columns of the inventory file.

The order-list file

name	description
ref	The component reference used in the schematic.
value	The value of the component.
quantity	Number of components used in the design for one PCB.
manufacturer	The name of the manufacturer. This is the value of the Manu custom field.
manufacturer part number	The part number used by the manufacturer. This is the value of the Manu# custom field.
number	The inventory number of the component.
manufacturer package	The code of the package of the component (e.g. 0805, SOT23).
distributor	The distributor selling the component.
distributor part number	The distributor part number of the component.
distributor description	The description of the component.
cost per unit	The cost per unit.
stock	Number of components available in the stock.
# boards	The number of boards for which the order list was created.
rem. stock	The number of components remaining in stock.
quantity order	The number of components to order from the distributor.

Table 4: The columns of the order-list file.

The pnp-checklist file

name	description
ref	The component reference used in the schematic.
number	The inventory number of the component.
parts needed	The number of parts needed per PCB.
n boards	The number of boards scheduled for assembly.
total needed	The total number of parts needed to assemble n_boards PCBs.
parts used	Use this column to enter the number of parts really used. This column is later used to update the inventory.
value	The value of the component.
package	The code of the package of the component (e.g. 0805, SOT23).
manufacturer	The name of the manufacturer. This is the value of the Manu custom field.
manufacturer part number	The part number used by the manufacturer. This is the value of the Manu# custom field.
mount	The type of mount (e.g. THM, SMD, CON)
stock	Number of components available in the stock.
comment	Comments. Used to highlight components where not enough parts are available in stock.

Table 5: The columns of the pnp-checklist file.

Connector pin assignment

Power supply connector - Ruwai case

Table 6: The pin assignment of the Ruwai case power supply connector.

pin	label	description	color
1	VCC	Positive pole of the DC power supply 9 - 36 V.	red
2	VCC	Positive pole of the DC power supply 9 - 36 V.	red
3	GND	Negative pole of the DC power supply 9 - 36 V.	black
4	GND	Negative pole of the DC power supply 9 - 36 V.	black

Ethernet connector - Ruwai case

For the Ethernet connector the T-568B pinouts scheme is used.

pin	label	description	color
1	TX+	Transmit data +.	white/orange
2	TX-	Transmit data -.	orange
3	RX+	Receive data +.	white/green
4	-	Not used.	blue
5	-	Not used.	white/blue
6	RX-	Receive data -.	orange
7	-	Not used.	white/brown
8	-	Not used.	brown

Table 7: The pin assignment of the Ruwai case Ethernet connector for a 10BASE-T and 100BASE-TX connection using the T-568B pinout scheme.

Analog sensor connector - Ruwai case

pin	label	description	color
1	CH1+	Channel 1 +	orange
2	CH1-	Channel 1 -	white/orange
3	CH2+	Channel 2 +	green
4	CH2-	Channel 2 -	white/green
5	CH3+	Channel 3 +	brown
6	CH3-	Channel 3 -	white/brown
7	CH4+	Channel 4 +	violet
8	CH4-	Channel 4 -	white/violet
9	-	Not used	
10	-	Not used	

Table 8: The pin assignment of the Ruwai case analog sensor connector.

Power supply connector - Arduino stack

pin	label	description	color
1	VCC	Positive pole of the DC power supply 9 - 36 V.	red
2	GND	Negative pole of the DC power supply 9 - 36 V.	black

Table 9: The pin assignment of the Arduino stack power supply connector.

BeagleBone power supply - Arduino stack

pin	label	description	color
1	VCC	+ 5.1 V	red
2	VCC	+ 5.1 V	red
3	GND	Ground reference.	black
4	GND	Ground reference	black

Table 10: The pin assignment of the Arduino stack BeagleBone power supply connector.

Analog sensor input - Arduino stack

pin	label	description	color
1	GND	Ground reference.	
2	CH4-	Channel 4 -	white/violet
3	CH4+	Channel 4 +	violet
4	CH3-	Channel 3 -	white/brown
5	CH3+	Channel 3 +	brown
6	CH2-	Channel 2 -	white/green
8	CH1-	Channel 1 -	white/orange
7	CH2+	Channel 2 +	green
9	CH1+	Channel 1 +	orange
10	GND	Ground reference.	

Table 11: The pin assignment of the Arduino stack analog input connector.

5V power supply DC jack - BeagleBone Black

pin	label	description	color
1	VCC	+ 5 V (center post)	red
2	GND	Ground reference (outer barrel)	black

Table 12: The pin assignment of the BeagleBone Black 5V input power DC jack. The 5V DC power jack has a 2.1mm diameter center post and a 5.5mm diameter outer dimension.

USB pinout

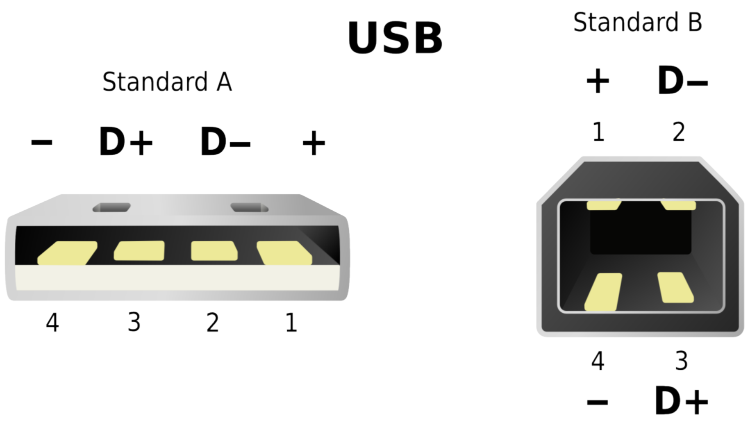

Figure 44: USB-A and USB-B connector pinout viewed from the front. source: Simon Eugsterm, CC BY-SA 3.0, `https://commons.wikimedia.org/w/index.php?curid=3353998`

pin	label	description	color
1	VBUS	+ 5 V	red
2	D-	Data -	white
3	D+	Data +	green
4	GND	Ground reference	black

Table 13: The pin assignment of a USB connector.

Bill of material - case and connectors

Table 14: BOM Peli 1200 case shielded

ref	**value**	**manufacturer**	**manufacturer number**	**description**	**quantity**
CS2		Bulgin	PX0413/04P	Circular Connector, Buccaneer 400 Series, Panel Mount Plug, 4 Contacts, Nylon (Polyamide) Body	1
CS3		Bulgin	PX0413/08P	Circular Connector, Buccaneer 400 Series, Panel Mount Plug, 8 Contacts, Nylon (Polyamide) Body	1
CS4		Bulgin	SA3348/1	Circular Connector Contact, Buccaneer, 400 Series Buccaneer, Pin, Solder, 22 AWG, 26 AWG	12
CS5		Bulgin	PX0484	Dust Cap / Cover, Dust Cap, 400 Series Buccaneer Connectors, Nylon (Polyamide) Body, 400 Series	2
CS6		Bulgin	PX0414/0M50	RF / Coaxial Cable Assembly, SMB Plug, 50ohm, Free Ends, 1.6 ft, 500 mm, Black	1
CS7		Bulgin	PX0480	Dust Cap / Cover, Dust Cap, Fits PX0412 style (chassis body)., Nylon (Polyamide) Body, 400 Series	1
CS8		Bulgin	PXM7012/10P/CR	Bulgin Buccaneer Series 7000, 10 Pole Panel Mount Connector Socket, Male Contacts, Quick Connect Mating	1
CS9		Bulgin	SA3544/P	Bulgin 6000 Series, size 8 10A Male Crimp Contact for use with Circular Connector	10
CS10		Bulgin	PXP7082	Dust Cap / Cover, Plug, Sealing Cap	1

Table 14 – continued from previous page

ref	value	manufacturer	manufacturer number	description	quantity
CS11		Telegärtner	J01150A0019	IMS Straight 50ohm Cable Mount SMA Connector, Plug, Crimp Termination RG174/U, RG188 A/U, RG316/U	1
CS12		Molex	50-57-9402	Molex SL Series 2.54mm Pitch 2 Way 1 Row Female Straight Crimp Connector Housing 70066	1
CS13		Molex	50-57-9404	Molex SL Series 2.54mm Pitch 4 Way 1 Row Female Straight Crimp Connector Housing 70066	1
CS14		Molex	50-57-9410	Molex SL Series 2.54mm Pitch 10 Way 1 Row Female Straight Crimp Connector Housing 70066	1
CS15		Molex	16-02-0088	Molex SL, 70058 Series Number Crimp Terminal, Female, 24AWG to 22AWG, Crimp, Gold over Nickel Plating	16
CS16		RS	771-9186	RS Pro DC, DC Adapter Rated At 1A, 12 V, Cable Mount, length 44mm, Nickel Plate	1
CS17		Hirose	ZX40-B-5S-UNIT(12)	USB Connectors MICRO B PLUG ASBY SOLDER CABLE	1
CS18		Hirose	ZX40-B-SLDA	USB Connectors MICRO B PLUG SHIELD TOP FOR ZX40	1
CS19		Hirose	ZX40-SLDB	USB Connectors MICRO AB PLUG SHIELD BOTTOM FOR ZX40 3.3	1
CS20		Assmann WSW	A-USBPA-N	ASSMANN WSW Type A USB Connector, Cable Mount Plug, 30 V, 1A	1
CS21		Assmann WSW	A-USBPB-N	ASSMANN WSW 1 Port Straight Cable Mount Male Type B USB Connector, 30 V, 1A	2

Table 14 – continued from previous page

ref	value	manufacturer	manufacturer number	description	quantity
CS22		TE Connectivity	5-554739-3	COMMSCOPE Cat5 RJ45 Connector Plug, Unshielded, Straight, Cable Mount	1
CS23		RS	812-4797	RS Pro Grey Cat5e Cable, Twisted Pair UTP 300 V ac 100m	0.05
CS24		RS	190-440	Plain Stainless Steel Pan Head Machine Screws, M3 x 10mm	4
CS25		RS	189-563	A4 Stainless Steel, Hex Nut, M3	4
CS26		RS	527-987	Plain Nylon Cheese Head Machine Screws, M3 x 12mm	3
CS27		RS	525-701	Nylon, Hex Nut Natural, M3	3
CS28		Richco	469.09.05	469.09.05, 5mm High Polyamide Spacers with 6mm diameter and 3.2mm Bore Diameter	7
CS29		Hammond	1550k	1550 Alumimium Enclosure, IP54, 140 x 102 x 77mm	1
CS30				ERROR: part not found in inventory.	0.41

Table 15: BOM Ethernet cable

ref	value	manufacturer	manufacturer number	description	quantity
C-ETH1	connector	Bulgin	PX0410/08S/6065	Circular Connector, Buccaneer 400 Series, Cable Mount Receptacle, 8 Contacts	1
145	connector	Bulgin	PX0481	Dust Cap / Cover, Sealing Cap, 400 Series Buccaneer Connectors, Nylon (Polyamide) Body, 400 Series	1
C-ETH3	connector	Bulgin	SA3347/1	Circular Connector Contact, Buccaneer, 400 Series Buccaneer, Socket, Solder, 22 AWG, 26 AWG	8

Table 15 – continued from previous page

ref	value	manufacturer	manufacturer number	description	quantity
C-ETH4	connector	TE Connectivity	5-554739-3	COMMSCOPE Cat5 RJ45 Connector Plug, Unshielded, Straight, Cable Mount	1
C-ETH5	cable	RS	812-4797	RS Pro Grey Cat5e Cable, Twisted Pair UTP 300 V ac 100m	2

Table 16: BOM GPS active antenna cable

ref	value	manufacturer	manufacturer number	description	quantity
C-GPS1	connector	Bulgin	PX0415/1	RF / Coaxial Connector, SMB Coaxial, Straight Plug, Crimp, 50 ohm, RG174, Brass	1
C-GPS2	connector	Bulgin	PX0481	Dust Cap / Cover, Sealing Cap, 400 Series Buccaneer Connectors, Nylon (Polyamide) Body, 400 Series	1
C-GPS3	gps	u-Blox	ANN-MS (SMA)	Active antenna with SMA connector	1

Table 17: BOM power supply cable

ref	value	manufacturer	manufacturer number	description	quantity
138	connector	Bulgin	PX0410/04S/4550	Circular Connector, Buccaneer 400 Series, Cable Mount Receptacle, 4 Contacts	1
141	connector	Bulgin	SA3347/1	Circular Connector Contact, Buccaneer, 400 Series Buccaneer, Socket, Solder, 22 AWG, 26 AWG	4
145	connector	Bulgin	PX0481	Dust Cap / Cover, Sealing Cap, 400 Series Buccaneer Connectors, Nylon (Polyamide) Body, 400 Series	1

Table 18: BOM sensor cable connector

ref	**value**	**manufacturer**	**manufacturer number**	**description**	**quantity**
C-SENS1	connector	Bulgin	PXM7010/10S/CR/0911/SN	Bulgin Buccaneer Series 7000, 10 Pole Free Hanging Connector Plug, Female Contacts, Quick Connect Mating	1
C-SENS2	connector	Bulgin	PXP7081	Dust Cap / Cover, Plug, Sealing Cap, Buccaneer 7000 Series PXP7010 Flex Cable Connectors	1
C-SENS3	connector	Bulgin	SA3544/S	Bulgin 6000 Series, size 8 10A Female Crimp Contact for use with Circular Connector	10

PUBLISHED BY MERTL RESEARCH GMBH
KIENMAYERGASSE 22, 1140 VIENNA, AUSTRIA, FB-NR.: 378631 K

`http://www.mertl-research.at`

This work was funded by the Austrian Academy of Sciences within the project SeisRockHT.

Performance of the seismic data recorder Ruwai

Stefan Mertl

Version 1.0 , April 4, 2017.

Technical report number 20170207-01

Mertl Research GmbH

The Ruwai data recorder is a free hardware design[1] seismic data logger with the aim to meeting the needs of scientific data collection and the deployment in rugged conditions. Important performance features of a seismograph are the internal noise, the dynamic range, the timing and the overall sensitivity including the used sensor. These features have been tested with regard to the usability of the Ruwai data recording for seismological research within the SeisRockHT project[2].

The Ruwai recording system

The Ruwai seismic data recorder provides sampling of 4 differential analog input channels at the sampling rates 100 to 800 Hz at steps of 100 Hz. A preamplification of the analog input signal between 0.125 and 176 is available. All parameters can by set by software. The sample accurate timing of the digitized data is done by using a GPS disciplined clock for the analog to digital converter and the GPS pulse per second for time stamping. The reference voltage of each channel is +/- 2.5 V.

The Ruwai consists of the Arduino Stack and the BeagleBone Black[3] single board computer. The block diagram of the major components of the Ruwai data recorder is shown in figure 1. For deployment, the Arduino Stack is shielded using an aluminum box and mounted together with the BeagleBone Black in a PeliCase housing (see figure 2). The housing and the connectors where chosen to withstand rugged environmental conditions.

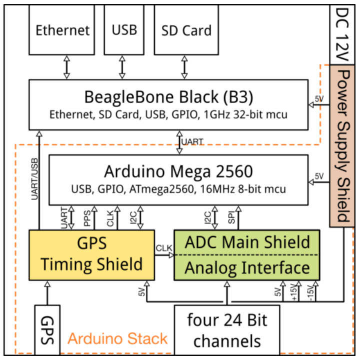

Figure 1: The block diagram of the Ruwai seismograph. The orange dashed line marks the components of the Arduino Stack.

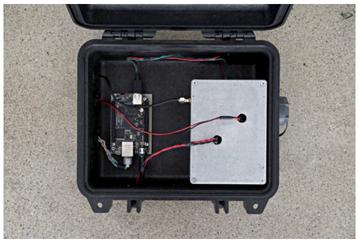

Figure 2: The Ruwai data recorder mounted in a PeliCase.

The Arduino Stack consists of four stacked printed circuit boards which are called *shields*:

- the power supply shield (PSS),
- the GPS timing shield (GTS),
- the ADC main shield (AMS),
- and the Analog Interface PGA shield (AIPS).

The GTS provides the GPS time accurate timing of the sampled data. The timing was tested by running the Ruwai recorder side-by-side with a commercial data recorder and comparing the recorded waveform. The timing of the recorded waveform of both recorders was equal at sample level. No time shift was observable.

The AIPS provides analog preamplification and anti aliasing filtering. The AMS samples the preprocessed input signal with a 4-channel 24 Bit ADC. The internal noise of those two shields is

[1] `https://www.gnu.org/philosophy/free-hardware-designs.en.html`

[2] `https://www.zamg.ac.at/cms/de/forschung/klima/klimafolgen/seisrockht`

[3] `http://beagleboard.org/`

crucial for the overall performance of the Ruwai data recorder. The self noise of the AMS and AIPS has been tested thoroughly and compared to seismic noise models[4] to evaluate the usage of the Ruwai for seismological research. The results are presented in this report.

The shorted input noise of the ADC Main shield

The ADC Main shield of the Ruwai Arduino stack is equipped with a Texas Instruments ADS1274 analog to digital converter (ADC). The first task was to evaluate if the design of the ADC Main shield allows the operation of the ADS1274 within it's specification. A common method to test the self-noise of ADCs is recording the output of the ADC with shorted differential inputs. Shortening the input means zero amplitude at the ADC input. In an ideal case, the output of the ADC would be zero as well. Actually, the output contains the internally created electronic noise and therefore is a measure of the quality of the ADC operation.

In the data sheet of the ADS1274[5], the shorted input noise of the ADC is given as the root mean square amplitude of 8 μV for the low-speed mode which is used in the Ruwai system.

For the test, the Analog Interface PGA shield was removed from the Arduino stack and the analog inputs of the ADC Main shield were shorted with jumper wires (see figure 3). The Ruwai was powered by a 12V battery.

The test data was recorded with the sampling rates 100, 200, 400 and 800 samples per second (sps). Waveform data with a length of 180 seconds was used for the analysis. As an example, the raw waveform data of channel 1 is shown in figure 4.

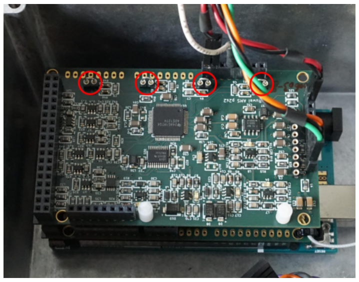

Figure 3: The ADC Main shield with shorted analog inputs. The points where the inputs were shorted are marked with red circles.

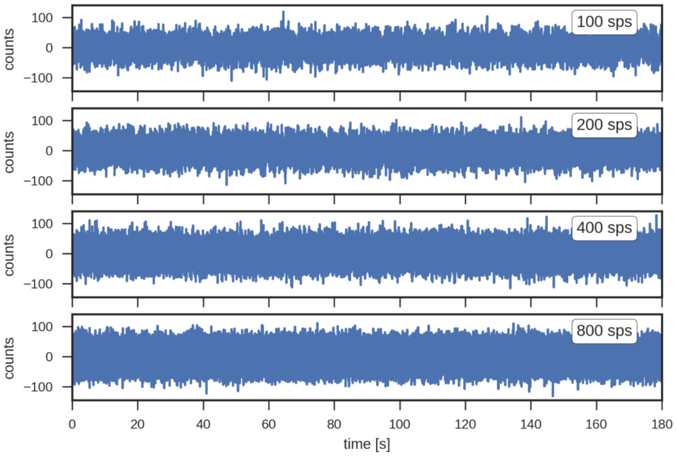

Figure 4: The waveform data of channel 1 used for the data analysis. The mean value was removed from the data to center the time series around amplitude 0.

The waveform data was converted from counts to Volt using the bit-weight (least significant bit) of the ADS1274 ADC. The ADC has

---

[4] Jon Peterson. Observations and modelling of background seismic noise. Open-file report 93-322, U. S. Geological Survey, Albuquerque, New Mexico, 1993

[5] ADS1274/ADS1278 - Quad/Octal, Simultaneous Sampling, 24-Bit Analog-to-Digital Converters (Rev. F), October 2007

a bipolar input range of +/- 2.5 V. In the ADS1274 data sheet, the bit-weight of the 24-bit ADC is given by

$$bw = \frac{2.5}{(2^{23} - 1)} \tag{1}$$

. This gives a value for the bit-weight $bw = 2.9802325940409415 * 10^{-7}$ V/cnt. The full scale input range is $-(2.5 + bw)$ to $+2.5$ Volt.

For each channel and sampling rate, the RMS voltage was computed. The results are shown in figure 5. As already seen in the example waveform in figure 4, the noise doesn't vary much with the sampling rate. All 4 channels and all 4 sampling rates show a similar RMS voltage of approximately 8.2 μV. This is similar to the typical value of the RMS voltage for shorted input of 8 μV given in the data sheet of the ADS1274.

The RMS voltage of the ADC Main shield equals 27.5 counts or 4.78 bits. This leads to 18.22 effective bits for bipolar mode and a signal to noise ratio of 109.7 dB.

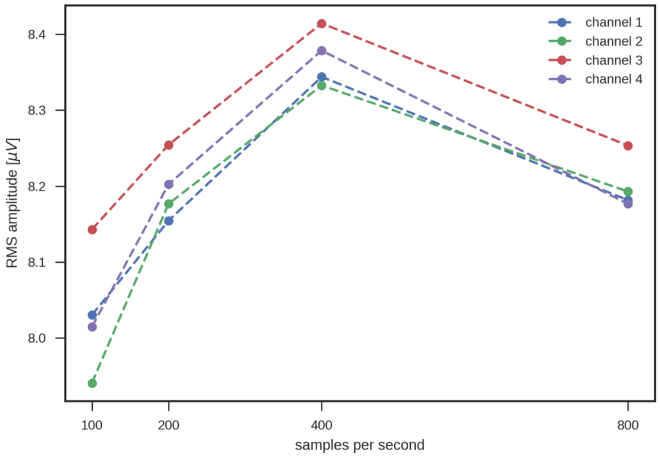

Figure 5: The RMS voltage of the 180 s long data recorded with shorted inputs.

The power spectral density was computed using the description of Havskov and Alguacil[6] given in chapter 6.3:

$$P_n^d = 2\left|F_n^{DFT}\right|^2 \frac{\Delta t^2}{T} \tag{2}$$

, where F_n^{DFT} are the spectral coefficients computed using the `fft` command of the Python NumPy[7] package, Δt is the sampling interval and T is the length of the analyzed time series.

The power spectral densities were similar for all channels and all sampling rates. As a representative example, the power spectral densities of the 4 channels and a sampling rate of 800 sps are shown in figure 6. The noise is mainly white noise with a slight tendency of increasing amplitude with higher frequencies. Two sharp frequency peaks per channel can be observed at frequencies around 1 Hz. The location of the two frequency peaks varies from

[6] Jens Havskov and Gerardo Alguacil. *Instrumentation in Earthquake Seismology*. Springer, 2004

[7] `http://www.numpy.org/`

channel to channel. A similar frequency analysis given in the ADS1274 data sheet show similar peaks, although at slightly higher frequency around 10 Hz.

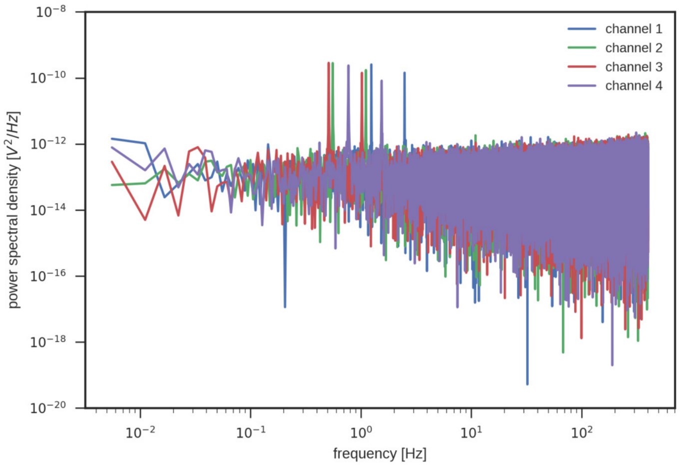

Figure 6: The power spectral density of the 180 s long data recorded with shorted inputs. The power spectral densities were computed for the data recorded with 800 sps.

The shorted input noise of the Analog Interface PGA shield

The determination of the internal noise of the ADC Main shield showed that the ADS1274 can be operated within its specification. The Analog Interface PGA shield includes the programmable gain amplifier (PGA) PGA281 from Texas instruments and an active 5-pole anti aliasing filter. To test the influence of the AIPS on the internal noise of the Arduino stack, the Arduino stack was tested with shorted analog inputs and compared to the results of the test of the ADC only given in section The shorted input noise of the ADC Main shield. The analog inputs where shorted with jumpers at the analog connector of the AIPS (see figure 7).

Similar to the analysis of the ADC Main shield, data with a length of 180 seconds was used for the analysis. The four channels of the Ruwai were tested with all combinations of the sampling rates 100, 200, 400 and 800 and the PGA gains of 1, 32, 64, 128 and 176. Figure 8 shows an example of the recorded waveform data of channel 1 and gain 32. It can already be seen from the waveform, that the noise differs from the tests running the AMS only. The amplitude level is higher and low frequency noise can be observed.

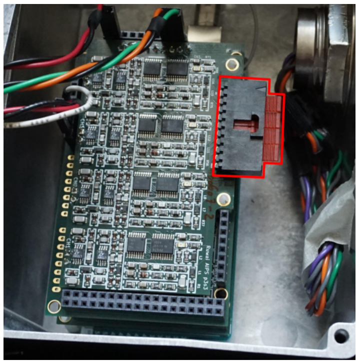

Figure 7: The Arduino stack with the analog inputs shorted at the analog connector of the AIPS. The connector where the inputs were shorted is marked with a red outline.

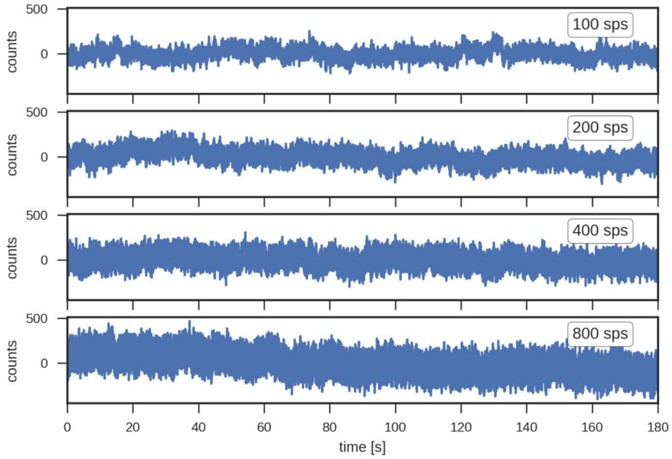

Figure 8: Example waveform of the AIPS self noise test. The mean value was removed from the data to center the time series around amplitude 0.

The RMS amplitude computed from the waveform is shown in figure 9. It can be seen, that the RMS amplitude varies between the channels especially for lower gain settings, but in general an equal behavior can be observed for all channels. The average of all 4 channels shows an increase of the RMS amplitude with increasing gain and with increasing sampling rate. Whereat the increase is significant for gains above 32. The variation between gain 1 and 32 is small except for 800 sps sampling rate.

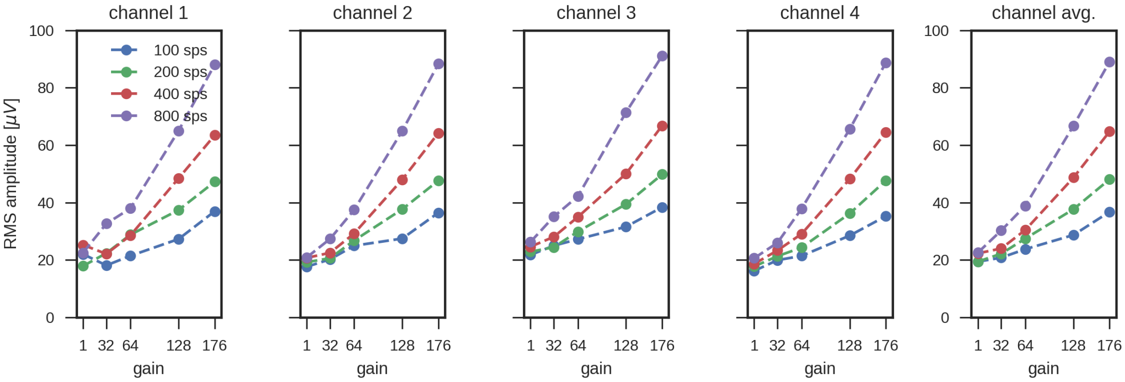

Figure 9: The RMS amplitude of the test data for the sampling rates 100, 200, 400 and 800 and the gains 1, 32, 64, 128, 176.

In table 1 the effective number of bits and the signal to noise ratio computed using the average RMS amplitudes given in figure 9 is shown. The best performance at 100 sps and gain 1 is about 7 dB less than the signal to noise ratio of the ADC Main shield alone.

The power spectral density of the data showed no significant variation between the results of the different channels. The increase of the RMS amplitude with sampling rates is due to the broadening of the bandwidth. Therefore the averaged power spectral densities

gain	1		32		64		128		176	
sps	eb	snr [dB]	eb	snr [dB]	eb	snr [dB]	eb	snr [dB]	eb	snr [dB]
100	17.0	102.2	16.9	101.6	16.7	100.4	16.4	98.8	16.1	96.6
200	17.0	102.2	16.8	101.0	16.5	99.2	16.0	96.4	15.7	94.3
400	16.8	101.0	16.7	100.3	16.3	98.3	15.6	94.2	15.2	91.7
800	16.8	100.9	16.3	98.3	16.0	96.2	15.2	91.5	14.8	89.0

Table 1: The effective bits (eb) and the signal to noise ratio (snr) in dB of the tested sps and gain combinations.

of all 4 channels and sampling rate 800 shown in figure 10 is used for the interpretation. For comparison, the power spectral density of the ADC Main shield only is shown as well.

At gain 1, it can be seen, that the noise floor of the PGA shield almost matches the one of the ADC Main shield. But towards lower frequencies, soon 1/f noise [8] (flicker noise) starts to dominate the noise floor. The slope of the 1/f noise is ca. -1 decade per decade. The noise corner frequency [9] f_{nc}, which is the frequency at which the 1/f noise excels the white noise[10], is at ca. 100 Hz for gain = 1. With increasing gain, the amplitude of the white noise increases and shifts the noise corner frequency towards lower frequencies. The amplitude of the flicker noise does not change with the gain.

It can also be seen, that with increasing gain, the disturbance of mains power frequencies (50 Hz and harmonics) are present. The Ruwai was powered by a 12 V battery for this test, so the noise is not originating from the power supply. But the test was accomplished in a lab environment with equipment powered from mains nearby which represent possible sources for electromagnetic interference.

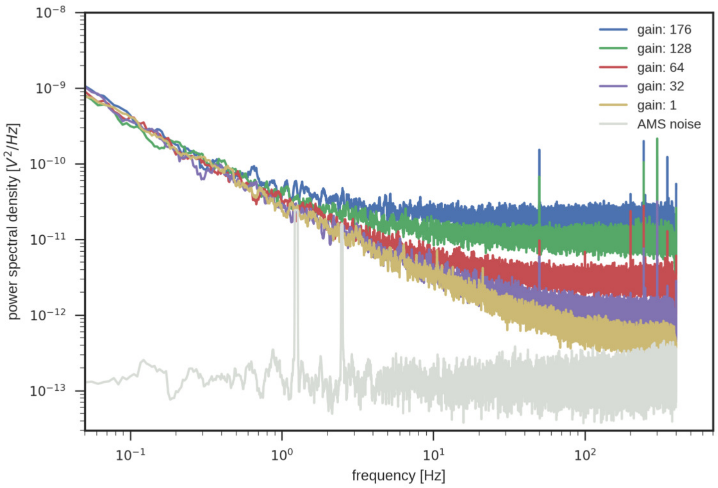

Figure 10: Power spectral density averaged for all 4 channels and sampling rate 800 sps. The light grey line represents the noise of channel 1 of the AMS shield only. All power spectral densities were smoothed using an 11 samples long moving average filter.

From the analysis of the test data with shorted inputs it can be seen, that the AIPS adds a significant amount of noise to the system. At gain 1, the RMS amplitude of the noise of the whole system is ca.

---

[8] Hanspeter Schmid. Offset, flicker noise, and ways to deal with them. In *Circuits at the Nanoscale: Communications, Imaging, and Sensing*, pages 95–116. CRC Press, 2009

[9] Noise Analysis in Operational Amplifier Circuits. Application Report SLVA043B, Texas Instruments, 2007

[10] White noise has a constant amplitude in the power spectral density.

3 times larger than the one of the ADC Main shield alone. 1/f noise is the major contributor to this increase. With higher gain settings, white noise starts to dominate the noise characteristics.

The source of the 1/f noise is most likely the active anti aliasing filter or the power supply of the Analog Interface PGA shield.
The source of the high frequency white noise dominating the power spectral density at large gain settings is supposed to be the preamplification circuit. A possible explanation for the observations made might be electromagnetic interference or high frequency noise originating from the circuit before the inputs of the programmable gain amplifier which in sequence is amplified by the PGA.

Two tasks for further improvement can be formulated:

1. Determine the major contribution of the 1/f noise and improve the electronic circuit to minimize this noise.
2. Indicate the source of the high frequency noise to improve the efficiency of the programmable gain amplifier at high frequencies.

The minimum resolvable ground motion

Four main components of a seismic recording system determine the sensitivity of the overall system:

1. the sensitivity of the seismic sensor;
2. the amount of preamplification of the analog input signal;
3. the signal to noise ratio of the analog to digital converter; and
4. the full-scale input voltage of the analog to digital converter.

The shorted input noise of the Ruwai and the transfer function of a seismic sensor can be used to estimate the minimum resolvable ground velocity. The inverse transfer function is used to reconstruct the ground motion that would have created the signal of the shorted input noise. This signal represents the noise floor of the whole recording system. Any ground motion with an amplitude below the noise floor would not create a voltage high enough to exceed the internal noise of the Ruwai.

Comparing the noise floor with the new low noise model (NLNM) and the new high noise model (NHNM)[11], which give the minimum and maximum general seismic background ground motion which can be expected worldwide, reveals the capabilities of the recording system for seismic studies.

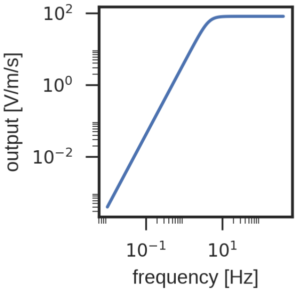

Figure 11: The amplitude response of the GS-11D 4.5 Hz geophone.

For the SeisRockHT monitoring project, Geospace GS-11D 4.5 Hz geophones with a coil resistance of 4000 ohm and a damping of 0.7 are used. The sensitivity of this geophone is 81 V/m/s. The amplitude response of the geophones is shown in figure 11.

The noise floor of the Ruwai recording system was computed by multiplying the power spectral density of the shorted input noise described in section The shorted input noise of the Analog

---

[11] Jon Peterson. Observations and modelling of background seismic noise. Open-file report 93-322, U. S. Geological Survey, Albuquerque, New Mexico, 1993

Interface PGA shield with the inverse squared transfer function of the GS-11D 4.5 Hz geophone.

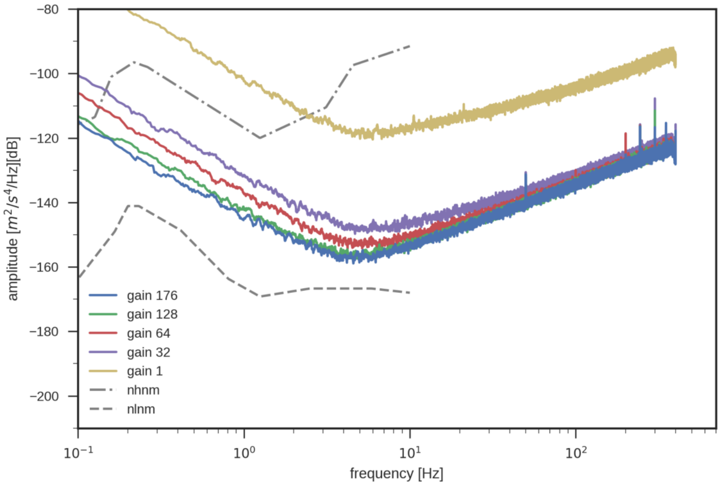

Figure 12: Minimum noise floor of the Ruwai system with a 4.5Hz GS-11D (81 V/m/s) sensor and a sampling rate of 800 sps.

The Ruwai noise floors for different preamplification gain in figure 12 show, that the Ruwai system is suitable for seismic studies, although a minimum preamplification of 32 should be used for a proper sensitivity. Increasing the preamplification further lowers the sensitivity, but this effect weakens with higher frequencies due to the high noise described in section The shorted input noise of the Analog Interface PGA shield. An increase of the preamplification comes with the loss of dynamic range, which means a decrease of the maximum amplitude which can be recorded without clipping. Table 2 gives the maximum velocities and the corresponding Modified Mercalli Intensity according to Wald et al.[12].

gain	max. velocity [mm/s]	intensity
1	30.86	IV
32	0.96	II - III
64	0.48	II - III
128	0.24	II - III
176	0.18	II - III

Table 2: The maximum ground motion that can be recorded with the Ruwai without amplitude clipping.

The preamplification of 32 is seen as the best setting with a good noise behavior over the whole bandwidth and a sufficient sensitivity.

If an increase in sensitivity is needed, the best solution would be the selection of a more sensitive seismic sensor. Although one has to keep in mind, that this would also decrease the maximum recordable amplitude.

[12] D. J. Wald, V. Quitoriano, T. H. Heaton, and H. Kanamori. Relationships between peak ground acceleration, peak ground velocity, and modified mercalli intensity in California. *Earthquake Spectra*, 15(3): 557–564, 1999

Performance under real conditions

The minimum resolvable ground motion of the Ruwai data recorder and a Geospace GS-11D 4.5 Hz geophone was computed in the section above. To validate this noise floor which was determined in the lab, it is compared to the recordings from 4 stations deployed at the Hoher Sonnblick, Austria. The stations are equipped with the same Ruwai recording system as used for the noise tests.

Two days with different characteristics were selected for the test. One day, October 21, 2016, represents a normal day with no extraordinary seismic events happening. The second day, October 29, 2016, contains multiple earthquakes. For the comparison, the probability power spectral density[13] were computed using obspy[14].

The probability power spectral densities of the normal day (figure 13) and the day with earthquakes (figure 14) show, that the computed noise floor of the Ruwai recording system fits the real-world measurements. Moreover, the recordings at the stations don't include any mains power supply noise as it was recorded in the lab.

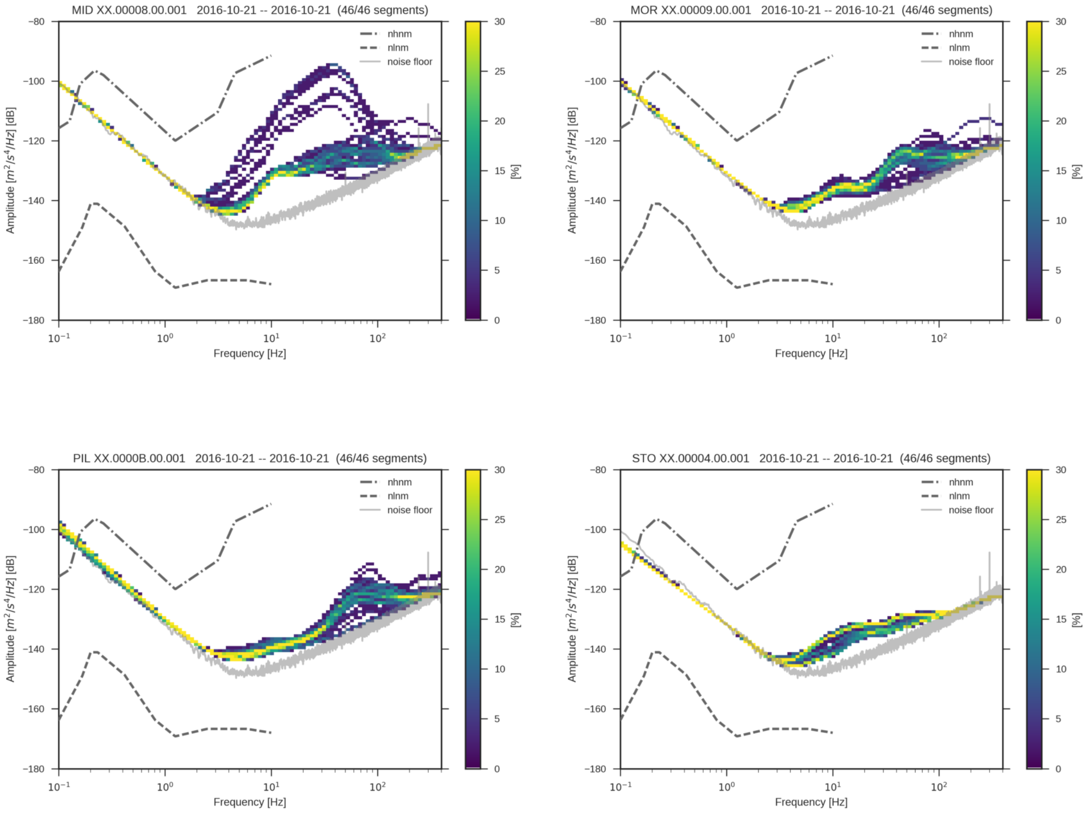

Figure 13: The power spectral densities of the 4 stations MID, MOR, PIL and STO located at the foot of mount Hoher Sonnblick. This day represents a normal ground motion with no outstanding events like large earthquakes.

---

[13] Daniel E. McNamara and Raymond P. Buland. Ambient Noise Levels in the Continental United States. *Bulletin of the Seismological Society of America*, 94(4):1517–1527, 2004

[14] `www.obspy.org`

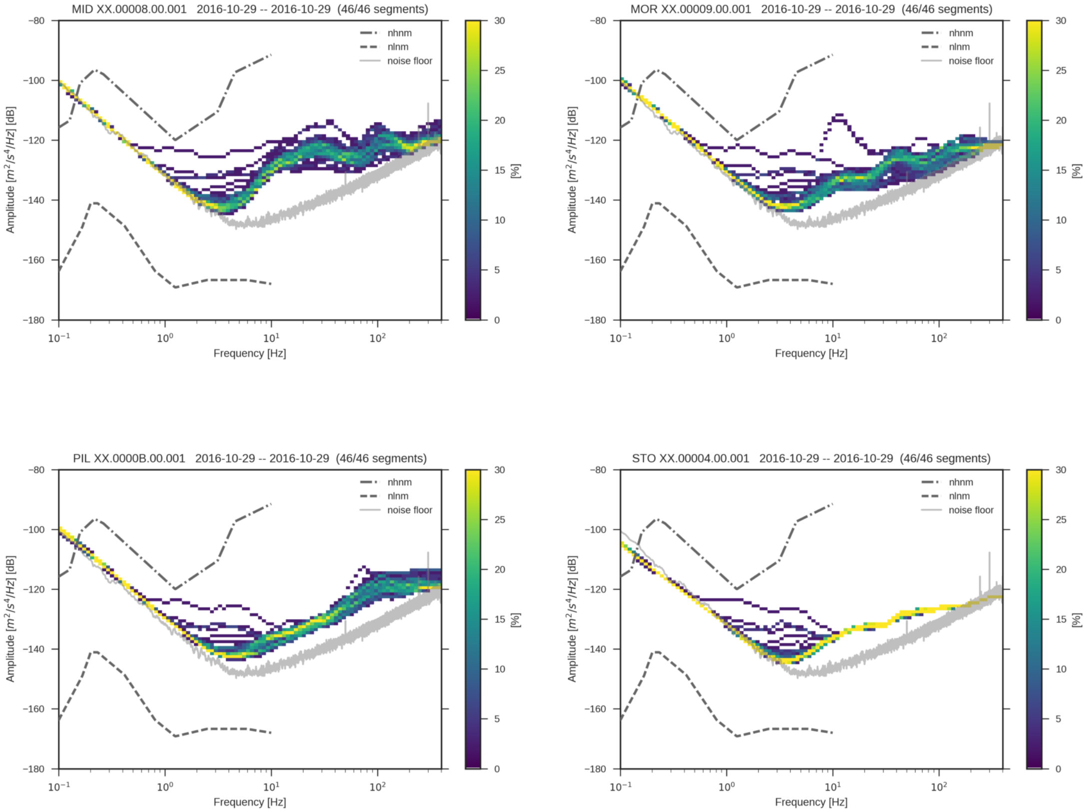

Figure 14: The power spectral densities of the 4 stations MID, MOR, PIL and STO located at the foot of mount Hoher Sonnblick. This day represents a day with several earthquakes.

For the normal day the recorded signal is above the noise floor for frequencies larger than 2 Hz. At high frequencies above 100 Hz the signal sometimes drops within the range of the noise floor. Frequencies below 2 Hz don't show any signal energy above the noise floor.

The day with earthquakes shows a similar background ground motion as the normal day, but the signal content of the earthquakes is above the noise floor down to frequencies of ca. 0.5 Hz.

This comparison shows, that the Ruwai recording system is suitable for the analysis of the seismicity of the north face of mount Hoher Sonnblick. In general the system is capable for seismic monitoring at sites with moderate seismic background noise. At sites where the seismic background noise reaches the lower half of the NLNM/NHNM range, the sensitivity of the system has to be increased either by increasing the sensitivity of the sensor or by increasing the gain of the preamplification. Although these steps have negative effects of reducing the dynamic range as described in section The minimum resolvable ground motion.

Another potential in increasing the sensitivity of the Ruwai system is lowering the electronic noise introduced by the Analog Interface PGA shield. There's the theoretical potential to increase the sensitivity by ca. 9.5 dB, but this would mean to reduce the internal noise of the AIPS to almost 0 V_{rms} which is not realistic because at least an anti-aliasing filter is needed as an analog signal processing in front of the ADC.

Nevertheless, if the monitoring situation and the sensitivity requirements are known in advance, the sampling rate and preamplification could be simplified to fixed values which would allow simpler analog signal processing circuits using only passive electronic components. This is most likely to lower the noise of the AIPS with a loss of flexibility of the recording parameters.

PUBLISHED BY MERTL RESEARCH GMBH
KIENMAYERGASSE 22, 1140 VIENNA, AUSTRIA, FB-NR.: 378631 K

http://www.mertl-research.at

This work was funded by the Austrian Academy of Sciences within the project SeisRockHT.

Electromagnetic Interference and the Ruwai recording system

Stefan Mertl

Version 1.0 , April 4, 2017.

Technical report number 20170217-01

Mertl Research GmbH

A test deployment of the first prototype of the Ruwai recording system showed major electromagnetic interference on the recorded data if the system was placed nearby equipment powered from mains power supply. This situation was used to analyze the noise sources causing the recorded interference and the possibilities to remove them by shielding the recording system.

First encounters with electromagnetic interference

The deployment of the first set of Ruwai data recorders was done within the project SeisRockHT[1] funded by the Austrian Academy of Sciences. For the first installation at the station STO at Hoher Sonnblick we used an unshielded Ruwai (see figure 1). Testing the unshielded Ruwai in the lab showed no major disturbance despite a 50 Hz noise (including harmonics), which could be removed by frequency filtering. Therefore we thought to give it a try and see what will happen.

Figure 1: The unshielded Ruwai.

The station STO is located at the end of a ca. 50m long gallery at the foot of mount Hoher Sonnblick. Mains power is available in the gallery and was used for charging the battery. The Ruwai was placed inside a plastic box together with the battery, the battery charger and a solar charger which was used for deep discharge protection (see figure 2). The mains power supply cable was fed into the box through a whole. The used sensor was a Geospace GS-11D 4.5 Hz three components geophone. The geophone housing and the cable were not shielded.

Figure 2: The unshielded Ruwai together with the power supply equipment in a plastic box.

The test data of the installation showed major electromagnetic interference which made the data unusable (see figure 3). Large peak to peak amplitudes of ca. 30 mV and regular dc-offsets of the data were present. This was the starting point of the search for the entering points of the electromagnetic interference (EMI) into the Ruwai system including sensors and cables.

First test recordings of the Ruwai powered from the battery only with no connection to the mains power and at some meters distance from the equipment with mains power supply already showed a significant reduction of the electromagnetic interference. The in depth tests described below show the influence of electromagnetic interference on different parts of the Ruwai recording system and solutions to remove or reduce them.

[1] `https://www.zamg.ac.at/cms/de/forschung/klima/klimafolgen/seisrockht`

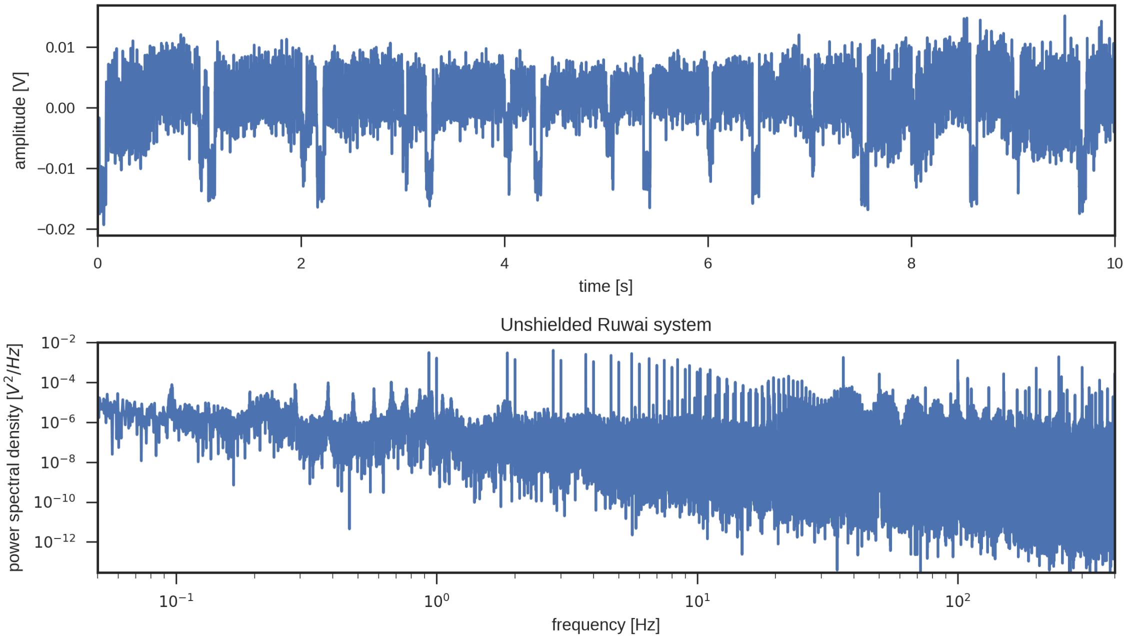

Unshielded Ruwai system

Figure 3: The example data of the recordings at station STO at Hoher Sonnblick with an unshielded recording system. 10 seconds of the waveform data (top) and the psd of a 1 hour recording (bottom) is shown.

Shielding the Arduino Stack

The mains power was supposed to be the major source of the electromagnetic interference disturbing the Ruwai recording system. The Ruwai data recorder allows sampling rates up to 800 Hz, which results in input frequencies of up to 400 Hz. At these low frequencies, the electromagnetic field can be seen as a quasi-stationary electric field and a quasi-stationary magnetic field[2].

To effectively shield a quasi-stationary electric field, a Faraday cage can be used. Shielding a quasi-stationary magnetic field is much more complex and was not considered for the EMI protection of the Ruwai.

A Faraday cage uses the compensation of charge carriers in conductive materials[3]. It is usually a metal housing enclosing the electronic system which should be protected. The compensation of the charge carriers in the enclosure creates an electric field opposing the disturbing electric field. As a result, the interior of the enclosure is field free.

So the first step was to put the Ruwai Arduino Stack into a metal enclosure and to use a metal connector for the sensor input to allow for a shielding of the sensor cable and sensor housing as well (see figure 4). This protects the sensitive circuit of the analog to digital converter from any quasi-stationary electric field.

The shielding of the Arduino Stack removed any disturbance from nearby electric equipment due to the interference of the quasi-stationary electric field.

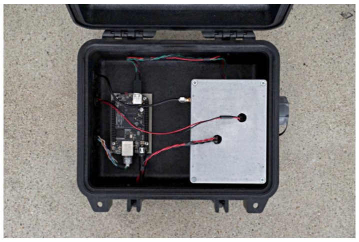

Figure 4: The shielded Arduino Stack mounted in the Peli case.

[2] Adolf J. Schwab and Wolfgang Kürner. *Elektromagnetische Verträglichkeit*. Springer Berlin Heidelberg, 5 edition, 2007. ISBN 978-3-540-42004-0

[3] Hans A. Wolfersperger. *Elektromagnetische Schirmung*. VDI-Buch. Springer Berlin Heidelberg, Berlin, Heidelberg, 2008. ISBN 978-3-540-76912-5 978-3-540-76913-2

Noise from the mains adapter

An additional noise source is introduced, if the Ruwai is not powered from an isolated battery but a battery connected to a battery charger or directly to a 12 V mains adapter. This is a common setup of a seismic station when mains power supply is available at the station location. Although the battery charger is usually isolated from mains ground and the DC-DC converter[4] of the Ruwai is an isolated converter as well, 50 Hz noise enters the system.

The test setup is shown in figure 5. The resulting 50 Hz noise can be seen in the power spectral density in figure 6.

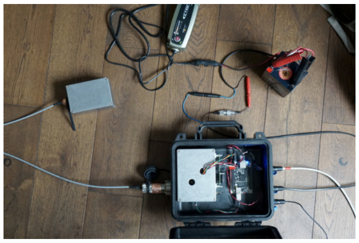

Figure 5: Measurement setup of the noise caused by the battery charger.

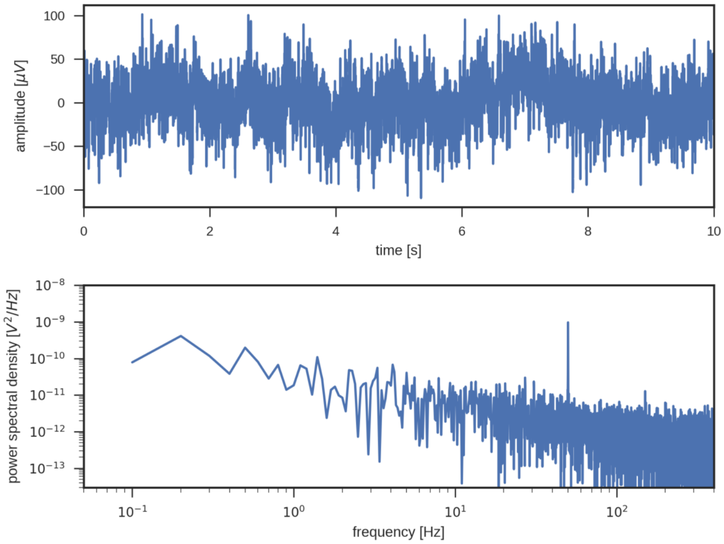

Figure 6: Psd of the ungrounded Ruwai system.

One identified source of this noise is that the reference potential of the Arduino Stack, which by theory should be isolated from the input power supply by the DC-DC converter, floats above the earth potential at a 50 Hz sine wave with ca. 100 V peak-to-peak amplitude (see figure 7). This floating potential interferes with the analog input of the Analog Interface PGA shield of the Arduino Stack.

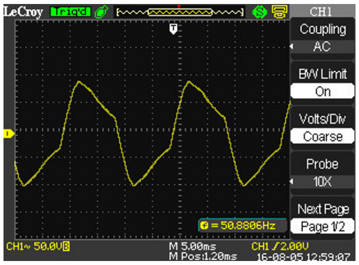

Coupling AC
BW Limit On
Volts/Div Coarse
Probe 10X
= 50.8806Hz
CH1~ 50.0V
M 5.00ms
M Pos:1.20ms
CH1 ∫ 2.00V
16-08-05 12:59:07

Figure 7: Oscilloscope measurements between the earth ground potential and the circuit reference of the Arduino Stack.

This noise can be removed by connecting the negative pole of the battery to the earth ground. This creates a short circuit preventing the floating of the Arduino Stack reference relative to the earth ground.

Shielding the sensor and the sensor cable

With the modifications of the Ruwai described above, the recorder itself was protected against the quasi-stationary electric field. Another crucial part of the Ruwai recording system to pick up electromagnetic interference is the sensor and the cable from the Ruwai

[4] Traco THL 10-2411WI

recorder to the sensor. To protect the sensor and the sensor cable from the electric field, both parts have to be enclosed by the Faraday cage. The less holes the conductive enclosure has, the better.

For the test, a 10 m long shielded, twisted pair cable and an aluminum box acting as the sensor shield was used. The cable shield was connected to the Arduino Stack metal box and the sensor box with circular metal connectors with an all around connection of the cable shield to the connector.

To test the interference of the electric and the magnetic field with the sensor, different sensors were used:

- A 3.9 k Ohm resistor to test the electrostatic field. 3.9 k Ohm is approximately the resistance of a GS-11D geophone.
- A self-built coil with ca. 30 windings and a 3.9 k Ohm resistor in series with the coil. The coil should pick up magnetic interference.
- A coil of a GS-11D geophone without spring suspension and the magnet.
- A fully functional GS-11D geophone coil.

The signal was preamplified with a gain of 32 and sampled with 800 samples per second. The setup of the Ruwai recorder for this test is shown in figure 8. In the photo it can be seen, that the power supply shield of the Arduino Stack was placed outside the shield box. This was done as a precaution to eliminate any noise which might be created by the power supply shield.

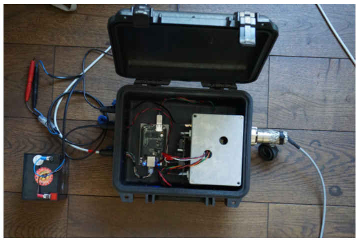

Figure 8: The Ruwai powered by a 12V battery. The Arduino Stack is shielded with a metal box and the sensor cable shield is all around connected to the Arduino Stack shield.

Shielded resistor and coil

The setups for the resistor and coil sensor tests are shown in figure 9 and the corresponding power spectral densities in figure 10. The sensor boxes were closed for the tests, they were opened only to show the used sensor inside.

First, the 3.9 k Ohm resistor was mounted inside the sensor box. The cable to the resistor was twisted to minimize the influence of the magnetic field. There was no interference measured for this setup. For comparison, the resistor was positioned outside the sensor box which resulted in significant noise at 50 Hz and harmonics visible in the spectrum.

These tests show, that the metal sensor box effectively protects the sensor from the electric field. The magnetic field penetrates the shield and induces a 50 Hz noise into the coil.

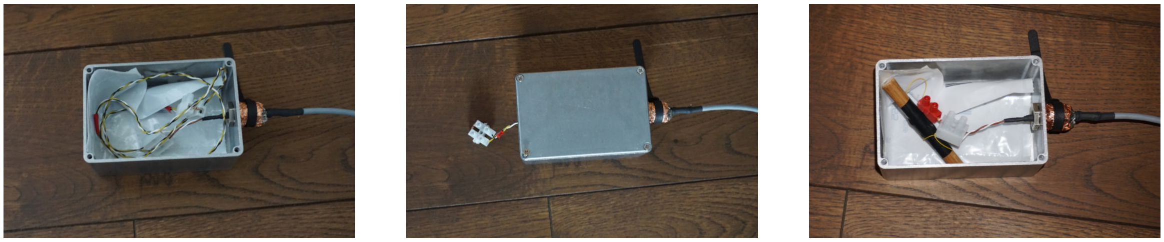

(a) Shielded 3.9 kOhm resistor (b) Unshielded 3.9 kOhm resistor (c) Shielded coil (3.9 kOhm res.)

Figure 9: The measurement setup of the resistor tests.

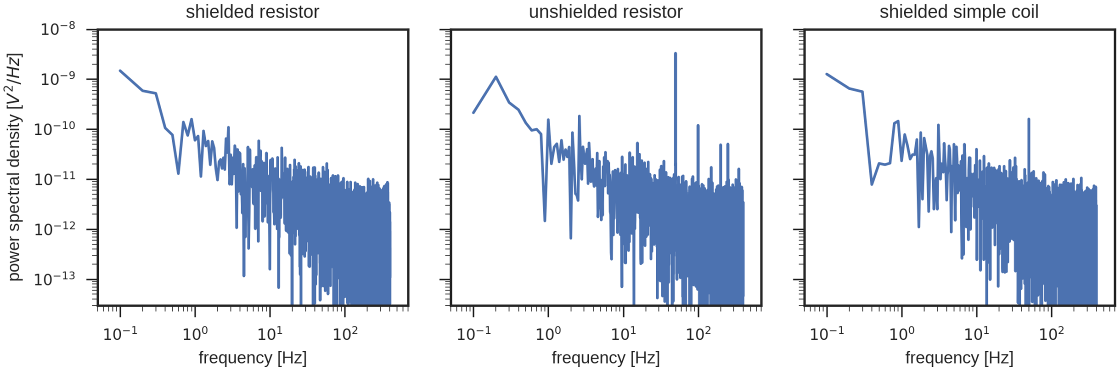

Figure 10: The power spectral densities of the resistor tests.

GS-11D coil only

To test the purely electromagnetic noise induced to the GS-11D geophone, a disassembled GS-11D coil was used. The spring suspension and the magnet were removed. This removes any noise created by the vibrating coil.

The coil was placed inside the metal box at three different positions (see figure 11). The corresponding power spectral densities are given in figure 12).

(a) Shielded GS-11D coil, pos. 1 (b) Shielded GS-11D coil, pos. 2 (c) Shielded GS-11D coil, pos. 3

Figure 11: The measurement setup of the GS-11D coil without spring suspension and magnet.

As expected, interference is visible at 50 Hz and harmonic frequencies. At position three, the amplitudes are smaller which could be due to the orientation of the magnetic field. These tests were

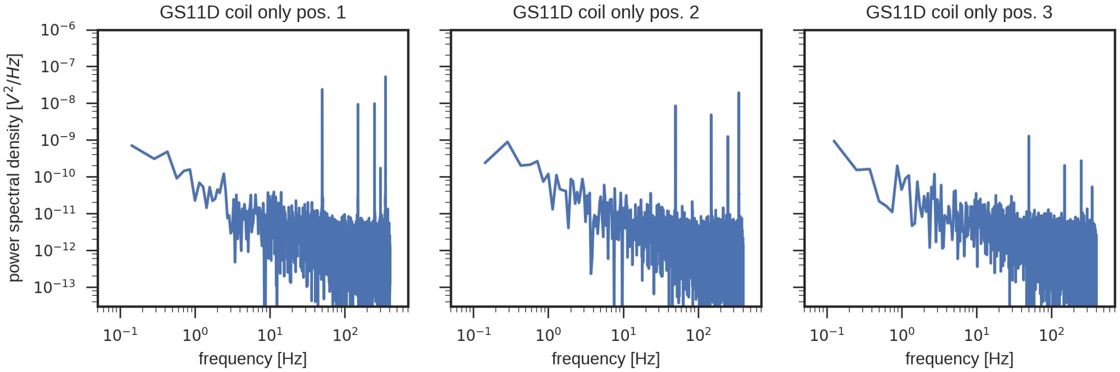

Figure 12: The power spectral densities of the GS-11D geophone coil only.

reproducible, so it's unlikely, that the difference in the amplitude of the induced noise is due to a changing strength of the magnetic field. Compared with the previous test of the simple coil it can be seen, that the amplitudes are higher and multiple harmonics are included.

GS-11D geophone

As shown by the prior test, the GS-11D geophone should interfere with the magnetic field due to the induction to the geophone coil. This signal is overlain by the ground motion picked up by the geophone. The geophone was placed at the same positions as shown in figure 11. Figure 13 shows the geophone in position 1 as an example.

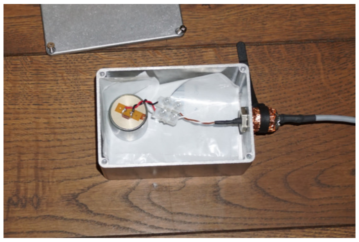

Figure 13: The GS-11D geophone in position 1.

The power spectral densities in figure 14 show the same frequency peaks as in the test of the GS-11D coil only overlain by the characteristic of the ground motion picked up by the geophone.

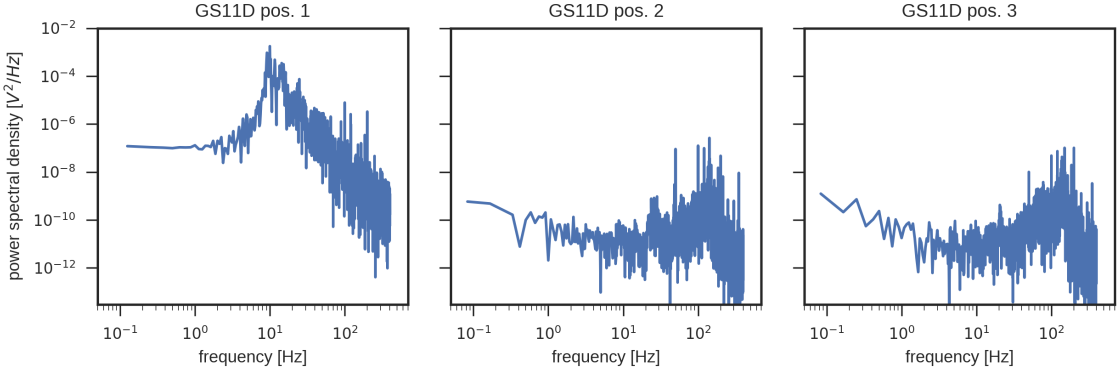

Figure 14: The power spectral densities of the GS-11D geophone.

Sensor cable shield connection

The connection of the sensor cable shield to a shielded system (a data recorder or a sensor) is a frequent topic of discussion. Is an all around connection important or is a simple pig tail connection sufficient.

I have tested these options using a 3.9 k Ohm resistor as the test sensor. Section Shielding the sensor and the sensor cable showed, that this sensor only picks up interference from the electric field and it can be completely shielded using a Faraday cage.

Three connection options were tested: a completely disconnected cable shield, a shield connection using a simple wire, and the same wire connection but with a longer part of the unshielded cable exposed. The three situations are shown in figure 15 and the corresponding power spectral densities in figure 16.

As expected, a disconnected shield resulted in 50 Hz and harmonics noise. This can be removed by the connection of the cable shield to the sensor shield using a simple cable connection. No all around connection is mandatory. If the part of the unshielded cable gets larger, the same wire connection doesn't shield the complete interference of the electric field.

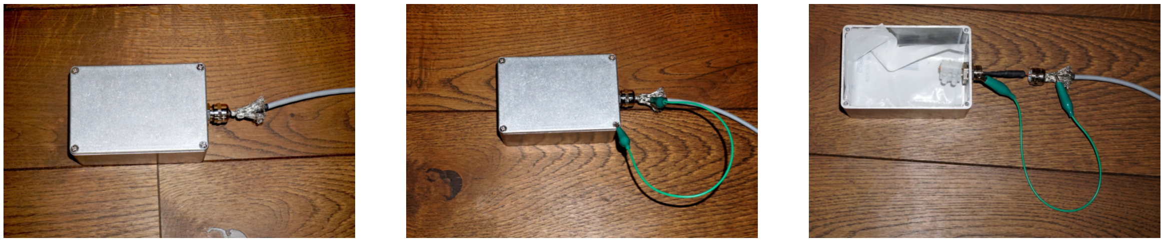

(a) Shielded GS-11D coil, pos. 1

(b) Shielded GS-11D coil, pos. 2

(c) Shielded GS-11D coil, pos. 3

Figure 15: The measurement setup of 3 different shield connections.

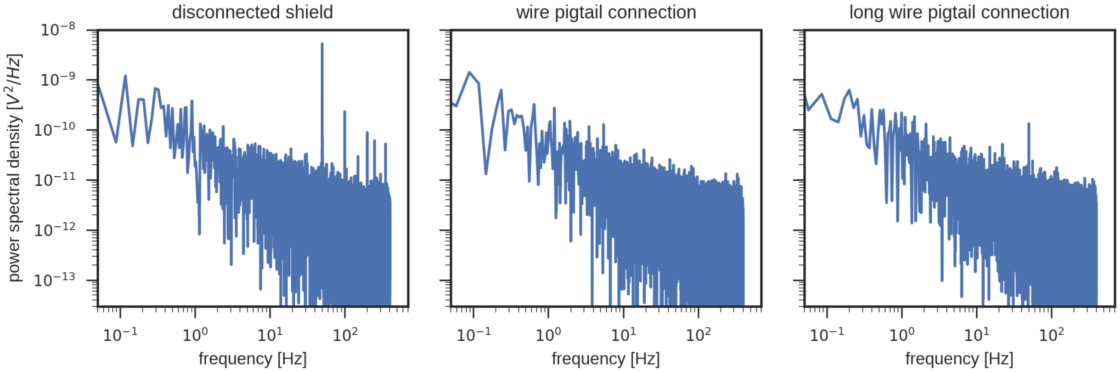

Figure 16: The power spectral densities of the tested 3 shield connections.

The shielded Ruwai recording system

With the findings of the accomplished tests, the Ruwai data recorder itself and the cable and sensors where shielded to improve the electromagnetic compatibility of the recording system. This resulted in a major improvement of the data quality for stations located nearby mains power supply. The only remaining part of the electromagnetic interference is the one originating from the quasi-stationary magnetic field.

As an example, the waveform data and power spectral density of the shielded recording system installed at the station STO at the foot of mount Hoher Sonnblick is shown in figure 17. Compared to the unshielded data in figure 3 the improvement is obvious. The general noise level is lowered by the factor 100 and the step-like disturbances are eliminated.

Although the shielding and grounding measures reduced the noise at the station STO, the noise remained at the stations at Kitzsteinhorn after applying the same changes to the Ruwai units. The grounding situation seems to be different at Kitzsteinhorn compared to the station STO. The noise situation will be evaluated on site to take proper counter measurements.

An important task to improve the insensitivity of the Ruwai to external mains power supply noise will be to identify the entry point of this noise into the system. This information is indispensable to apply selective improvements to the circuit design of the Ruwai Arduino stack.

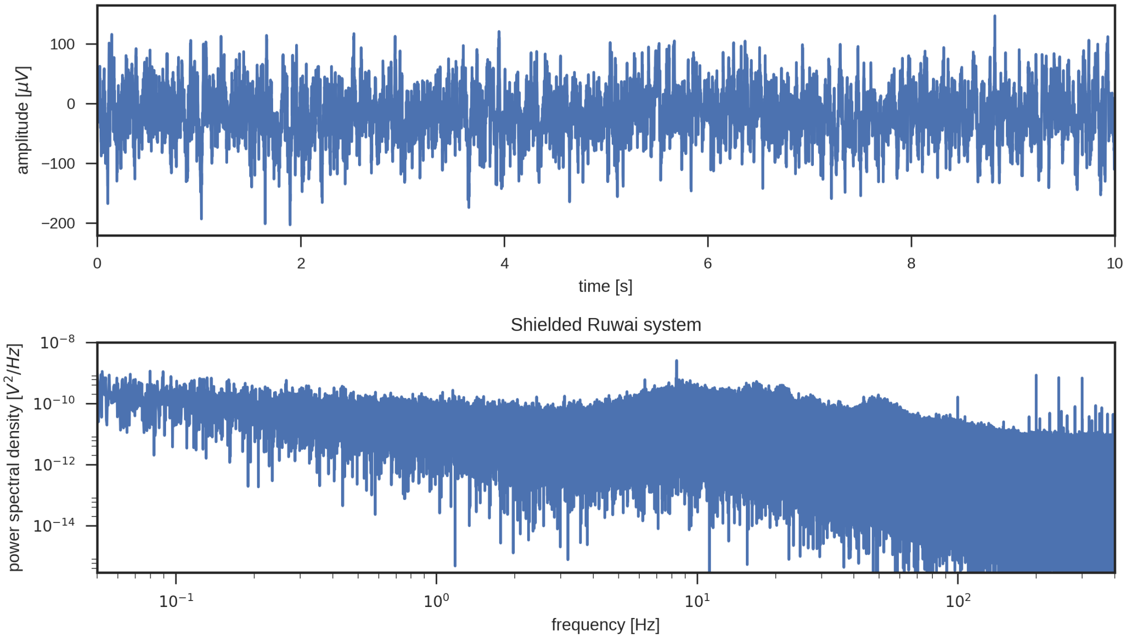

Figure 17: The example data of the recordings at station STO at Hoher Sonnblick with an shielded recording system. 10 seconds of the waveform data (top) and the power spectral density of a 1 hour recording (bottom) is shown.

References

Adolf J. Schwab and Wolfgang Kürner. *Elektromagnetische Verträglichkeit*. Springer Berlin Heidelberg, 5 edition, 2007. ISBN 978-3-540-42004-0.

Hans A. Wolfersperger. *Elektromagnetische Schirmung*. VDI-Buch. Springer Berlin Heidelberg, Berlin, Heidelberg, 2008. ISBN 978-3-540-76912-5 978-3-540-76913-2.

PUBLISHED BY MERTL RESEARCH GMBH
KIENMAYERGASSE 22, 1140 VIENNA, AUSTRIA, FB-NR.: 378631 K

http://www.mertl-research.at

This work was funded by the Austrian Academy of Sciences within the project SeisRockHT.

Appendix E: Miscellaneous

→Pelicase 1200 Mast Mount

→Station Service Sheet

→Ruwai Service Script

→Ruwai Service Script Terminal Output

→High-Capacity Battery Pack

Pelicase 1200 Mast Mount

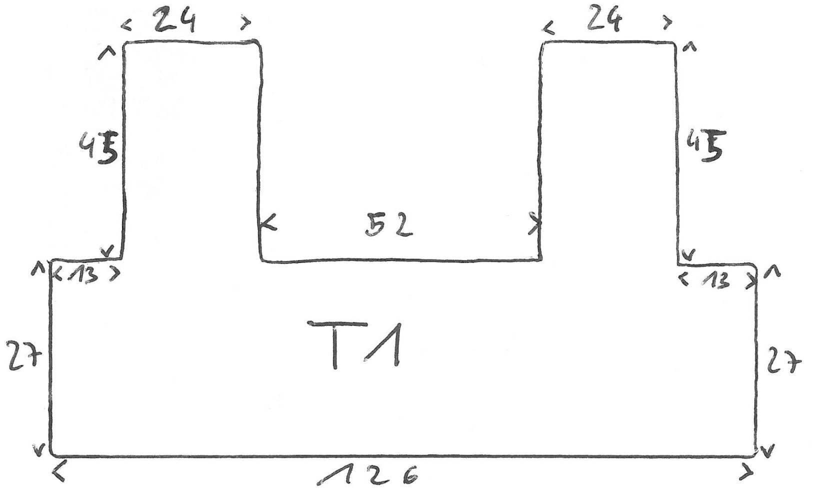
24
24
45
45
52
13
13
27
27
T1
126

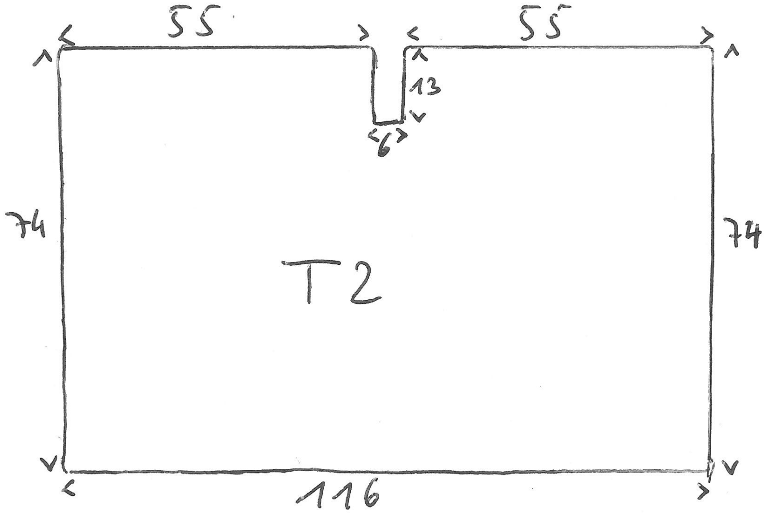
55
55
13
6
74
74
T2
116

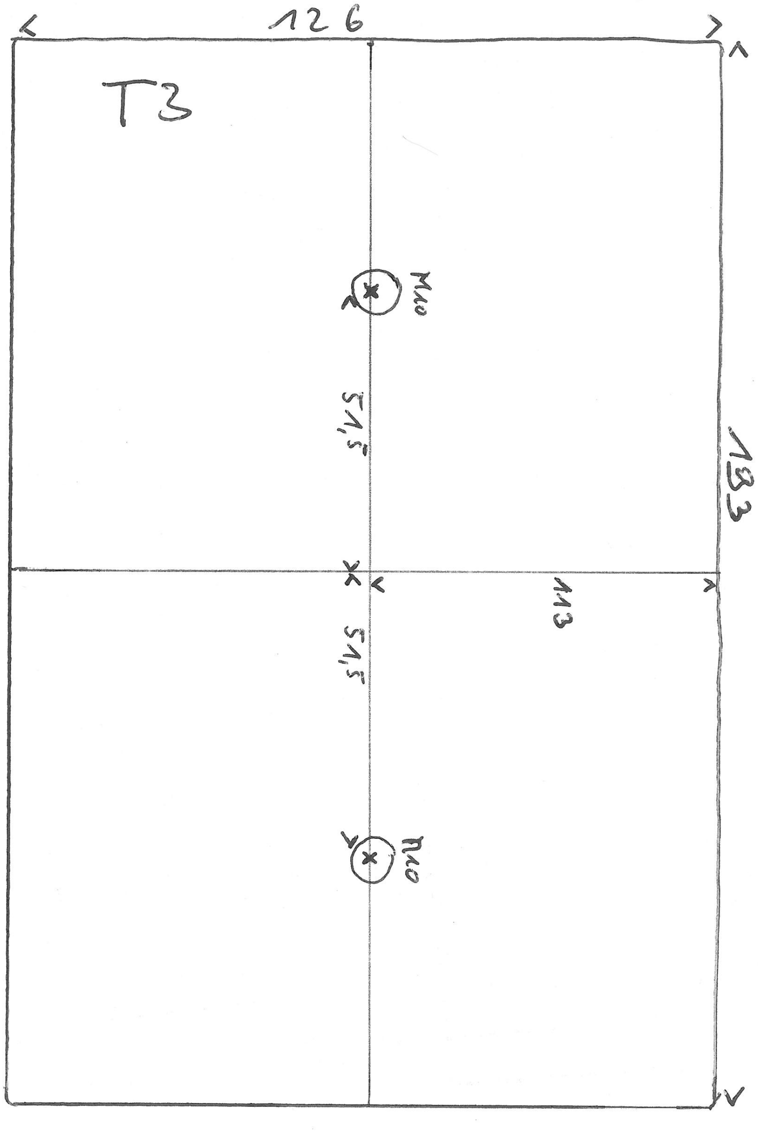
126
T3
M10
51,5
133
113
51,5
M10

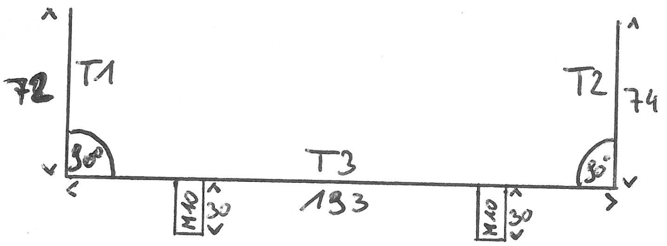
72
T1
T2
74
30°
30°
T3
193
M10
30
M10
30

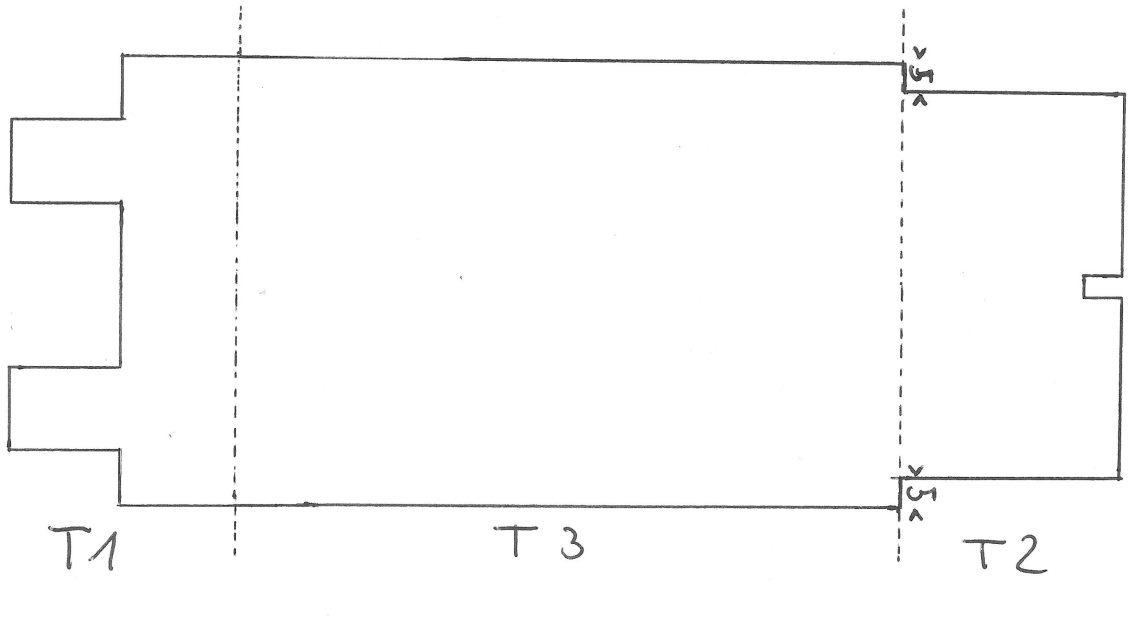
41
41
T1
T 3
T 2

INNENMAßE

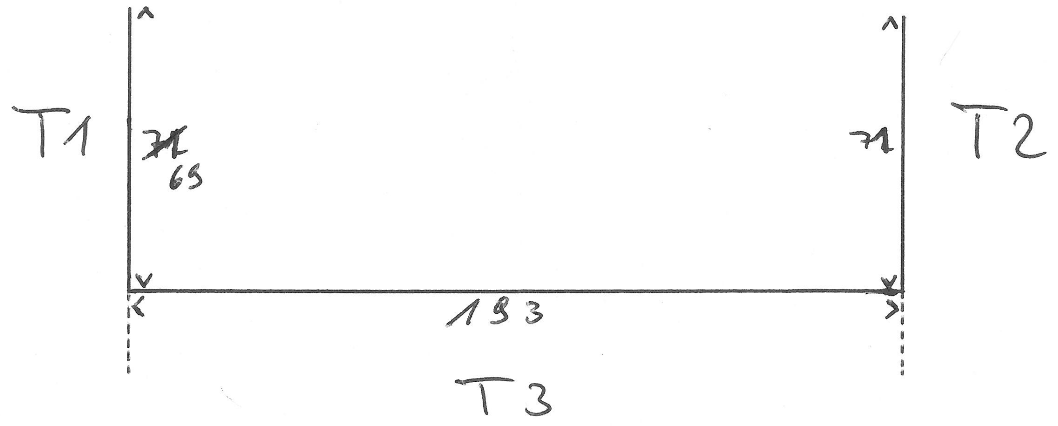

LASCHEN

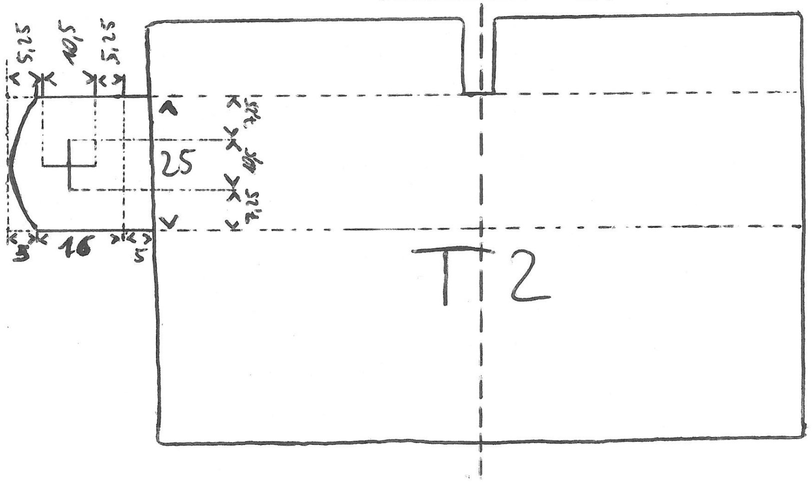

LASCHENWINKEL

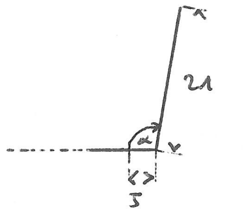

$\alpha = 100°$

Station Service Sheet

Ruwai Service Sheet (v1.1)

PROJECT	**DATE**	**LOCAL TIME**	**WEATHER**
STATION	**SERIAL NUMBER**	**SERVICE TEAM**	

ON ARRIVAL

Power		**Ruwai Logging**	
☐ *on*	☐ *off*	☐ *yes*	☐ *no*
Battery Voltage	**Without Charging Device**	**Fuses (T/10A)**	**In Stock**
		checked	

DISK SWAP

Power Off the Ruwai Logger		*checked*	
OLD DISK OUT		**NEW DISK IN**	
Serial Number	**Used Disk Space [GB]**	**Serial Number**	**Used Disk Space [GB]**
	/		/
Power On the Ruwai Logger		*checked*	

CHECK		**NOTES**
Battery Connections	*checked*	
Solar Regulator	*checked*	
Cable Conditions	*checked*	
Solar Panel ☐ **Battery Charger** ☐	*checked*	
GPS Antenna	*checked*	
Water Penetration	*checked*	

BEFORE LEAVING

Run Script (ruwai_check_*.sh) And Check Log File (ruwai_check.log):

1. remove all saved keys for 192.168.20.100:

ssh-keygen -f “/home/seisrock/.ssh/known_hosts” -R 192.168.20.100

2. Establish ssh-connection (**ssh ruwai@192.168.20.100**).Confirm connection and exit.

3. run **./ruwai_check_*.sh** in **/home/data/*/ServiceRuns/20*/.**

-> if not possible:

(Re-)Establish ssh-connection. Copy and check **/var/log/ruwai.log** *and* **/home/ruwai/ruwaicom/mseed_tmp/.***)*

☐ *Log File Active* ☐ *SD CARD STATUS* ☐ *GPS STATUS* ☐ *UTC STATUS* ☐ *Ruwai Logging*

Shake Test	*checked*	
Logging Files Saved (*.msd, ruwai.log)	*checked*	
Padlocked	*checked*	

NOTES:

Ruwai Service Script

```
#!/bin/sh

#checks data flow of ruwai datalogger
#saves mseed_tmp/, ruwai.log and ruwai_check.log on the computer
#ruwai logger IP adress: 192.168.20.100
#Required packages: sshpass
#Ruwai Serial Nrs.:     SBK:    OBS     00006
#                               PIL     0000B
#                               MOR     00009
#                               MIT     00008
#                               STO     00004
#
#                       KITZ:   BH1     00007
#                               BH2     0000A
#                               BH3     00005
#
#Daniel Binder, 16.01.2017
#edited:        September/October 2018


#remove authentication key
ssh-keygen -f "/home/seisrock/.ssh/known_hosts" -R 192.168.20.100

#establish ssh-connection and exit to get over host key verification
#ssh -o StrictHostKeyChecking=no ruwai@192.168.20.100
#exit


#create current timestamp
ymd=`date +%Y%m%d`
d="$ymd"

#check if current service run folder exists, if not it's created
if [ ! -d "sr$d" ]; then
        mkdir sr$d
fi

#jump into folder
cd sr$d

#move stdout into log-file and stderr into /dev/null
#exec > >(tee -i ruwai_check_Sbk.log)
exec 1>ruwai_check.log
#exec 2>/dev/null

#print date and produce timestamp for 'grep'-query
d=`date`
echo "\n$d:"
md=`date +'%b %d'`
d1="$md"

#check and print ruwaicom process id
#ssh-connection without host authentication
p=`sshpass -p "pfauenauge" ssh -o StrictHostKeyChecking=no ruwai@192.168.20.100 'pid
of ruwaicom'`
echo "\nProcess ID - ruwaicom: $p"

#download mseed_tmp/ and ruwai.log/ ruwai.log-* files
sshpass -p "pfauenauge" scp -r ruwai@192.168.20.100:/home/ruwai/ruwaicom/mseed_tmp .
sshpass -p "pfauenauge" scp ruwai@192.168.20.100:/var/log/ruwai.log .
sshpass -p "pfauenauge" scp ruwai@192.168.20.100:/var/log/ruwai.log-* .

#check sd card status with ruwaicom process id
tmp1=`cat ruwai.log | grep -a "ruwaicom\[$p\].*SD" | tail -n 10`
tmp11=`cat ruwai.log-* | grep -a "ruwaicom\[$p\].*SD" | tail -n 10`
echo "\n---------------------------------------------------------------------------"
echo "SD CARD STATUS:"
echo "---------------------------------------------------------------------------"
echo "$tmp11"
echo "$tmp1"

#check GPS status with ruwaicom pid
#d3="$d1.*GPS_FIX"
```

```
#tmp2=`cat ruwai.log | grep "$d3"`
tmp2=`cat ruwai.log | grep -a "ruwaicom\[$p\].*GPS_FIX" | tail -n 10`
tmp21=`cat ruwai.log-* | grep -a "ruwaicom\[$p\].*GPS_FIX" | tail -n 10`
echo "\n--------------------------------------------------------------------------"
echo "GPS STATUS:"
echo "--------------------------------------------------------------------------"
echo "$tmp21"
echo "$tmp2"

#UTC status over actual date
#d4="$d1.*UTC_AVAILABLE"
#tmp3=`cat ruwai.log | grep "$d4"`
tmp3=`cat ruwai.log | grep -a "ruwaicom\[$p\].*UTC_AVAILABLE" | tail -n 10`
tmp31=`cat ruwai.log-* | grep -a "ruwaicom\[$p\].*UTC_AVAILABLE" | tail -n 10`
echo "\n--------------------------------------------------------------------------"
echo "UTC STATUS:"
echo "--------------------------------------------------------------------------"
echo "$tmp31"
echo "$tmp3"

#last log-file output
tmp4=`cat ruwai.log | grep -a "ruwaicom\[$p\]" | tail -n 10`
tmp41=`cat ruwai.log-* | grep -a "ruwaicom\[$p\]" | tail -n 10`
echo "\n--------------------------------------------------------------------------"
echo "LAST LOG-FILE OUTPUT:"
echo "--------------------------------------------------------------------------"
echo "$tmp41"
echo "$tmp4"

#check size of mseed_tmp/ and ruwai.log and wait 10 sec
fs1=`du ./mseed_tmp | cut -f1`
echo "\n\nCurrent mseed_tmp/ size $fs1 kB. \n"
fs11=`du ./ruwai.log | cut -f1`
echo "Current ruwai.log size $fs11 kB. \n"
fs12=`du ./ruwai.log-* | cut -f1`
echo "Current ruwai.log-* size $fs12 kB. \n\n"
sleep 10s

#re-download mseed_tmp/ and ruwai.log and check size
sshpass -p "pfauenauge" scp -r ruwai@192.168.20.100:/home/ruwai/ruwaicom/mseed_tmp .
sshpass -p "pfauenauge" scp ruwai@192.168.20.100:/var/log/ruwai.log .
sshpass -p "pfauenauge" scp ruwai@192.168.20.100:/var/log/ruwai.log-* .
fs2=`du ./mseed_tmp | cut -f1`
echo "\nCurrent mseed_tmp/ size $fs2 kB. \n"
fs21=`du ./ruwai.log | cut -f1`
echo "Current ruwai.log size $fs21 kB. \n"
fs22=`du ./ruwai.log-* | cut -f1`
echo "Current ruwai.log-* size $fs22 kB. \n\n"

#check if mseed_tmp/ size is increasing -> ruwai is logging
if [ $fs2 -gt $fs1 ]; then
        echo "--------------------------------------------------------------------------"
        echo "\nRuwai IS logging :) \n"
        echo "--------------------------------------------------------------------------\n"
else
        echo "--------------------------------------------------------------------------"
        echo "\nRuwai ISN'T logging :( \n"
        echo "--------------------------------------------------------------------------\n"
fi

#check ruwai datafile system and list all folders under /media/sd/mseed/`date +%Y`
sshpass -p "pfauenauge" ssh ruwai@192.168.20.100 'df -h'

echo "\n--------------------------------------------------------------------------"
echo "$(date +%Y%m%d) -> doy $(date +%j)"
echo "Content /media/sd/mseed/$(date +%Y):"
echo "--------------------------------------------------------------------------"
sshpass -p "pfauenauge" ssh ruwai@192.168.20.100 "ls /media/sd/mseed/$(date +%Y)"
```

```
#Assign data: check ruwai serial-nr., create station directory and move data into di
rectory
if ls mseed_tmp/*00006_00*>/dev/null; then
        echo "----------------------------------------------------------------------
----"
        if [ ! -d "OBS" ]; then
                mkdir OBS
                echo "\nCreated OBS-folder. \n"
        fi
        cp -r ./mseed_tmp/ ./OBS/
        rm -rf ./mseed_tmp/
        mv ./ruwai.log ./OBS/
        mv ./ruwai.log-* ./OBS/
        echo "\nData dumped in OBS-folder. \n"
        mv ./ruwai_check.log ./OBS/

elif ls mseed_tmp/*0000B_00*>/dev/null; then
        echo "----------------------------------------------------------------------
----"
        if [ ! -d "PIL" ]; then
                mkdir PIL
                echo "\nCreated PIL-folder. \n"
        fi
        cp -r ./mseed_tmp/ ./PIL/
        rm -rf ./mseed_tmp/
        mv ./ruwai.log ./PIL/
        mv ./ruwai.log-* ./PIL/
        echo "\nData dumped in PIL-folder. \n"
        mv ./ruwai_check.log ./PIL/

elif ls mseed_tmp/*00009_00*>/dev/null; then
        echo "----------------------------------------------------------------------
----"
        if [ ! -d "MOR" ]; then
                mkdir MOR
                echo "\nCreated MOR-folder. \n"
        fi
        cp -r ./mseed_tmp/ ./MOR/
        rm -rf ./mseed_tmp/
        mv ./ruwai.log ./MOR/
        mv ./ruwai.log-* ./MOR/
        echo "\nData dumped in MOR-folder. \n"
        mv ./ruwai_check.log ./MOR/

elif ls mseed_tmp/*00008_00*>/dev/null; then
        echo "----------------------------------------------------------------------
----"
        if [ ! -d "MIT" ]; then
                mkdir MIT
                echo "\nCreated MIT-folder. \n"
        fi
        cp -r ./mseed_tmp/ ./MIT/
        rm -rf ./mseed_tmp/
        mv ./ruwai.log ./MIT/
        mv ./ruwai.log-* ./MIT/
        echo "\nData dumped in MIT-folder. \n"
        mv ./ruwai_check.log ./MIT/

elif ls mseed_tmp/*00004_00*>/dev/null; then
        echo "----------------------------------------------------------------------
----"
        if [ ! -d "STO" ]; then
                mkdir STO
                echo "\nCreated STO-folder. \n"
        fi
        cp -r ./mseed_tmp/ ./STO/
        rm -rf ./mseed_tmp/
        mv ./ruwai.log ./STO/
        mv ./ruwai.log-* ./STO/
        echo "\nData dumped in STO-folder. \n"
        mv ./ruwai_check.log ./STO/

elif ls mseed_tmp/*00007_00*>/dev/null; then
```

```
        echo "----------------------------------------------------------------------
----"
        if [ ! -d "BH1" ]; then
                mkdir BH1
                echo "\nCreated BH1-folder. \n"
        fi
        cp -r ./mseed_tmp/ ./BH1/
        rm -rf ./mseed_tmp/
        mv ./ruwai.log ./BH1/
        mv ./ruwai.log-* ./BH1/
        echo "\nData dumped in BH1-folder. \n"
        mv ./ruwai_check.log ./BH1/

elif ls mseed_tmp/*0000A_00*>/dev/null; then
        echo "----------------------------------------------------------------------
----"
        if [ ! -d "BH2" ]; then
                mkdir BH2
                echo "\nCreated BH2-folder. \n"
        fi
        cp -r ./mseed_tmp/ ./BH2/
        rm -rf ./mseed_tmp/
        mv ./ruwai.log ./BH2/
        mv ./ruwai.log-* ./BH2/
        echo "\nData dumped in BH2-folder. \n"
        mv ./ruwai_check.log ./BH2/

elif ls mseed_tmp/*00005_00*>/dev/null; then
        echo "----------------------------------------------------------------------
----"
        if [ ! -d "BH3" ]; then
                mkdir BH3
                echo "\nCreated BH3-folder. \n"
        fi
        cp -r ./mseed_tmp/ ./BH3/
        rm -rf ./mseed_tmp/
        mv ./ruwai.log ./BH3/
        mv ./ruwai.log-* ./BH3/
        echo "\nData dumped in BH3-folder. \n"
        mv ./ruwai_check.log ./BH3/

else
        echo "----------------------------------------------------------------------
----"
        echo "\nRuwai Serial Number doesn't fit any station! \n"
        if [ ! -d "tmp" ]; then
                mkdir tmp
                echo "\nCreated tmp-folder. \n"
        fi
        cp -r ./mseed_tmp/ ./tmp/
        rm -rf ./mseed_tmp/
        mv ./ruwai.log ./tmp/
        mv ./ruwai.log-* ./tmp/
        echo "\nData dumped in tmp-folder. \n"
        mv ./ruwai_check.log ./tmp/
fi
```

Ruwai Service Script Terminal Output

The terminal output is also saved by default in the file *ruwai_ check.log* .
The following example is from the MIT station service on September 23, 2019.

```
Mon Sep 23 09:08:12 CEST 2019:

Process ID - ruwaicom: 730

--------------------------------------------------------------------------
SD CARD STATUS:
--------------------------------------------------------------------------
Nov 11 13:22:39 beaglebone ruwaicom[730]: Initial check for the SD card.
Nov 11 13:22:39 beaglebone ruwaicom[730]: [root] SD card block device found at /dev/
disk/by-label/ruwai_sd.
Nov 11 13:22:39 beaglebone ruwaicom[730]: [root] The SD card is correctly mounted at
 /media/sd.
Nov 11 13:22:39 beaglebone ruwaicom[730]: [root] The SD card is correctly mounted at
 /media/sd.
Nov 11 13:22:38 beaglebone ruwaicom[730]: Initial check for the SD card.
Nov 11 13:22:38 beaglebone ruwaicom[730]: [root] SD card block device found at /dev/
disk/by-label/ruwai_sd.
Nov 11 13:22:38 beaglebone ruwaicom[730]: [root] The SD card is correctly mounted at
 /media/sd.
Nov 11 13:22:38 beaglebone ruwaicom[730]: [root] The SD card is correctly mounted at
 /media/sd.


--------------------------------------------------------------------------
GPS STATUS:
--------------------------------------------------------------------------
Sep 22 20:45:45 beaglebone ruwaicom[730]: [add_timestamp_sample] GPS_FIX_OK changed:
 timestamp = 2019-09-22T20:45:44.810000, gps_fix = 3, gps_fix_ok = 0, utc_available
= 1
Sep 22 20:47:50 beaglebone ruwaicom[730]: [add_timestamp_sample] GPS_FIX_OK changed:
 timestamp = 2019-09-22T20:47:49.810000, gps_fix = 3, gps_fix_ok = 1, utc_available
= 1
Sep 23 03:06:06 beaglebone ruwaicom[730]: [add_timestamp_sample] GPS_FIX_OK changed:
 timestamp = 2019-09-23T03:06:04.810000, gps_fix = 3, gps_fix_ok = 0, utc_available
= 1
Sep 23 03:06:10 beaglebone ruwaicom[730]: [add_timestamp_sample] GPS_FIX_OK changed:
 timestamp = 2019-09-23T03:06:08.810000, gps_fix = 3, gps_fix_ok = 1, utc_available
= 1
Sep 23 05:12:05 beaglebone ruwaicom[730]: [add_timestamp_sample] GPS_FIX changed: ti
mestamp = 2019-09-23T05:12:03.810000, gps_fix = 2, gps_fix_ok = 1, utc_available = 1
Sep 23 05:12:09 beaglebone ruwaicom[730]: [add_timestamp_sample] GPS_FIX changed: ti
mestamp = 2019-09-23T05:12:06.810000, gps_fix = 3, gps_fix_ok = 1, utc_available = 1
Sep 23 05:30:37 beaglebone ruwaicom[730]: [add_timestamp_sample] GPS_FIX changed: ti
mestamp = 2019-09-23T05:30:34.810000, gps_fix = 2, gps_fix_ok = 1, utc_available = 1
Sep 23 05:39:40 beaglebone ruwaicom[730]: [add_timestamp_sample] GPS_FIX changed: ti
mestamp = 2019-09-23T05:39:37.810000, gps_fix = 3, gps_fix_ok = 0, utc_available = 1
Sep 23 05:39:40 beaglebone ruwaicom[730]: [add_timestamp_sample] GPS_FIX_OK changed:
 timestamp = 2019-09-23T05:39:37.810000, gps_fix = 3, gps_fix_ok = 0, utc_available
= 1
Sep 23 05:39:52 beaglebone ruwaicom[730]: [add_timestamp_sample] GPS_FIX_OK changed:
 timestamp = 2019-09-23T05:39:49.810000, gps_fix = 3, gps_fix_ok = 1, utc_available
= 1


--------------------------------------------------------------------------
UTC STATUS:
--------------------------------------------------------------------------
Sep 22 13:28:37 beaglebone ruwaicom[730]: [add_timestamp_sample] UTC_AVAILABLE chang
ed: timestamp = 2019-09-22T13:28:38.810000, gps_fix = 3, gps_fix_ok = 1, utc_availab
le = 1


--------------------------------------------------------------------------
LAST LOG-FILE OUTPUT:
--------------------------------------------------------------------------
Sep 23 06:15:20 beaglebone ruwaicom[730]: [soh][gps_pos] 12.971837, 47.061867, 2127.
614990
Sep 23 06:16:20 beaglebone ruwaicom[730]: [soh][gps_pos] 12.971818, 47.061877, 2124.
603027
Sep 23 06:17:20 beaglebone ruwaicom[730]: [soh][gps_pos] 12.971802, 47.061832, 2124.
232910
Sep 23 06:18:20 beaglebone ruwaicom[730]: [soh][gps_pos] 12.971796, 47.061806, 2122.
```

```
802002
Sep 23 06:19:20 beaglebone ruwaicom[730]: [soh][gps_pos] 12.971757, 47.061793, 2119.
875000
Sep 23 06:20:20 beaglebone ruwaicom[730]: [soh][gps_pos] 12.971774, 47.061813, 2122.
863037
Sep 23 06:21:20 beaglebone ruwaicom[730]: [soh][gps_pos] 12.971798, 47.061789, 2118.
423096
Sep 23 06:22:20 beaglebone ruwaicom[730]: [soh][gps_pos] 12.971794, 47.061774, 2115.
090088
Sep 23 06:23:20 beaglebone ruwaicom[730]: [soh][gps_pos] 12.971786, 47.061844, 2117.
822998
Sep 23 06:24:20 beaglebone ruwaicom[730]: [soh][gps_pos] 12.971789, 47.061862, 2122.
062012
Sep 23 07:00:05 beaglebone ruwaicom[730]: [copy_files] Moving file 2019_266_060000_0
0008_002.msd from tmp directory to /media/sd/mseed/2019/266/00008.
Sep 23 07:00:05 beaglebone ruwaicom[730]: [copy_files] Moving file 2019_266_060000_0
0008_003.msd from tmp directory to /media/sd/mseed/2019/266/00008.
Sep 23 07:00:20 beaglebone ruwaicom[730]: [soh][gps_pos] 12.971819, 47.061811, 2126.
812988
Sep 23 07:01:20 beaglebone ruwaicom[730]: [soh][gps_pos] 12.971778, 47.061824, 2121.
466064
Sep 23 07:02:20 beaglebone ruwaicom[730]: [soh][gps_pos] 12.971767, 47.061794, 2120.
395020
Sep 23 07:03:20 beaglebone ruwaicom[730]: [soh][gps_pos] 12.971737, 47.061830, 2118.
662109
Sep 23 07:04:20 beaglebone ruwaicom[730]: [soh][gps_pos] 12.971701, 47.061822, 2114.
606934
Sep 23 07:05:20 beaglebone ruwaicom[730]: [soh][gps_pos] 12.971762, 47.061779, 2116.
998047
Sep 23 07:06:20 beaglebone ruwaicom[730]: [soh][gps_pos] 12.971743, 47.061757, 2117.
470947
Sep 23 07:07:20 beaglebone ruwaicom[730]: [soh][gps_pos] 12.971758, 47.061819, 2121.
191895


Current mseed_tmp/ size 768 kB.

Current ruwai.log size 8 kB.

Current ruwai.log-* size 1184 kB.



Current mseed_tmp/ size 788 kB.

Current ruwai.log size 8 kB.

Current ruwai.log-* size 1184 kB.


--------------------------------------------------------------------------

Ruwai IS logging :)

--------------------------------------------------------------------------

Filesystem      Size  Used Avail Use% Mounted on
udev            217M     0  217M   0% /dev
tmpfs            49M  8.7M   41M  18% /run
/dev/mmcblk1p1  3.5G  1.9G  1.5G  56% /
tmpfs           244M     0  244M   0% /dev/shm
tmpfs           5.0M     0  5.0M   0% /run/lock
tmpfs           244M     0  244M   0% /sys/fs/cgroup
/dev/mmcblk0p1   30G  168M   28G   1% /media/sd
tmpfs            49M     0   49M   0% /run/user/1001

--------------------------------------------------------------------------
20190923 -> doy 266
Content /media/sd/mseed/2019:
--------------------------------------------------------------------------
265
266
--------------------------------------------------------------------------
```

```
Created MIT−folder.

Data dumped in MIT−folder.
```

High-Capacity Battery Pack

HOW TO build a
LOW-COST POWER PACK (12 V, ~300 Ah)

@ Daniel Binder
daniel.binder@zamg.ac.at
Salzburg, August 2019

Material Costs:
~ € 850 – 900.- (→ 4x AGM Nitro Cyclic LPC12-75 Batteries included)

Bill of Materials:

1x	Used Zarges A5 Box (available at e.g. ebay for € 100 - 200.-)
4x	Batteries (~75 Ah)
	→ AGM Nitro Cyclic LPC12-75 (~€ 160.-, L x W x H: 259 x 168 x 214 mm)
	→ Banner DB72 FT (~€ 250.-, L x W x H: 260 x 171 x 210 mm)
1x	Phocos Eco 10 Solar Regulator (Max. Charge/ Load Current 10 A)
1x	Insulation Board (Thickness: 20 mm)
2x	Rubber Pad (L x W x H: 550 x 360 x 3 mm)
(8x	Battery Pole Insulation Caps → see section 7)
4x	M3 x 30 Screws + Nuts
8x	M3 Spring Washers
4x	M3 Distance Sleeves (Length: 16 mm)
1x	M20 Cable Gland (Solar Panel Power Cable Inlet)
1x	M12 Cable Gland (Load Power Cable Outlet)
1x	Transparent Silicone Sealant
1x	Electric Wire (Length ~250 cm, Diameter ~1.5 mm²)
1x	Wire Fuse Casing + Fuse (e.g. 10 A, Speed T)
10x	M6 Ring Tongue

Bill of Tools:
Drill
Drill Bits (3, 4, 12, 20 mm)
Utility Knife
Fine Toothed Saw (e.g. Jab/ Hack Saw)
Dispenser Gun + Silicone Sealant Cartridge
Screw Driver
Wire Crimp Tool
Ratchet and Socket Set
Rivet plier including 4 mm rivets

NOTE: Max. charge/load current of built-in solar regulator is 10 A. Consequently, the maximum power of the optionally connected solar panel must be smaller than 120 W.

1. Preparing the Zarges A5 Box

→ Old ‘Deutsche Bundeswehr’ Version (Construction Period ~1960-1980)
- Outside Dimensions (L x W x H): 600 x 400 x 250 mm
- Inside Dimensions (L x W x H): 530 x 340 x 210 mm

→ In case, remove installations inside the box (drill out the rivets and seal the holes with e.g. new rivets).

- The sharp-edged aluminum mounting pieces for the lid-support strap is a very likely source for short circuits (at least for the AGM Nitro Cylic LPC12-75 battery).

- Drill out the rivets with the 4 mm drill bit and seal the holes with new rivets.

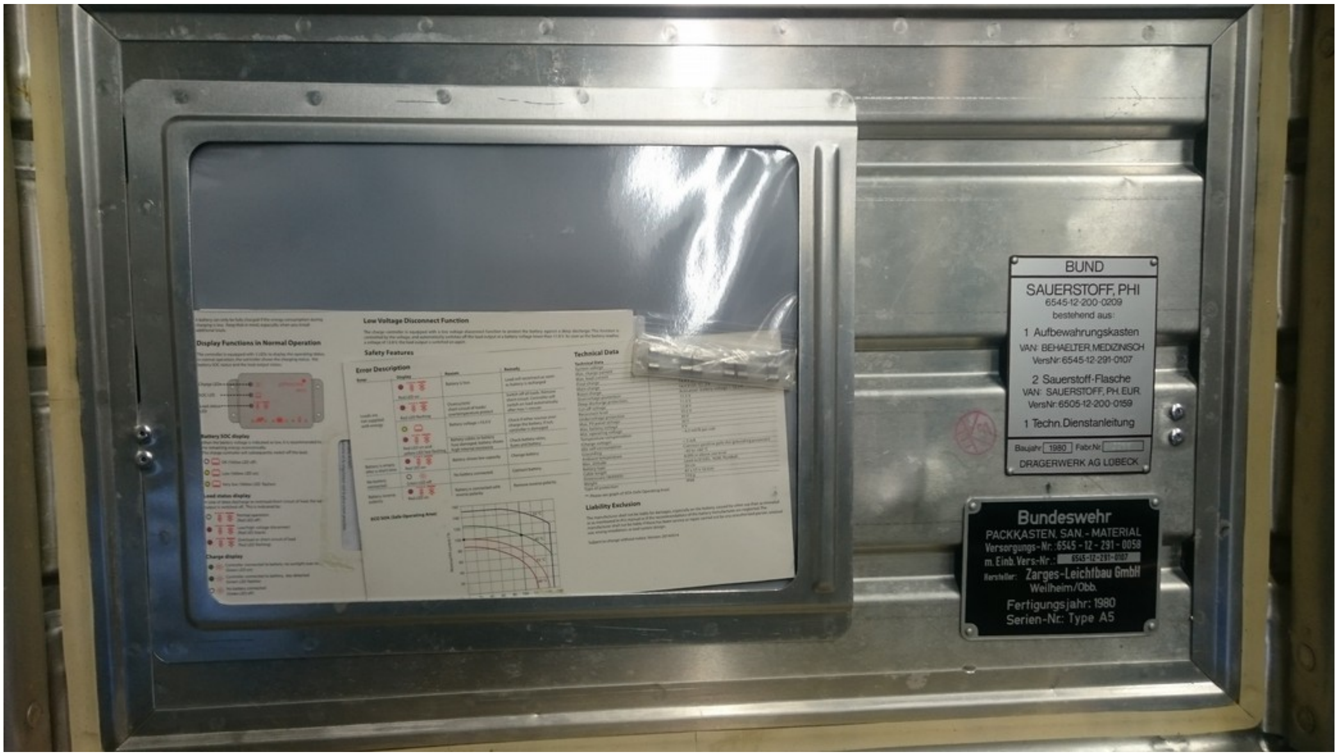

2. Mounting the Phocos Eco 10 Solar Regulator

- Place it at the top front corner of one of the side walls. Mark the two mounting holes facing towards the box center and drill the holes with the 3 mm drill bit.

- Fix the solar regulator outside the box. Mark and drill the other two holes.

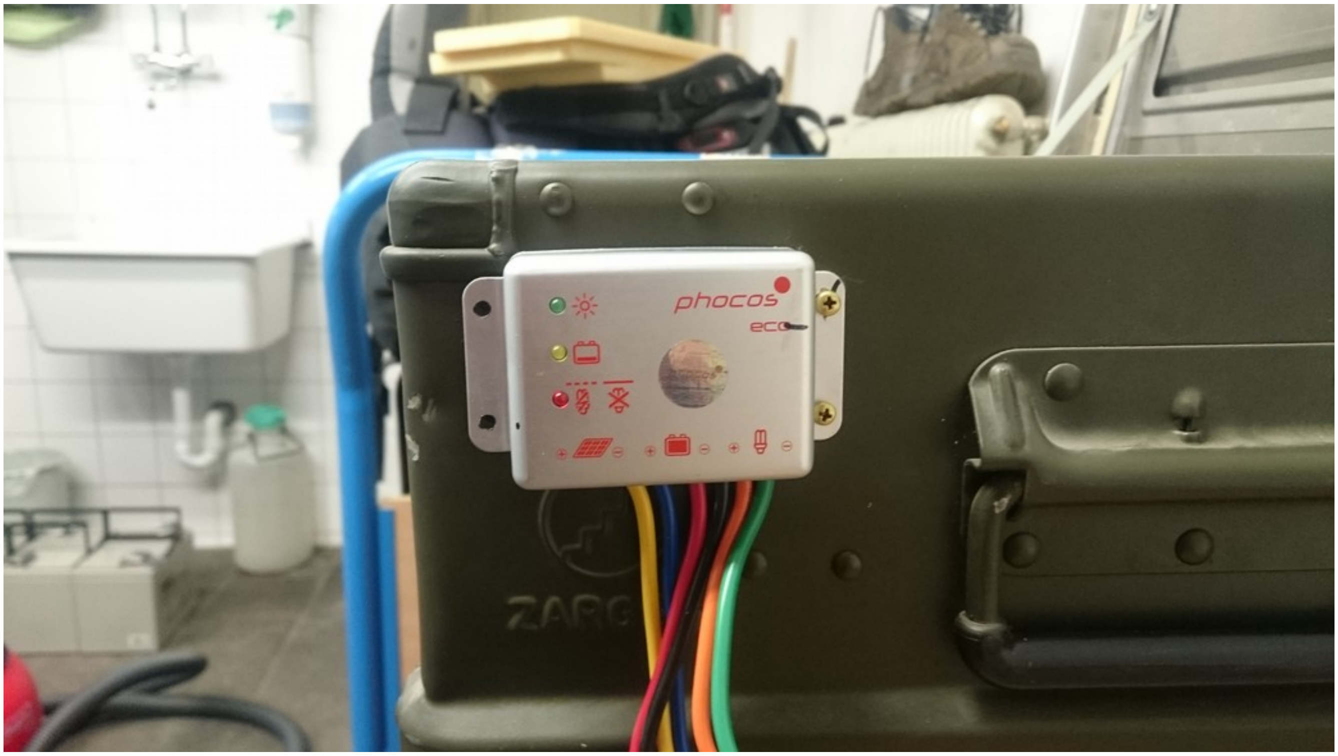

- Fix the solar regulator template and drill the LED-holes with the 4 mm drill bit.
→ The Phocos Eco 10 solar regulator template can be found at the end of this document.

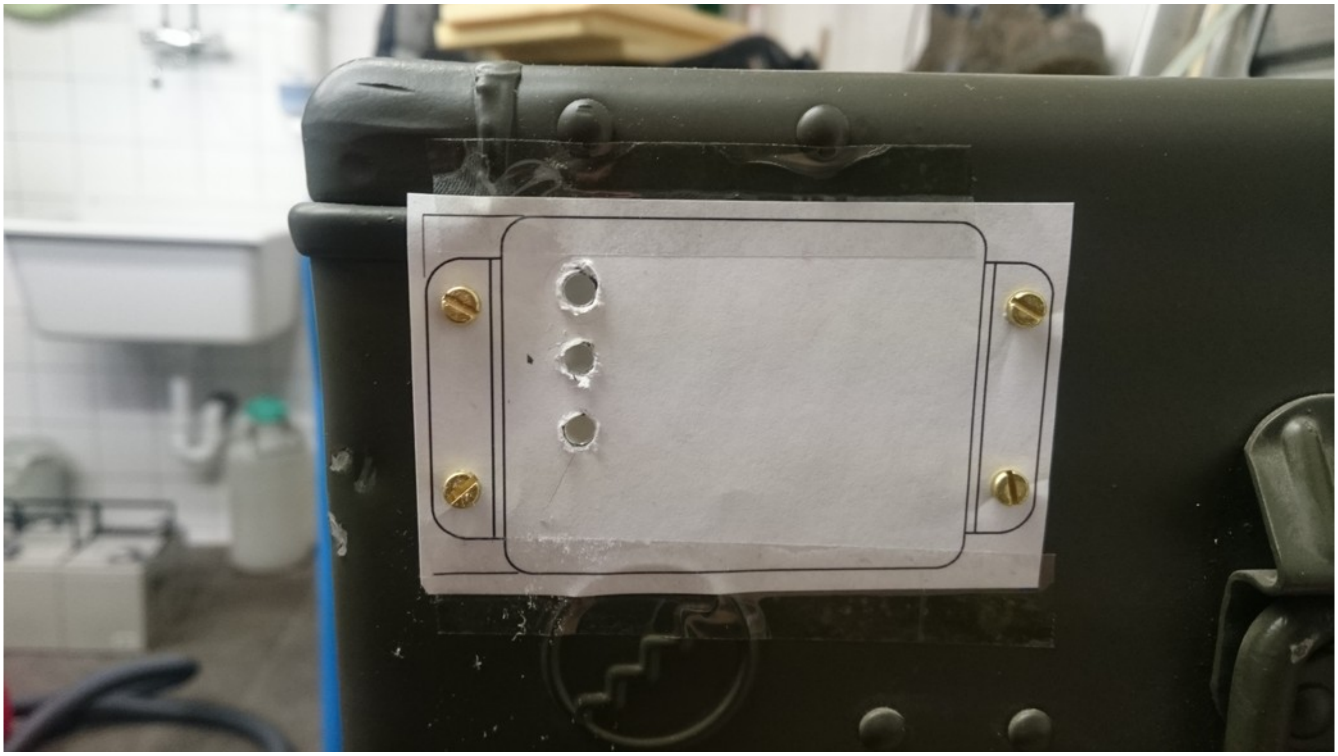

- Mount the solar regulator with the M3x30 screws, distance sleeves and spring washers.

- Trim the screws.

- Seal up the screw and LED holes with the transparent silicone adhesive.

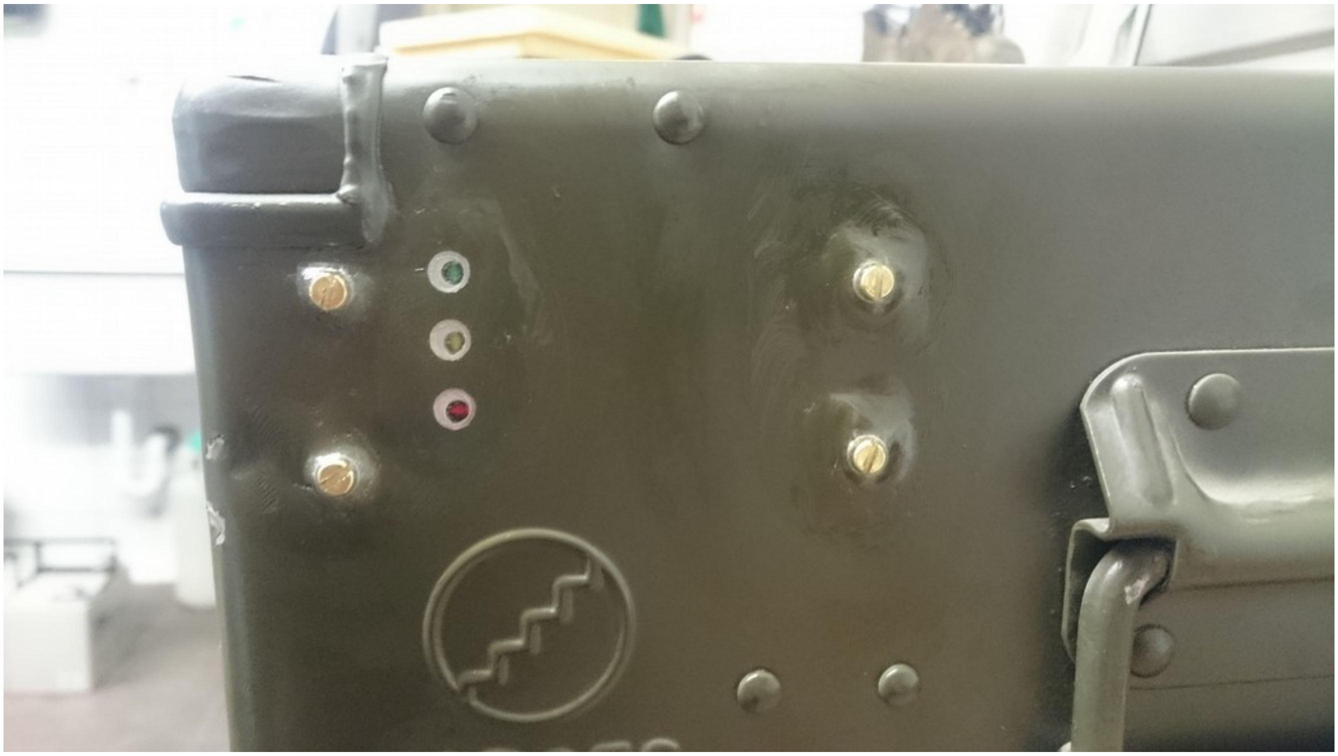

3. Installing Cable Glands

→ E.g. a 20 mm cable gland for the incoming solar panel power cable, and a 12 mm cable gland for the outgoing load power cable.
→ The 20 mm drill hole center is placed 60 mm inwards from the top and the side edge, respectively.

4. Cutting Out the Insulation Side Walls

2x	570 x 190 mm
→ Cut out 60 x 20 mm at one corner of a board (‘solar regulator notch’)
1x	335 x 190 mm

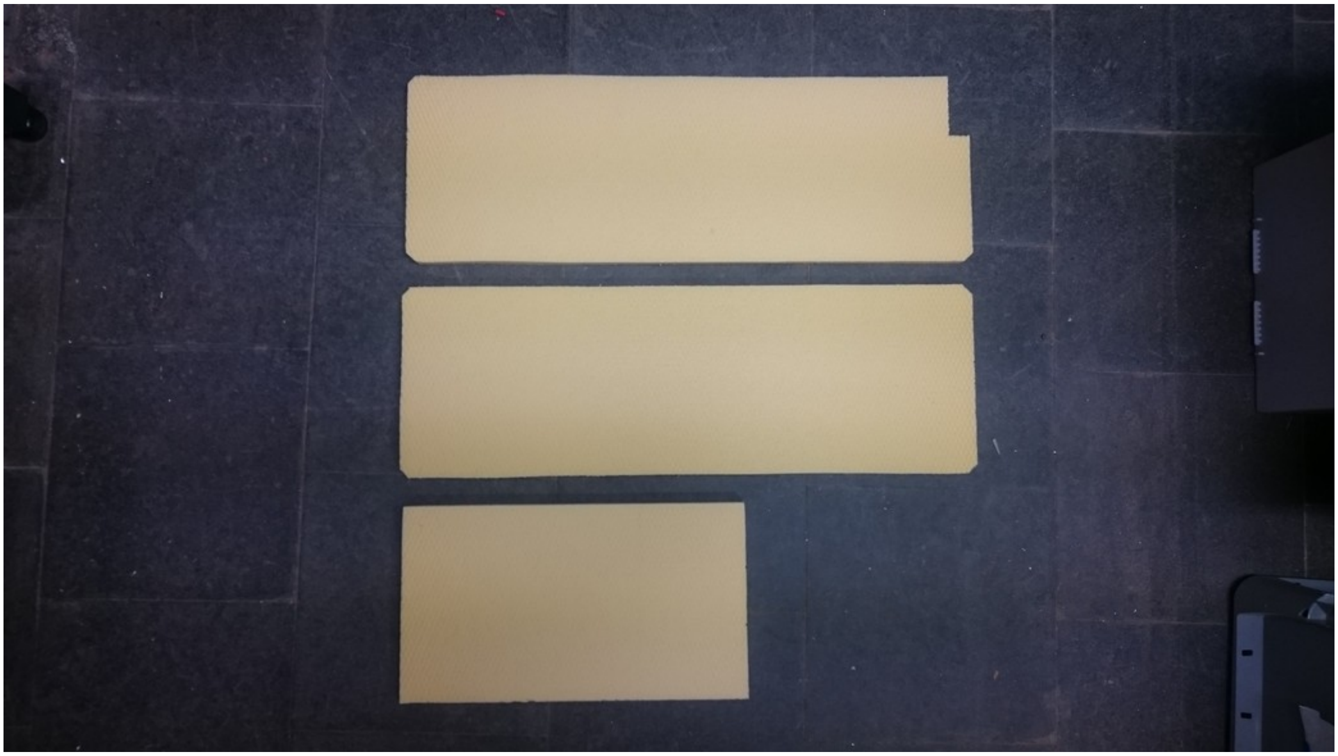

- Place a rubber pad at the bottom of the box and arrange the insulation walls.
→ bottom rubber pad might need to be left away if e.g. solid battery pole caps are used for electric insulation (see section 7) and box lid can’t be closed anymore.

5. Wiring

- Extend the solar regulator battery connections by ~300 mm and insert the fuse casing on the wire connecting the positive battery contact.

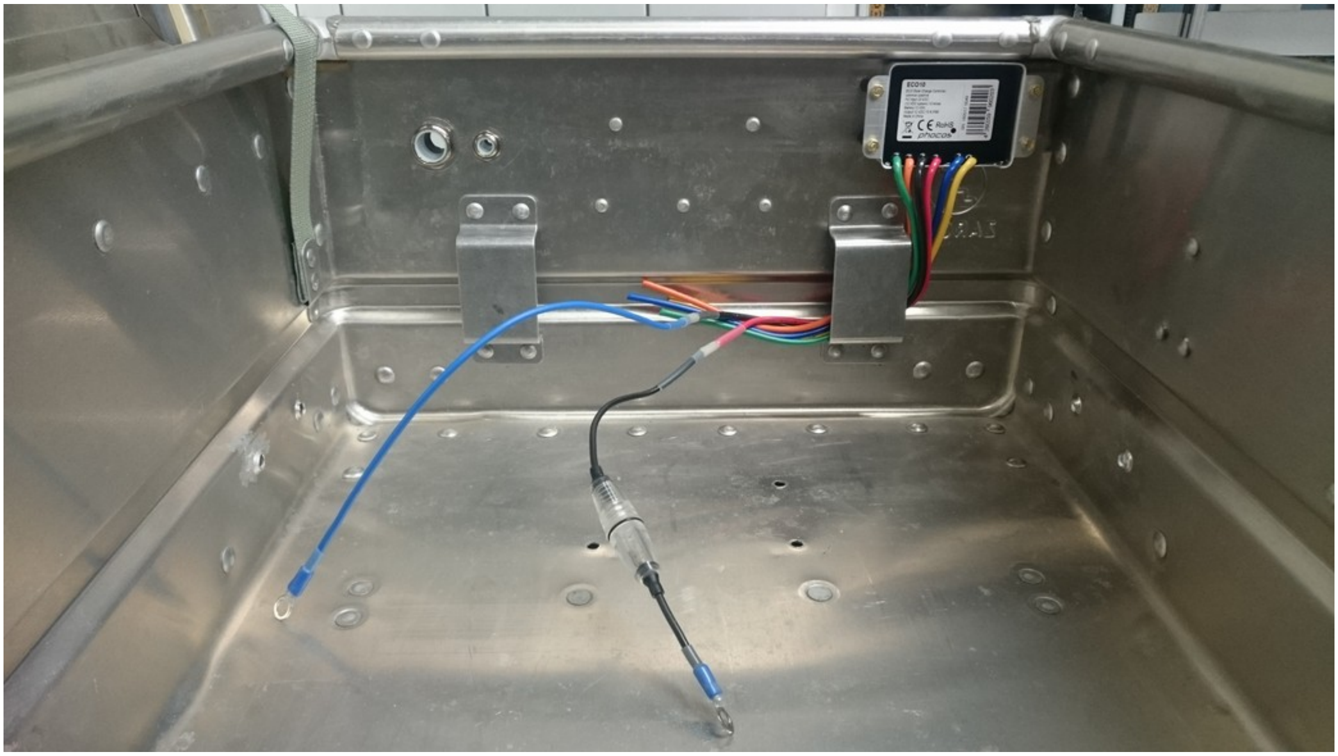

- Prepare the battery connection wires. The single wire length is about 280 mm.

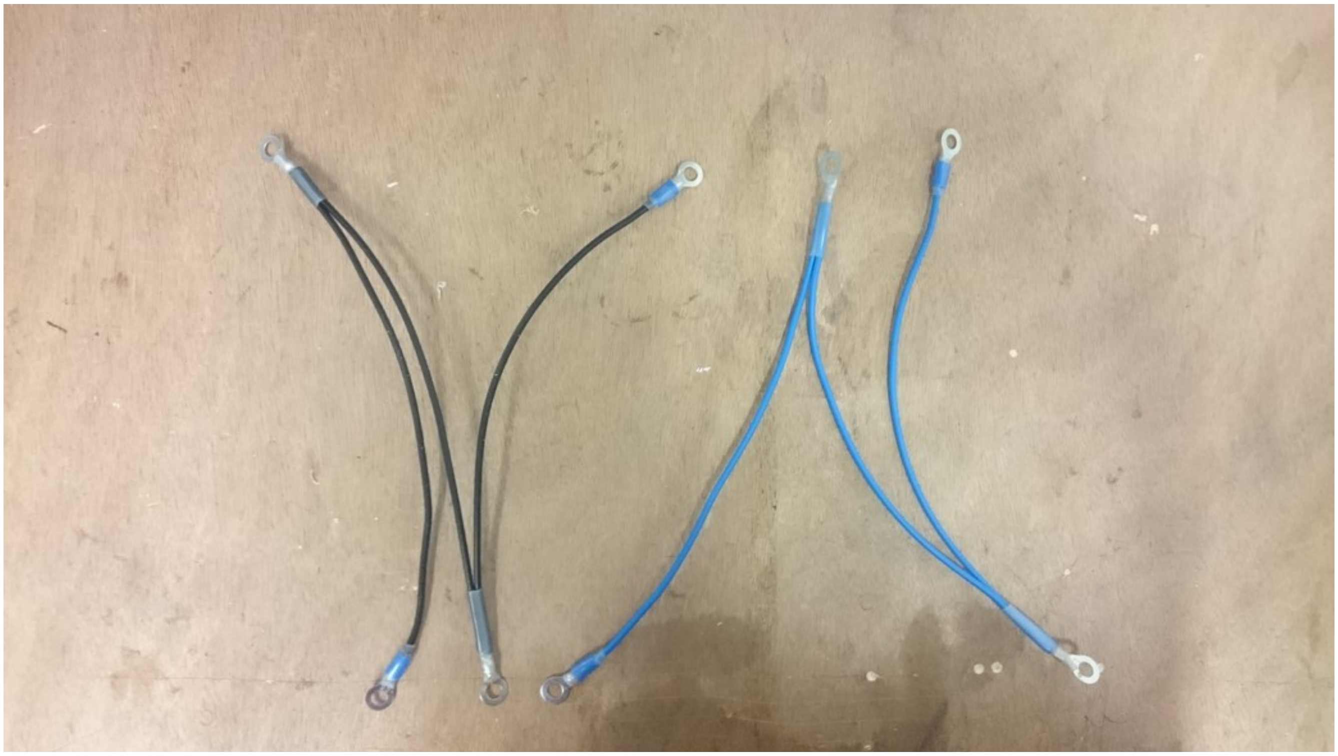

- Place the four batteries in the box, switch them in parallel, and connect the solar regulator battery wires. The photo shows the box with four AGM Nitro Cylic LPC12-75 batteries. Banner DB72 FT batteries would work as well.

→ Note on the wiring

An optimum wiring prolongs the power pack lifetime. This is achieved by *anticyclic parallel wiring* which assures equal strain on the individual batteries. Anticyclic parallel wiring means in this case, that the positive battery wire of the solar regulator is connected to the individual batteries following the order 1+, 2+, 3+ and 4+. Whereas, the negative battery wire of the solar regulator is following the order 4-, 3-, 2- and 1-.

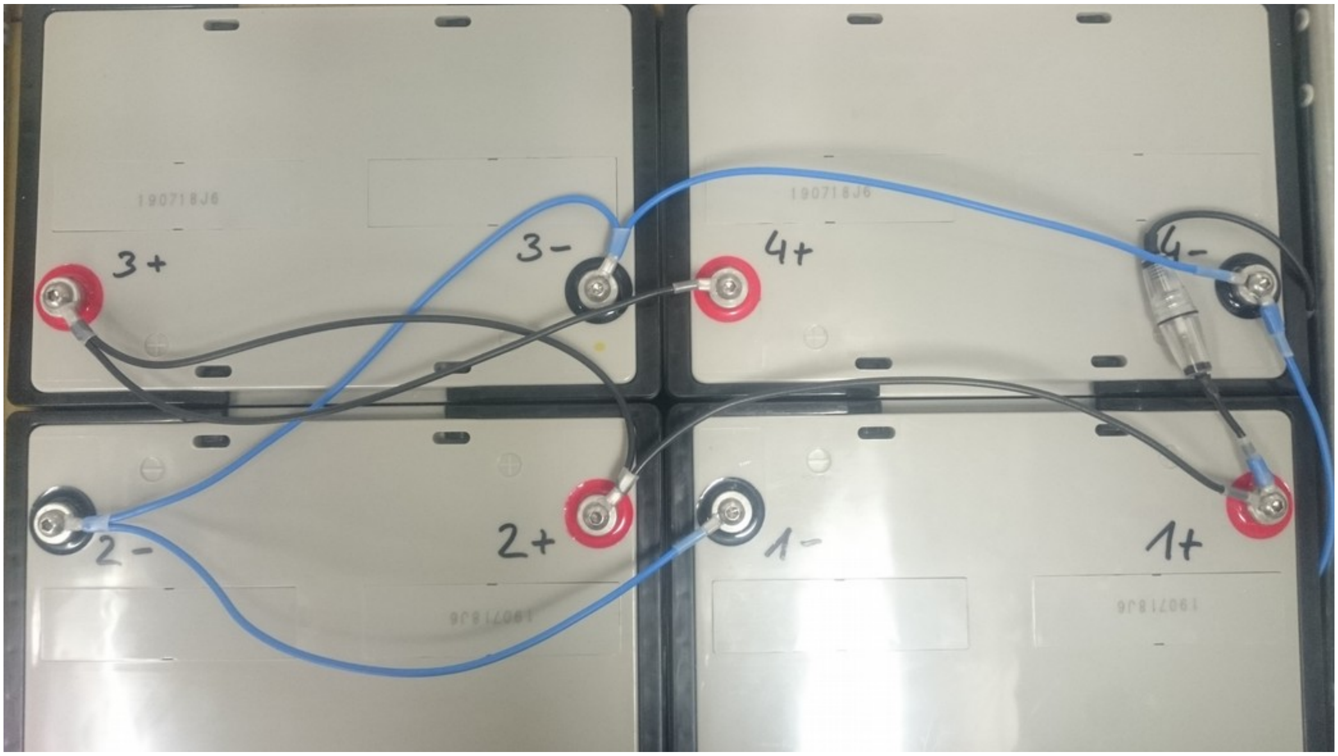

7. Closing the lid

Due to the height of the battery poles the closing of the lid requires some force. Before closing the lid, place some non-conducting, mechanical robust material on top of the battery poles to prevent short-circuiting. This fact points out a general weak spot of the Zarges power pack which is the potential risk of short-circuiting between the battery poles and the Zarges box lid. Special attention must therefore be paid to this issue!

The AGM Nitro battery is cheaper, but slightly higher than the Banner DB72 battery. Because of the low-cost approach, the AGM Nitro battery was applied, but the standard battery pole screws were replaced with round, flat headed screws.

In the case of short-term deployments, a second rubber pad on top of the batteries should be sufficient, whereas wear and tear of the rubber pad must not be underestimated. Insulation tape on the individual battery poles is an additional short-circuit prevention. However, in the case of longer period deployments with potential snow loading, it is definitely recommended to apply robust, solid pole caps instead of the rubber pad.

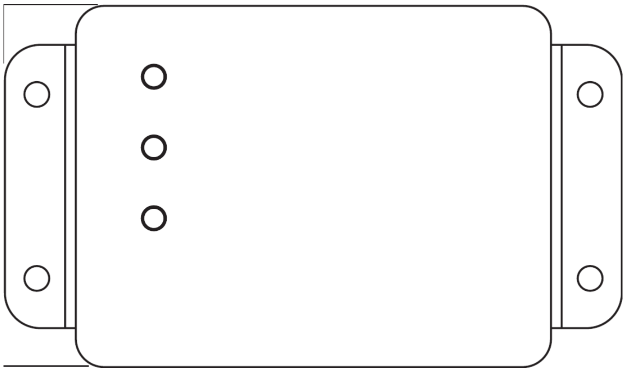

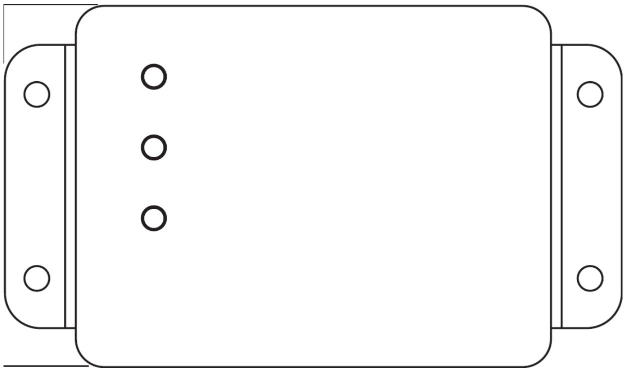

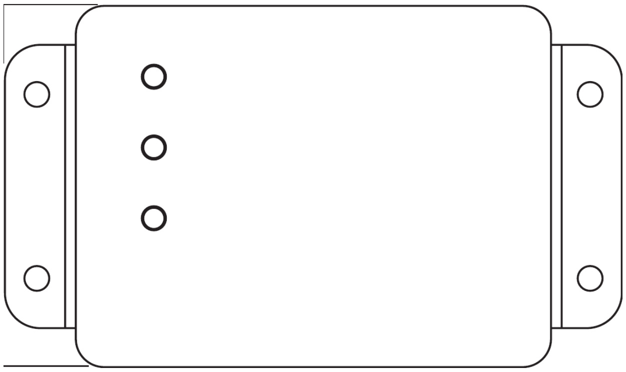

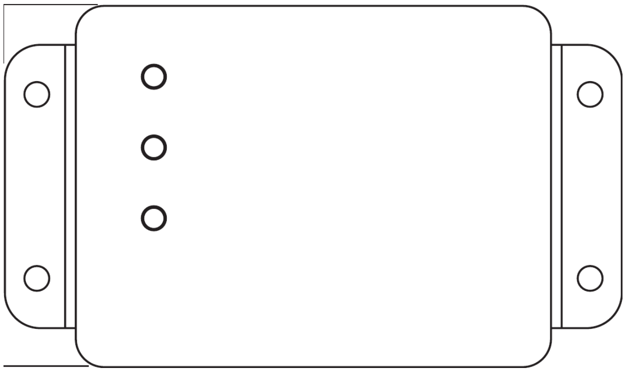

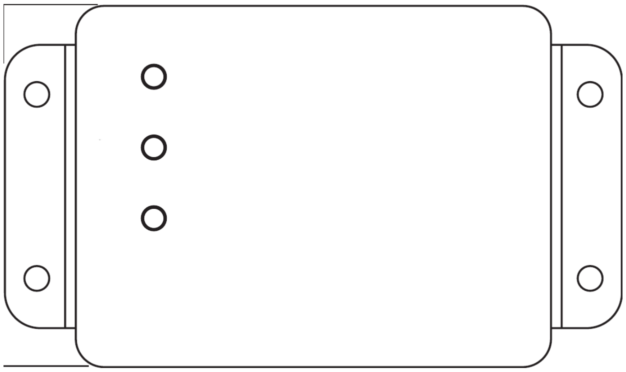

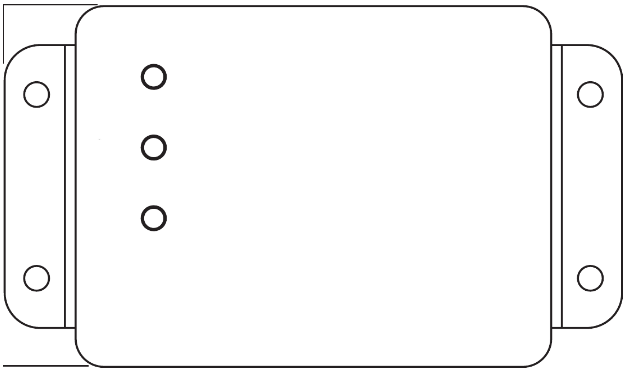

Appendix F: Dissemination and Outreach

ZAMG Press Release and Review

ZAMG
Zentralanstalt für
Meteorologie und
Geodynamik

11. August 2015

Projekt SeisRockHT:
Steinschlag-Aktivität in den Hohen Tauern

Am Sonnblick-Observatorium der ZAMG dürfte dieser Sommer so wenige Frosttage wie selten zuvor in der mehr als 100jährigen Messgeschichte bringen. Die in den letzten Jahrzehnten stetig steigenden Temperaturen im Hochgebirge führen zum Auftauen des Permafrostes. Das kann zu einem Anstieg alpiner Gefahren führen, wie etwa Steinschlag.

Das von der ZAMG geleitete Projekt SeisRockHT (Seismic Rockfall Monitoring in the Hohe Tauern Region) untersucht die Häufigkeit von Steinschlag und mögliche Zusammenhänge mit Faktoren wie Wetter und Klima.

Der extrem heiße Sommer 2015 bringt auch im Hochgebirge ungewöhnlich hohe Temperaturen. Am Sonnblick-Observatorium der Zentralanstalt für Meteorologie und Geodynamik (ZAMG) wurden heuer seit Anfang Juni nur 22 Frosttage gemessen, also Tage an denen die Temperatur zumindest für kurze Zeit unter 0 °C liegt. Im vieljährigen Mittel liegt die Zahl der Frosttage am Sonnblick im klimatologischen Sommer (Juni, Juli, August) bei 44 Tagen. Momentan zeichnet sich für 2015 sogar einer der zehn extremsten Werte der seit 1886 bestehenden Messgeschichte ab. Den absoluten Rekord verzeichnet weiterhin der Sommer 2003 mit nur 18 Frosttagen am Sonnblick.

Wie sehr beeinflussen die Änderungen im Permafrost die alpine Sicherheit?

Die in den letzten Jahren sinkende Zahl der Frosttage im Hochgebirge entspricht dem Szenario einer langfristigen Klimaerwärmung. Weltweit sind rund 20 bis 25 Prozent der Erdoberfläche von Permafrost beeinflusst. Eine Konsequenz der Klimaerwärmung ist das Auftauen des Permafrostes, was sich auf Steinschlag- und Felssturz Ereignisse auswirkt. Permafrost wird thermisch definiert als Untergrund, der mindestens zwei Jahre Temperaturen kleiner oder gleich 0 °C aufweist. Topographie, Exposition, Höhe oder Untergrundeigenschaften beeinflussen die Permafrostverbreitung. In Österreich ist ab einer Seehöhe von ca. 2.500 m (Nordexposition) mit größeren Permafrostvorkommen zu rechnen. Besonders in den letzten Jahren wurde eine Zunahme von Steinschlag- und Felssturzereignissen nicht nur von Wissenschaftlern sondern auch von Bergsteigern und Hüttenwirten beobachtet. Ein möglicher Grund ist die Erhöhung der Permafrosttemperatur und eine einhergehende, signifikante Reduktion der Felsstabilität. Durch Permafrost beeinflusste Felswände sind bereits ein bedeutender Risikofaktor für Mensch und Infrastruktur im Hochgebirge. Mit einer Zunahme des Risikos ist zu rechnen. Somit ist die Erhebung fundamentaler Daten für die zukünftige Entwicklung von entscheidender Bedeutung.

Installation der Messgeräte wird mit Sommer 2015 abgeschlossen

Das mit 2015 gestartete Projekt SeisRockHT der ZAMG, Mertl Research GmbH und Geoconsult Research & Development konzentriert sich auf zwei Gebiete unterschiedlicher räumlicher Skalen. Einerseits wird die mächtige Nordflanke des Hohen Sonnblicks (3106m), andererseits der kleinräumigere nördliche Gipfelbereich des Kitzsteinhorns (3203m) untersucht. Mit Hilfe von zwei seismologischen Netzwerken wird ein Steinschlag und Felssturz Ereigniskatalog entwickelt. „Wir verwenden im Prinzip kleinräumige, seismologische Erdbebennetze, die die Bodenerschütterung messen. Herabstürzende Felsen regen kleinräumig Bodenerschütterungen an und werden so von uns registriert“, sagt ZAMG-Geophysiker Daniel Binder, „zunächst geht es darum den momentanen Status der Steinschlagaktivität in den Untersuchungsgebieten festzustellen“.

Ergänzt werden die seismischen Netzwerke durch eine systematische Oberflächenüberwachung mit terrestrischem Laserscan und der Erfassung von meteorologischen Daten (Temperatur, Niederschlag, etc.) und Bohrlochtemperaturen. „Damit können potentielle Zusammenhänge zwischen Permafrostveränderungen und Felsstürzen untersucht und unter dem Aspekt der Klimaerwärmung diskutiert werden.“ betont Markus Keuschnig, Geoconsult Research & Developement. Aktuell sind die Instrumentierungsarbeiten im vollen Gange, mit ersten Ergebnissen ist 2016 zu rechnen. Die bereits erwähnte Notwendigkeit einer langfristigen Beobachtungsstrategie wird durch die Eingliederung der SeisRockHT-Netzwerke in das bestehende Österreichische Erdbebennetz angestrebt. Der Österreichische Erdbebendienst (ZAMG) ist ein SeisRockHT-Projektpartner.

Citizen Science: Forschung für alle

Neben dem prioritären wissenschaftlichen Anspruch verfolgt SeisRockHT auch die ‚Citizen Science‘-Idee. „Eine Besonderheit der verwendeten Messgeräte ist, dass sie als Open Hardware entwickelt worden sind. Das bedeutet, dass alle Interessierten die Baupläne der Messgeräte sowie die notwendige Software aus dem Internet herunterladen und frei verwenden, aber auch abändern und weiterentwickeln können. Damit lässt sich unkompliziert eine professionelle und kostengünstige Erdbebenstation bauen. Durch den relativ geringen finanziellen Aufwand und die gemeinsame Weiterentwicklung des Messsystems können wissenschaftliche Projekte einfacher umgesetzt werden. Im Idealfall entwickelt sich daraus ein Citizen Science Projekt mit interessierten Menschen, die nicht aus dem klassischen Forschungsbereich kommen“, erklärt der Seismologe und Entwickler der Messgeräte, Stefan Mertl, und ergänzt, „Jetzt werden wir aber zuerst einmal sehen wie sich die Geräte in der hochalpinen Umgebung der Hohen Tauern schlagen. Um die wertvollen Daten im Falle von Problemen mit den neuen Messgeräten nicht zu verlieren, verwenden wir auch redundante, bereits etablierte Messgeräte.“

Kooperation wissenschaftlichen Organisationen und privaten Unternehmen

Das von der Österreichischen Akademie der Wissenschaften (ÖAW) geförderte Projekt SeisRockHT besteht aus Wissenschaftlern der ZAMG, Mertl Research GmbH und Geoconsult Research & Developement.

Abbildungen (bei Nennung der Quelle kostenlos nutzbar)

Download volle Auflösung auf www.flickr.com/photos/zamg

Steinschlag-Messungen in den Hohen Tauern: Vorbereitung des seismischen Messgeräts für die Montage im Bohrloch beim Sonnblick-Observatorium. Quelle ZAMG/Binder.

Steinschlag-Messungen in den Hohen Tauern: Installation des Messgeräts im 20 Meter tiefen Bohrloch beim Sonnblick-Observatorium. Quelle ZAMG/Binder.

Steinschlag-Messungen in den Hohen Tauern: Auch am Fuße des Sonnblicks, in einem alten Bergwerkstollen in Kolm Saigurn, werden Messgeräte installiert. Quelle ZAMG/Binder.

Steinschlag-Messungen in den Hohen Tauern: Erste Funktionstests nach der Montage im Bohrloch. Das Ziel ist, in den nächsten Jahren die Häufigkeit von Steinschlag und seine Ursachen zu erforschen. Quelle ZAMG/Binder.

Download volle Auflösung auf www.flickr.com/photos/zamg

Web-Links

Mertl Research GmbH: www.mertl-research.at

Projekt 'Community Environmental Observation Network':

www.mertl-research.at/research_project/ceon

ZAMG Sonnblick-Observatorium: www.sonnblick.net

ZAMG Wettervorhersage: www.zamg.at/prognose

ZAMG Warnungen Österreich: www.zamg.at/warnungen

Warnungen Europa: www.meteoalarm.eu

ZAMG allgemein: www.zamg.at und www.facebook.com/zamg.at

Kontakte für Medien-Rückfragen

ZAMG Projekt SeisRockHT

Daniel Binder (daniel.binder@zamg.ac.at)	01 36026 2225
Wolfgang Lenhardt (wolfgang.lenhardtd@zamg.ac.at)	01 36026 2501

ZAMG Presse

Thomas Wostal (thomas.wostal@zamg.ac.at)	0664 75057109

Über die Zentralanstalt für Meteorologie und Geodynamik (ZAMG)
Die ZAMG ist der nationale österreichische meteorologische und geophysikalische Dienst und eine nachgeordnete Dienststelle des Bundesministeriums für Wissenschaft, Forschung und Wirtschaft (BMWFW). Die ZAMG hat ihren Hauptsitz auf der Hohen Warte in Wien und Kundenservicestellen in Graz, Innsbruck, Klagenfurt und Salzburg.

Der Tätigkeitsbereich der rund 280 Mitarbeiterinnen und Mitarbeiter erstreckt sich von Wettervorhersagen und Wetterwarnungen über angewandte meteorologische, klimatologische und geophysikalische Forschung bis hin zum Erdbebendienst und zu umweltmeteorologischer Gutachtertätigkeit.

Die ZAMG wurde 1851 gegründet und ist der älteste selbstständige Wetterdienst der Welt. Die ZAMG betreibt ein meteorologisches und ein seismisches Messnetz mit insgesamt 280 Stationen. Außerdem betreibt sie das Sonnblick Observatorium, das Conrad Observatorium und das Cobenzl Observatorium.

Die Expertinnen und Experten der ZAMG vertreten Österreich in zahlreichen internationalen Organisationen und Vereinigungen wie z.B. WMO (Weltmeteorologische Organisation der Vereinten Nationen), ECMWF (Europäisches Zentrum für Mittelfristige Wettervorhersagen) und EUMETSAT (Europäische Vereinigung zur Entwicklung von Wetter- und Klimasatellitensystemen).

Die ZAMG ist die führende meteorologische Institution in Österreich und bietet ihre Leistungen unter anderem öffentlichen und privaten Fernseh- und Rundfunkanstalten, Tageszeitungen und Dienstleistern wie Versicherungen, Energiewirtschaft, Winterdienstfirmen, Bauunternehmen und Gemeinden an.

"Der Standard" vom 12.08.2015 Seite: 9 Ressort: InlandChronik Niederösterreich

BURGENLANDÖSTERREICH

Immer weniger Frosttage im hochalpinen Sommer

Salzburg – Jüngste Fakten zum heurigen Supersommer: Am Sonnblick-Observatorium nimmt die Zahl an Frosttagen dramatisch ab. Seit Anfang Juni gab es in 3106 Metern Seehöhe nur 22 Tage, an denen die Temperatur zumindest für kurze Zeit unter null Grad Celsius sank. Das vieljährige Mittel liegt bei 44 Tagen. Welche Gefahren das Auftauen des Permafrostes im alpinen Bereich mit sich bringt, wird gerade erforscht. (red)

Faksimile Seite 9 Niederösterreich

"Kronen Zeitung" vom 12.08.2015 Seite: 16 Ressort: Lokal Sbg

Nur 22 „Frosttage“ auf dem Sonnblick Forschungsprojekt

Mehr Steinschlag bedroht die Bergsteiger und Hüttenwirte

So heiß war es kaum einmal in den letzten 100 Jahren auf dem Hohen Sonnblick im Rauriser Tal: Die Wetterforscher im berühmten Observatorium auf 3106 m maßen seit Juni nur 22 „Frosttage“ – an denen das Thermometer wenigstens für einige Minuten unter die Null-Grad-Marke fiel. Nur 2003 war es noch wärmer.

Forscher stellen Messgeräte im alten Stollen in Kolm-Saigurn auf

Die extremen Temperaturen sind ideal für ein großes Forschungsprojekt, das heuer am Sonnblick sowie am Kitzsteinhorn anläuft: Auf beiden Bergen richteten die Experten der Zentralanstalt für Meteorologie und Geodynamik ein Netz von Messpunkten ein. Sie erkennen, wie oft kleinere Steine oder große Felsbrocken hinunterstürzen in die Wände unterhalb des Gipfels.

„SeisRockHT“ nennt sich das Projekt (Seismic Rockfall Monitoring in the Hohe Tauern). Und es stellt fest, wie stark der „Permafrost“ auftaut – das ist die Zone im Gebirge, wo Eis die lockeren Felsbrocken zusammenhält. „Taut der Permafrost, gibt es weit öfter Steinschlag und Felsstürze“, weiß ZAMG-Geophysiker Daniel Binder. Dann wird der Klimawandel für Bergsteiger und Hüttenwirte lebensgefährlich.

ROBERT REDTENBACHER

Faksimile Seite 16 Salzburg Morgen

"Salzburger Nachrichten" Nr. 185 vom 12.08.2015 Seite: L8 Ressort: Lokal

Sonnblick leidet unter der Hitze

SALZBURG. Am Sonnblick-Observatorium wurden heuer seit 1. Juni nur 22 Frosttage gemessen – so wenige wie selten zuvor seit Beginn der Aufzeichnungen 1886. Die seit Jahrzehnten steigenden Temperaturen im Hochgebirge führen zum Auftauen des Permafrosts. Das kann zu einem Anstieg von Steinschlägen führen. Das ist ein Ergebnis eines Projekts der ZAMG, das die Häufigkeit von Steinschlägen im Zusammenhang von Wetter und Klima untersucht.

MITTWOCH, 12. AUGUST 2015 Salzburger Nachrichten

Sie rebelliert gegen die Wirtschaftskammer

Katharina Kirchmayr sieht ihr Handwerk sterben. Daher verweigert sie die Kammerumlage.

NICOLE SCHNELL

SALZBURG-STADT. 326 Euro Grundumlage 2015 muss Katharina Kirchmayr an die Wirtschaftskammer Salzburg überweisen. Für die gelernte Raumausstattermeisterin, die mit dem Atelier Raum 44 in Salzburg seit acht Jahren selbstständig tätig ist, kommt das nicht mehr infrage. Mit einem Brief hat sie sich am Dienstag mit ihrem Anliegen an die Wirtschaftskammer gewandt.

„Ich war niemals ein freiwilliges Mitglied Ihrer Organisation", schreibt sie. Bisher habe sie die Grundumlage stets bezahlt, nun aber habe sie beschlossen: „Ich kann nicht mehr ständig nur alles bezahlen. Man wird derartig mit Gebühren, Abgaben und Zinsen belastet, dass kaum noch etwas übrig bleibt", erzählt die Salzburgerin. Was sie besonders ärgert: „Fleiß wird vom Staat tatsächlich auch noch bestraft, ich bin wahnsinnig enttäuscht."

Wer zur Bezahlung der Grundumlage verpflichtet ist, erklärt die Wirtschaftskammer: „Die Verpflichtung, Grundumlage zu bezahlen, trifft alle Mitglieder, und zwar für jede einzelne Berechtigung zum selbstständigen Betrieb eines Unternehmens, die in den Wirkungsbereich einer Fachgruppe eines Bundeslandes fällt." Da die Grundumlage jährlich von jeder Fachgruppe beschlossen werde, sei sie auch unterschiedlich hoch.

Kirchmayr fällt in die Fachorganisation „Maler und Tapezierer". Der Textilbranche gehe es besonders schlecht. „Das Einrichtungshandwerk liegt im Sterben", sagt sie. Immer mehr Färbereien, Spinnereien oder Webereien gingen in Konkurs. „Gegen die Probleme, die der Kammer doch bestimmt bekannt sein müssen, wird aber nichts unternommen."

Fünf Prozent der Unternehmer hätten die Grundumlage im Jahr 2014 nicht bezahlt, sagt Caroline Grömer von der Wirtschaftskammer Salzburg. Was dann passiere? Nach drei Mahnungen folge die Exekution. So weit muss es nicht kommen: Einwendungen über die Höhe der Beitragsvorschreibungen werden vom Umlagenbüro der Wirtschaftskammer geprüft. Kirchmayr hat gerade die zweite Mahnung erhalten. „Was sollen sie mir denn nehmen?"

Raumausstattermeisterin Katharina Kirchmayr führt das Atelier Raum 44.

Sonnblick leidet unter der Hitze

SALZBURG. Am Sonnblick-Observatorium wurden heuer seit 1. Juni nur 22 Frosttage gemessen – so wenige wie selten zuvor seit Beginn der Aufzeichnungen 1886. Die seit Jahrzehnten steigenden Temperaturen im Hochgebirge führen zum Auftauen des Permafrosts. Das kann zu einem Anstieg von Steinschlägen führen. Das ist ein Ergebnis eines Projekts der ZAMG, das die Häufigkeit von Steinschlägen im Zusammenhang von Wetter und Klima untersucht.

LEO

„Eine Salzburger Raumausstatterin legt sich jetzt mit der Wirtschaftskammer an und beklagt, dass der Staat die Fleißigen bestrafte. Das ist richtig. Bei den Faulen ist nämlich für den Staat nichts zu holen."

Faksimile Seite L9 Lokal

APA0278 5 CI 0398 XI Di, 11.Aug 2015 Von: af/hai

So wenige Frosttage am Sonnblick wie selten zuvor in einem Sommer

Utl.: Steigende Temperaturen im Hochgebirge führen zum Auftauen des Permafrostes - ZAMG-Projekt untersucht Häufigkeit von Steinschlag in den Hohen Tauern =

Salzburg/Wien (APA) - Die Hitzewelle dürfte diesen Sommer am Sonnblick-Observatorium der ZAMG so wenige Frosttage wie selten zuvor in der mehr als 100-jährigen Messgeschichte bringen. Die stetig steigenden Temperaturen im Hochgebirge führen zum Auftauen des Permafrostes, was zu einem Anstieg alpiner Gefahren führen kann. Eine davon, Steinschlag, wird derzeit im Rahmen eines ZAMG-Projekts untersucht.

Das von der Zentralanstalt für Meteorologie und Geodynamik geleitete SeisRockHT (Seismic Rockfall Monitoring in the Hohe Tauern Region) beschäftigt sich mit der Häufigkeit von Steinschlag und möglichen Zusammenhängen mit Wetter und Klima. Denn auch im Hochgebirge werden derzeit ungewöhnlich hohe Temperaturen gemessen. Am Sonnblick wurden heuer seit Anfang Juni nur 22 Frosttage registriert, also Tage an denen die Temperatur zumindest für kurze Zeit unter 0 Grad Celsius liegt. Im vieljährigen Mittel liegt deren Zahl im klimatologischen Sommer von Juni bis August bei 44 Tagen. Momentan zeichnet sich für heuer sogar einer der zehn extremsten Werte der seit 1886 bestehenden Messgeschichte ab. Den absoluten Rekord verzeichnet weiterhin der Sommer 2003 mit nur 18 Frosttagen am Sonnblick, so die Meteorologen am Dienstag.

Weltweit sind rund 20 bis 25 Prozent der Erdoberfläche von Permafrost beeinflusst. In Österreich ist ab einer Seehöhe von etwa 2.500 Metern (Nordexposition) mit größeren Permafrostvorkommen zu rechnen. Besonders in den vergangenen Jahren wurde eine Zunahme von Steinschlag- und Felssturzereignissen nicht nur von Wissenschaftern, sondern auch von Bergsteigern und Hüttenwirten beobachtet. Ein möglicher Grund ist die Erhöhung der Permafrosttemperatur und eine einhergehende Reduktion der Felsstabilität.

Das heuer gestartete Projekt SeisRockHT der ZAMG, Mertl Research GmbH und Geoconsult Research & Development konzentriert sich auf zwei Gebiete: Einerseits wird die Nordflanke des Hohen Sonnblicks (3.106 Meter), andererseits der nördliche Gipfelbereich des Kitzsteinhorns (3.203 Meter) untersucht."Wir verwenden im Prinzip kleinräumige, seismologische Erdbebennetze, die die Bodenerschütterung messen. Herabstürzende Felsen regen kleinräumig Bodenerschütterungen an und werden so von uns registriert", sagte ZAMG-Geophysiker Daniel Binder. Zunächst geht es darum, den momentanen Status der Aktivität festzustellen.

Ergänzt werden die seismischen Netzwerke durch eine systematische Oberflächenüberwachung mit terrestrischem Laserscan und der Erfassung von meteorologischen Daten und Bohrlochtemperaturen. "Damit können potenzielle Zusammenhänge zwischen Permafrostveränderungen und Felsstürzen untersucht und unter dem Aspekt der Klimaerwärmung diskutiert werden", weiß Markus Keuschnig von Geoconsult Research & Developement. Mit ersten Ergebnissen sei 2016 zu rechnen.

(Schluss) af/hai

APA0278 2015-08-11/12:48

111248 Aug 15

"oe24.at" gefunden am 11.08.2015 18:03 Uhr

oe24.at: Heuer 300 Hitze- Tote befürchtet

Der heißeste Sommer aller Zeiten führt zu mehr als 300 Hitzetoten, meint ein Experte.

Österreich stöhnt unter der Hitzewelle, am Dienstag kletterte das Thermometer auf 37 Grad und für Donnerstag werden 38 Grad vorhergesagt. Ein Sommer der Rekorde: Es gab heuer bisher so viele Wüstentage (Tage mit mehr als 35 Grad) wie nie – und die körperliche Belastung steigt mit jedem Tag.

Rotes Kreuz: Wegen Hitze mehr als 1.400 Einsätze

Die Folge: Viele leiden extrem, wählen den Rettungsnotruf. Das Rote Kreuz berichtet von 1.400 Einsätzen pro Tag, betroffen sind laut Bundesrettungskommandant Gerry Foitik meist „ältere Menschen mit chronischen Erkrankungen, deren Gesamtzustand schlechter wird". In Wien muss die Rettung täglich zu mehr als 800 Einsätzen ausrücken. Besonders tragisch: Immer mehr Menschen sterben wegen der Hitze, sei es direkt bei einem Badeunfall oder an den Folgen der Hitzewelle. Gab es von 2003 bis 2012 pro Jahr im Schnitt 240 Hitzetote, wird dieser Wert heuer ansteigen: „Ich rechne mit mehr als 300 Hitzetoten", sagt Sozialmediziner Michael Kunze.

Alarmierend: Laut einer Studie der Alpen-Adria-Universität könnte ein weiterer starker Klimawandel ab 2016 für „bis zu 1.200 Hitzetote pro Jahr in Österreich" sorgen.

Für Hitzegeplagte richtete das Gesundheitsministerium am Dienstag eigens ein Hitze-Telefon ein (116-123), das 24 Stunden besetzt ist. Tipp vom Roten Kreuz: „Es hilft, pro Tag drei Stunden in kühlen Räumen zu verbringen", sagt Rot-Kreuz-Experte Foitik.

>> Die Temperaturen der Badeseen in Österreich

>> Biowetter: So wirkt sich das Wetter heute auf Ihr Wohlbefinden aus

Auf der nächsten Seite der Liveticker zum Nachlesen!

Die Wüstentage gehen weiter. Auch heute bleibt es im Großteil des Landes wieder sonnig und tagsüber sehr heiß - bis zu 37 Grad! Ein paar Regenschauer und Gewitter sind im Westen aber wieder möglich, sonst bleibt die Gewitterneigung auch über den Bergen recht gering. Mit der trokenen Hitze steigt im Osten die Gefahr für Waldbrände weiter. In Niederösterreich sind am Montag und in der Nacht auf Dienstag fast 700 Feuerwehrleute bei drei Bränden im Einsatz gestanden. Im Burgenland kam es durch Selbstentzündung zu einem Flurbrand. Hier wird es heute am heißesten: Klicken Sie auf die Grafik, um zur interaktiven Version der Karte zu gelangen >> Die Temperaturen der Badeseen in Österreich >> Biowetter: So wirkt sich das Wetter heute auf Ihr Wohlbefinden aus Wir berichten hier live über alle aktuellen Entwicklungen 16:46 Uhr: Hitze-Hotspot Der heißeste Ort heute ist Hohenau (Niederösterreich) mit 37,6 Grad. 16:18 Uhr: Vorschau für Dienstag Es stellt sich im ganzen Land ein sonniger und heißer Tag ein. Die Luft wird auch im Westen vorübergehend trockener und somit sind nur ganz vereinzelt kleinräumige Gewitter möglich, meist bleibt es trocken. Frühtemperaturen 15 bis 24 Grad, Tageshöchsttemperaturen meist 30 bis 37 Grad, am heißesten ist es weiterhin im Osten. 15:55 Uhr: Waldbrand in Reichenau a. d. Rax Zehn Feuerwehren mit 110 Mann haben am Dienstagnachmittag einen Flur- und Waldbrand in Reichenau a.d. Rax bekämpft. Die Flammen auf einem Hektar Fläche wurden rasch unter Kontrolle gebracht, berichtete Franz Resperger vom Landeskommando NÖ auf Anfrage. Nachlöscharbeiten wegen glühender Baumstämme waren jedoch notwendig. 15:35 Uhr: Es wird noch heißer In Hohenau werden aktuell 37,2 grad gemessen. Damit ist der Ort in Niederösterreich einmal mehr der Hitze-Hotsport Österreichs. Es folgen Zwerndorf mit 36,6 und Wolkersdorf (beide NÖ) mit 36,4°. 15:10 Uhr: Das aktuelle Hitze-Radar Per Klick auf die Grafik gelangen Sie zur interaktiven Version der Karte 14:55 Uhr: So geht es morgen weiter Es stellt sich im ganzen Land ein sonniger und heißer Tag ein. Die Luft wird auch im Westen vorübergehend trockener und somit sind nur ganz vereinzelt kleinräumige Gewitter möglich, meist bleibt es trocken. Frühtemperaturen 15 bis 24 Grad, Tageshöchsttemperaturen meist 30 bis 37 Grad, am heißesten ist es weiterhin im Osten. 14:35 Uhr: Kühler ist es hingegen im Westen Österreichs. Innsbruck meldet aktuell 28,6°, Bregenz gar nur 24,8°. 14.20 Uhr: Vier Orte über 36 Grad Hohenau an der March, Langenlebarn, Zwerndorf (alle NÖ) sowie Andau (Burgenland) melden Temperaturen von über 36 Grad. 35,2 Grad werden aktuell in Wien gemessen. 14.10 Uhr: Feuerwehr rettet Baby aus heißem Auto Dramatischer Hitze-Einsatz für die Feuerwehr in Hintersee (Salzburg-Umgebung): Die Einsatzkräfte befreiten am Montag ein Baby aus einem versperrten Auto. Der Wagen hatte sich selbst versperrt - die geschockte Mutter alarmierte die Feuerwehr. Die Retter mussten die Scheibe des Kombis einschlagen, um das Baby zu befreien, berichtet der ORF. 13.34 Uhr: 36-Grad-Marke geknackt Hohenau an der March (NÖ) ist einmal mehr der heißeste Ort Österreichs. Der Ort im Dreiländereck meldet aktuell 36,1 Grad. Wolkersdorf folgt mit 35,7°, Andau mit 35,3°. 13.00 Uhr: Hier lässt die Hitze ein Auto schmelzen In praller Sonne geparkter Renault hielt den hohen Temperaturen nicht stand. >> Lesen Sie mehr 12.55 Uhr: Hitzewelle: Kaum Frost am Sonnblick Der Rekordsommer lässt den Permafrost auftauen - Steinschläge werden dadurch häufiger. >> Lesen Sie mehr Foto: ZAMG 12.35 Uhr: Ozon-Warnschwelle in Wien überschritten An der Wiener Messstelle Lobau Ozonkonzentrationen größer als 180 Mikrogramm/m3 als Einstundenmittelwert gemessen worden. Damit wurde die Informationsschwelle überschritten. Ozonkonzentrationen über der Informationsschwelle können bei einzelnen, besonders empfindlichen Personen und erhöhter körperlicher Belastung geringfügige Beeinträchtigungen hervorrufen. Der normale Aufenthalt im Freien, z. B. Spaziergang, Baden oder Picknick, ist auch für empfindliche Personen unbedenklich. Die Stadt Wien ersucht, auf nicht unbedingt notwendige Autofahrten zu verzichten und öffentliche Verkehrsmittel zu benützen. 12.23 Uhr: Die Hitze trifft einmal mehr das östliche Flachland. Im Nordburgenland, im niederösterreichischen Industrie- und Weinviertel sowie in Wien liegen die Werte bereits jenseits der 30-Grad-Marke. In Salzburg herrschen dagegen "normale" Sommertemperaturen von 25,0 Grad in Sankt Johann im Pongau bis zu 28,6 in der Stadt Salzburg. 12.15 Uhr: Wüstentag Nun ist der nächste "Wüstentag" perfekt. Wolkersdorf (NÖ) knackt die dafür erforderliche Temperaturgrenze von 35,0 Grad. 11.45 Uhr: Neue Waldbrände in Tschechien Auch im benachbarten Tschechien sind Waldbrände ausgebrochen. Bei dem Dorf Horni Hradiste im Bezirk Pilsen waren rund 50 Einsatzkräfte Tag und Nacht im Einsatz, wie die Agentur CTK am Dienstag berichtete. Gut 50 Hektar Felder und 20 Hektar Wald fielen dort den Flammen zum Opfer. Ein Feuer im südböhmischen Bezirk Strakonice zerstörte rund 60 Hektar Wald und Wiesen. Mutmaßliche Brandursache war in beiden Fällen Funkenschlag aus einer Landwirtschaftsmaschine. 11.30 Uhr: Extreme Hitze: Das raten Experten Besonders Kleinkinder und ältere Menschen sind während der Hitzewelle gefährdet. Darauf sollten Sie laut Experten achten. >> Lesen Sie mehr auf gesund24.at. 11.25 Uhr: 32,6 Grad in Wolkersdorf Wolkersdorf nördlich von Wien ist aktuell der Hitzepol Österreichs mit 32,6 Grad. Ebenfalls schon über 32 Grad heiß: Berndorf (NÖ) und Andau (Burgenland). Wien meldet 31,7 Grad. Kältepol Österreichs ist Mariapfarr in Salzburg - bei 15,7 Grad lässt sich durchaus mehr als eine Badehose tragen. 10.55 Uhr: Waldbrand: Alarmstufe 3 in OÖ Auch in Oberösterreich rief die Feuerwehr Oberösterreich wegen eines Brandes im Wald bei Loibersdorf (Bezirk Freistadt) am Montagnachmittag Alarmstufe 3 aus. Ein Holzstoß am Waldrand stand in Vollbrand, 14 Feuerwehren mit weit über 150 Kräften standen im Großeinsatz, um ein Übergreifen der Flammen auf den Wald zu verhindern. Erst um 22.00 Uhr war das Feuer soweit gelöscht, dass bis auf eine Brandwache alle Wehren abrücken konnten. Drei Feuerwehrleute mussten wegen Kreislaufproblemen behandelt werden, ein vierter erlitt einen Kollaps und wurde in das Linzer AKH gebracht. Die Brandursache steht noch nicht fest. Bild: foto-kerschi.at 10.40 Uhr: Hitze: Vorsicht beim Reifendruck Der Autofahrerclub ÖAMTC warnt vor hitzebedingten Schwankungen beim Reifendruck. "Wird der Reifen warm, erhöht sich der Druck. Das passiert beim Fahren in jedem Fall. Durch die hohen Außentemperaturen kann sich der Effekt aber noch verstärken und der Druck sich - speziell bei längerer Autobahnfahrt - um mehr als ein halbes Bar erhöhen", so Friedrich Eppel. Die zwei wichtigsten Tipps des ÖAMTC: "Den Reifendruck sollte man bei möglichst kalten Reifen, also z. B. in der Früh und nicht nach einer Fahrt, einstellen. Und man sollte generell immer mit dem 'richtigen' Luftdruck unterwegs sein." 10.29 Uhr: Die ersten Dreißiger sind da Rechnitz (30,8°), Wolkersdorf (30,4°) und Pottscchach (30,0°) knacken die 30-Grad-Marke. Knapp dran ist auch schon Wien - die Innere Stadt meldet aktuell 29,4 Grad. 9.58 Uhr: Grillverbot in Wien bleibt aufrecht Die anhaltende Hitze sorgt weiterhin für höchste Waldbrandgefahr in Wien. "Das Rauchen, Hantieren mit offenem Feuer und Licht sowie jegliches Feuerentzünden im Wald und dessen Gefährdungsbereich im Gebiet der Stadt Wien bleibt weiterhin verboten", so Roland Havel vom Forstamt. Erst bei "nachhaltigen" Regenschauern werde das Verbot wieder aufgehoben. 9.40 Uhr: Die Hitzepole Mit 28,7 Grad überflügelte Rechnitz im Burgenland die Leiser Berge (NÖ) in Sachen Temperatur. Ebenfalls vorne dabei: Wien (27,6°), Eisenstadt und Wolkersdorf (je 27,7°). 9.15 Uhr: Polizisten löschen Flurbrand an der A3 Die Trockenheit sorgt auch im Burgenland für Einsätze. An der Südostautobahn (A3) bei Hornstein (Bezirk Eisenstadt-Umgebung) einen Flurbrand gelöscht. Bei ihrem Eintreffen brannte bereits das Gras im Straßengraben. Mit dem Feuerlöscher aus dem Dienstwagen löschten sie die Flammen. Die Stadtfeuerwehr Eisenstadt übergoss den Brandherd mit Löschwasser, um ein neuerliches Aufflammen zu verhindern. Als Brandursache wird eine Selbstentzündung des durch die Hitze verdorrten Grases angenommen. 9.00 Uhr: Waldbrände in NÖ: Höchste Alarmstufe In Niederösterreich standen am Montag und in der Nacht auf Dienstag fast 700 Feuerwehrleute bei drei Bränden im Einsatz. Sowohl im Bezirk Melk als auch im Bezirk Waidhofen a.d. Thaya waren stundenlange Nachlöscharbeiten im Gang. >> Lesen Sie mehr Foto: BFK WAIDHOFEN A. D. THAYA / STEFAN MAYER 8.30 Uhr: Tipps: Wo Sie trotz Hitze noch Abkühlung finden Nicht jeder jubelt über die heißen Temperaturen von 37 Grad. Es gibt trotzdem einige Plätze, wo sich dieser Super-Sommer doch aushalten lässt – eine kleine Übersicht: Voll im Trend ist die Flucht in die Berge. Immerhin kühlt es in 1.500 Metern auf 17 Grad ab, viele Hütten in Niederösterreich und der Steiermark sind deshalb bis auf drei Wochen ausgebucht. Die meisten Kinosäle und Shopping-Center sind klimatisiert. Zumindest für 90 Minuten ist Abkühlung angesagt. Die Tropfsteinhöhlen und Schaubergwerke bieten Temperaturen um 20 Grad. Eine Super-Aktion bieten derzeit die Austria Trend Hotels: Um gerade einmal 30 Euro pro Person bieten sie klimatisierte Zimmer. 8.00 Uhr: Das sind die Hotspots von heute Morgen Das sind die Hotspots von heute Morgen: Wärmster Ort Österreichs sind derzeit die Leiser Berge (NÖ). Mit 27,9 Grad liegt die Temperatur sogar über den Werten in Wien, wo die Jubiläumswarte 26,7 Grad meldet.

"salzburg.com" gefunden am 11.08.2015 14:30 Uhr

salzburg.com: So wenige Frosttage am Sonnblick wie selten zuvor in einem Sommer

Die Hitzewelle dürfte diesen Sommer am Sonnblick-Observatorium der ZAMG so wenige Frosttage wie selten zuvor in der mehr als 100-jährigen Messgeschichte bringen. Die stetig steigenden Temperaturen im Hochgebirge führen zum Auftauen des Permafrostes, was zu einem Anstieg alpiner Gefahren führen kann. Eine davon, Steinschlag, wird derzeit im Rahmen eines ZAMG-Projekts untersucht.

Das von der Zentralanstalt für Meteorologie und Geodynamik geleitete SeisRockHT (Seismic Rockfall Monitoring in the Hohe Tauern Region) beschäftigt sich mit der Häufigkeit von Steinschlag und möglichen Zusammenhängen mit Wetter und Klima. Denn auch im Hochgebirge werden derzeit ungewöhnlich hohe Temperaturen gemessen. Am Sonnblick wurden heuer seit Anfang Juni nur 22 Frosttage registriert, also Tage an denen die Temperatur zumindest für kurze Zeit unter 0 Grad Celsius liegt. Im vieljährigen Mittel liegt deren Zahl im klimatologischen Sommer von Juni bis August bei 44 Tagen. Momentan zeichnet sich für heuer sogar einer der zehn extremsten Werte der seit 1886 bestehenden Messgeschichte ab. Den absoluten Rekord verzeichnet weiterhin der Sommer 2003 mit nur 18 Frosttagen am Sonnblick, so die Meteorologen am Dienstag.

Mehr zum Thema

Weltweit sind rund 20 bis 25 Prozent der Erdoberfläche von Permafrost beeinflusst. In Österreich ist ab einer Seehöhe von etwa 2.500 Metern (Nordexposition) mit größeren Permafrostvorkommen zu rechnen. Besonders in den vergangenen Jahren wurde eine Zunahme von Steinschlag- und Felssturzereignissen nicht nur von Wissenschaftern, sondern auch von Bergsteigern und Hüttenwirten beobachtet. Ein möglicher Grund ist die Erhöhung der Permafrosttemperatur und eine einhergehende Reduktion der Felsstabilität.

Das heuer gestartete Projekt SeisRockHT der ZAMG, Mertl Research GmbH und Geoconsult Research & Development konzentriert sich auf zwei Gebiete: Einerseits wird die Nordflanke des Hohen Sonnblicks (3.106 Meter), andererseits der nördliche Gipfelbereich des Kitzsteinhorns (3.203 Meter) untersucht."Wir verwenden im Prinzip kleinräumige, seismologische Erdbebennetze, die die Bodenerschütterung messen. Herabstürzende Felsen regen kleinräumig Bodenerschütterungen an und werden so von uns registriert", sagte ZAMG-Geophysiker Daniel Binder. Zunächst geht es darum, den momentanen Status der Aktivität festzustellen.

Ergänzt werden die seismischen Netzwerke durch eine systematische Oberflächenüberwachung mit terrestrischem Laserscan und der Erfassung von meteorologischen Daten und Bohrlochtemperaturen. "Damit können potenzielle Zusammenhänge zwischen Permafrostveränderungen und Felsstürzen untersucht und unter dem Aspekt der Klimaerwärmung diskutiert werden", weiß Markus Keuschnig von Geoconsult Research & Developement. Mit ersten Ergebnissen sei 2016 zu rechnen.

"arf.at" gefunden am 11.08.2015 16:38 Uhr

arf.at: ZAMG: Steinschlag-Projekt in den Hohen Tauern

***Am Sonnblick-Observatorium der ZAMG dürfte dieser Sommer so wenige Frosttage wie selten zuvor in der mehr als 100jährigen Messgeschichte bringen. Die in den letzten Jahrzehnten stetig steigenden Temperaturen im Hochgebirge führen zum Auftauen des Permafrostes. Das kann zu einem Anstieg alpiner Gefahren führen, wie etwa Steinschlag. ***

*Das von der ZAMG geleitete Projekt SeisRockHT (Seismic Rockfall Monitoring in the Hohe Tauern Region) untersucht die Häufigkeit von Steinschlag und mögliche Zusammenhänge mit Faktoren wie Wetter und Klima. *

Der extrem heiße Sommer 2015 bringt auch im Hochgebirge ungewöhnlich hohe Temperaturen. Am Sonnblick-Observatorium der Zentralanstalt für Meteorologie und Geodynamik (ZAMG) wurden heuer seit Anfang Juni nur 22 Frosttage gemessen, also Tage an denen die Temperatur zumindest für kurze Zeit unter 0 °C liegt. Im vieljährigen Mittel liegt die Zahl der Frosttage am Sonnblick im klimatologischen Sommer (Juni, Juli, August) bei 44 Tagen. Momentan zeichnet sich für 2015 sogar einer der zehn extremsten Werte der seit 1886 bestehenden Messgeschichte ab. Den absoluten Rekord verzeichnet weiterhin der Sommer 2003 mit nur 18 Frosttagen am Sonnblick.

* Wie sehr beeinflussen die Änderungen im Permafrost die alpine Sicherheit?*

Die in den letzten Jahren sinkende Zahl der Frosttage im Hochgebirge entspricht dem Szenario einer langfristigen Klimaerwärmung. Weltweit sind rund 20 bis 25 Prozent der Erdoberfläche von Permafrost beeinflusst. Eine Konsequenz der Klimaerwärmung ist das Auftauen des Permafrostes, was sich auf Steinschlag- und Felssturz Ereignisse auswirkt. Permafrost wird thermisch definiert als Untergrund, der mindestens zwei Jahre Temperaturen kleiner oder gleich 0 °C aufweist. Topographie, Exposition, Höhe oder Untergrundeigenschaften beeinflussen die Permafrostverbreitung. In Österreich ist ab einer Seehöhe von ca. 2.500 m (Nordexposition) mit größeren Permafrostvorkommen zu rechnen. Besonders in den letzten Jahren wurde eine Zunahme von Steinschlag- und Felssturzereignissen nicht nur von Wissenschaftlern sondern auch von Bergsteigern und Hüttenwirten beobachtet. Ein möglicher Grund ist die Erhöhung der Permafrosttemperatur und eine einhergehende, signifikante Reduktion der Felsstabilität. Durch Permafrost beeinflusste Felswände sind bereits ein bedeutender Risikofaktor für Mensch und Infrastruktur im Hochgebirge. Mit einer Zunahme des Risikos ist zu rechnen. Somit ist die Erhebung fundamentaler Daten für die zukünftige Entwicklung von entscheidender Bedeutung.

*Installation der Messgeräte wird mit Sommer 2015 abgeschlossen *

Das mit 2015 gestartete Projekt SeisRockHT der ZAMG, Mertl Research GmbH und Geoconsult Research & Development konzentriert sich auf zwei Gebiete unterschiedlicher räumlicher Skalen. Einerseits wird die mächtige Nordflanke des Hohen Sonnblicks (3106m), andererseits der kleinräumigere nördliche Gipfelbereich des Kitzsteinhorns (3203m) untersucht. Mit Hilfe von zwei seismologischen Netzwerken wird ein Steinschlag und Felssturz Ereigniskatalog entwickelt. „Wir verwenden im Prinzip kleinräumige, seismologische Erdbebennetze, die die Bodenerschütterung messen. Herabstürzende Felsen regen kleinräumig Bodenerschütterungen an und werden so von uns registriert", sagt ZAMG-Geophysiker Daniel Binder, „zunächst geht es darum den momentanen Status der Steinschlagaktivität in den Untersuchungsgebieten festzustellen".

Ergänzt werden die seismischen Netzwerke durch eine systematische Oberflächenüberwachung mit terrestrischem Laserscan und der Erfassung von meteorologischen Daten (Temperatur, Niederschlag, etc.) und Bohrlochtemperaturen. „Damit können potentielle Zusammenhänge zwischen Permafrostveränderungen und Felsstürzen untersucht und unter dem Aspekt der Klimaerwärmung diskutiert werden." betont Markus Keuschnig, Geoconsult Research

& Developement. Aktuell sind die Instrumentierungsarbeiten im vollen Gange, mit ersten Ergebnissen ist 2016 zu rechnen. Die bereits erwähnte Notwendigkeit einer langfristigen Beobachtungsstrategie wird durch die Eingliederung der SeisRockHT-Netzwerke in das bestehende Österreichische Erdbebennetz angestrebt. Der Österreichische Erdbebendienst (ZAMG) ist ein SeisRockHT-Projektpartner.

Citizen Science: Forschung für alle

Neben dem prioritären wissenschaftlichen Anspruch verfolgt SeisRockHT auch die ‚Citizen Science'-Idee. „Eine Besonderheit der verwendeten Messgeräte ist, dass sie als Open Hardware entwickelt worden sind. Das bedeutet, dass alle Interessierten die Baupläne der Messgeräte sowie die notwendige Software aus dem Internet herunterladen und frei verwenden, aber auch abändern und weiterentwickeln können. Damit lässt sich unkompliziert eine professionelle und kostengünstige Erdbebenstation bauen. Durch den relativ geringen finanziellen Aufwand und die gemeinsame Weiterentwicklung des Messsystems können wissenschaftliche Projekte einfacher umgesetzt werden. Im Idealfall entwickelt sich daraus ein Citizen Science Projekt mit interessierten Menschen, die nicht aus dem klassischen Forschungsbereich kommen", erklärt der Seismologe und Entwickler der Messgeräte, Stefan Mertl, und ergänzt, „Jetzt werden wir aber zuerst einmal sehen wie sich die Geräte in der hochalpinen Umgebung der Hohen Tauern schlagen. Um die wertvollen Daten im Falle von Problemen mit den neuen Messgeräten nicht zu verlieren, verwenden wir auch redundante, bereits etablierte Messgeräte."

Kooperation wissenschaftlichen Organisationen und privaten Unternehmen

Das von der Österreichischen Akademie der Wissenschaften (ÖAW) geförderte Projekt SeisRockHT besteht aus Wissenschaftlern der ZAMG, Mertl Research GmbH und Geoconsult Research & Developement.

Steinschlag-Messungen in den Hohen Tauern: Vorbereitung des seismischen Messgeräts für die Montage im Bohrloch beim Sonnblick-Observatorium. Quelle ZAMG/Binder.

heute österreich vom 11.08.2015 17.05 Uhr heute österreich 1705

heute österreich (17:05) - ZAMG: Wenige Frosttage erwartet

Teubenbacher Peter (ORF) Wer es lieber kühl hat, der ist zur Zeit in den Bergen gut aufgehoben - wenngleich es auch dort immer wärmer wird. Am Sonnblick-Observatorium der Zentralanstalt für Meteorologie werden heuer so wenige Frosttage wie selten in der 100-jährigen Messgeschichte erwartet.

Videofile: http://www.hektor.apa.at/InstantVideos/20150811/5742219.m4v

"salzburg.com" gefunden am 10.08.2015 11:03 Uhr

salzburg.com: Manche mögen's kühl: Das sind Salzburgs erfrischendste Orte

Von Michaela Hessenberger | 10.08.2015 - 10:59 | aktualisiert: vor 0 Minuten | Kommentieren

Christian Ortner von der ZAMG (Zentralanstalt für Meteorologie und Geodynamik) reicht ein Blick in seinen Computer und schon weiß er, welche die kühlste Gemeinde im Lande ist: "In Obertauern hat es 16,7 Grad", sagt der Meteorologe am Montagvormittag. Doch es geht auch kühler. Am Sonnblick, auf mehr als 3100 Metern Seehöhe, hat es derzeit acht Grad. "Mehr als zehn werden es dort heute nicht mehr werden", sagt er. In den Niederungen kann der Lungau mit den niedrigsten Werten aufwarten: In Mariapfarr etwa hat es 17,3 Grad. In Bischofshofen ist es im Vergleich zu anderen Landesteilen mit 20 Grad auch noch mild.

Null Grad in der eisigen Höhle

Wer frostige Erlebnisse vorzieht, dem wird eine Reise nach Werfen gefallen: In der

Eisriesenwelt hat es null Grad - konstant das ganze Jahr über. "Eine Tour dauert je nach Gehgeschwindigkeit zwischen 70 und 90 Minuten", berichtet Harald Schlager. Im Skianzug muss man trotzdem nicht durch die bizarre Welt aus Eis gehen. "1400 Treppen sorgen schon dafür, dass einem nicht kalt wird", sagt der Experte. Eine normale Jacke reicht in diesen Tagen also völlig aus.

Feiner Sprühnebel sorgt für wohliges Frösteln

21 Grad hat es am Montagvormittag in Krimml. Wer vom großen Parkplatz aus 15 Minuten spaziert, kommt beim untersten Wasserfall an. Dort kann man der brütenden Sommerhitze entgehen. "Auf Bänken können sich Besucher entspannen und dann zu den weiteren Wasserfällen gehen", erzählt Monika Widmann vom Alpenverein. Und je näher man den Wassermassen bei den Krimmler Wasserfällen kommt, desto angenehmer wird es: Sprühnebel liegt in der Luft. Die feinen Wassertröpfchen kühlen die Haut.

Mehr zum Thema

In Krimml ist nun Hochsaison. Bis zu 4000 Tagesbesucher zieht es in den Pinzgau. "Einige kommen schon extra, damit sie sich von der Hitze erholen", sagt Widmann.

Mit der Rutsche ins kühle Dunkel

"Glück auf" heißt es über Hallein. Zehn Grad hat es in den Salzwelten, dem ältesten Besucherbergwerk der Welt - das ganze Jahr über. Helga Pucher erlebt immer wieder Menschen, die extra aus der Stadt auf den Dürrnberg kommen, um der Hitze zu entkommen. Zwischen 1500 und 2500 Besucher zählt das Bergwerk im Moment täglich. Während früher mehr Leute bei Schlechtwetter kamen, kommen mittlerweile auch an heißen Tagen viele auf die Idee, in den Berg abzutauchen.

Weiterer Vorteil der Salzwelten: Während Klimaanlagen in Autos, Büros oder Geschäften den Organismus strapazieren und einige Menschen verkühlt sind, schwärmen Besucher in Hallein von der Luft im Berg, die nicht nur erfrischend ist, sondern auch auf die Atemwege beruhigend wirkt.

Erfrischende Seen: Es gibt sie noch

Mit 23 Grad ist der Zeller See der kälteste, dicht gefolgt vom Fuschlsee, der bei 23,7 Grad hält. Temperaturrekord: Der Wallersee hat 26,3 Grad. Das Land Salzburg justiert die Werte regelmäßig nach. Im Waldbad Anif kann man durch das 18 Grad kühle Wasser schwimmen.

Ein Blick ins benachbarte Bayern: Der Königssee hat 20,8 Grad, die Aache ist noch etwas kälter.

"salzburg.com" gefunden am 10.08.2015 12:24 Uhr

salzburg.com: Genug von der Hitze? Das sind Salzburgs kühlste Orte

Von Michaela Hessenberger | 10.08.2015 - 12:18 | aktualisiert: vor 2 Minuten | Kommentieren

Christian Ortner von der ZAMG (Zentralanstalt für Meteorologie und Geodynamik) reicht ein Blick in seinen Computer und schon weiß er, welche die kühlste Gemeinde im Lande ist: "In Obertauern hat es derzeit 16,7 Grad", sagt der Meteorologe am Montagvormittag. Doch es geht auch kühler. Am Sonnblick, auf mehr als 3100 Metern Seehöhe, sind es acht Grad. "Mehr als zehn werden es dort heute nicht mehr werden", sagt er. Wer sich kurzfristig in kühlere Gefilde begeben will, ohne dabei baden zu gehen, kann es mit einem der folgenden Orte versuchen:

Feiner Sprühnebel sorgt für wohliges Frösteln

21 Grad hat es am Montagvormittag in Krimml. Wer vom großen Parkplatz aus 15 Minuten spaziert, kommt beim untersten Wasserfall an. Dort kann man der brütenden Sommerhitze entgehen. "Auf Bänken können sich Besucher entspannen und dann zu den weiteren Wasserfällen gehen", erzählt Monika Widmann vom Alpenverein. Und je näher man den Wassermassen bei den Krimmler Wasserfällen kommt, desto angenehmer wird es: Sprühnebel liegt in der Luft. Die feinen Wassertröpfchen kühlen die Haut.

Mehr zum Thema

In Krimml ist nun Hochsaison. Bis zu 4000 Tagesbesucher zieht es in den Pinzgau. "Einige kommen schon extra, damit sie sich von der Hitze erholen", sagt Widmann.

Mit der Rutsche ins kühle Dunkel

"Glück auf" heißt es über Hallein. Zehn Grad hat es in den Salzwelten, dem ältesten Besucherbergwerk der Welt - das ganze Jahr über. Helga Pucher erlebt immer wieder Menschen, die extra aus der Stadt auf den Dürrnberg kommen, um der Hitze zu entkommen. Zwischen 1500 und 2500 Besucher zählt das Bergwerk im Moment täglich. Während früher mehr Leute bei Schlechtwetter kamen, kommen mittlerweile auch an heißen Tagen viele auf die Idee, in den Berg abzutauchen.

Weiterer Vorteil der Salzwelten: Während Klimaanlagen in Autos, Büros oder Geschäften den Organismus strapazieren und einige Menschen verkühlt sind, schwärmen Besucher in Hallein von der Luft im Berg, die nicht nur erfrischend ist, sondern auch auf die Atemwege beruhigend wirkt.

Null Grad in der eisigen Höhle

Wer frostige Erlebnisse vorzieht, dem wird eine Reise nach Werfen gefallen: In der

Eisriesenwelt hat es null Grad - konstant das ganze Jahr über. "Eine Tour dauert je nach Gehgeschwindigkeit zwischen 70 und 90 Minuten", berichtet Harald Schlager. Im Skianzug muss man trotzdem nicht durch die bizarre Welt aus Eis gehen. "1400 Treppen sorgen schon dafür, dass einem nicht kalt wird", sagt der Experte. Eine normale Jacke reicht in diesen Tagen also völlig aus.

Erfrischende Seen: Es gibt sie noch

Mit 23 Grad ist der Zeller See der kälteste, dicht gefolgt vom Fuschlsee, der bei 23,7 Grad hält. Temperaturrekord: Der Wallersee hat 26,3 Grad. Das Land Salzburg justiert die Werte regelmäßig nach. Im Waldbad Anif kann man durch das 18 Grad kühle Wasser schwimmen.

Ein Blick ins benachbarte Bayern: Der Königssee hat 20,8 Grad, die Aache ist noch etwas kälter.

"derstandard.at" gefunden am 08.08.2015 17:09 Uhr

derstandard.at: Zwei Wiener Wegbereiter der Klimaforschung

Julius Hann war Pionier der modernen Meteorologie, Eduard Brückner beschrieb erstmals den menschlichen Einfluss auf das Klima

Wien – Dass der Mensch das Klima verändert, ist längst eine unbestrittene Tatsache. Und die Lage ist mittlerweile so dramatisch, dass rasches Handeln nötig ist. Seit wann aber weiß die Forschung, dass der Mensch ins Klimageschehen eingreift?

Zwar prägte der französische Mathematiker Joseph Fourier bereits im Jahr 1827 den Begriff "Treibhauseffekt", und der schwedische Chemiker Svante Arrhenius beschrieb als Erster den Einfluss von Kohlendioxid auf die Atmosphäre. Der eigentliche Pionier, der Klimaschwankungen wie auch menschliche Einflüsse auf das Klima analysierte, war ein Professor der Uni Wien: der 1862 geborene Geograf Eduard Brückner. Im Jahr 1890 veröffentlichte der aus Jena stammende Forscher das Werk

Klimaschwankungen seit 1700 , das ihn zu einer der führenden europäischen Autoritäten in Klimafragen machte, wie es ein US-Kollege formulierte.

Die Dynamik des Klimas

Brückners Studie war in zumindest zweifacher Hinsicht wegweisend, erläutert sein Wiederentdecker, der deutsche Soziologe Nico Stehr: "Zum einen trug sie dazu bei, Klima nicht als ein statisches, sondern als ein dynamisches Geschehen zu betrachten." Zum anderen sei Brückner davon ausgegangen, dass sich das Klima aufgrund des menschlichen Einflusses veränderte. Konkret bezog er sich etwa auf die Abholzung der Wälder rund um das Kaspische Meer und das Mittelmeer.

1906 wurde Brückner dann Professor an der Universität und blieb das bis zu seinem frühen Tod 1927. Brückner war nicht nur Gelehrter, sondern auch Popularisator und sehr daran interessiert, seine Ergebnisse in die Öffentlichkeit zu tragen: Er hielt öffentliche Vorträge, schrieb für Zeitungen, und seine Erkenntnisse wurden sogar in parlamentarischen Kommissionen erörtert.

Noch einflussreicher als Brückner war dessen um 23 Jahre älterer Kollege Julius Hann, einer der maßgeblichen Pioniere der modernen Meteorologie. Der im Mühlviertel geborene Hann kam 1867 an die heutige Zentralanstalt für Meteorologie und Geodynamik, deren Leitung er zehn Jahre später übernahm. Daneben war er Professor für die Physik der Erde an der Universität Wien.

In beiden Funktionen wurde er zum Wegbereiter einer modernen Erforschung des Wetters wie auch des Klimas: Hann entwickelte nicht nur Methoden, die komplexen meteorologischen Daten verwertbar zu machen. Vor allem bemühte sich Hann, die neuen Erkenntnisse der Physik – wie etwa die Thermodynamik – für die Analyse des Wettergeschehens nutzbar zu machen und konnte so erstmals die Entstehung des Föhns wissenschaftlich beschreiben.

Diese Verbindung von Empirie und Theorie hatte auch praktische Folgen, nämlich die Gründung von meteorologischen Observatorien wie jenem auf dem Sonnblick oder auf dem Hochobir, die auf Hanns Initiative zurückgehen: Ihm war aufgrund seiner Forschungen klar, dass Daten aus großer Höhe unumgänglich sind zur Vorhersage des Wetters in den Alpen.

Von den Alpen in die Welt

Hann, der ebenso wie Brückner ein Spezialist für das Wetter und das Klima Österreichs war, dachte aber auch räumlich weit darüber hinaus: Er beschäftigte sich unter anderem mit der Entstehung tropischer Wirbelstürme und veröffentlichte 1883 das zunächst einbändige Handbuch für Klimatologie , das in dritter Auflage 1911 bereits auf drei Bände angewachsen war. Und als er

1910 als Professor der Universität Wien emeritierte, dankte ihm der Kaiser für sein Lebenswerk mit der Erhebung in den Adelsstand.

Der Zusatz Julius von Hann ging nach 1918 ebenso verloren wie das Wissen um die Pionierleistungen Eduard Brückners: In der Klimatologie setzte sich für Jahrzehnte die irrige Annahme durch, dass Klima etwas Statisches sei. Umso überraschter waren Klimaforscher, als Nico Stehr sie mit Brückners Behauptungen konfrontierte: "Die Naturwissenschaft hat ja sehr oft nur ein bescheidenes historisches Gedächtnis. Oft genug kennen heutige Forscher jene Riesen nicht mehr, auf deren Schultern sie stehen." (Klaus Taschwer, 5.8.2015)

NOW Project Application

NOW – NOise of thaW

Project Type: pilot project (opstartsprojekt)
Project Duration: 1 May 2020 to 1 May 2022
Project Leader: Michele Citterio, GEUS

Societal Relevance & GeoCenter Strategy

This project is highly relevant to the UN Sustainable Development Goals (SDGs) of Climate Action (SDG 13) – which promotes the development of national climate change mitigation and adaptation plans – and Sustainable Cities and Communities (SDG 11) – which promotes resilience to climate change hazards.

The *NOW* project will build on constantly growing GeoCenter expertise with monitoring of the cryosphere, as well as climate-related geohazards. *NOW* directly addresses the GeoCenter strategy of funding pilot projects capable of attracting larger externally-funded follow-on projects.

1. Motivation

Climate change potentially enhances geohazards on global (e.g. sea level rise), regional (e.g. landslide-triggered tsunamis) and local scale (e.g. rock fall). Geohazards are often initiated or accompanied by processes taking place below the surface and with a detectable seismic expression. Continuous monitoring strategies with high temporal resolution are thus required to identify and study the trigger mechanisms. Due to the nature of the seismic signal (e.g. transient ground motion of small amplitude), seismological observation demands high temporal resolution of ground coupled sensors, which so far can’t be replaced by any remote sensing approach. Environmental seismology studies near-surface (non-tectonic, including depths typical of large slope instabilities) processes originating, or affected by external triggers, outside the solid earth. This includes for instance the coupling between the solid earth and the atmosphere, cryosphere, and/or the hydrosphere. Therefore, high quality complementary data on surface weather are indispensable to properly investigate these coupled processes. The *NOW* project aims to enable already established field sites with a seismic component. Each site is situated in a geohazard-relevant area together featuring a suite of crucial near-surface processes. The *NOW* project will site-specifically evaluate the benefit of including local seismic information for the scientific understanding of subsurface processes and their links to surface conditions.. This joint effort will strengthen the involved institutions and monitoring programs by building in-house technical knowhow as base for future research projects and advisory assignments, from site- and process-understanding to potentially providing recommendations on in situ geohazard monitoring and early-warning concepts.

2. Rationale

Environmental seismology monitoring has been successfully applied in studies of a range of near-surface processes, and the local character of the newly acquired data can integrate and complement the existing regional seismic monitoring operated by GEUS. Dietze and others (2017a,b) monitored small-volume rockfall activity in an alpine setting and were able to relate single rockfalls to environmental triggers, whereof the major was rainfall. Using seismic data, Díaz and others (2019) hierarchically classified snow melt events of a river in the Pyrenees, Spain. Terrestrial rivers and streams produce high-frequency (>1 Hz) ambient seismic tremor through turbulent water flow and sediment transport, with lower-frequency signals radiating from turbulent water flow and higher-frequency signals potentially radiating from bed load transport (Gimbert and other 2014; Tsai and others 2012). Flowing water in subglacial conduits also produce seismic tremor (‘glaciohydraulic tremor’), which can be used as a proxy for subglacial water flow (Bartholomaus and others 2015), as well as a proxy for the spatiotemporal evolution of the subglacial water system (Vore and others 2019). Besides monitoring of discrete seismic events, the past decades have witnessed rapid advances in imaging and monitoring subsurface structures with passive signals such as ambient seismic noise (Schuster 2009; Larose and others 2015; Podolsky and Walter 2016). Chaput and others (2018) report ambient noise spectral peak changes at frequencies >5 Hz across the Ross Ice Shelf, Antarctica. Spectral peak changes coincide with melt/freeze events, as well as with storm-driven redistribution of snow. They conclude that melt events have a unique spectral signature and can be modeled in terms of the penetration depth to which these thermal anomalies diffuse in the firn layer. For steep bedrock permafrost, Weber and others (2018) found a relation between ambient seismic noise resonance frequency and rock temperature, exhibiting an annually repeated pattern with hysteretic behavior. Their findings suggest that the temporal resonance frequency variations are linked to the formation and melt of ice-fill in bedrock fractures.

The velocity of seismic waves is dependent on the mechanical properties of the medium, which vary with temperature, water/ice content and stress conditions. Seismic noise interferometry (Schuster 2010; Waapenar and others 2010; Behm and others 2014) is a novel ambient seismic noise methodology providing relative changes of seismic velocities with high accuracy. The seismic impulse response between two different sites can be reconstructed by cross-correlating ambient noise signals recorded simultaneously, effectively turning one of the receivers into a virtual source (Larose and others 2015; Galetti and Curtis, 2012; Wapenaar and others 2010a,b). With ubiquitous and constant ambient seismic noise throughout the data recording, this method can continuously monitor mechanical changes in the subsurface through changing arrival times for a given seismic wave-packet (Larose and others 2015; Planes and others 2015; Behm 2016). Applying seismic interferometry, James and others (2019) observed clear seasonal seismic velocity variations for the permafrost-prone Poker Flat Research Range, Alaska. Short timescale seismic velocity changes highlighted the importance of infiltration events for seasonal active-layer melt/freeze cycles. Behm and others (2020) observed systematic seismic velocity variations for an Arctic glacier throughout its melt season. The observed seismic velocity variation potentially indicated a switch of the subglacial drainage system characteristic initiated by a glacial lake outburst event. Mainsant and others (2012) observed a drop of seismic velocities for the Les Diablerets landslide (Switzerland) five days before the landslide collapsed.

3. Methods

In the sense of environmental seismology, the *NOW* project is following a multidisciplinary data collection strategy. To minimize costs, *NOW* can build upon already established in situ instrumentation of the *PROMICE*and *GEM GlacioBasis* long term monitoring programs as well as those from ongoing projects such as the Greenland Landslides Project. *T*he *PROMICE* and *GlacioBasis* stations are situated on glaciers, and the Landslides Project stations in Vaigat are on permafrost terrain. These different site characteristics allow covering a range of crucial near-surface processes linked with climate. The *NOW* project will upgrade in total five operational monitoring sites with a seismic component. Three *NOW* stations will be on glaciers, whereas two will be installed on the A.P. Olsen Ice Cap (NE-Greenland), and one will be installed in the ablation zone of the Greenland ice sheet. One A.P. Olsen Ice Cap station will be situated in the accumulation zone. The remaining two *NOW* stations will be deployed within the *Landslides Project* sites in the Vaigat Strait (W-Greenland), of which one *NOW* station will be deployed next to the Paatuut landslide where regular rock fall events can be observed. The *NOW* stations deployment will happen alongside planned *PROMICE*, *GlacioBasis*, and *Landslides Project* field trips to minimize *NOW* fieldwork costs. *NOW* will analyze discrete events, as well as the ambient noise of the gathered seismic data. The Paatuut site with it’s frequent rock falls is especially suited for discrete event detection and back azimuth calculation. Ambient seismic noise will be analyzed for all *NOW* stations. Furthermore, novel single- and multistation seismic interferometry will be performed. All seismic results will be analyzed in view of the available complementary data which cover comprehensive meteorological parameters, as well as subsurface temperatures. Finally, an outlook for future project initiatives will be formulated and potential alternative applications of the *NOW* monitoring strategydiscussed.

Novel approaches in seismology involve new strategies for data collection, unconventional instrumentation and the development of new algorithms to process the data. The combination of these needs limits the usage of costly commercial off the shelf hardware and software packages.

Consequently, the *NOW* project will rely on proven open software and free hardware designs which also provide a substantial technology and science knowledge transfer to the involved institutions. The open software project *pSysmon* is especially dedicated to non-standard seismological studies. The *pSysmon* main developer is project partner S. Mertl *(Mertl Research GmbH)*. Under the supervision of project partner Prof. M. Behm *(University of Oklahoma)*, the *NOW* project will add a seismic interferometry module to the *pSysmon* software. The *Ruwai* seismic datalogger is a free hardware design project by project partner S. Mertl, and meets our needs of data collection in rugged conditions. The main focus of the *Ruwai* project is on full documentation and easy reproducibility. Currently, the *Ruwai* datalogger is successfully deployed within a rockfall monitoring project in the Austrian Alps by project partners S. Mertl and D. Binder (Binder and others 2017). The *Ruwai* datalogger can also handle non-seismic sensors with different sampling rates which makes it especially suitable for environmental seismology applications. All *Ruwai* dataloggers will be built in-house at GEUS by the Glaciology and Climate Department's workshop. Due to the high frequency (>1 Hz) nature of near-surface processes, *NOW* project applies robust, low-cost industrial geophones as seismic sensors (e.g. Geospace GS-One LF Geophone). This sensor strategy was already successfully applied on ice (Behm and others 2020) and on land (Binder and others 2017), where signal frequencies of <1 Hz could be resolved.

4. *NOW* Research Questions

Research questions for the ice-based *NOW* sites are:
→ Are there ambient noise spectral peak changes coinciding with melt/freeze events?
→ Can we estimate the penetration depth to which thermal anomalies diffuse in the firn layer?
→ Can we identify supra- and subglacial melt water flow?
→ Can we estimate melt water flow rates?
Research questions for the land-based *NOW* sites are:
→ Can we identify and count rock fall events with the *NOW* setup?
→ Is there a relation between the ambient noise resonance frequency and rock temperature?
→ Can we monitor active-layer dynamics by seasonal and episodic seismic velocity variations?
→ Can we identify infiltration and/or high groundwater flow events in the active layer and at depth below the permafrost?

5. Timeline and Workpackages

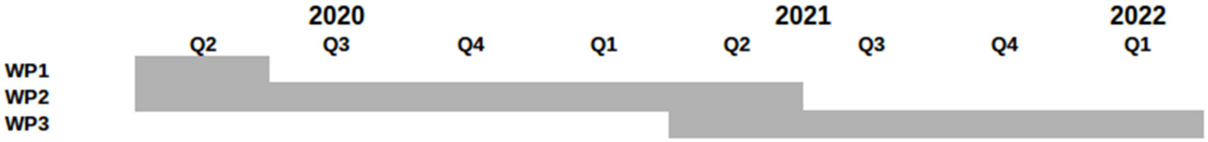

Workpackage #1: Construction of the seismic monitoring systems

GEUS technician, Stefan Mertl (Mertl Research GmbH)

The seismic monitoring systems will be built in-house at GEUS by the Glaciology and Climate Department's workshop. Stefan Mertl will serve as a consultant for the *Ruwai* datalogger assembly.

Workpackage #2: Field work and data collection

Michele Citterio (GEUS, GlacioBasis project manager), Robert S. Fausto (GEUS, PROMICE project mangaer), Kristian Svennevig (GEUS)

NOW station deployment will happen within *PROMICE*, *GlacioBasis*, and *FJELDSKREDS* field trips. In close collaboration with the individual project managers, Michele Citterio and Kristian Svennevig will be responsible for field work planning and execution. One year of data collection is aimed for each monitoring site.

Workpackage #3: Data analysis, interpretation

Michael Behm (University of Oklahoma), Trine Dahl-Jensen (GEUS), Daniel Binder (GEUS, ZAMG), Stefan Mertl (Mertl Research GmbH), Michele Citterio (GEUS), Ylva Sjöberg (KU), Kristian Svennevig (GEUS)

Seismic data will be analyzed by Daniel Binder under the supervision of Michael Behm and Trine Dahl-Jensen. Stefan Mertl will serve as *pSysmon* consultant. A two months research stay at the University of Oklahoma is planned for Daniel Binder. Ylva Sjöberg, Michele Citterio and Kristian Svennevig will be deeply involved in the process-based interpretation of the seismological and complementary monitoring data, as well as hypothesis formulation for future follow-on projects. Furthermore, a master thesis at IGN (KU) under the supervision of Ylva Sjöberg is aimed.

6. References

Bartholomaus, T. C., Amundson, J. M., Walter, J. I., O'Neel, S., West, M. E., & Larsen, C. F. (2015). Sublacial discharge at tidewater glaciers revealed by seismic tremor. Geophys. Res. Lett., 42, 6391–6398. https://doi.org/10.1002/2015GL064590

Behm M., Walter J., Binder D., Citterio M., Kulessa B., Langley K., Limpach P., Mertl S., Schöner W., Tamstorf M., and Weyss G. (2020) Time-lapse Seismic Characterization of a Rapidly Rising Glacial Lake Outburst Flood (Jökulhlaup) at the A.P. Olsen Ice Cap, NE-Greenland. Journal of Glaciology, accepted.

Behm, M. (2016), Feasibility of borehole ambient noise interferometry for permanent reservoir monitoring. Geophys. Prospect., 65(2), 563-580, doi:10.1111/1365-2478.12424.

Behm M., Leahy G.M., and Snieder R. (2014), Retrieval of local surface wave velocities from traffic noise–an example from the La Barge basin (Wyoming), Geophysical Prospecting 62 (2), 223-243

Binder D., I. Hartmeyer, M. Keuschnig, S. Mertl, W. Lenhardt (2017) SeisRockHT – Seismic Rockfall Monitoring in the Hohe Tauern region (A). Geophys. Res. Abstr., 19, EGU2017-17451.

Chaput, J., Aster, R. C., McGrath, D., Baker, M., Anthony, R. E., Gerstoft, P., et al. (2018). Near-surface environmentally forced changes in the Ross Ice Shelf observed with ambient seismic noise. Geophysical Research Letters, 45. https://doi.org/10.1029/2018GL079665

Díaz J, Sánchez-Pastor P., and Ruiz M (2019) Hierarchical classification of snowmelt episodes in the Pyrenees using seismic data. PLoS ONE 14(10): e0223644. https://doi.org/10.1371/journal.pone.0223644

Dietze, M. and 4 others (2017), Seismic monitoring of small alpine rockfalls – validity, precision and limitations. Earth Surf. Dynam., 5, 653-668, doi.org/10.5194/esurf-5-653-2017.

Dietze, M. and 3 others (2017b), Spatiotemporal patterns, triggers and anatomies of seismically detected rockfalls. Earth Surf. Dynam., 5, 757-779, doi.org/10.5194/esurf-5-757-2017.

Galetti, E., A. Curtis (2012), Generalised receiver functions and seismic interferometry. Tectonophys., 532-535, 1-26, doi:10.1016/j.tecto.2011.12.004.

Gimbert, F. and 2 others (2014), A physical model for seismic noise generation by turbulent flow in rivers. J. Geophys. Res., 119, 2209-2238, doi:10.1002/2014JF003201.

James, S. R., Knox, H. A., Abbott, R. E., Panning, M. P., & Screaton, E. J. (2019), Insights into permafrost and seasonal active-layer dynamics from ambient seismic noise monitoring. Journal of Geophysical Research: Earth Surface, 124

Larose, E. and 11 others (2015), Environmental seismology: What can we learn on earth surface processes with ambient noise? J. Appl. Geophys., 116, 62-74, doi:10.1016/j.jappgeo.2015.02.001.

Mainsant, G., Larose, E., Broennimann, C., Michoud, C., Jongmans, D. (2012) Ambient seismic noise monitoring of a clay landslide: toward failure prediction. J. Geophys. Res., 39(L19301).

Planes, T. and 5 others (2015) Time-lapse monitoring of internal erosion in earthen dams and levees using ambient seismic noise. Geotechnique, 66(4), 301-312.

Podolsky, E.A., F. Walter (2016), Cryoseismology. Rev. Geophys., 54, doi:10.1002/2016RG000526.

Schuster, G.T. (2009), Seismic Interferometry, Cambridge University Press

Tsai, V.C. and 3 others (2012), A physical model for seismic noise generation from sediment transport in rivers. Geophys. Res. Lett., 39(2), doi.org/10.1029/2011GL050255.

Vore M.E. and 4 others (2019), Seismic Tremor Reveals Spatial Organization and Temporal Changes of Subglacial Water System. J. Geophys. Res.: Earth Surf., 124. https://doi.org/10.1029/2018JF004819

Wapenaar K., Draganov D., Snieder R., Campman X. and Verdel A. (2010), Tutorial on seismic interferometry: Part 1 – Basic principles and applications, Geophysics, 75, 75A195–75A209

Wapenaar, K. and 3 others (2010b), Tutorial on seismic interferometry: Part 2 – Underlying theory and new advances. Geophys., 75(5), 75A211-75A227, doi:10.1190/1.3463440.

Weber S. and 5 others (2018) Ambient seismic vibrations in steep bedrock permafrost used to infer variations of ice-fill in fractures. Earth and Planetary Science Letters, 501, 119-127. https://doi.org/10.1016/j.epsl.2018.08.042